Inversion of 2D and 3D DC resistivity imaging data for high contrast geophysical regions using artificial neural networks

by

Ahmad Neyamadpour

Thesis submitted to the Faculty of Science of the University of Malaya for the fulfillment of the degree of Doctor of Philosophy

University of Malaya

2010

To

my beautiful daughter, Atena

Abstract

In electrical resistivity imaging surveys, the field data along a profile are normally acquired as a subsurface distribution of apparent resistivity. One common method to obtain the true resistivity distribution is by inverting the apparent resistivity values. However, the inversion of DC resistivity imaging data is complex due to its non-linearity. This is especially true for regions with high resistivity contrast.

For the complicated subsurface structure, especially when regions of high resistivity contrast exist, a conventional inversion technique based on least squares methods may not be able to invert the DC resistivity data with adequate accuracy. Therefore, in this study, we investigate the applicability of artificial neural networks in the inversion of 2D and 3D electrical resistivity imaging data obtained with five common electrode arrays, i.e., Wenner-Schlumberger, Wenner, dipole-dipole, pole-dipole, and pole-pole arrays. The basics of the DC resistivity survey and that of the 1D, 2D and 3D surveys are discussed in this thesis. The common arrays used for the 2D and 3D surveys are compared using the following characteristics: (i) the signal strength, (ii) the horizontal data coverage, (iii) the sensitivity of the array to horizontal structures, (iv) the sensitivity of the array to vertical structures, and (v) the depth of investigation for each array.

In order to study the numerical simulation of the measured data for a given subsurface parameter, the basis of the finite difference method and the various boundary conditions are explained here. By comparing the common non-linear least square inversion methods (i.e., the steepest descent method, the nonlinear conjugate gradients method, Newton-type methods and smoothness-constrained least squares methods), the L1_ norm smoothness-constrained optimization method (or robust inversion technique) has been

recognized as the most efficient of the least squares methods mentioned here, because it sometimes gives relatively better results in high resistivity zones with sharp boundaries.

In order to study the effect of data pool formation in training the neural network, two methods have been used to generate the synthetic data. These methods are M1 and M2, and they basically differ in the type of input-output data used to train the artificial neural network. The effect of the input-output data type is investigated by 2D and 3D study. The results suggest that the synthetic data generated by M2_2D and M2_3D methods may be the best data type for training and testing the neural networks in this study.

The effect of the number of nodes in each layer of the network (for 2D and 3D cases) have been studied which determined the simplest architecture for the neural network that can reach the desired threshold error for each array. The effect of the training data pool volume in the 2D and 3D parts of this study has also been evaluated, and the sufficient volume for each data type is selected.

Furthermore, five common training paradigms, i.e., batch training with weight and bias learning rules, conjugate gradient with Fletcher reverse updates, resilient propagation, gradient descent with momentum and adaptive learning rate and Levenberg-Marquardt with weight and bias learning rules, are compared for both 2D and 3D. These results show that, for all the arrays (2D and 3D) except 3D pole - dipole data, resilient propagation is the most efficient algorithm for training the DC resistivity data. In the case of 3D study of pole - dipole data, the gradient descent with momentum and an adaptive learning rate algorithm is found to be the most efficient paradigm.

In addition, an interpolation and extrapolation properties of the neural network have been studied using another 24 synthetic datasets generated for each array. The RMS errors

for all the interpolation and extrapolation test sets related to each array are in the range of 0.3 - 9.0%. It is therefore, concluded that the networks are properly designed and trained.

The ability of the trained neural networks to invert the 2D and 3D DC resistivity imaging data is also checked using real field datasets from a site with high resistivity contrast. The inverted field data from the neural network is then compared with inverted results from the conventional robust inversion method for each array. Further study using a synthetic example similar to the field data is conducted for each array in order to evaluate the reliability and accuracy of the inversion results using both the neural network and the robust inversion technique.

All the subsurface features were nearly resolved by the results of both these methods. However, the neural network results are found to be more realistic, especially for the vertical columns and horizontal pipes. In contrast, the robust inversion method produced a relatively smaller vertical dimension than the actual size of the real field data.

When the inversion results of both the neural network and the robust inversion methods for the synthetic test models were compared with their corresponding physical resistivity models, it has been found that the depths of the anomalies in the results of the robust inversion method results are less pronounced than their actual values. In addition, the robust inversion method produced smaller resistivity values than their actual values, but in comparison the result from neural network produced better physical models. It is thus, concluded that the neural network results are more accurate than the results from robust inversion method.

Acknowledgements

The present work could not have been possible without the help of other people that I would like to thank now. I gratefully acknowledge the guidance and support of my supervisors, Prof Dr. Wan Ahmad Tajuddin Wan Abdullah (Department of physics, University of Malaya) and Assoc. Prof Dr. Samsudin Hj Taib (Department of Geology, University of Malaya) during the course of this work. This study was generously supported by the University of Malaya through a PhD fellowship and two postgraduate studies grants (PS203/2008B, and PS318/2009B).

I am indebted to Prof Dr. Viacheslav Spichak of the Geoelectromagnetic Research Institute RAS, Russia and Dr. God El-Qady of the National Research Institute of Astronomy & Geophysics (NRIAG), Egypt, for their constructive criticism, which helped to improve the results of this study. Thanks are also due to Prof. Dr. Josef Pek of the Institute of Geophysics, Acad. Sci. Czech Republic, for his valuable advices.

Finally, my warmest thanks go to my parents for all their love and continuing support throughout this endeavour.

Ahmad Neyamadpour

Kuala Lumpur, Malaysia

January 2010

Table of contents

List of Figures

List of Tables

List of symbols and abbreviations

General notations	
a	scalar value
x	numerical vector (assembled scalars)
x_i	i_{th} component of **x**
A	numerical matrix (assembled vectors)
A_{ij}	element of i_{th} row and j_{th} column
$\vec{F}$	vectorial property of space
Diag(**x**)	diagonal matrix built up of the elements of **x**

DC symbols	
ρ	Electrical resistivity
ρ_a	Apparent resistivity
K	Geometric factor
V	Electric potential
σ	Electric conductivity
I	Electric current
$\vec{j}$	Current density
$\vec{E}$	Electric field
$\vec{B}$	Magnetic field
$\overline{C1P1}$	Distance between electrode C1 and P1

Artificial neural network symbols	
f	activation function
x_i	output from the previous layer
w_{ij}	weight of the link connecting unit *i* to unit *j*
b_j	externally applied bias to neuron j
$f(\mathbf{x}, \mathbf{w})$	output of the network at the output node
ε	learning rate
α	momentum coefficient
MSE	mean square error
d_{pj}	target response value of the output neuron j
a_{pj}	actual response value of the output neuron j
N	number of output units
Q	the number of training samples
Δ_{ij}	step size or update value
D_{ds}	degree of determination of the system

Inversion symbols	
N	number of data
$\boldsymbol{DJ}$	error-weighted sensitivity matrix
$\mathbf{W}(\vec{r}) \in \mathfrak{R}^{\mathbf{N\times M}}$	constraint eigenvector matrix
ζ	regularization / Lagrangian parameter
$\mathbf{m}_{zero}$	starting (or a-priori) model
$\boldsymbol{C} \in \mathfrak{R}^{\mathbf{P\times M}}$	model constraint matrix
$\mathbf{R_d}$ *and* $\mathbf{R_m}$	weighting matrices in L1_ norm
ξ_i	data error
$\boldsymbol{D} \in \mathfrak{R}^{\mathbf{N\times M}}$	data weighting matrix
Ψ_d	data functional
$\mathbf{H}$	Hessian matrix
∇_m	gradient with respect to the model
$\boldsymbol{C_d}$	covariance matrix
$\mathbf{D^T D}$	inverse of the data covariance matrix
$\Delta\boldsymbol{d}$	data discrepancy vector
$\Delta\boldsymbol{m}$	model update vector
$\mathbf{J} \in \mathfrak{R}^{\mathbf{N\times M}}$	sensitivity matrix
$\boldsymbol{q(m)} \in \mathfrak{R}^{\mathbf{N}}$	forward response of m
$\mathbf{m_k}$	model vector of the k_{th} iteration step
$\boldsymbol{m} \in \mathfrak{R}^{\mathbf{M}}$	model vector assembling the model
m_i	single model parameter
M	number of model parameter
αx, αy and αz	relative weights given to the smoothness filters in the x-, y- and z-directions

Chapter 1

Introduction

1.1. Background and scope of research

Electrical resistivity surveys have been widely used to study the electrical properties of underground structures. Two of the earliest recorded electrical resistivity studies in earth science were executed by Gray and Wheeler in 1720 and Watson in 1746 (Jakosky, 1950; Van and Cook, 1966). Gray and Wheeler have measured the electrical conductivities of various subsurface materials and Watson has discovered that ground transmits electricity (Van and Cook, 1966). However, they did not use quantitative techniques in their studies. The first successful attempt on the application of direct currents (DC) to evaluate earth resistivity was made by Conrad Schlumberger in 1920 (Loke, 2009). Although electrical resistivity studies in geology were performed in the early eighteenth century, their applications came into wide use only after the advent of computer technology during 1970s (Reynolds, 1997). Modern multi-channel resistivity instrumentation has then facilitated an increased use of electrical resistivity surveying over large and complex areas.

In the past few years, the technique of electrical resistivity imaging (ERI) has become one of the most significant geophysical approaches to investigating underground near-surface structures. In electrical resistivity imaging surveys, field data along a profile are normally acquired as a subsurface distribution of the apparent resistivity. One common procedure to obtain the true resistivity distribution is by inverting the apparent resistivity values. However, the inversion of DC ERI data is complex due to its non-linear behavior (Singh et al., 2005). This is especially true for regions with high resistivity contrast (El-

Qady and Ushijima, 2001). During the past few decades, various approaches to inverting 1D DC resistivity data have been published (e.g., Pekeris, 1940; Argilo, 1967; Meheni et al., 1996). The inversion of 2D DC resistivity method (based on the finite difference or finite element method) has been used to interpret geoelectrical resistivity data (Dey and Morrison, 1979; Loke and Barker, 1996a). Because many of the problems associated with geophysical exploration are of three-dimensional (3D) nature, several algorithms for treating the 3D ERI problem have been developed (Loke and Barker, 1996a; Zhao and Yedlin, 1996; Dahlin and Loke, 1997; Spitzer, 1998; Tsourlos and Ogilvy, 1999). These algorithms are also based on the finite element, finite difference, and integral method. Developing a stable inverse problem solution that could resolves complicated geological structures is an obstacle in the inversion of geophysical data (El-Qady and Ushijima, 2001).

Geophysical prospecting uses various techniques that can be addressed using artificial neural networks. These include: interpreting well logs (Wiener et al., 1991), processing EM sounding data (Poulton et al., 1992; Winkler, 1994), ground penetration radar (Poulton and El-Fouly, 1991; Al-Nuaimy et al, 2000), filtering (Wang and Mendel, 1992), recognizing seismic waveforms (Ashida, 1996), sub-basalt imaging (Elaine et al, 2001), seismic deconvolution (Kahoo et al., 2006) and inverting vertical electrical sounding (VES) data to delineate geothermal reservoirs (El-Qady et al., 2000). Neural networks have been used by the petroleum industry to process seismic data during the past few years (Murat and Rudman, 1992). Singh et al. (2005) and Calderon-Macias et al. (2000) studied the applicability of neural networks to solve some geophysical inverse problems for 1D VES and seismic data, respectively. El-Qady and Ushijima (2001) launched an investigation into the applicability of neural networks in inverting 1D and 2D resistivity data obtained by VES surveys for area with nearly low resistivity regions. Ho (2009) has

performed a 3D inversion of borehole-to-surface electrical resistivity data using neural networks.

1.2. Aims and objectives

In 2D and 3D ERI surveys, a few hundred to several thousand measured data points are used. For a complicated subsurface structure, especially with high resistivity contrast pockets, the conventional inversion technique based on least squares methods may not be a suitable choice to invert the DC resistivity data accurately. Therefore, the aim of this study is to investigate the applicability of artificial neural networks in the inversion of 2D and 3D electrical resistivity imaging data obtained from five common electrode arrays, i.e., Wenner-Schlumberger, Wenner, dipole-dipole, pole-dipole and pole-pole arrays. The main research objectives are:

- To create 2D and 3D synthetic datasets to train and test the neural networks.
- To examine the effect of the input-output data type in the training process.
- To examine the effect of the number of nodes in each layer of the networks for 2D and 3D studies and set the proper learning rate and momentum.
- To investigate the effect of the training data pool volume in 2D and 3D study.
- To determine an efficient neural network learning paradigm.
- To apply the trained neural networks to 2D and 3D DC resistivity data collected from a site with high resistivity contrast regions.

1.3. Thesis structure

Chapter two of this thesis reviews conventional methods allowing the measurement of DC electrical resistivity. The DC resistivity method is based on the stationary flow of electric current. A thorough understanding of DC resistivity is important because the inversion of measured field data using artificial neural networks can be regarded as a generalization of the DC method. Here, an explanation is given about the common arrays used in 2D, quasi-3D and 3D surveys; i.e., Wenner-Schlumberger, Wenner, dipole-dipole, pole-dipole and pole-pole arrays, and analyze the published literature regarding the 3D resistivity problem from 1991 onward. The following characteristics is then compared for these common arrays: (i) the signal strength, (ii) the horizontal data coverage, (iii) the sensitivity of the array to horizontal structures, (iv) the sensitivity of the array to vertical structures, and (v) the depth of investigation.

In order to study the suitability of different arrays in resistivity surveys, several parameters are considered for this study, including the depth of investigation and the vertical and horizontal resolutions. As a common way to study these parameters, the sensitivity functions for each array is calculated and the respective 2D and 3D plots are then prepared.

The third chapter provides an insight into the inversion process in an abstract way without touching the special problems of DC data. The importance of the inversion of the measured data obtained through DC resistivity surveys is presented in this chapter. Firstly, the basis of the finite difference method and different boundary conditions is discussed, in order to study the numerical simulation of the measured data for given subsurface parameters. Here, it is also demonstrated how the DC sensitivities can be obtained for a given physical model. Then, the methodology of non-linear inversion and the common

inversion methods is discussed, i.e., steepest descent method, nonlinear conjugate gradients method, Newton-type methods and smoothness constrained least squares methods. These methods have been used to evaluate which non-linear inversion method is the most appropriate for our study.

Chapter four briefly describes the architectures of the artificial neural network. One of the widely used neural networks for multivariate correlation and pattern recognition is the feed-forward network. The mathematical basis of the most common learning law, i.e., back propagation, is discussed as a training law for the feed forward neural network. In order to find an efficient training paradigm, the following, most common training algorithms are compared, i.e., batch training with weight and bias learning rules, conjugate gradient with Fletcher reverse updates, resilient propagation, gradient descent with momentum and adaptive learning rate, and Levenberg-Marquardt with weight and bias learning rules. The mathematical aspect of the resilient propagation algorithm (RPROP) is discussed because it has been recognized as the most efficient algorithm in this study as mentioned in chapter five. A brief introduction of some important terms is also presented in this chapter, e.g., the learning rate and momentum coefficient, choosing the number of hidden layers and selecting the initial weights to design and train the artificial neural network. The network generalization ability is discussed at the end of this chapter.

The synthetic data generation used to train and test the neural networks is explained in chapter five. The process of training the ANN and selecting training parameters is discussed for data obtained from five common arrays of the 2D and 3D surveys.

In order to study the effect of data pool formation in the training process, two methods were used to generate the synthetic data. These methods are called M1 and M2, which basically differ in terms of input-output data in training the network. The details of each method are discussed for both 2D and 3D synthetic datasets.

The effects of the number of nodes in each layer and the training data pool volume in 2D and 3D parts of this study are investigated. A comparison between five common training paradigms as mentioned in chapter four for 2D and 3D has been made for data obtained by each array.

In order to study the interpolation and extrapolation properties of the 2D and 3D trained networks, 24 synthetic datasets were generated for each array. The range of 100 – 1000 Ωm was divided into 100, 200, 300, 400, 500, and 600 Ωm as background resistivity, and different resistivity values for the anomalous body were considered.

In chapter six, the ability of the trained networks to invert the DC resistivity imaging data using real field data related to a site with high resistivity contrast regions is checked. Therefore, in this chapter the application of the neural networks in inverting 2D and 3D DC resistivity data obtained from five common electrode configurations, i.e., Wenner-Schlumberger, Wenner, dipole-dipole, pole-dipole and pole-pole arrays, is explained. The inverted field data from the neural networks is then compared with those obtained from conventional robust inversion technique for each array. Further study using a synthetic example similar to the field data is carried out for each array in order to compare the reliability of the results of both methods. Furthermore, known information about the subsurface features of the site help us check the network performance.

Chapter 2

Direct current resistivity

The DC resistivity technique is the traditional method used to evaluate the resistivity of subsurface materials. It is one of the most popular geophysical methods in electrical exploration. As a result of the availability of automated data-acquisition systems, this method has the ability to produce efficient images of underground structures. Figure 2.1 shows a schematic diagram of a DC resistivity survey. Two current electrodes (C1 and C2) introduce a current into the ground, creating a stationary current flow in the earth. Two potential electrodes (P1 and P2) measure a change in electrical potential by measuring the voltage drop at the surface. From these measurements, a spatial distribution of inherent resistivity can be obtained, which represents a physical model of the subsurface after interpretation.

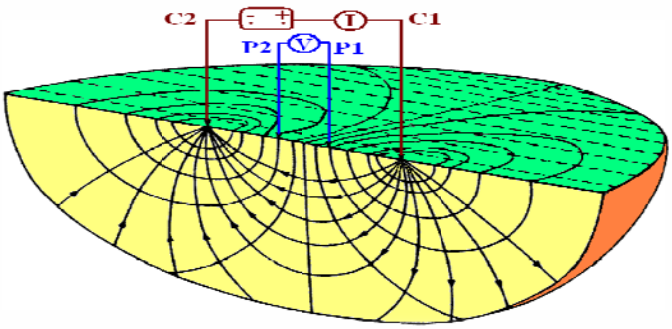

Figure 2. 1. Principle of DC resistivity measurements.

2.1. Basic theory

The comprehensive theory of DC resistivity is given in geophysical textbooks such as Dobrin and Savit (1988), Telford et al. (1990) , Reynolds (1997) and Parasnis (1997). The basics is that of a steady and continuous electric current flow in a homogeneous and

isotropic conductive half space (Kuras, 2002). Following Maxwell's equations of the stationary case, the electric field $\vec{E}$ is the negative gradient of the electrical potential V (Telford et al., 1990):

$$\vec{E} = -\nabla V, \tag{2.1}$$

since $\nabla \times \vec{E} = 0$ for $\frac{\partial \vec{B}}{\partial t} = 0$, this is a comprehensive assumption because it excludes any variation of the field with time. The current density $\vec{j}$ is related to the electrical field, $\vec{E}$, by the conductivity σ, represented by Ohm's law:

$$\vec{j} = \boldsymbol{\sigma}\, \vec{E}\,. \tag{2.2}$$

In general, the material parameter $\boldsymbol{\sigma}$ (Conductivity) connecting the vectors $\vec{j}$ and $\vec{E}$, is a tensor. Derivations from multiples of the identity matrix can be physically interpreted as anisotropy (Thomas, 2004). Since, many subsurface materials have their preferential directions defined by the original pressure conditions of the sedimentary formations; anisotropy is very much expected for such rocks. However, in geophysical studies, anisotropy is rarely incorporated into inversion algorithms (Pain et al., 2003). As a consequence, σ is considered to be a scalar parameter. The conductivity is often related to hydrological parameters such as salinity, while the resistivity $\rho = \frac{1}{\sigma}$ often represents the petrophysical description of rocks.

Since for a stationary current in a homogeneous medium $\nabla . \vec{j} = 0$, therefore

$$\nabla\sigma . \nabla V + \sigma \nabla^2 V = 0\,. \tag{2.3}$$

In regions with constant σ ($\nabla\sigma = 0$), it reduces to Laplace's equation:

$$\nabla^2 V = 0. \tag{2.4}$$

For a single source of current I at a position $\vec{r_s}$, the term $I\delta(\vec{r} - \vec{r}_s)$ must be considered as its divergence, which leads to the following equation:

$$\nabla.(\sigma\,\nabla V) = \nabla\sigma.\nabla V + \sigma\nabla^2 V = -I\delta(\vec{r} - \vec{r}_s). \tag{2.5}$$

Equation (2.5) symbolizes an elliptical partial differential operator of the Poisson type. A difficult task for solving equation (2.5) is the infinite source term, which must be considered in the discrete problem. Since equation (2.5) is linear, the potential of an electrode combination can be obtained by superposing the individual potentials related to each electrode.

2.1.1. Single current electrode

Ideally, an electrical current is injected by a single point electrode located at the ground surface. The point at which the current returned to the source of voltage is supposed to be at infinity, so its effect can be neglected. Since, spherical symmetry exists in the earth, the Laplace's equation is considered in spherical coordinates. As a result, the potential will be a function of the radial distance ***r*** from the current electrode only. For an isotropic half-space of constant conductivity σ_0 with a single current source located at $\vec{r}_s$= (x, y, 0),

$$\nabla^2 V = \frac{\partial^2 V}{\partial r^2} + \frac{2}{r}\frac{\partial V}{\partial r} = 0. \tag{2.6}$$

Since the air is nonconductive (σ = 0), $E_z = \frac{\partial V}{\partial z} = 0$ is required at $z = 0$ to satisfy the boundary condition. Then, the solution is

$$V(r) = -\frac{A}{|\vec{r} - \vec{r_s}|} + B, \tag{2.7}$$

where A and B are constant with respect to r. It is convenient to require a potential gauge such as $V = 0$ for $r \to \infty$ so that $B = 0$. The total current crossing a hemispherical surface into the underground is

$$I = 2\pi |\vec{r} - \vec{r}_s|^2 j = -2\pi |\vec{r} - \vec{r}_s|^2 \sigma_0 \frac{\partial v}{\partial r} = -2\pi\sigma_0 A, \quad (2.8)$$

where

$$A = -\frac{I}{2\pi\sigma_0}, \quad (2.9)$$

and by substituting (2.9) into equation (2.7), we get

$$V(r) = \frac{I}{2\pi\,\sigma_0 |\vec{r} - \vec{r}_s|}. \quad (2.10)$$

This means that the potential is constant at a given radial distance from the current electrode. Thus, the equipotential surfaces are hemispheres around the point of current injection.

In order to incorporate the effect of the earth's surface, i.e., $E_z = 0$ at $z = 0$, the solution can be superposed by the source $\vec{r}_s = (x_s, y_s, z_s)$ and a mirror source $\vec{r}'_s = (x_s, y_s, -z_s)$, giving

$$V = \frac{I}{4\pi\,\sigma_0} \left(\frac{1}{|\vec{r} - \vec{r}_s|} + \frac{1}{|\vec{r} - \vec{r}'_s|}\right). \quad (2.11)$$

Note that equation (2.11) is identical to (2.10) for $z = 0$. Potentials that satisfy the above equation are possible solutions of the geoelectrical problem.

2.1.2. The four-electrode array

In practice, two electrodes are required in order to inject an electrical current into the ground (Fig. 2.1). In general, the current electrodes are referred to as $C1$ and $C2$. The potential at any surface point nearby will be affected by both these electrodes, because of the finite distance between them.

From equation (2.10), the potential due to current electrode *C*1 observed at a potential electrode *P*1 is

$$V_2 = \frac{I}{2\pi\sigma_0 \overline{C1P1}} . \quad (2.13)$$

The electric current at *C*2 is of equal size but opposite in direction, hence the observed potential at *P*1 due to *C*2 is

$$V_2 = -\frac{I}{2\pi\sigma_0 \overline{C2P1}} . \quad (2.14)$$

The superposition of both potentials observed at *P*1

$$V_{P1} = V1 + V2 = \frac{I}{2\pi\sigma_0}\left(\frac{1}{\overline{C1P1}} - \frac{1}{\overline{C2P1}}\right) . \quad (2.15)$$

The equipotential and the current flow lines are shown in Figure 2.1. A potential difference observed between the potential electrodes *P*1 and *P*2 (Fig. 2.1) is given by

$$\Delta V_P = V_{P1} - V_{P2} = \frac{I}{2\pi\sigma_0}\left(\frac{1}{\overline{C1P1}} - \frac{1}{\overline{C2P1}} - \frac{1}{\overline{C1P2}} + \frac{1}{\overline{C2P2}}\right) . \quad (2.16)$$

where, ΔV is a function of the half space conductivity, σ_0, the injected current, *I*, and the geometry of the electrode spread.

2.1.3. Geometric factor and apparent resistivity

A resistivity, $\rho = \frac{1}{\sigma_0}$, can be obtained from equation (2.16) and is equal to the bulk resistivity of the homogeneous half space and hence constant for any injection current and electrode geometry

$$\rho = K \times \frac{\Delta V}{I} . \quad (2.17)$$

where the parameter K denotes a geometric factor

$$K = \frac{2\pi}{\frac{1}{\overline{C1P1}} - \frac{1}{\overline{C2P1}} - \frac{1}{\overline{C1P2}} + \frac{1}{\overline{C2P2}}} . \quad (2.18)$$

The geometric factor K depends on the arrangement of four electrodes C1, C2, P1 and P2. In the general case of subsurface electrodes, the positions of the mirror current electrodes $C'1$ and $C'2$ must be incorporated to calculate the geometric factor, yielding

$$K = \frac{2\pi}{\frac{1}{C1P1} + \frac{1}{C'1\,P1} - \frac{1}{C1P2} + \frac{1}{C'1\,P2} - \frac{1}{C2P1} - \frac{1}{C'2P1} + \frac{1}{C2P2} - \frac{1}{C'2P2}}. \qquad (2.19)$$

In case of inhomogeneous earth, when the array is moved or the geometry of the electrode spread changed, different values of ρ are measured. The measured quantity by equation (2.17), ρ, is hence referred to as the apparent resistivity ρ_a, indicating that it reflects the properties of a homogeneous half space that may not exist in practice (Kuras, 2002). Equations (2.18) and (2.19) are valid only for a ground with a flat surface. In case of variable topography, the geometric factor is unknown and can only be evaluated by numerical modeling using a homogeneous resistivity (Thomas, 2004).

2.2. One-dimensional resistivity survey

The electrical resistivity technique has been first applied in 1920s by the Schlumberger brothers (Loke, 2009). For the next 60 years, one-dimensional (1D) conventional sounding surveys were used for numerical interpretation (Koefoed, 1979). In general, the 1D-arrays using four electrodes, (C1, C2, P1 and P2), have been used in the laboratory for resistivity calibration (Rhoades and van Schilfgaarde, 1976).They are also used in surveys for vertical electrical sounding (VES).

In VES, the distances between the electrodes are successively increased, in order to attain a deeper depth of penetration. Typical values for the electric current (I) and voltage (V) are 1 to 1000 mA and 10 to 400 V, respectively. The measurement then displays the

distribution of subsurface resistivity with respect to depth without considering lateral changes (Loke, 2009). In the interpretation of VES data, it is common to assume that underground structures are made up of several horizontal layers (Pozdnyakova et al., 2001). Thus, this technique can give useful information about the subsurface geological conditions, such as water table, for which the 1D model is the most appropriate (Loke, 2009). One of the successful studies implementing the VES to record information about the vertical discontinuities associated with various soil horizons was reported by Bottraud et al. (1984). Al- Amri (1998) applied a VES survey to delineate the hydrostratigraphy of the southern Red Sea coastal area, Saudi Arabia.

During geophysical explorations, the lateral resistivity of the subsurface geology can vary over short distances. Thus, horizontal changes in the subsurface resistivity may cause considerable changes in the apparent resistivity data, which can be misinterpreted as changes in the resistivity of the subsurface with depth. As a result, for complex formations with lateral changes over short distances, the VES technique may not be sufficiently accurate (Loke, 2009).

2.3. Two-dimensional resistivity surveys

In two-dimensional (2D) surveys, multi-electrode arrays provide a 2D cross-section of the underground structures. The current and potential electrodes are kept at a regular fixed distance from each other. The whole array is then progressively moved along a line at the surface. In each step, one measurement is recorded by the resistivity meter. The set of all measured data using the first inner electrode spacing gives a data level of resistivity values. The inter-electrode spacing is then increased by a factor of two, and a second data level is measured. This process is repeated until the maximum spacing between the electrodes is reached (Fig. 2.2). The depth of the measured data points will be discussed in

section 2.6.1 in detail. The data are then arranged in a 2D ‘‘pseudo-section’’ plot that represents a simultaneous display of both the lateral and vertical changes in resistivity (Edwards, 1977; Loke, 2009).

2.3.1. Common array types for 2D resistivity surveys

Several electrode configurations are commonly used with DC resistivity surveys. Each configuration has specific advantages and limitations. The simplicity of their use in the field and spatial resolution of underground inhomogeneities play essential roles in choosing an array for a particular survey. Since the signal-to-noise ratios during the survey vary between different arrays, the quality of measured data is affected by the choice of electrode configuration. In practice, the most commonly used arrays for 2D imaging are the Wenner (W), dipole-dipole (DD), Wenner-Schlumberger (WS), pole-pole (PP) and pole-dipole (PD) configurations. Figures 2.2 to 2.6 show these electrode configurations together with their geometric factors. The geometric factor K differs from one configuration to other. Table 2.1 compares the following characteristics for these common arrays: (i) the signal strength, (ii) the horizontal data coverage, (iii) the sensitivity of the array to horizontal structures, (iv) the sensitivity of the array to vertical structures, and (v) the depth of investigation (Hesse, 1986; Griffiths and Barker, 1993; Loke, 2009). The signal strength is related to the joint signal-response of the measured data, which is reciprocally proportional to the geometric factor K. When a survey is carried out in areas with high background noise, the signal strength is important and must be taken into account. Seaton and Burbey (2002) reported that the electrode layout has an important effect on the horizontal data coverage, resolution, sensitivity and depth of investigation. Hesse et al. (1986) reported that in some situations using multiple arrays may help to investigate different features of the underground structures and their interpretation in a better way.

Table 2. 1. Attributes of the different array types classified from 1 to 4, representing poor to good.

Array type	Signal strength	Horizontal data coverage	Sensitivity to horizontal structures	Sensitivity to vertical structures	Depth of investigation
W	4	1	4	1	1
WS	3	2	2	2	2
DD	1	3	1	4	3
PD	2	3	2	1	3
PP	4	4	2	2	4

2.3.1.1. The W array

The W array is a robust electrode configuration that was popularized by the work of researchers at the University of Birmingham (Griffiths and Turnbull, 1985; Griffiths, Turnbull and Olayinka, 1990). The W array maintains a constant spacing between the electrodes, as shown in Figure 2.2. The W array can be used to investigate vertical changes in a better way as compared to horizontal changes (Loke, 2009). For this array, there are three types of electrode configurations (Carpenter and Habberjam, 1956), i.e., the W Alpha array, the W Gamma array and the W Beta array the W (Fig. 2.2). As compared to other two arrays, the W Alpha array has a moderate depth of investigation. The geometric factor for the W Alpha array is smaller than that of the other arrays, but it has the strongest signal strength. This can be important if the survey is conducted in areas with high background noise. However, the horizontal coverage of the W Alpha array is relatively poor, as the electrode spacing is increased (Loke, 2009). The W Gamma array has an unusual electrode configuration in which the current and potential electrodes are interleaved. The W Beta

array is a special case of the DD array, which maintain the same spacing between the electrodes (see section 2.3.1.2).

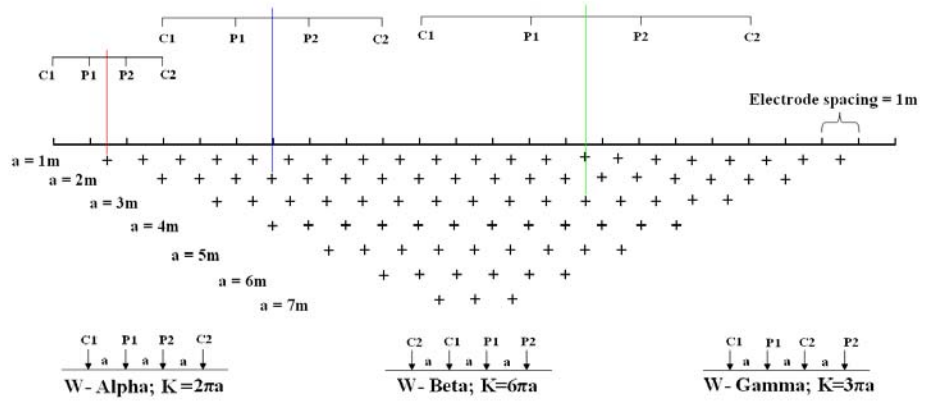

Figure 2. 2. Pseudo-section data pattern for the W array with 24 electrodes. Three types of W arrays together with their geometric factors are also shown at the bottom.

2.3.1.2. The DD array

The DD array has been widely used in resistivity surveys because of the low electromagnetic coupling between the current and potential circuits. The arrangement of the electrodes is shown in Figure 2.3. The spacing between the current electrode pair, C2-C1, and between the potential electrode pair P1-P2 is given as "*a.*" The DD array has another factor called "*n*" (Fig. 2.3), which is the ratio of the distance between C1 and P1 to C2-C1 (or P1-P2) dipole length "*a.*" During surveys with DD array, the "*a*" spacing is initially kept fixed with smallest unit electrode separation and the "*n*" factor is increased from 1 to 6 in order to increase the depth of investigation. The DD array is useful in mapping vertical structures, such as dikes, but it is relatively poor in mapping horizontal structures, such as sedimentary layers (Loke, 2009). The median depth of investigation of the DD array depends on both the "*a*" spacing and the "*n*" factor. This array generally has a shallower depth of investigation than the W array. The pseudo-section data pattern for the DD array

with 24 electrodes is shown in Figure 2.3, where the two numbers on the left side of each data level are the factor "*n*" and electrode spacing "*a*", respectively. The geometric factor for this array is also shown at the top of the pseudo-section. As an advantage, the DD array has better horizontal data coverage than the W array (Fig. 2.3). This is an important advantage when the number of electrodes available with the multi-electrode system is small. The very small signal strength for large values of "*n*" is one disadvantage of the DD array. While surviving with this array, there should be agood contact between the electrodes and the ground.

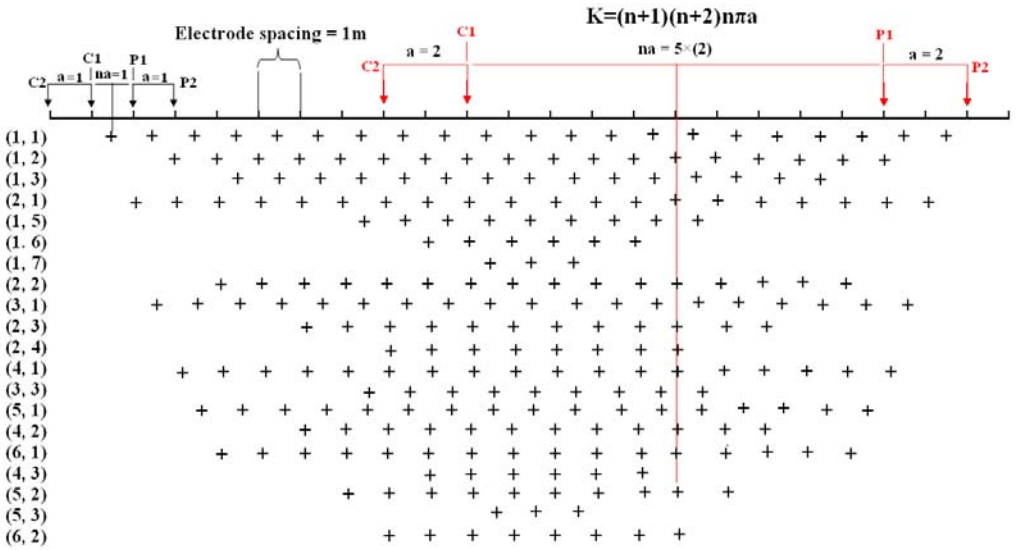

Figure 2. 3. Pseudo-section data pattern for the DD array with 24 electrodes. The two numbers on the left side of each data level are the "*n*" factor and electrode spacing "a," respectively.

2.3.1.3. The WS array

The WS array is a new hybrid between the Wenner and Schlumberger arrays (Pazdirek and Blaha, 1996). The positive and negative current electrodes are denoted by C1 and C2, respectively. Similarly, the positive and negative potential are denoted by P1 and P2, respectively. The "*n*" factor for this array is the ratio of the distance between the C1-P1

(or P2-C2) electrodes to the spacing between the P1-P2 potential pair. In areas where both horizontal and vertical subsurface structures are expected, this array might be a good compromise as compared with W and DD arrays. The signal strength for WS array is weaker than that of the W array, but it is stronger than the DD array and twice that of the PP array (Loke, 2009). Figure 2.4 shows the pattern of the data points through a pseudo-section for the WS arrays. For the red data points, the "*n*" factor and electrode spacing "*a*" are both 2 and 2. As shown in the Figure 2.4, the WS array has a slightly better horizontal coverage than the W array, but narrower than that obtained with the DD array.

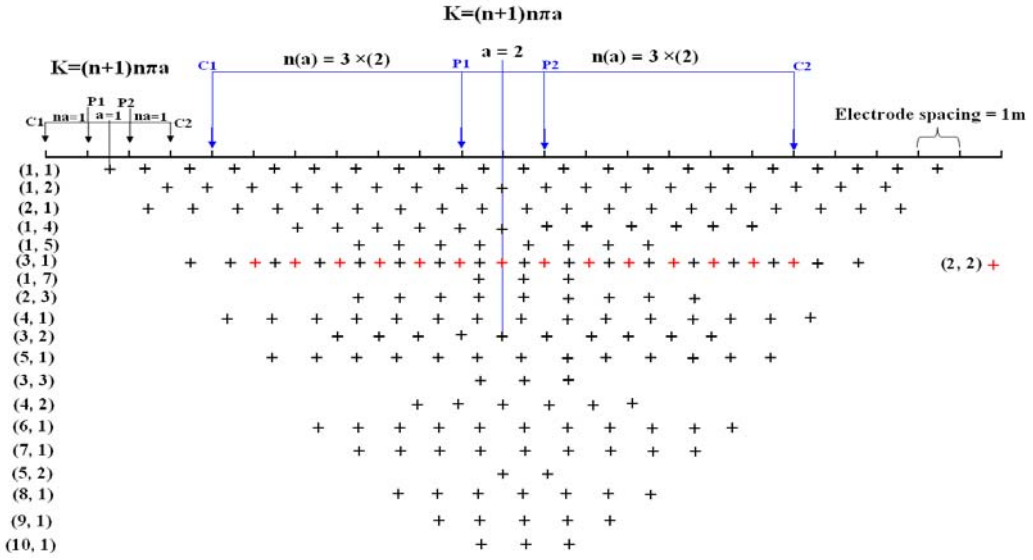

Figure 2. 4. Pseudo-section data pattern for the WS array with 24 electrodes. The two numbers on the left side of each data level are the "*n*" factor and electrode spacing "a," respectively.

2.3.1.4. The PP array

The use of PP array is not as common as the W, DD and WS arrays. This array ideally has only one current and one potential electrode. In practice, to approximate the PP array, the electrodes C2 and P2 must be placed at a distance more than 20 times the

maximum separation between the C1 and P1 electrodes (Loke, 2009). In surveys where the inter-electrode spacing is more than a few meters, there might be practical problems in finding suitable locations for the remote electrodes. Large distance between the potential electrodes pair can also be susceptible to strong telluric noise, which can degrade the quality of the measured data. Thus, the PP array is often used in surveys where all electrode spacings are less than a few meters (such as archaeological surveys). Figure 2.5 shows the pattern of data points in the pseudo-section for the PP array. As shown in the electrode configuration, the electrode separation "*a*" in this Figure has been increased from 1 to 23 in order to obtain all possible measurements. Although the PP array has the widest horizontal coverage and the deepest depth of investigation (Fig. 2.5), it has the poorest resolution of the arrays. Nevertheless, it has also been used for 3D surveys (Li and Oldenburg, 1992).

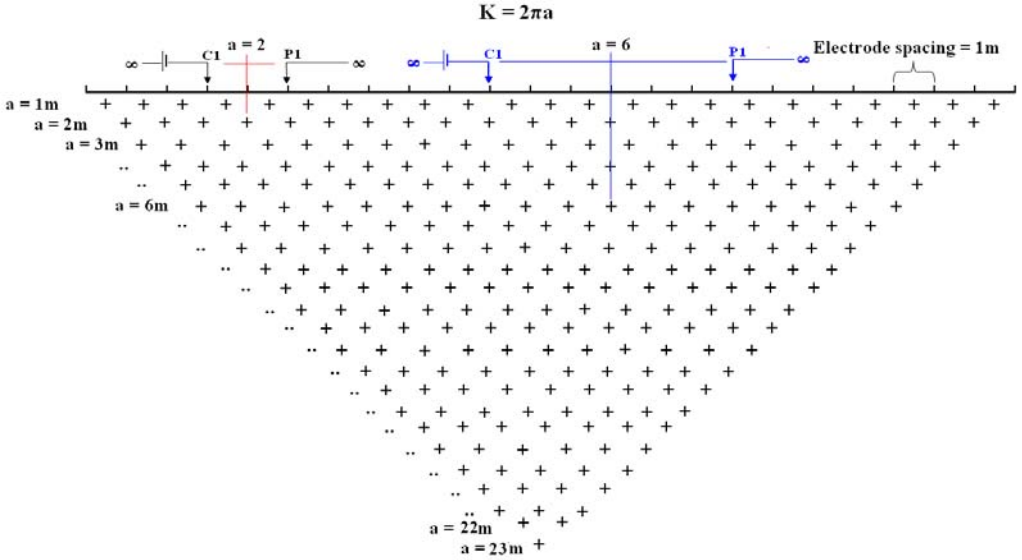

Figure 2. 5. Pseudo-section data pattern for the PP array with 24 electrodes.

2.3.1.5. The PD array

The PD array has a remote electrode (C2), which must be located far from the survey line. This array is less affected by the remote electrode than the PP array (Loke, 2009) and it is an asymmetrical array (Fig. 2.6). In some cases, a asymmetry in the

measured apparent resistivity values can affect the calculated model after inversion. One option to eliminate the effect of this asymmetry is to repeat the measurements by arranging the electrodes in reverse manner (Fig. 2.6). Similar to DD array, the PD array is more sensitive to vertical structures (Loke, 2009). Because of its good horizontal coverage, the PD array is useful for surveys with a small number of electrodes. The signal strength is higher than the DD array but lower than those from the W and WS arrays (Loke, 2009). It is not advisable to use values greater than 8 for the "*n*" factor, otherwise the "*a*" spacing between the P1-P2 dipole pair should be increased to obtain a stronger signal.

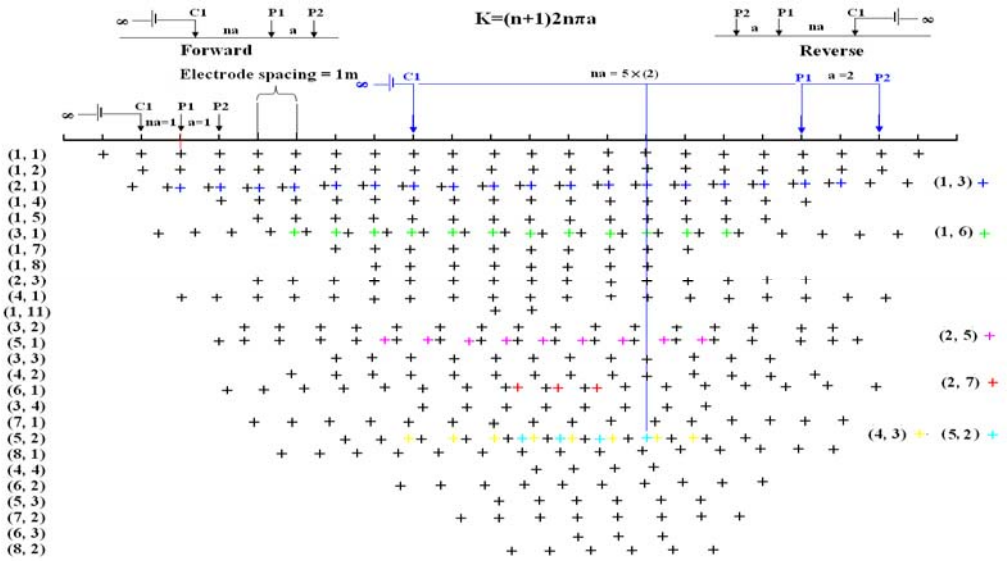

Figure 2. 6. Pseudo-section data pattern for the PD array with 24 electrodes. The forward and reverse orientations of this array are shown. The two numbers on the left side of each data level are the "*n*" factor and the electrode spacing "a," respectively

2.4. Three-dimensional resistivity survey

Many of the problems associated with geophysical exploration are due to three-dimensional (3D) effects. Nowadays, 3D survey is the subject of active research, but its use has not yet reached the level as that of the 2D surveys (Loke, 2009). The main reason for this is that the cost of 3D surveys is much higher for large areas as compared to 2D surveys. The development of multi-channel resistivity meters that can take more than one reading at

a time and faster micro computers to enable the inversion of large datasets should make 3D resistivity surveys a more cost–effective.

2.4.1. Common array types for 3D resistivity surveys

The PP, PD and DD arrays are used for 3D resistivity surveys more frequently than the W and WS arrays. This is because the W and WS arrays have poorer data coverage near the edges of the survey grid. The advantages and disadvantages of the PP, PD, DD, W and WS arrays that were discussed for 2D resistivity surveys are also valid for 3D resistivity surveys. The PP electrode configuration is commonly used for 3D resistivity surveys, as in the ESCAN method (Li and Oldenburg, 1994). One alternative to the PP array for surveys grids 12 by 12 and above is the PD array. It has a better resolving power and is less susceptible to telluric noise as compared to the pole-pole array. The DD array is used for grids larger than 12 by 12 because the horizontal data coverage at the sides is poor.

2.4.2. Measurement methods in 3D resistivity survey

One possible measurement for a 3D resistivity survey is shown in Figure 2.7, where a grid of 25 electrode positions is used. The electrodes are usually arranged in a square grid, with the same electrode spacing along *x* and *y* directions.

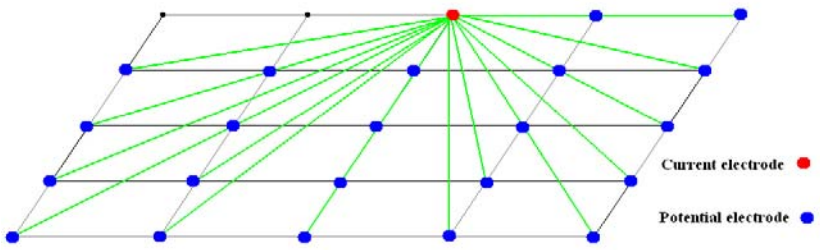

Figure 2. 7. Measurement sequences for a 3D survey. The locations of potential electrodes (blue) correspond to a single current electrode (red) in the arrangement used by a survey to measure the complete dataset.

Habberjam and Watkins (1967) reported that such an array provides a measure of resistivity that is less orientation-dependent than that given by in-line array. Matias (2002) also emphasized that the data were orientationally stable, so there was no need for prior knowledge of the electrical heterogeneity orientation. The maximum number of independent measurements, n_{max}, which can be made with n_e electrodes, is given by

$$n_{max} = \frac{n_e(n_e - 1)}{2}. \quad (2.20)$$

In this case, each electrode can be used as a current electrode and a potential where all the other electrodes are measured (Loke, 2009). The reciprocity makes it necessary to measure the potentials at the electrodes with a higher index number than the current electrode. There are 300 possible measurements for 5 by 5 electrode grid and 2016 for 8 by 8 electrode grid. It can take several hours to take up to such a large number of measurements. To reduce the number of measurements required and eventually the measurement time, without seriously degrading the quality of the obtained model, an alternative method, the "cross-diagonal survey", can be introduced. By this method, the potential measurements are only made at the electrodes along the x- and, y-directions and along the 45 degree diagonal lines passing through the current electrode (Fig. 2.8).

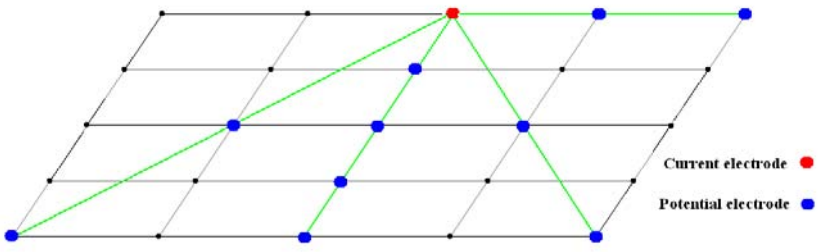

Figure 2. 8. Measurement sequences for a 3D survey. The locations of potential electrodes (blue) correspond to a single current electrode (red) in the arrangement used by a cross-diagonal survey.

Several suggestions have been made to help migrate 2D techniques in to 3D acquisition, including the serpentine roll-along (Loke et al., 1996) and the leap frog roll-along (Dahlin and Bernstone., 1997; Dahlin et al., 2002). These enhanced 3D acquisition techniques have an improvement over the traditional methods of running individual wires to the electrodes because they use recently developed multi-electrode cables and multi-channel meters. To map slightly elongated bodies, a rectangular grid with different numbers of electrodes and spacings in the *x* and *y* directions could be used (Fig. 2.9). In the Figure 2.9, two cables were used, with 20 used take outs in each cable. A roll-along measurement can be carried out to cover the entire grid. If 3D resistivity survey is carried out with a series of parallel lines, and the cross-line measurements are not made, the distance between the lines should be two to three times as compared to electrode spacing (Loke, 2009). This procedure has been followed to ensure that the subsurface material between different lines is sufficiently mapped by the in-line measurements (al Hagrey et al., 1999; Chambers et al., 1999, 2002; Oglivy et al., 1999; Zhou et al., 2001, 2002; Oglivy et al., 1999; Zhou et al., 2001).

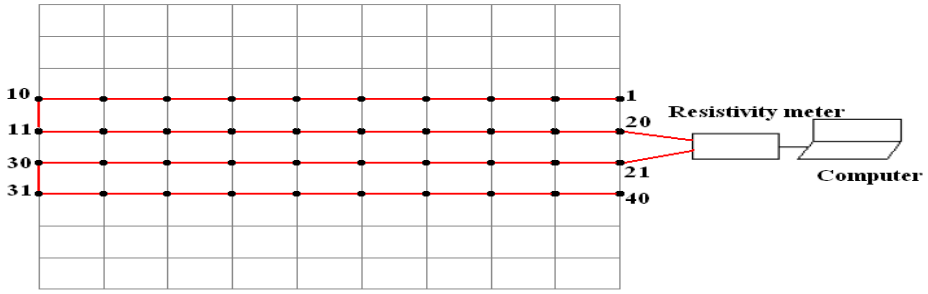

Figure 2. 9. A possible measurement sequence for a 3D survey.

2.5. Quasi-3D resistivity survey

The 3D roll-along method has proven to be a useful tool only for small survey area, because a large number of cables and electrodes are needed for 3D data acquisitions in large areas. One technique that can be suitable for larger survey areas is quasi-3D

acquisition, where 2D data are collected along parallel and orthogonal lines in a grid pattern (Dahlin and Loke, 1997). By this way, less number of electrodes, cables and time will be required for 3D data acquisition. Gharibi et al. (2005) have been reported that data acquired by the quasi-3D technique using the proper geometric constraints are suitable for processing and interpretation. An analysis of 3D resistivity surveys in the literature (Table 2.2) suggests that the quasi-3D approach is the most practical one among different techniques. The table lists the progression of the 3D resistivity problem from Park et al. (1991), who used a pure 3D grid, to the most recent results of Koch et al. (2009), who used the quasi-3D technique.

2.6. Sensitivity analysis

To study the suitability of different arrays in resistivity surveys, several parameters must be considered, including the depth of investigation and the vertical and horizontal resolutions. One common way to study such parameters is by calculating the sensitivity function (Edwards, 1977). Consider the simplest possible electrode configuration with just one current electrode located at the origin (0, 0, 0) and one potential electrode located at (a, 0, 0). Mathematically, the sensitivity function for a homogeneous half-space is given by the Frechet derivative (McGillivray and Oldenburg 1990)

$$F_{3d}(x,y,z) = \frac{x(x-a) + y^2 + z^2}{4\pi^2\left((x^2+y^2+z^2)((x-a)^2+y^2+z^2)\right)^{1.5}}. \qquad (2.21)$$

This is the sensitivity function for the pole-pole array. The sensitivity function shows the degree to which a change in the resistivity of the subsurface can influence the potential measured by the array (Edwards, 1977; Loke, 2009). To obtain the sensitivity function for

four-electrode array, the contributions from the appropriate four current-potential pairs of current-potential electrodes must be added up.

Table 2. 2. Published studies using three-dimensional electrical resistivity imaging.

Authors	Location	Data Acquisition	Electrode Spacing (m)	Array Type	Processing	Year
Park et al.	Nevada	3D grid	50	PP	3D	(1991)
Loke et al.	UK	3D grid	0.5	PP	3D	(1996)
Chambers et al.	UK	2D orthogonal	5	PD	3D	(1999)
Jackson et al.	UK	3D grid	1	PD	3D	(2001)
Yi et al.	Korea	3D grid	20	PP & DD	3D	(2001)
Chambers et al.	UK	2D orthogonal	0.5	DD & W	3D	(2001)
chambers et al.	UK	2D parallel	0.25	DD & W	3D	(2001)
Dahlin et al.	Sweden	3D roll-along	5	PP	3D	(2002)
Ogilvy et al.	UK	2D parallel	5	PD	3D	(2002)
Gemail et al.	Egypt	3D grid	10 &20	PD & PP	3D	(2004)
Bentley et al.	Canada	2D orthogonal	1	DD	3D	(2004)
Nyquist et al.	New Jersey	2D orthogonal	3	DD	3D	(2005)
Lebourg et al.	French	2D orthogonal	10-15	PP & DD	3D	(2005)
Freidel et al.	Switzerland	2D orthogonal	0.5	WS & DD	3D	(2006)
Chambers et al.	Scotland	2D orthogonal	5	W & WS	3D	(2006)
Mansoor et al.	New Jersey	2D orthogonal	1.5	W	3D	(2007)
Chambers et al.	UK	2D orthogonal	1	DD	3D	(2007)
Drahor et al.	Turkey	2D orthogonal	1	W	3D	(2008)
Soupios et al.	Greece	2D parallel	0.25 & 1	DD	3D	(2008)
Park et al.	Korea	2D parallel	5	DD &PP	3D	(2009)
Koch et al.	Germany	2D parallel	0.5	DD & W	3D	(2009)

2.6.1. Depth of investigation

By increasing the electrode spacing, the array can evaluate the resistivity of the deeper layers. To get a numerical value for the depth of investigation, the sensitivity function of the array is used (Loke, 2009). In VES surveys, a change in the potential is estimated if the resistivity of a thin horizontal layer is changed. For a horizontal layer, the x and y limits extend from -∞ to +∞. Thus, the sensitivity function is obtained by integrating the 3D Frechet derivative (2.21) in the x and y directions, i.e.

$$F_{1d}(z) = \int_{-\infty}^{+\infty}\int \frac{x(x-a) + y^2 + z^2}{4\pi^2\left((x^2+y^2+z^2)((x-a)^2+y^2+z^2)\right)^{1.5}}\, dxdy\,. \qquad (2.22)$$

A simple analytical solution for equation (2.22) is given by Roy and Apparao (1971) as following

$$F_{1d} = \frac{2z}{\pi(a^2 + 4z^2)^{1.5}}\,. \qquad (2.23)$$

Equation (2.23) is called the depth investigation characteristic and has been used by many authors to determine the properties of various arrays in resistivity sounding surveys (Edwards, 1977, Barker, 1991, Merrick, 1997). Figure 2.10 shows a plot of sensitivity function for the PP array. Some authors have used the maximum point as depth of investigation. However, the median depth of investigation is a more robust estimate introduced by Edwards (1977) and Barker (1991). This is the depth above which the area under the curve is equal to half the total area under the curve (Loke, 2009). The median depth of investigation does not depend on the measured data. Although the depths are strictly valid for a homogeneous earth model, they are probably sufficient for planning field surveys (Loke, 2009). Table 2.3 gives the median depth of investigation for different arrays. For WS, DD and PD arrays, the *n* factor must also be taken into account.

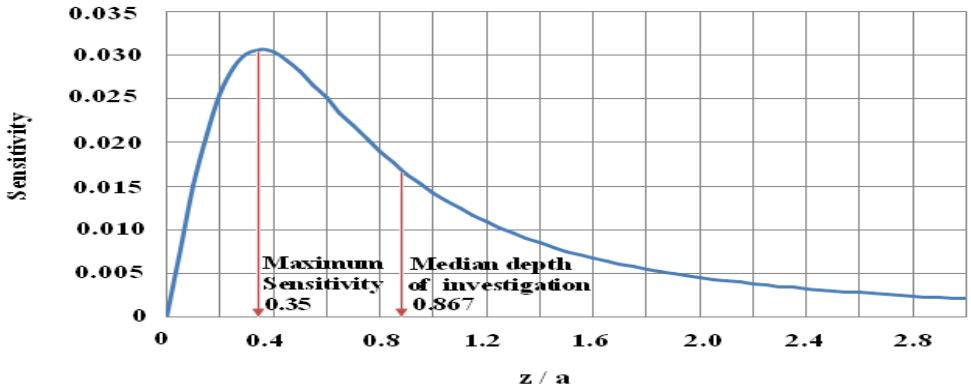

Figure 2. 10. Plot of the 1D sensitivity function for the PP array. Note that the median depth of investigation (0.876a) is more than twice the depth of maximum sensitivity (0.35a). In this plot, the electrode spacing, a, is 2 meters.

Table 2. 3. Median depth of investigation (z) for the different arrays (after Edwards, 1977).

Array type		z /a	Array type		z /a
W	Alpha	0.519	DD	n = 1	0.416
	Beta	0.416		n = 2	0.697
	Gamma	0.594		n = 3	0.962
WS	n=1	0.519		n = 4	1.220
	n=2	0.925		n = 5	1.476
	n=3	1.318		n = 6	1.730
	n=4	1.706	PD	n = 1	0.519
	n=5	2.093		n = 2	0.925
	n=6	2.478		n = 3	1.318
	n=7	2.863		n = 4	1.706
	n=8	3.247		n = 5	2.093
	n=9	3.632		n = 6	2.478
	n=10	4.015		n = 7	2.863
PP		0.867		n = 8	3.247

2.6.2. Horizontal and vertical resolutions of different arrays

For a particular (x, z) location in 2D case, all points contribute y-values ranging from $+\infty$ to $-\infty$. This involves integrating the 3D Frechet derivative (2.21) with respect to y, which is

$$F_{2d}(z) = \int_{-\infty}^{+\infty} \frac{x(x-a) + y^2 + z^2}{4\pi^2\left((x^2+y^2+z^2)((x-a)^2+y^2+z^2)\right)^{1.5}}\, dy. \qquad (2.24)$$

Loke and Barker (1995) reported an analytical solution for equation (2.24). The difference in the contour patterns of the sensitivity function plots are studied in order to explain the response of the different arrays to different structures and to compare the suitability of various arrays for particular surveys. In the following plots of sensitivity sections, the distance between the first and last electrodes is normalized to 1.0 meter. The sensitivity values are shown from a depth of 0.01, in order to avoid the singularities at the electrodes down to 1.0.

2.6.2.1. The W array

Figure 2.11 shows the sensitivity plots for W Alpha and W Gamma arrays. The W Beta is a special case of the DD array with n=1, so it is described in the sensitivity section of the DD array. The contours in the sensitivity plot for W Alpha array are almost horizontal beneath the center of the array. This array is relatively more sensitive to vertical changes than to horizontal changes in subsurface resistivity. Furthermore, the W Alpha array has a moderate depth of investigation as compared to the other arrays. In Figure 2.11, the minimum electrode spacing, a, is 3.333(= 10/3). Thus, according to Table 2.3 the median depth of investigation for the W Alpha array is 0.1730 (=3.333×0.519). The sensitivity section in Figure 2.11 shows that the deepest regions mapped by the W Gamma array are below the two outer electrodes (C1 and P2). Similar to the W Alpha array, the median depth of investigation for the W Gamma array in Figure 2.11 can be calculated and is about 0.1980 (=3.333×0.594).

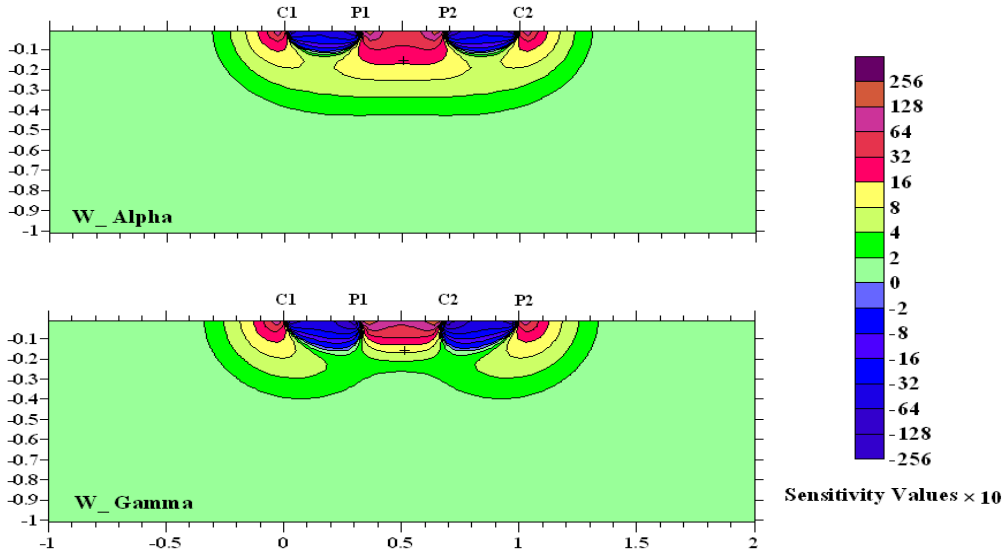

Figure 2. 11. 2D sensitivity sections for the W Alpha and W Gamma arrays. The median depths of investigation are denoted by "+." The horizontal distance between the outer electrodes is normalized to 1.

2.6.2.2. The WS array

Figure 2.12 shows the sensitivity pattern for the WS array; where as the *n* factor is increased from 1 to 8. As the *n* factor is increased, the highest positive sensitivity zone below the center of the array becomes more concentrated beneath the central P1-P2 electrodes. At n=4 to n=8, the high positive sensitivity lobe beneath the P1-P2 electrodes moves away from the high positive sensitivity values near the C1 and C2 electrodes. This means that this array is moderately sensitive to both horizontal (low *n* values) and vertical structures (high *n* values). The median depths of investigation for n=1 to n=10 in Figure 2.12 are shown in Table 2.4.

Table 2. 4. Depth of investigation for the WS array in Figure 2.12.

n-factor	1	2	3	4	5	6	7	8	9	10
Depth of investigation $\times 10^4$	1730	1850	1882	1896	1902	1906	1909	1910	1911	1912

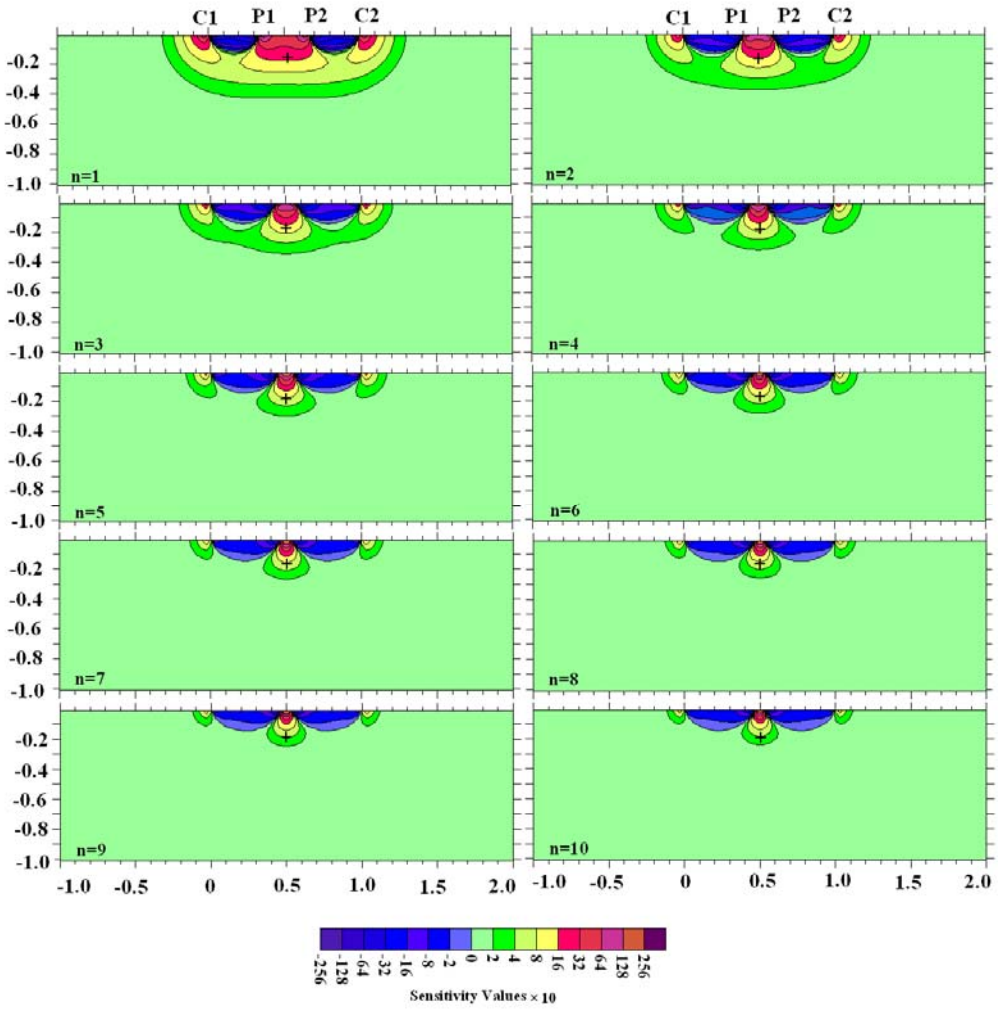

Figure 2. 12. 2D sensitivity sections for WS arrays. The median depths of investigation are denoted by "+." Both the vertical and the horizontal axes are in meters. The horizontal distance between the outer electrodes is normalized to 1.

2.6.2.3. The DD array

Figure 2.13 shows the sensitivity sections for the DD array with *n* values ranging from 1 to 6. This array is very sensitive to resistivity changes below each dipole pair, because the highest sensitivity values are located between the current and potential dipole pairs. As the *n* factor is increased, the sensitivity values beneath the center of the array decrease and the high sensitivity values become more concentrated beneath the current and potential dipole pairs. The sensitivity values at the pseudo-section plotting points "+" for *n*

≥2 become negligible, and the sensitivity contour patterns become almost vertical. Thus, the DD array is very sensitive to horizontal changes in resistivity, but it is relatively insensitive to vertical changes in resistivity (Loke, 2009). The median depth of investigation for n=1 to 6 in Figure 2.13 are shown in Table 2.5.

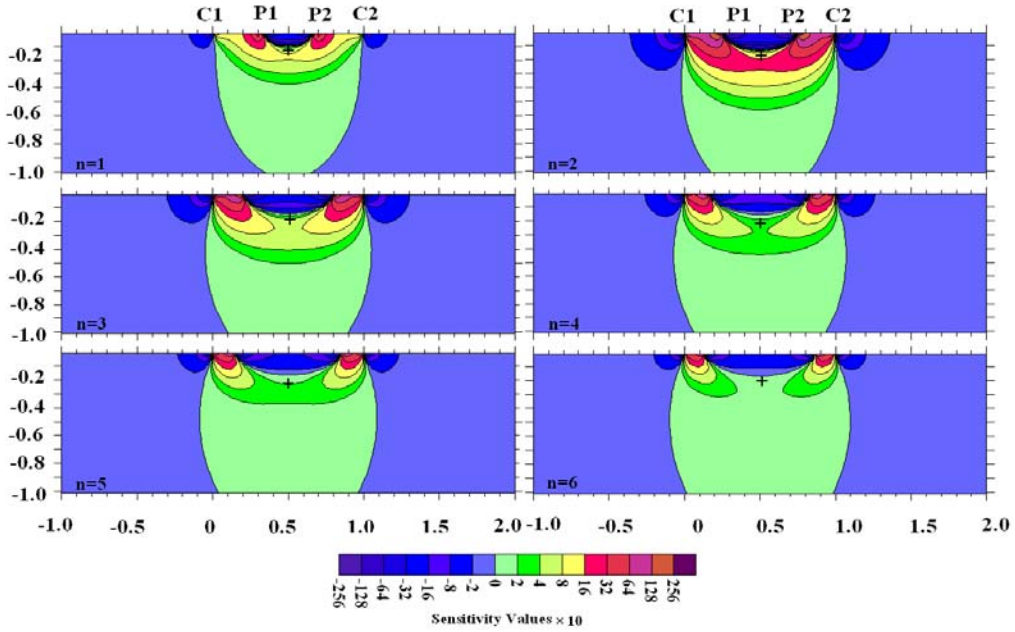

Figure 2. 13. 2D sensitivity sections for DD arrays. The median depths of investigation are denoted by " +." The units of both the vertical and the horizontal axes are meters. The horizontal distance between the outer electrodes is normalized to 1.

Table 2. 5. Median depth of investigation for the DD array in Figure 2.13.

n-factor	1	2	3	4	5	6
Depth of investigation $\times 10^4$	1386	1743	1923	2034	2108	2162

2.6.2.4. The PP array

Figure 2.14 shows the sensitivity plots for the PP array. This array is sensitive to resistivity changes below each electrode because the high sensitivity values become more concentrated beneath the current and potential electrodes. The sensitivity values beneath the center of the array are almost negative from the surface down to a depth of about 0.36

m. The sensitivity value at point "+" in the pseudo-section is still positive. The median depth of investigation in Figure 2.14 is 0.8413. Thus the PP array has the deepest depth of investigation as compared to all the other.

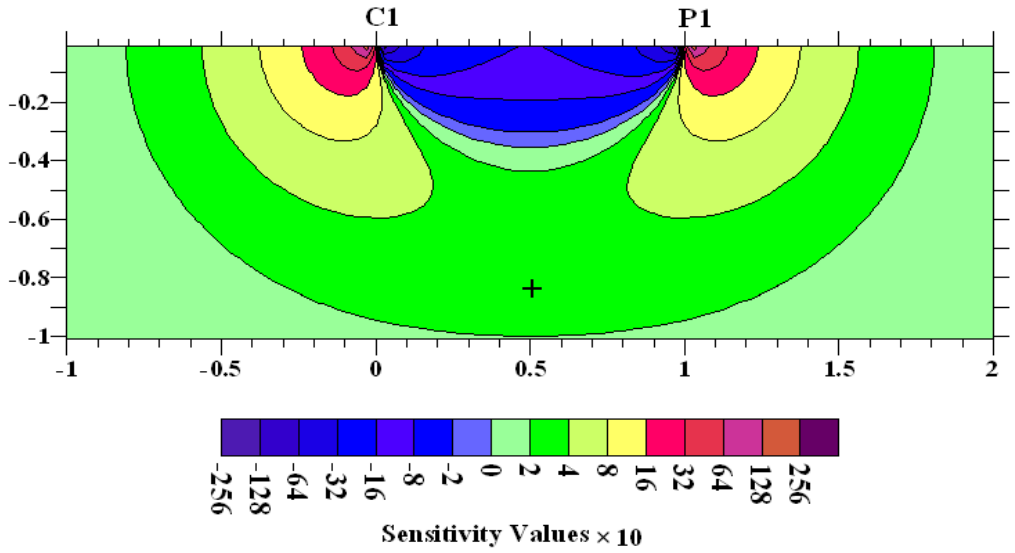

Figure 2. 14. PP array 2D sensitivity section. The median depth of investigation is denoted by " +." The vertical and horizontal axes are in meters. The horizontal distance between the outer electrodes is normalized to 1.

2.6.2.5. The PD array

Figure 2.15 shows the sensitivity sections for the PD array for *n* values ranging from 1 to 8. Since the high positive sensitive region beneath the potential dipole ($n \geq 2$) becomes vertical, the PD array is more sensitive to vertical structures. Because of the negative sensitivity values between C1 and P1 electrodes and the high positive values to the left of the C1, the measurements of this array should be repeated in the reverse manner in order to obtain better results. The median depths of investigation for n=1 to 8 in Figure 2.15 are shown in Table 2.6.

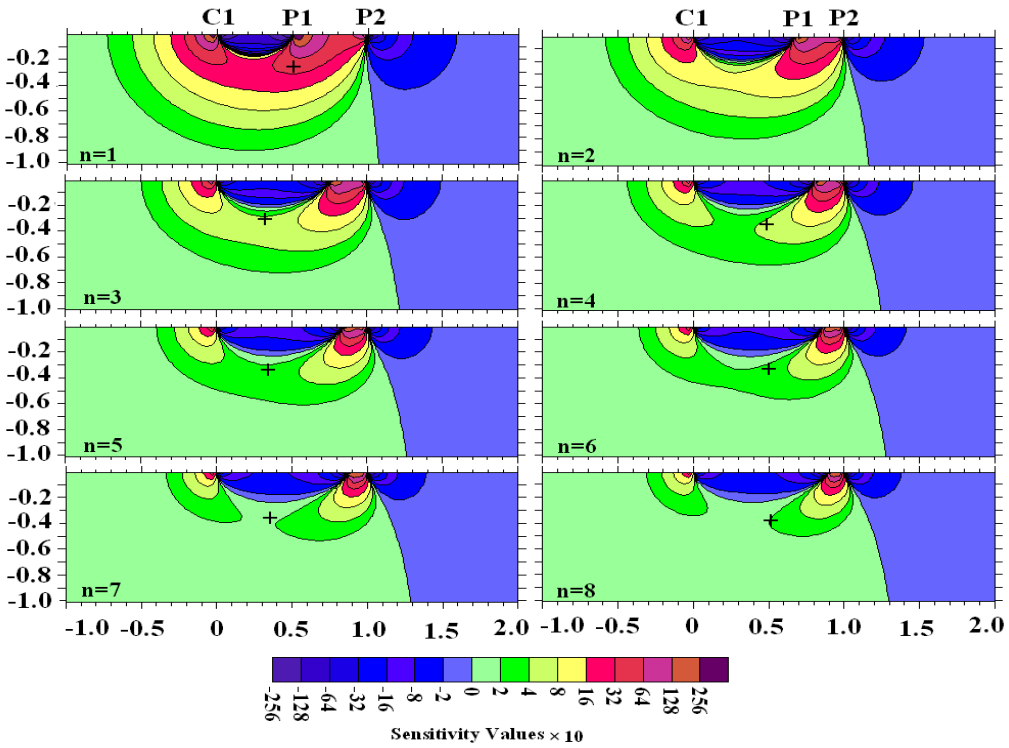

Figure 2. 15. 2D sensitivity sections for PD arrays. The median depths of investigation are denoted by "+." Both the vertical and the horizontal axes are in meters. The horizontal distance between the outer electrodes is normalized to 1.

Table 2. 6. Depth of investigation for the PD array in Figure 2.15.

n-factor	1	2	3	4	5	6	7	8
Depth of investigation $\times 10^4$	2595	3083	3294	3412	3484	3540	3579	3609

2.6.3. 3D Sensitivity Analysis

Loke (2009) has studied the 3D sensitivity plots for the W (Alpha and Gamma), WS, DD, PD, PP arrays. According to his work, the W Alpha array is less sensitive to off-line structures than the DD array, i.e., it is less sensitive to 3D structures. The sensitivity plots for W Gamma array show that this array is more sensitive to 3D structures near the C1 and C2 electrodes. He found that the DD array is more sensitive to 3D structures off the array axis than the W, WS, PP and PD arrays. According his sensitivity plots from PP and

PD –arrays, he has concluded that to attain a complete 3D coverage, if the measurements are only made in the x-direction, the spacing between the lines should not be much more than the smallest electrode spacing.

2.7. Summary

As evident from the contents of this chapter, the basics of the DC resistivity survey and the 1D, 2D and 3D surveys are discussed here. The common arrays used in the 2D and 3D surveys, i.e., the WS, W, DD, PD and PP arrays have been explained. In addition, all the published literatures regarding the 3D resistivity problem from 1991 onward have been analyzed. The W array detected vertical changes in a better way but relatively poor results have been obtained for horizontal changes. The W array has the strongest signal strength but relatively poor horizontal coverage as compared to other common arrays. The signal strength for the WS array is found to be weaker than that of the W array, but it is stronger than that of the DD array and twice that of the PP array. On the other hand, the DD array has better horizontal coverage than the W array. This is an important advantage when the number of electrodes available with the multi-electrode system is small. Although, the PP array has the widest horizontal coverage and the deepest depth of investigation, it has the poorest resolution of the arrays used. Similar to the DD array, the PD array is more sensitive to vertical structures. Because of its good horizontal coverage, the PD array is useful for surveys with a small number of electrodes, and its signal strength is higher than that of the DD array but lower than the W and WS arrays. As a common way to study the suitability of different arrays, the sensitivity function of each array is calculated and their respective 2D and 3D sensitivity plots have been prepared.

Chapter 3
Forward modeling and non-linear inversion

The measured apparent resistivity data from DC surveys can give some useful information about the locations of subsurface structures, but their size, depth and extent cannot be correctly estimated. Furthermore, using pseudo-sections as a base for reliable interpretation can be misleading (Dahlin et al., 2002). Therefore, in order to obtain more realistic images of the underground structures, the apparent resistivity data should be inverted in to true resistivity of the subsurface materials.

In geophysics, every inversion scheme includes an essential numerical simulation of the measured data for a given parameter distribution. This forward modeling is normally made by solving the partial differential equations (PDE). The first numerical solutions for arbitrary 2D resistivity were presented by Mufti (1976) and Dey and Morrison (1979b) using the finite difference methods.

3.1. DC Forward modeling

The term forward modeling refers to the simulation of synthetic data for a given model parameterization (Thomas, 2004). The Poisson equation for a point source of current I at the position $\vec{r}_s$ yields

$$\nabla.(\sigma\nabla V) = \nabla\sigma.\nabla V + \nabla^2 V = -I\delta(\vec{r} - \vec{r}_s), \qquad (3.1)$$

which must be solved for the potential $V(r)$ by appropriate methods. Note that a non-unique solution for the domain Ω requires specifying boundary conditions at its boundary Γ. The continuity equation (3.1) is defined if the potential is twice differentiable ($V \in C^2$) and the conductivity is differentiable once ($\sigma \in C^1$), which holds within the sub-domains Ω of the constant σ_i (Thomas, 2004). At the inner boundaries of two sub-domains Ω_m and Ω_n,

the continuity equation $\sigma_m \nabla V_m = \sigma_n \nabla V_n$ must be satisfied. For bodies with close geometry, boundary integral methods can be used, which are seldom of interest in inverse problems (Thomas, 2004). With the rapid development of computers in the last decades, finite difference (FD) and finite element (FE) techniques have been applied to solve differential equations in many aspects. The FD and FE methods are better suited to model any complex arbitrary 3D earth (Spitzer, 1995). In the following sections, it has been explained that how FD calculations can be used efficiently.

3.1.1. Finite Difference Discretization

The aim of the finite difference technique is the construction of a discrete model in the form of hexahedral grid with nodes at the cell corners (Thomas, 2004). The existing partial derivatives are replaced by finite differences. An overview of the finite difference modeling techniques and discretization schemes for DC problems has been given by Spitzer (1999). The basis of the forward calculation based on finite differences is reported by various authors, e.g., Dey and Morrison (1979a), Spitzer (1995). Lowry et al. (1989) and Zong et al. (1995) have conducted their studies to improve the quality of the modeling. Spitzer and Wurmstich (1995) have also investigated the speed and accuracy of various discretization methods and equation solvers. Rapid advancement in computer technology has enabled geophysicists to carry out accurate computations for large models with high resistivity contrast regions. The three dimensions of the modeling domain are subdivided into a grid by the node positions x_i (i ∈ 1 . . . i_{max}), y_j (j ∈ 1 . . . i_{max}) and z_k (k ∈1 . . . k_{max}). Many discretization schemes exist with various locations of conductivities and partial derivatives (Dey and Morrison, 1979a; Zhang et al., 1995; Spitzer, 1995). In the following paragraph, the discretization technique of Dey and Morrison (1979a) has been discussed.

Figure 3.1 shows a section of the finite difference grid. As a reference, the elementary domain $\Omega_{i,j,k}$ with the conductivity $\sigma_{i,j,k}$ is bounded by the grid nodes *(i, j, k), (i+1,j,k), (i,j+1,k), (i+1,j+1,k), (i,j,k+1), (i+1,j,k+1), (i,j+1,k+1)* and *(i+1,j+1,k+1).* Similarly, the elementary domain $\Omega_{i-1,j-1,k-1}$ is bounded by the grid nodes $(i-1, j-1, k-1)$, $(i-1, j, k-1)$, $(i, j, k-1)$, $(i, j-1, k-1)$, $(i-1, j-1, k)$, $(i-1, j, k)$, (i, j, k) and $(i, j-1, k)$, and its conductivity supposed to be $\sigma_{i-1,j-1,k-1}$. Integration of equation (3.1) on the elementary domain $\omega_{i,j,k}$, which surrounds the grid node (i, j, k) in Figure 3.1, yields:

$$\oiint \nabla.(\sigma\nabla V)\mathrm{d}^3\vec{\mathrm{r}} = \oiint \mathrm{I}\delta^3(\vec{\mathrm{r}} - \vec{\mathrm{r}_\mathrm{s}})\mathrm{d}^3\vec{\mathrm{r}} = -\mathrm{I}(\vec{\mathrm{r}_\mathrm{s}}). \qquad (3.2).$$

Using Gauss' theorem, the volume integral is transformed into a surface integral:

$$\oiint \nabla.(\sigma\nabla V)\mathrm{d}^3\vec{\mathrm{r}} = \oiint \sigma\frac{\partial \mathrm{V}}{\partial \eta}\mathrm{d}\Gamma = -\mathrm{I}(\vec{\mathrm{r}_\mathrm{s}}). \qquad (3.3)$$

where $\Gamma_{i,j,k}$ denotes the enclosing surface of $\omega_{i,j,k}$ and η is its normal vector. The potential gradient $\frac{\partial V}{\partial \eta}$ is approximated using central differences on every edge. Thus, an integral is replaced by a sum over six faces.

$$\mathrm{IS}_{\Delta\Gamma^{+\mathrm{k}}_{\mathrm{i,j,k+\frac{1}{2}}}} + \mathrm{IS}_{\Delta\Gamma^{-\mathrm{k}}_{\mathrm{i,j,k-1/2}}} + \mathrm{IS}_{\Delta\Gamma^{-\mathrm{j}}_{\mathrm{i,j-1/2,k}}} + \mathrm{IS}_{\Delta\Gamma^{+\mathrm{j}}_{\mathrm{i,j+1/2,k}}} + \mathrm{IS}_{\Delta\Gamma^{-\mathrm{i}}_{\mathrm{i-1/2,j,k}}} + \mathrm{IS}_{\Delta\Gamma^{+\mathrm{i}}_{\mathrm{i+1/2,j,k}}}$$
$$= -\mathrm{I}(\mathrm{x_s}, \mathrm{y_s}, \mathrm{z_s}). \qquad (3.4)$$

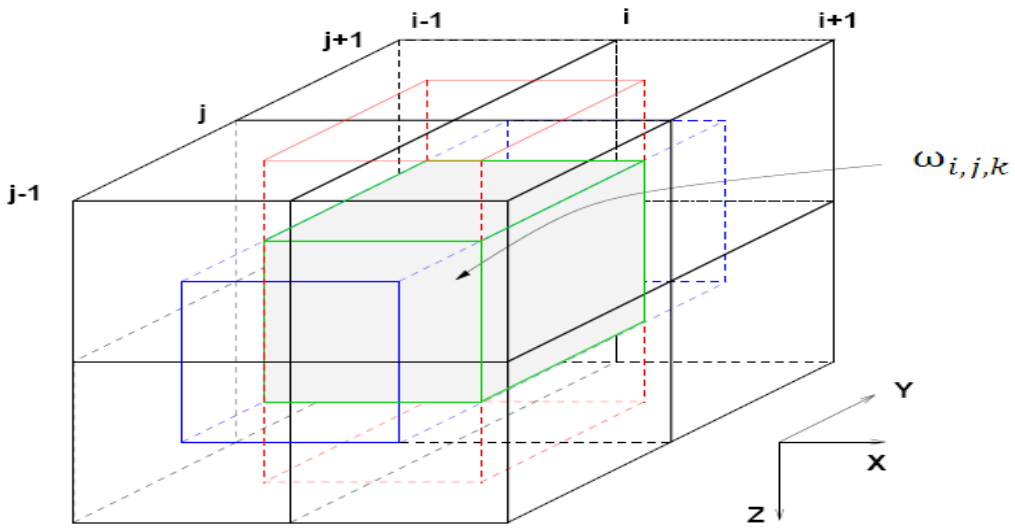

Figure 3. 1. The FD grid for the grid node (i, j, k). The dashed line denotes the definition of the average conductivity at the grid nodes (Thomas, 2004).

Figure 3.2 shows the conductivities at the edge in the *+i, -i, +j, -j, +k* and *-k*-directions. The conductivity σ is the weighted mean of four adjacent conductivity cells, so the integrals at the bottom, top, front, back, left and right faces are as follows:

Bottom face:

$$IS_{\Delta\Gamma^{+k}_{i,j,k+\frac{1}{2}}} = \iint \sigma \frac{\partial V}{\partial z} dx\, dy = \frac{V_{i,j,k+1} - V_{i,j,k}}{\Delta z_{k+1}} \left(\sigma_{i-1,j-1,k} \frac{\Delta x_{i-1} \times \Delta y_{j-1}}{4} + \sigma_{i,j-1,k} \frac{\Delta x_{i+1} \times \Delta y_{j-1}}{4} + \sigma_{i-1,j,k} \frac{\Delta x_{i-1} \times \Delta y_{j+1}}{4} + \sigma_{i,j,k} \frac{\Delta x_{i+1} \times \Delta y_{j+1}}{4} \right).$$

Top face:

$$IS_{\Delta\Gamma^{-k}_{i,j,k-1/2}} = \iint \sigma \frac{\partial V}{\partial z} dx\, dy$$

$$= \frac{V_{i,j,k} - V_{i,j,k-1}}{\Delta z_{k-1}} \left(\sigma_{i-1,j-1,k-1} \frac{\Delta x_{i-1} \times \Delta y_{j-1}}{4} + \sigma_{i-1,j,k-1} \frac{\Delta x_{i-1} \times \Delta y_{j+1}}{4} + \sigma_{i,j,k-1} \frac{\Delta x_{i+1} \times \Delta y_{j+1}}{4} + \sigma_{i,j-1,k-1} \frac{\Delta x_{i+1} \times \Delta y_{j-1}}{4} \right).$$

Front face:

$$IS_{\Delta\Gamma^{-j}_{i,j-\frac{1}{2},k}} = \iint \sigma \frac{\partial V}{\partial y} dx\, dz =$$

$$\frac{V_{i,j,k} - V_{i,j-1,k}}{\Delta y_{j-1}} \left(\begin{array}{c} \sigma_{i-1,j-1,k-1} \frac{\Delta x_{i-1} \times \Delta z_{k-1}}{4} + \sigma_{i,j-1,k-1} \frac{\Delta x_{i+1} \times \Delta z_{k-1}}{4} + \\ \sigma_{i,j-1,k} \frac{\Delta x_{i+1} \times \Delta z_{k+1}}{4} + \sigma_{i-1,j-1,k} \frac{\Delta x_{i-1} \times \Delta z_{k+1}}{4} \end{array} \right).$$

Back face:

$$IS_{\Delta\Gamma^{+j}_{i,j+1/2,k}} = \iint \sigma \frac{\partial V}{\partial y} dx\, dz = \frac{V_{i,j+1,k} - V_{i,j,k}}{\Delta y_{j+1}} \left(\sigma_{i-1,j,k-1} \frac{\Delta x_{i-1} \times \Delta z_{k-1}}{4} + \sigma_{i,j,k-1} \frac{\Delta x_{i+1} \times \Delta z_{k-1}}{4} + \right.$$

$$\left. \sigma_{i-1,j,k} \frac{\Delta x_{i-1} \times \Delta z_{k+1}}{4} + \sigma_{i,j,k} \frac{\Delta x_{i+1} \times \Delta z_{k+1}}{4} \right).$$

Left face:

$$IS_{\Delta\Gamma^{-i}_{i-\frac{1}{2},j,k}} = \iint \sigma \frac{\partial V}{\partial x} dy\, dz = \frac{V_{i,j,k} - V_{i-1,j,k}}{\Delta x_{i-1}} \left(\sigma_{i-1,j-1,k-1} \frac{\Delta y_{j-1} \times \Delta z_{k-1}}{4} + \sigma_{i-1,j,k-1} \frac{\Delta y_{j+1} \times \Delta z_{k-1}}{4} + \right.$$

$$\left. \sigma_{i-1,j,k} \frac{\Delta y_{j+1} \times \Delta z_{k+1}}{4} + \sigma_{i-1,j-1,k} \frac{\Delta y_{j-1} \times \Delta z_{k+1}}{4} \right).$$

Right face:

$$IS_{\Delta\Gamma^{+i}_{i+1/2,j,k}} = \iint \sigma \frac{\partial V}{\partial x} dx\, dy = \frac{V_{i+1,j,k} - V_{i,j,k}}{\Delta x_{i+1}} \left(\sigma_{i,j-1,k-1} \frac{\Delta y_{j-1} \times \Delta z_{k-1}}{4} + \sigma_{i,j,k-1} \frac{\Delta y_{j+1} \times \Delta z_{k-1}}{4} + \right.$$

$$\left. \sigma_{i,j,k} \frac{\Delta y_{j+1} \times \Delta z_{k+1}}{4} + \sigma_{i,j-1,k} \frac{\Delta y_{j-1} \times \Delta z_{k+1}}{4} \right).$$

3.1.2. Boundary conditions

At the boundary of the modeling domain, the neighbors in the outward directions are missing. Therefore, the behavior of the potential field must be defined by boundary conditions. In general, there exist three different types of conditions:

- Neumann boundary conditions fix the potential derivative with respect to the outward direction. This is essential for the earth's surface, where the current flow perpendicular to the surface is zero. They can be applied by introducing an additional conductivity-free layer above the surface.

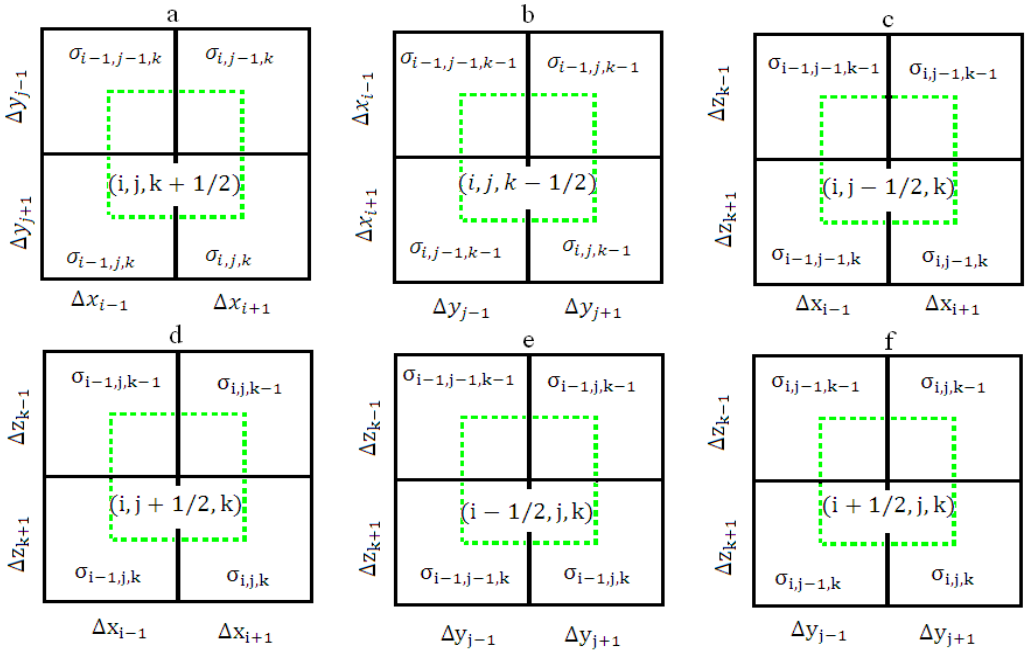

Figure 3. 2. Plan view of the different faces of the grid and the domain ω_(i,j,k) shown in Figure 3.1 (a-bottom face, b-top face, c-front face, d- back face, e- left face and f- right face). The dashed lines denote the average conductivity at the grid nodes.

- Dirichlet boundary conditions are used to fix the potential values. They can be calculated analytically for a homogeneous or layered half-space. Since the potentials are not known, their outward values are usually set to zero. To improve the accuracy in the modeling domain, layers with prolonged grid spacings are added to the parameter model boundaries.
- Mixed boundary conditions relate the potential and its derivative by assuming the potential characteristics. Dey and Morrison (1979a) presented boundary conditions for a single current electrode at the origin:

$$\frac{\partial V}{\partial \eta} + \frac{V}{|\vec{r}|}\cos\theta = 0\,. \qquad (3.5)$$

where θ is the angle between the position vector $\vec{r}$ and the outward vector $\vec{\eta}$. Using the dot product for the boundary at *x* the following equation can be obtained*:*

$$\frac{\partial V}{\partial \eta} + \frac{x}{r^2} V = 0, \tag{3.6}$$

which can easily be discretized and introduced into the system of equations.

Using equation (24.2) for all nodes yields a discrete differential equation represented by a system of equations:

$$\mathbf{K} \cdot \mathbf{V} = \mathbf{b}, \tag{3.7}$$

which must be solved for the vector **V** containing the potentials for all existing nodes. The coupling matrix **K** works as discretized differential operator, which is a sparse matrix of band-structure. **K** is guaranteed to be positive semi-definite and regular and thus has a unique solution for all **b**. The source vector **b** represents a discrete Dirac function, where all elements are zero except for the node where the current electrode is placed. All electrodes must match the finite difference grid, which can lead to huge node numbers for irregular electrode positions. Since the potential follows a behavior proportional to 1/r, it can hardly be discretized by a piecewise linear function (Thomas, 2004). Hence, large discretization errors occur near the electrodes, which can only be reduced by using a very fine grid (Thomas, 2004). The matrix becomes singular if Neumann conditions are applied to all boundaries. Hence, at least at one point Dirichlet or mixed conditions must be installed.

3.2. Non-linear inversion

In the early 1980s, some initial approaches to 2D inversion were developed (e.g., Inman, 1975, Tripp et al., 1984). The first attempt on 3D inversion of the PP data by Park and Van (1991) was followed by Newton methods (e.g., Li and Oldenburg, 1999). Ellis and Oldenburg (1994) and Zhang et al. (1995) used algorithms based on non-linear conjugate gradient methods. Most inversion programs assume a flat earth surface. Topography in 2D

models can be included by means of a Schwarz-Christoffel transformation (Tong and Yang, 1990). Finite difference methods cannot solve the 3D problems in which the effect of topography must be considered (Thomas, 2004); a suitable alternative in such cases is the finite element method (Sasaki, 1994; Sugimoto, 1999).

Besides the development of inversion routines, the resolution properties have also been improved (e.g., Narayan, 1992; Sasaki, 1992; Dahlin and Loke, 1998). The first numerical resolution for DC data was carried out by Oldenburg and Li (1999). Friedel (1997), Spitzer (1998) and Dietrich (1999) gained an intuitive understanding of resolution by sensitivity studies. Meke (1989) has studied the uncertainty in linear problems. The resolution matrices for nonlinear problems were also defined by Meju (1994a), and they have been investigated in detail for DC resistivity by Friedel (2000). As suggested by Friedel (2000), the quality of the inversion results can be appraised directly from the resolution matrices. Moreover, resolution analysis provides a base for optimizing experimental design (Maurer et al., 2000), which can be of particular interest in multi-electrode DC measurements (Stummer et al., 2004).

3.2.1. Inversion methodology

Assume a set of N measured data points, $\mathbf{d} = (d_1, d_2, d_3, \ldots d_N)^{\mathrm{T}}$, affected by the physical property $\mathbf{q}$ of the subsurface. The goal is to find a spatial parameter distribution $\mathbf{q}(\vec{r})$ of this property that explains the parameter $\mathbf{d}$. Since the collected data are usually contaminated with noise, efforts have been made to fit a part of the data that is generated by parameter variations (Thomas, 2004). The function $\mathbf{q}(\vec{r})$ is represented using a limited number M of model parameters m_i serving as weighting coefficients for the basis functions $\mathbf{W}(\vec{r})$;

$$\mathbf{q}(\vec{r}) = \sum_{k=1}^{M} \mathbf{W_k}(\vec{\mathbf{r}})\, \mathbf{m_k} \,. \qquad (3.8)$$

where $\mathbf{m} = (m_1, m_2, m_3, \ldots m_N)^T$.

One usual way to define the W_i is to subdivide the region of interest into sub-domains Θ_i that are convex bodies such as hexahedrons:

where $$W_k(\vec{r}) = \begin{cases} 1 & for\ \vec{r} \epsilon\ \Theta_i \\ 0 & elsewhere \end{cases}$$

The main objective of the inversion process is to obtain a model **m**, whose response **q(m)** should fits in the data **d**. For non-linear problems, the forward operation depends on the model **m** itself, which holds the key for all methods based on Maxwell's equations. Beginning from the initial stage (model $\mathbf{m}_{\mathrm{zero}}$), an iterative process is applied to update the model until the data fit well or convergence is achieved (Thomas, 2004). In each iteration of the inversion process (k), a new model is calculated by adding an update Δm_k:

$$\mathbf{m_{k+1}} = \mathbf{m_k} + \mathbf{\Delta m_k}. \tag{3.9}$$

The Taylor approximation of the first order yields:

$$\mathbf{q}(\mathbf{m_k} + \Delta\mathbf{m_k}) = \mathbf{q}(\mathbf{m_k}) + \left\{\frac{\partial \mathbf{q}}{\partial \mathbf{m}}(\mathbf{m_k})\right\}\Delta\mathbf{m_k} + \ \ldots \approx \mathbf{q}(\mathbf{m_k}) + \mathbf{J}\Delta\mathbf{m_k}$$

The coefficient of the second term of the above equation is called the Jacobian or sensitivity matrix $\mathbf{J} \in \mathfrak{R}^{\mathbf{N}\times\mathbf{M}}$ with the following elements:

$$J_{ij}(\mathbf{m_k}) = \frac{\partial q_i}{\partial m_j}(\mathbf{m_k})\ . \tag{3.10}$$

In fact, the Jacobian matrix **J**, is the partial derivative of the model response with respect to the its parameters. Setting a response of the new model $\mathbf{q(m + \Delta m)}$ equal to data , the non-quadratic equation is obtained as following:

$$\mathbf{J}\,\Delta\,\mathbf{m} = \mathbf{d} - \mathbf{q}(\mathbf{m}). \tag{3.11}$$

This equation must be solved in a sense to minimize the residual vector $\mathbf{d} - \mathbf{q}(\mathbf{m})$. . An error ξ_i can be estimated for each data point d_i that is used to weight the residual. A data function Ψ_d is defined using the L_p-norm of the weighted residual.

$$\Psi_d(\mathbf{m}) = \sum_{i=1}^{N} \left| \frac{[d_i - q_i(\mathbf{m})]}{\xi \mathrm{i}} \right|^p = \|\mathbf{D}(\mathbf{d} - \mathbf{q}(\mathbf{m}))\|_p^p . \quad (3.12)$$

with $\mathbf{D}$ = diag (1 / ξ_i), where Ψ_d must be minimized in the inversion process.

Depending on the expected noise characteristics, different values of p can be used (Farquharson and Oldenburg, 1998). If the noise has a long-tailed distribution, the L_1-norm is advantageous (Thomas, 2004). An L_1 minimization procedure is often called "robust inversion" (Claerbout and Muir, 1973), because it is less sensitive to outliers in the data. However, if the noise has a Gaussian distribution, the L_2-norm is the advantageous (Thomas, 2004). From a statistical point of view, the mean value of the data function is:

$\chi^2 = \Psi_d / N$

when χ^2 is equal to one, the fitted data are within their errors. Thus, the functional norm can be written as:

$$\Psi_d = [\mathbf{D}(\mathbf{d} - \mathbf{q}(\mathbf{m}))]^{\mathrm{T}} \left[\mathbf{D}\left(\mathbf{d} - \mathbf{q}(\mathbf{m})\right)\right] = \left(\mathbf{d} - \mathbf{q}(\mathbf{m})\right)^{\mathrm{T}} \mathbf{D}^{\mathrm{T}} \mathbf{D}\left(\mathbf{d} - \mathbf{q}(\mathbf{m})\right) . \quad (3.13)$$

The product $\mathbf{D}^{\mathrm{T}}\mathbf{D}$ is the inverse of the data covariance matrix $\boldsymbol{C_d}$ as used by Tarantola (1978) in the case of uncorrelated errors with standard deviations ξ_i and variances $\xi_i^{\,2}$. If correlations between the individual errors are present, the covariance matrix $\boldsymbol{C_d}$ does not remain diagonal (Thomas, 2004). Some of the common inversion methods are discussed as following.

3.2.1.1. Steepest descent method

The minimum of Ψ in the direction of the steepest descent of Ψ must be sought. The model update is $\delta_k = -\nabla_m \Psi$

where $\nabla_m = \left(\frac{\partial}{\partial m_1}, \frac{\partial}{\partial m_2}, \ldots, \frac{\partial}{\partial m_M}\right)^T$.

A step length $\boldsymbol{\theta}$ must be estimated so that $\Psi(\mathbf{m_k} + \boldsymbol{\theta}\boldsymbol{\delta_k})$ is minimized. After that, a 'Line Search' procedure inquires for an optimum solution along the line defined by varying θ

(Thomas, 2004). In every iteration, the functional's gradient is calculated by the precise use of the Jacobian matrix. Since the convergence rate of the steepest descent technique for ill-posed problems is very slow, forward calculations using this method are very time-consuming. This technique is very simple to implement, but rarely of practical use.

3.2.1.2. Nonlinear conjugate gradients method

Hestenes and Stiefel (1952) developed the method of conjugate gradients to solve a linear system of $\mathbf{Ax} = \mathbf{b}$ for a sparse matrix **A**. The principle of this technique is to find a set of perpendicular directions and to compute their corresponding weights. Since each search direction is used only once, the convergence is thus fast as compared to the steepest descent method. This technique can also be useful for non-linear minimization (Shewchuk, 1994; Vogel, 2002; Mackie and Madden, 1993; Rodi and Mackie, 2001), because it is based on an iterative minimization of the function $1/2\mathbf{x}^{\mathbf{T}}\mathbf{Ax} - \mathbf{x}^{\mathbf{T}}\mathbf{b}$ (Thomas, 2004). Zhang et al. (1995) has successfully used the conjugate gradients equation solver to invert 3D DC resistivity data. The gradient G_d of the function Ψ_d can be computed from the Jacobian matrix using the chain rule:

$$G_{d,k} = 2\nabla_m \Psi_{\mathrm{d}}(\mathbf{m_k}) = \mathbf{J^T D^T D}(\mathbf{q}(\mathbf{m_k}) - \mathbf{d}).$$

For each iteration (k), the model response $\mathbf{q}(\mathbf{m_k})$ and the gradient G_k must be calculated.

3.2.1.3. Newton-type methods

Assume a second order Taylor series for the function Ψ of an updated model $\boldsymbol{m}+\boldsymbol{\Delta m}$

$$\Psi(\mathbf{m}+\Delta\mathbf{m}) \approx \Psi(\mathbf{m}) + (\nabla_{\mathrm{m}}\Psi(\mathbf{m}))^{\mathrm{T}}\Delta\mathbf{m} + \frac{1}{2}\Delta\mathbf{m}^{\mathrm{T}}(\nabla_{\mathrm{m}}{}^2\,\Psi(\mathbf{m}))^{\mathrm{T}}\Delta\mathbf{m} + \cdots \qquad (3.14)$$

where $\nabla_{\mathrm{m}}{}^2$ is the Hessian matrix with elements:

$$(\nabla_m{}^2\,\Psi)_{ij} = (\nabla_m \nabla_m{}^T \Psi)_{ij} = \frac{\partial^2 \Psi}{\partial m_i \partial m_j}.$$

The second order Taylor series in the equation 3.14 is minimized by setting its first partial derivative with respect to $\Delta\mathbf{m}$ to zero: $\nabla_m\Psi(\mathbf{m}) + \nabla_m{}^2\Psi(\mathbf{m})\Delta\mathbf{m} = 0$. Thus, the model update $\Delta\mathbf{m_k}$ is calculated by solving the equation

$$\left((\nabla_m{}^2\Psi)\Delta\mathbf{m_k} = -\nabla_m\Psi\right). \tag{3.15}$$

For the function Ψ_d as defined by (3.13), the following holds

$$\mathbf{H_{k,d}} = \nabla_m\nabla_m{}^T\Psi_d = \nabla_m\left(2\mathbf{J^T D^T D(q(m_k) - d)}\right)$$

$$= 2\mathbf{J^T D^T DJ} + 2(\nabla_m^T\mathbf{J^T})\mathbf{D^T D(q(m_k) - d)}. \tag{3.16}$$

The term $2(\nabla_m^T\mathbf{J^T})\mathbf{D^T D(q(m_k) - d)}$ can be neglected if the problem is not strongly non-linear (Thomas, 2004).

3.2.1.3.1. Gauss-Newton method

The technique using the Hessian approximation $\mathbf{H_{k,d}} = 2\mathbf{J^T D^T DJ}$ is called the Gauss-Newton method. This method has two advantages: 1) the computation is easier than the other methods and 2) Hessian approximation in this method is positive semi-definite, where the latter one guarantees that the Gauss-Newton step is a descent direction. However, the quadratic convergence of the Newton's method loses its effectiveness due to strong non-linearity. If $\mathbf{\Delta d_k = d - q\ (m_k)}$, the linear equation (3.15) can be written as:

$$\left((\mathbf{DJ})^T(\mathbf{DJ})\right)\Delta\mathbf{m_k} = (\mathbf{DJ})^T\mathbf{D}\Delta\mathbf{d_k} \tag{3.17}$$

which is a least squares solution of $\mathbf{DJ}\Delta\mathbf{m_k} = \mathbf{D}\Delta\mathbf{d_k}$. Newton's method has a quadratic convergence, due to second order of the Taylor approximation (Vogel, 2002). Thus, if the starting model is in the neighborhood of the minimum, the number of iterations will be small (Thomas, 2004). However, if there are several local minima, the solution may not produce unique results. In order to overcome this deficiency, a different starting model, $\mathbf{m_{zero}}$ should be tested.

3.2.1.3.2. The Marquardt-Levenberg modification

In some cases, the matrix product **DJ** may be singular or nearly-singular. If it is singular, the least-squares equation does not have a solution for $\Delta\mathbf{m}$. The near- singular state for **DJ** can occur if an initial model that is quite different from the optimum model is used. The calculation of $\Delta\mathbf{m}$ using equation (3.11) can have too large components such that the new model calculated with (3.9), $\mathbf{m_{k+1}}$, might have unrealistic values. The Marquardt-Levenberg modification (Lines and Treitel 1984) to the Gauss-Newton equation is one common way to avoid the singularity problem. This method which is also known as the ridge regression method (Inman, 1975) is given by

$$(\mathbf{D\,J} + \zeta\,\mathbf{I})\Delta\mathbf{m_k} = \mathbf{D}\Delta\mathbf{m_k}. \qquad (3.18)$$

where **I** is the identity matrix and the symbol ζ is known as the Marquardt factor. The Marquardt factor effectively constrains the range of values that the elements of $\Delta\mathbf{m_k}$ can take. while the Gauss-Newton method in equation (3.17) attempts to minimize the sum of the squares of the $\Delta\mathbf{d_k}$. The method of Marquardt-Levenberg modification also minimizes a combination of the magnitude of the $\Delta\mathbf{d_k}$ and the $\Delta\mathbf{m_k}$. This method has been successfully used to invert VES data where the model consists of a small number of layers.

3.2.1.3.3. Quasi-Newton method

Newton's method assumes that the functional norm, $\boldsymbol{\Psi_d}$, can be locally approximated as a quadratic Taylor expansion in the region around the optimum, where the first and second derivatives are used to find the stationary point. Recalculation of the Hessian matrix in Newton's method for each iteration might be very time-consuming. However as an alternative choice the quasi-Newton technique can be used, which updates the Hessian by previous gradients (Thomas, 2004). In quasi-Newton methods, the Hessian matrix of second derivatives of $\boldsymbol{\Psi_d}$ to be minimized and does not need to be computed at

any stage. The Hessian is instead updated by analyzing successive gradient vectors. The Quasi-Newton method is a generalization of the secant method to find the root of the first derivative for a multidimensional problem.

The Broyden-Fletcher-Goldfarb–Shanno (BFGS) method is a technique to solve an unconstrained nonlinear optimization problem. It is derived from Newton's method, which seeks the stationary point of a function where the gradient is zero (Broyden, 1970, 1972). The BFGS method uses the following approximation:

$$\mathbf{H_{k+1}} = \mathbf{H_k} - \frac{\mathbf{H_k}\,\Delta\mathbf{m_k}\Delta\mathbf{m_k}^{\mathbf{T}}\mathbf{H_k}}{\Delta\mathbf{m_k}^{\mathbf{T}}\,\mathbf{H_k}\,\Delta\mathbf{m}} + \frac{\boldsymbol{\omega_k}\,\boldsymbol{\omega_k}^{\mathbf{T}}}{\Delta\mathbf{m_k}^{\mathbf{T}}\,\boldsymbol{\omega_k}}, \qquad (3.19)$$

where $\boldsymbol{\omega} = \nabla_m \Psi(\mathbf{m_{k+1}}) - \nabla_m \Psi(\mathbf{m_k})$

A slightly different form of this equation is used by Loke and Barker (1996b):

$$\mathbf{H_{k+1}} = \mathbf{H_k} + \frac{[\mathbf{q}(\mathbf{m_{k+1}}) - \mathbf{q}(\mathbf{m_k}) - \mathbf{H_k}\,\Delta\mathbf{m_k}]\Delta\mathbf{m_k}^{\mathbf{T}}}{\Delta\mathbf{m_k}^{\mathbf{T}}\,\Delta\mathbf{m}}. \qquad (3.20)$$

This method can sufficiently be used for most 2D DC resistivity problems (Loke and Dahlin, 2002).

3.2.1.4. Smoothness-constrained least squares method

In the inversion of 2D and 3D resistivity data with large number of model parameters, the produced model can have an erratic resistivity distribution with spurious low or high resistivity anomalies (Constable et al., 1987). To overcome this problem, the Gauss-Newton least-squares equation is further modified, which change the model resistivity values in a gradual manner.

3.2.1.4.1. L2_norm smoothness-constrained optimization method

The mathematical form of this smoothness-constrained method (Ellis and Oldenburg, 1994) is given by

$$(\mathbf{DJ} + \zeta\mathbf{F})\Delta\mathbf{m_k}\mathbf{D}\Delta\mathbf{d_k} - \zeta\mathbf{F}\mathbf{m_k}. \qquad (3.21)$$

where $\mathbf{F} = \boldsymbol{\alpha}_x \mathbf{C}_x^T \mathbf{C}_x + \boldsymbol{\alpha}_y \mathbf{C}_y^T \mathbf{C}_y + \boldsymbol{\alpha}_z \mathbf{C}_z^T \mathbf{C}_z$ and $\mathbf{C}_x$, $\mathbf{C}_y$ and $\mathbf{C}_z$ are the smoothing matrices. The α_x, α_y and α_z are the relative weights given to the smoothness filters in the x, y- and z-directions. One common form of the smoothing matrix is:

$$\mathbf{C} = \begin{pmatrix} -1 & 1 & 0 & 0 & .. & .. & .. & 0 \\ 0 & -1 & 1 & 0 & .. & .. & .. & 0 \\ 0 & 0 & -1 & 1 & 0 & .. & .. & 0 \\ & & & .. & & & & \\ & & & & .. & & & \\ & & & & & .. & & \\ & & & & & & 0 & \end{pmatrix} \qquad (3.22)$$

In this equation, C is the first-order difference matrix (de Groot-Hedlin and Constable, 1990). In fact, equation (3.21) represents an L_2 _ norm smoothness-constrained optimization method. This tends to produce a model with a smooth variation of resistivity values. This approach is acceptable if the actual subsurface resistivity varies in a smooth and gradational manner (Loke, 2009).

3.2.1.4.2. L1_ norm smoothness-constrained optimization method

In some cases, the subsurface geology consists of a number of zones that are almost homogeneous but with sharp boundaries between different zones. For such cases, equation (3.21) can be modified as follows:

$$(\mathbf{DJ} + \zeta \mathbf{F})\Delta \mathbf{m_k} = \mathbf{DR_d}\Delta \mathbf{d_k} - \zeta \mathbf{F_R} \mathbf{m_k}\,, \qquad (3.23)$$

where $\mathbf{F_R} = \boldsymbol{\alpha}_x \mathbf{C}_x^T \mathbf{R_m} \mathbf{C}_x + \boldsymbol{\alpha}_y \mathbf{C}_y^T \mathbf{R_m} \mathbf{C}_y + \boldsymbol{\alpha}_z \mathbf{C}_z^{\mathbf{TR_m}} \mathbf{C}_z$

In this equation, $\mathbf{R_d}$ and $\mathbf{R_m}$ are weighting matrices introduced so that different elements of the data misfit and model roughness vectors are given equal weights in the inversion process. With equation (3.23) the absolute changes in the model resistivity values can be minimized (Claerbout and Muir, 1973). Technically this is referred to as an L_1_ norm smoothness-constrained optimization method or a blocky inversion method (robust inversion technique), which can sometimes give significantly better results (Loke, 2009),

for instance, in a situation where the subsurface geology consists of high resistivity zones with sharp boundaries. It also provides a general technique that can be further modified to include known information about the subsurface geology (Loke, 2009).

3.3. Summary

In this chapter, the importance of inverting measured apparent resistivity data obtained with DC resistivity surveys has been discussed. Aspects of the finite difference method and different boundary conditions have also been explained to study the numerical simulation of measured data for given subsurface parameters. In addition, the methodology of non-linear inversion and the common inversion methods (i.e., steepest descent method, nonlinear conjugate gradients method, Newton-type methods and smoothness-constrained least squares methods) is introduced. Because the convergence rate of the steepest descent technique for ill-posed problems is very slow, forward calculations using this method are found to be very time-consuming.

In the nonlinear conjugate gradients technique, each search direction is used only once. Thus, convergence is fast compared with the steepest descent method. This technique can also be useful for non-linear minimization. In the Gauss-Newton method, the computation is found to be easier than the other methods. The Hessian approximation in this method is positive semi-definite, which provide a guarantee that the Gauss-Newton step is a descent direction. The singularity problem in the Newton-type methods can be avoided by using the Marquardt-Levenberg modification of the Gauss-Newton equation. Recalculating the Hessian matrix in the Newton's method for each iteration might be very time-consuming. However, the use of quasi-Newton technique, which updates the Hessian by previous gradients can be considered as an alternative option. The L_2_ norm smoothness-constrained optimization method tends to produce a model with a smooth variation of

resistivity values. This approach is acceptable if the actual subsurface resistivity varies in a smooth and gradational manner. The L1_ norm smoothness-constrained optimization method (robust inversion technique) can be used to minimize the absolute changes in the model resistivity values. This method can sometimes give significantly better results if zones of high resistivity contrast (with sharp boundaries) exist beneath the earth surface.

Chapter 4
Artificial neural network system

Nowadays, the geophysical inverse problem is a very active research area. It involves representing geophysical measurements by realistic geological models. Most geophysical inverse problems belong to a class of nonlinear inversion, and a misfit function is introduced. The inversion process seeks subsurface parameters in order to minimize the misfit function. In nonlinear inverse problems with a few degrees of freedom, the Monte Carlo method has been used. However when the complexity of the problem increases, this method cannot find an appropriate subsurface model (Press, 1968). In that case, an alternative of the Monte Carlo method, the gradient technique can be used. When the starting model is close to the global minima, the gradient method provides a correct solution. However, the problems of how to deal with local minima, too high memory requirements and time consumption are the disadvantages attached with this method (Tarantola, 1986, 1987; Fei, 1995).

Only a brief introduction of artificial neural networks (ANNs) is given in this section since several reviews of these systems have already been published in the literature (e.g., Lippman, 1987; Haykin, 1999). The ANN system is well suited to solving difficult and complex problems (Haykin, 1999). Recently, ANNs have been developed, which can provide a new geophysical inversion technique to overcome some of the inversion limitations. The training procedure of the ANN is considered as one of the global optimization methods (Fei, 1995). Research on ANNs started about 50 years ago, when the theory of perceptrons was presented by Rosenblatt (1962). During the mid-1960s, interest in ANNs decreased because of the limitations of the theory of perceptrons (Minsky and

papert, 1969). Since new paradigms in this system have overcome some of these limitations, the ANN has been emerged again as an active research area in the field of computer science, engineering, physics and geophysics. An ANN is a simplified computer simulation of the human brain. Unlike conventional computer programs that use a fixed algorithm to solve a particular problem, ANNs use a non-linear learning method to solve a complex problem. The ANN is trained by repetitively presenting samples of the inputs and desired outputs of the problem to be solved. One of the advantages of ANNs compared to multivariate linear analysis is that the underlying relationships between dependent and independent variables do not need to be known a priori. The ANN adjusts itself with examples to find the relationships between variables (Bui, 2004). Other advantages are that ANNs can have several outputs and can use discrete variables as inputs or outputs. As a result, the ANN is able to learn like a human brain in order to find the hidden relationships between inputs and outputs in the training phase. In addition, it is also able to predict the desired output from a new set of input data.

4.1. Neural network architectures

ANNs are computational systems that simulate the biological neural networks of the human brain. The human brain contains several billion neurons interconnected via synapses that constitute the network. ANNs are systems made up of a number of simple, highly interconnected processing algorithms (neurons), which process information by their dynamic state response to external inputs (Fausett, 1994). ANNs are also considered as exploration and development tools that can easily transform input data into desired output parameters. ANNs can use knowledge gained from past experiences and apply that to new problems and situations (Ripley, 1996). Figure (4.1) shows a schematic diagram of the ANN architecture. The system consists of (1) a set of nodes (artificial neurons) that perform

simple computations, (2) a set of interconnections, or synapses, linking pairs of nodes, and (3) a set of labels, known as weights, associated with each interconnection that identify some property of the interconnection. These weights correspond to the synaptic efficiency of the biological neurons (Aristodemou et al., 2005). Each node uses its input signals to compute an output signal; the output is the result of networking between nodes performing specific individual tasks. The mathematical relation between the input and output signals of a node is called the activation function. Several activation functions can be used. The choice of proper activation function depends on the problem to be solved. It is often determined by computational considerations of the training process (Bui, 2004). The most commonly used functions are the linear, $f(x) = ax + b$, the sigmoidal, $f(x) = \frac{1}{1+e^{-x}}$ and the Gaussian $f(x) = \frac{a+be^{x^2}}{e^{x^2}}$.

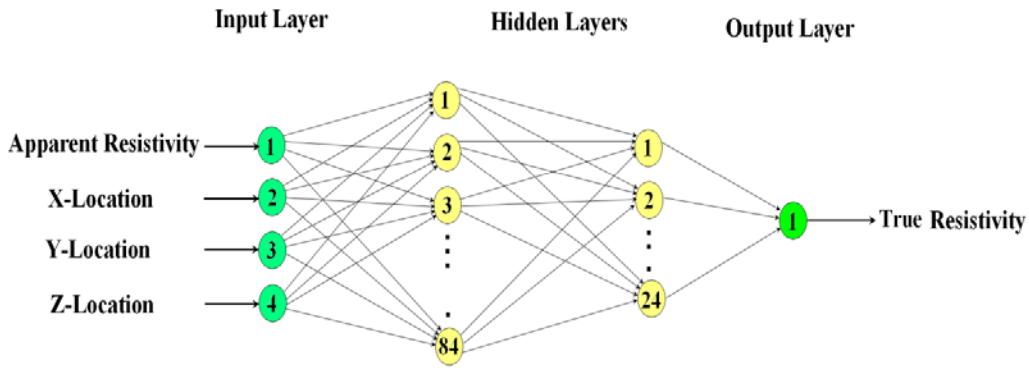

Figure 4. 1. Artificial Neural Network architecture used in this study.

4.1.1. Feed-Forward neural networks

ANN systems are specified by their respective architectures and training rules (Fausett, 1994). The rules specify the initial set of network connection weights, and the training indicates how the weights should be adapted to improve performance. One of the ANNs that is widely used for multivariate correlation and pattern recognition is the feed-

forward neural network (FFNN) (Rumelhart and McClelland, 1986; Bishop, 1995; Fausett, 1994; Garson, 1998).

The FFNNs, which are widely used in engineering applications, are parallel distributed information processing structures consisting of neurons interconnected via unidirectional signal channels. In FFNN, there are at least three successive layers of neurons: an input layer, one or more hidden layers and an output layer. The number of neurons in the input layer is equal to the number of variables in the input data. These neurons do not have input connections but only output ones. The number of neurons in the hidden layer can vary based on the complexity of the problem and the size of the input dataset. Neurons in the hidden layer have both input and output connections. The number of neurons in the output layer is the same as the number of output variables. These neurons have only input connections. The output of a node in one layer is directed as the input to each and every node in the immediately following layer. There are no lateral connections between nodes in the same layer and no feedback connection to the nodes in previous layers.

A signal x_i at the input of synapse i connected to neuron j is multiplied by the synaptic weight w_{ij}. A summing junction adds the input signals, which are weighted by the respective synapses of the neuron. Each processing unit (neuron) has an activation function that is commonly chosen to be the sigmoid function. We used the logsig function, which is a special type of sigmoid function:

$$\mathrm{f} = \frac{1}{1 + \mathrm{e}^{-\mathrm{x}}} . \qquad (4.1)$$

The activation function limits the amplitude of a neuron, by that it restricts the permissible amplitude range of the output signal to some finite value. The net input to a processing unit j is given by:

$$net_j = \sum_i w_{ij}\, x_i + b_j \tag{4.2}$$

where x_i is the output from previous layer, and w_{ij} is the weight of the link connecting unit *i* to *j*. The weights associated with each connection indicate the extent to which the conveyed signal is amplified or diminished. The externally applied bias (threshold) b_j increases or decreases the net input of the activation function, depending on whether it is positive or negative, respectively. It has a role similar to the constant term in multiple linear regressions, e.g., it allows the origin to be shifted depending on the input variables for the network output. It also determines the location of the logsig function on the horizontal axis. The activation value (output) of unit *j* is given by:

$$a_j = \mathrm{f}(net_j) = \frac{1}{1 + \mathrm{e}^{-net_j}} \tag{4.3}$$

Suppose that at each neuron in the first and second hidden layers (Fig. 4.1), activation functions f_{h1} and f_{h2} are applied, respectively, and at each node in the output layer, the function f_{out} is applied; then, the network shown in Figure 1 can be mathematically expressed as:

$$\mathrm{f}(\mathrm{x}, \mathrm{w}) = \mathrm{f}_{\mathrm{out}}\left\{\sum_{\mathrm{k}=1}^{\mathrm{N_{h2}}} w_{k1}\, \mathrm{f}_2\left(\sum_{\mathrm{j}=1}^{\mathrm{N_{h1}}} w_{jk}\, \mathrm{f}_1\left(\sum_{\mathrm{i}=1}^{\mathrm{N_i}} w_{ij} x_i\right)\right)\right\} \tag{4.4}$$

where x_i denotes the input value at input neuron *i*, w_{ij} is the connection weight between input neuron *i* and hidden neuron *j* in the first hidden layer, w_{jk} is the connection weight between hidden neuron *j* in the first hidden layer and hidden neuron *k* in the second hidden layer, w_{k1} is the connection weight between hidden neuron *k* in the second hidden layer and output neuron 1, and N_i=4, N_{h1}=84 and N_{h1}=24 are the number of input and hidden nodes. The notation $f(\mathbf{x}, \mathbf{w})$ implies that the output of the network at the output node is a function of given vector values $\boldsymbol{x}$ of the exploratory variable and the weight vector **w**.

Hornik et al. (1990) reported that FFNNs with one hidden layer are capable of estimating any mathematical continuous function. ANNs with more hidden layers, however, can speed up the training process (Hirose et al., 1991).

In the present study, the most common learning law, i.e., back propagation (BP) is applied.

4.1.2. Back-Propagation algorithm

The back propagation (BP) method is the most widely used training algorithm for FFNNs because of its simplicity and small programming cost (Rumelhart and McClelland, 1986; Ripley, 1996; Bishop, 1995).

With the BP learning rules, the goal of learning is to minimize the error between the desired outputs and the calculated outputs of the network. The learning process for the BPNN involves sending the input values forward through the network and then computing the difference between the calculated output and the corresponding desired output from the training dataset. In this algorithm, the error function is minimized using a gradient-descent technique. The necessary corrections to the weights of the network for each moment are obtained by calculating the partial derivative of the error function with respect to each weight. The resulting weight update is then computed.

In its simplest form, the weight-update is a scaled step in the opposite direction of the gradient. Hence, the weight-update rule is:

$$\Delta_p w_{ij}(t) = -\varepsilon \times \frac{\partial E_p}{\partial w_{ij}}(t) + \alpha \times \Delta_p w_{ij}(t-1)\,. \tag{4.5}$$

where α is the momentum term that determines the influence of the previous iteration on the present one. ε is a parameter that determines the step size and is called the learning rate. In this equation, the total error is given by

$$\mathrm{E} = \mathrm{MSE} = \sum_{\mathrm{p=1}}^{\mathrm{Q}} \frac{E_p}{\mathrm{Q}} = \frac{1}{\mathrm{Q}} \sum_{\mathrm{p=1}}^{\mathrm{Q}} \sum_{\mathrm{j=1}}^{\mathrm{N}} (d_{pj} - a_{pj})^2 . \qquad (4.6)$$

where d_{pj} and a_{pj} are the target and the actual response value of the output neuron j, which corresponds to each training sample *pth*. *Q* is the number of training samples and *N* represents the number of output units. This error information is propagated backwards through the ANN and the weights are adjusted. After some number of iterations, the training stops when the calculated output values best approximate the desired values.

The BP includes several kinds of paradigms (e.g., batch back propagation, gradient descent, conjugate gradient, Levenberg-Marquardt, and resilient propagation). The main difference between these paradigms is the method of calculating the weights and their updating (Werbos, 1994; El-Qady and Ushijima, 2001). The mathematical basis of these paradigms is well described in the literature (e.g., Scales, 1985; Battiti, 1992; Riedmiller, 1993; Hagan et al., 1996; Powell, 1977; El-Qady and Ushijima, 2001).

The mathematical basis of resilient propagation (RPROP) is considered to be the most successful paradigm in this study.

4.1.2.1. Resilient propagation algorithm

The resilient propagation (RPROP) algorithm is a local adaptive learning scheme, performing supervised batch learning in the FFNNs, and was introduced by Riedmiller and Braun in 1993. The mathematical basis of the RPROP algorithm is discussed here because the results in chapter five will show that it is the most efficient algorithm for this study. It is introduced as a second learning rule that determines the evolution of the updated value. This estimation is based on the observed behavior of the partial derivative during two successive weight-steps. Each weight *(W_{ij})* has its own step size or update value *(Δ_{ij}),* which varies with time t according to the following equation

$$\Delta_{ij}(t) = \begin{cases} \eta^{+} \times \Delta_{ij}(t-1) & \text{if} \quad \frac{\partial E}{\partial W_{ij}}(t) \times \frac{\partial E}{\partial W_{ij}}(t-1) > 0 \\ \eta^{-} \times \Delta_{ij}(t-1) & \text{if} \quad \frac{\partial E}{\partial W_{ij}}(t) \times \frac{\partial E}{\partial W_{ij}}(t-1) < 0 \\ \Delta_{ij}(t-1) & \text{else} \end{cases}, \tag{4.7}$$

where $0 < \eta^{-} < 1 < \eta^{+}$, and the weights are updated according to

$$\Delta w_{ij}(t) = \begin{cases} -\Delta_{ij}(t-1) & \text{if} \quad \frac{\partial E}{\partial W_{ij}}(t) > 0 \\ +\Delta_{ij}(t-1) & \text{if} \quad \frac{\partial E}{\partial W_{ij}}(t) < 0 \\ 0 & \text{else} \end{cases}, \tag{4.8}$$

4.1.3. Learning rate and momentum coefficient

The efficient selection of the training parameters and the network learning paradigm are very important to achieve good performance with ANN (Buam and Haussler, 1989). In BP algorithms, the learning rate, ε, is a small number ($0 < \varepsilon \leq 1.0$) (Aristodemou et al., 2005) that controls the amount of error that will be negatively added to the interconnection weights for the next iteration (Cranganu, 2007). If the learning rate is large, large weight changes are then allowed, and no learning occurs. Conversely, if the learning rate is small, then only small changes are allowed, which can increase the learning time. The momentum, α, dampens the amount of weight change by adding in a portion of weight change from the previous iteration. The momentum is credited with smoothing out large changes in the weights as well as helping the network converge faster when the error is changing in the correct direction. Typical values for the momentum fall between 0 and 1.0 (Aristodemou et al., 2005).

4.1.4. Choosing the number of hidden neurons

The number of hidden neurons affects the ability of the ANN to separate the data. A large number of hidden neurons will ensure correct learning (De Villiers and Barnard, 1993), and the network is able to correctly estimate the training data, but its performance on new data is compromised. On the other hand, the network may not be able to learn the relationships between the datasets with few hidden neurons and the error will not reach an acceptable threshold. As a result, the proper selection of the number of hidden neurons is important.

4.1.5. Selection of the initial weights

The first values of the weight vector are called the initial weights. The learning paradigms seek a valley in the weight space using a steepest descent technique. Thus, the choice of initial weights in the multidimensional weight space plays a critical role. However, there are no recommended rules for this selection, and several different initial weight values (randomly generated around zero) can be tried in order to improve the ANN results.

4.2. Artificial neural network paradigms

It is very difficult to know which ANN training paradigm will be the fastest for a given problem, as this depends on many factors, including the complexity of the problem, the number of data points in the training set, the number of weights and biases in the network, the error goal, and whether the network is being used for pattern recognition or function approximation. This section compares some of the most common training algorithms.

4.2.1. Batch training with weight and bias learning rules (BTWB)

In a BTWB algorithm, the weights and biases of the network are updated only after the entire training set has been applied to the network. The gradients calculated for each training example are added together to determine the change in the weights and biases. Momentum allows a network to respond not only to the local gradient but also to recent trends in the error surface (Hagan et al., 1996). Acting like a low-pass filter, the momentum allows the network to ignore small features in the error surface. This is important because without momentum, a network may get stuck in a shallow local minimum.

4.2.2. Conjugate gradient with Fletcher reverse updates (CGFR)

The CGFR method is an algorithm that numerically solves particular systems of linear equations, namely those with symmetric and positive–definite matrices. This method is iterative, so it can be applied to sparse systems that are too large to be handled by direction. Such systems arise regularly when numerically solving partial differential equations (Hagan et al., 1996).

4.2.3. Resilient propagation (RPROP)

Resilient propagation (RPROP) algorithms are local adaptive learning schemes, performing supervised batch learning in feed-forward neural networks. The basic principle of RPROP is to eliminate the harmful influence of the size of the partial derivative on the weight step. Only the sign of the derivative can determine the direction of the weight update; the magnitude of the derivative has no effect. The size of the weight change is determined by a separate update value. The update value for each weight and bias is

increased whenever the derivative of the performance function, with respect to that weight, has the same sign for two successive iterations. The update value is decreased whenever the derivative, with respect to that weight, changes sign from the previous iteration. If the derivative is zero, the update value remains the same. Whenever the weights oscillate, the weight change is reduced. If the weight continues to change in the same direction for several iterations, the magnitude of the weight change increases. The RPROP algorithm is the fastest one for pattern recognition problems and the memory requirements for this are relatively small as compared to the other considered algorithms.

4.2.4. Gradient descent with momentum and adaptive learning rate (GDMA)

The GDMA algorithm adjusts the weights in the direction of steepest descent (negative of the gradient), which is the direction in which the performance function is decreasing most rapidly. It turns out that although the function decreases most rapidly along the negative of the gradient, this does not necessarily produce the fastest convergence. The GDMA is usually much slower than the other methods, but it has about the same storage requirements as the RPROP. It can still be useful for some problems, however (Battiti, 1992).

4.2.5. Levenberg-Marquardt with weight and bias learning rules (LMWB)

The LMWB algorithm (Hagan and Menhaj, 1994) was designed to approach second-order training speeds without having to compute the Hessian matrix. This optimization technique is more sophisticated and powerful than gradient descent (Singh et al., 2005). In general, for function approximation problems and for networks that contain

up to a few hundred weights, the Levenberg-Marquardt algorithm will have the fastest convergence. In many cases, the LMWB obtains lower mean square errors than any of the other algorithms tested. However, as the number of weights in the network increases, the advantage of LMWB decreases. In addition, the LMWB performs relatively poorly for pattern recognition problems. The storage requirements of the LMWB are larger than the other algorithms tested (Hagan et al., 1996).

4.3. Training and testing neural networks

To achieve a best training procedure, a wide range of examples must be compiled. Thus, for complex problems, more examples are required. In turn, poor training data give rise to an unreliable network. In some cases, the ANN is overtrained because the output error falls below a particular error threshold. By overtraining, the network may become too adapted to learn the training data and may not be able to predict new data accurately. To familiarize the ANN with noise in real data, some noise can be added to the training data.

4.4. Network generalization ability

In all parameter determination problems, the degree of determination of the system, D_{ds}, is defined as:

$$\mathrm{D_{ds}} = \text{Number of available data points / Number of unknown parameters} \quad (4.9)$$

Since the ANN deals with parameter determination problems, its solution depends on D_{ds} . The unknown parameters for an ANN are the connection weights. The trained ANN is called over-determined if $\mathrm{D_{ds}} > 1$. The solution of an ANN probably over-fits the observed data if $\mathrm{D_{ds}} < 1$. In this case, although, the training error reaches a threshold error, the ANN may be unable to predict the desired target correctly. To overcome this problem, the

architecture of the ANN should be as simple as possible, so that, it can still estimate the desired target adequately.

One technique to select a simple network with good generalization ability is to start with a large number of hidden layers and their corresponding neurons, then iteratively simplify the architecture (LeCun et al., 1990). Another way is to start with a simple architecture and iteratively add neurons or hidden layers (Ash, 1989). Bishop (1995) and Ripley (1996) used validation approach to avoid over-fitting, in which the data pool volume is divided into two subsets: a training dataset used to train the ANN and a validating dataset used to evaluate the generalization ability of the ANN. During the training phase, once the error for the validation dataset starts to increase, the training is terminated; otherwise, the training continues and the error for the training dataset is calculated until the threshold error is reached (Wessels and Barnard, 1992; Bowden et al., 2002).

4.5. Summary

In this chapter, the architectures of ANNs are briefly descibed. The mathematical basis of the most common learning law (i.e., BP), which is a training law for the FFNN, is also discussed. In order to design and train the ANN, a brief introduction of some important terms is also presented, e.g., the learning rate, momentum coefficient, choosing the number of hidden layers and selection of the initial weights. As a next step, five common training paradigms: (including, BTWB, CGFR, RPROP, GDMA and LMWB) have been compared for 2D and 3D surveys. In a BTWB algorithm, which acts like a low-pass filter, the momentum allows the network to ignore small features in the error surface. This is important because without momentum, a network may get stuck in a shallow local minimum. The CGFR method is an algorithm that numerically solves particular systems of

the linear equations, i.e., those with symmetric and positive–definite matrices. The RPROP algorithm is the fastest algorithm for pattern recognition problems, and the memory requirement for this is relatively small as compared to other algorithms. The GDMA is usually much slower than the other methods, but it has about the same storage requirements as the RPROP. In general, for function approximation problems and networks that contain up to few hundred weights, the LMWB algorithm has the fastest convergence. However, as the number of weights in the network increases, the advantage of LMWB decreases. In addition, the LMWB performance is also relatively poor for pattern recognition problems. The storage requirements of the LMWB are larger than those of the other algorithms tested (Hagan et al., 1996). Finally, the network generalization ability is discussed.

Chapter 5
Training and testing the ANN using 2D and 3D synthetic data

In this chapter, a synthetic data generation is explained in order to train and test the ANN. The process of training the ANN and the selection of training parameters are discussed here for five common arrays (i.e., the WS, W, DD, PD and PP arrays) used in 2D and 3D surveys.

5.1. Generation of training and testing data pool formation

The model used here to produce synthetic data consists of a homogeneous medium of 100 Ωm resistivity with an embedded anomalous body of 1000 Ωm. High-resistivity contrast regions are expected from the target site that has been used for the real field data collection. In the synthetic data, these high-resistivity values were selected in order to train the ANN.

In order to reduce the computation time (without loss of generality), the data base used for this study was smaller than the total data base, where about 40% of the generated data were randomly selected for training, while 20% ~ 25% was randomly selected to test the ANN. In order to study the interpolation and extrapolation properties of the ANN, the remaining 35% ~ 40% of the synthetic datasets were generated with different resistivities for background and anomalous body, ranging from 100-1000 Ωm. The synthetic datasets were normalized in a range of [0, 1] for training and testing the ANN; this range allows the

logistic sigmoid activation function to restrict the size of the input data (El-Qady and Ushijima, 2001).

5.1.1. Synthetic data creation

In order to study the effect of data pool formation in training the ANN, two methods were used to generate the synthetic data. These methods are called M1 and M2, which basically differ in the type of input-output data used to train the ANN. In the following sections, details of each method for both 2D and 3D synthetic datasets are discussed.

5.1.1.1. 2D synthetic data creation using the method M1_2D

In the method M1_2D, a cross-section of the subsurface is divided into a mesh of elements with background resistivity of 100 Ωm and an anomalous element of 1000 Ωm moving to all of the model mesh elements (see Fig. 5.1). At each anomalous element position, forward modeling using the desired array configuration is carried out, and then their apparent resistivity data are calculated. In this method, the apparent resistivity data are considered as the input data and the true resistivity of all mesh elements is used as the output data in the training phase of the ANN. The testing set corresponds to a model that has been used only to test the performance of the ANN, not for the training. The anomalous body in the testing set was chosen on basis of several mesh elements, e.g., four mesh elements, instead of one in the training sets (Fig. 5.2). This anomalous body is moved in the whole layers of the model mesh (100×6). A total of 600 training patterns and 150 testing patterns (with four mesh elements as the anomalous body) were generated using the method shown in Fig. 5.1.

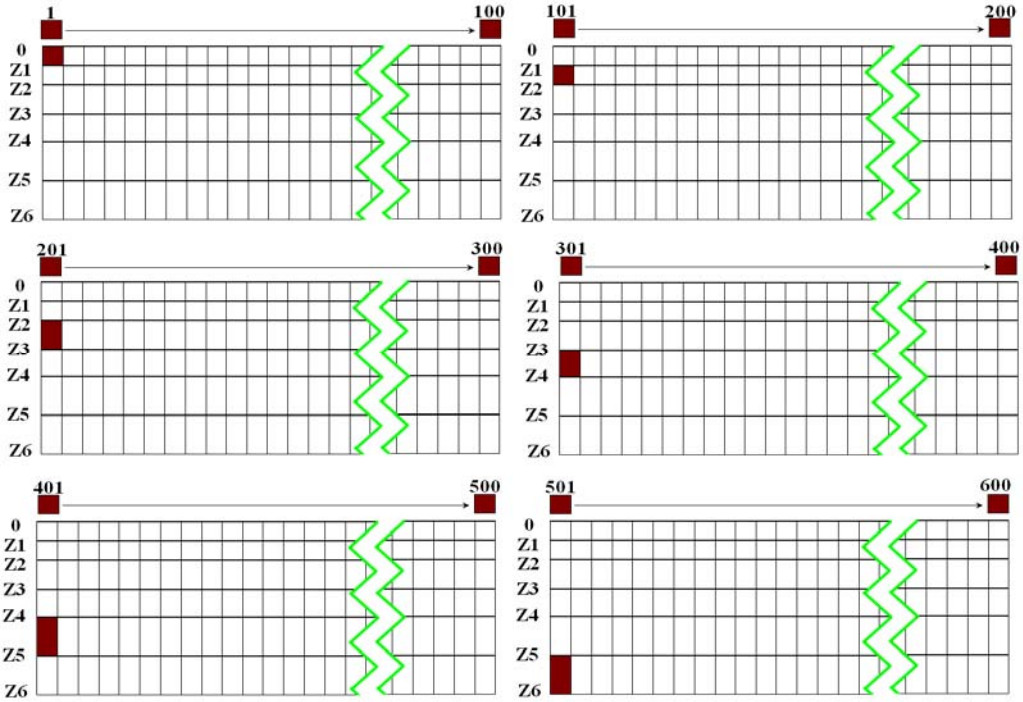

Figure 5. 1. Generation of training datasets using the method M1_2D.

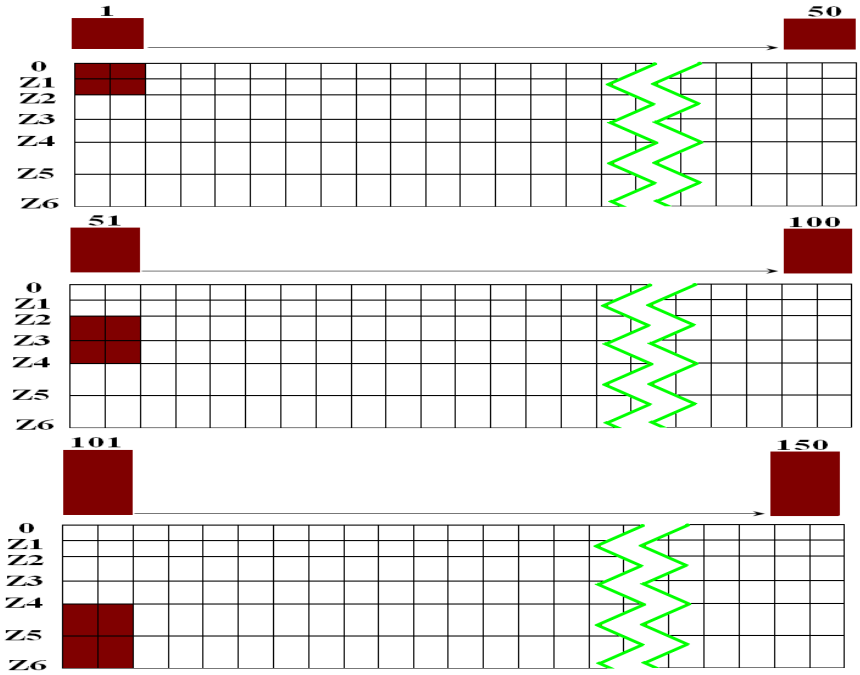

Figure 5. 2. Generation of testing datasets using the method M1_2D.

5.1.1.2. 2D synthetic data creation using the method M2_2D

In the second method, M2_2D, different sizes are selected for anomalous body, and their locations are moved to different positions within the homogeneous model mesh elements. Each element in the mesh is permitted to be either resistive or conductive. The 2D datasets are generated using a finite element forward modeling code adopted from Loke and Barker (1996b). Each synthetic profile consists of 101 electrodes, and the desired electrode configuration is used to generate synthetic data (Fig. 5.3).

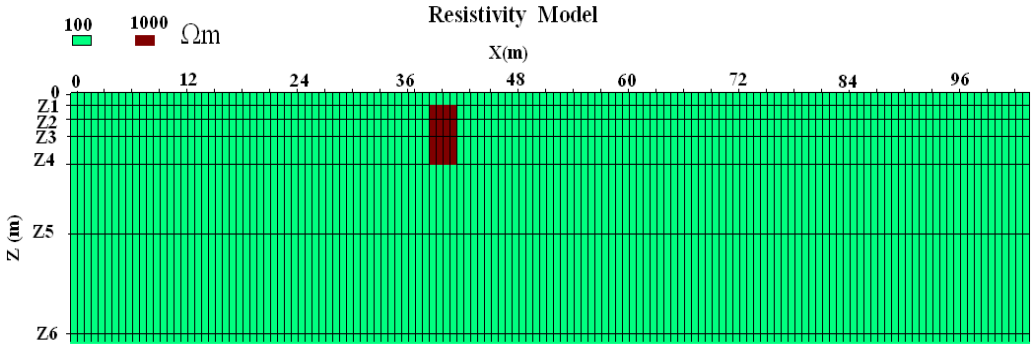

Figure 5. 3. Forward model used to generate the synthetic resistivity dataset using the method M2_2D. The Figure shows one of the positions of the anomalous body.

In the following paragraph, it is explained that how the horizontal and vertical locations of the synthetic resistivity data are determined. These locations are required to train and test the ANN. The horizontal location of the data point is placed at mid-point of the set of electrodes used to make measurements (Loke, 2009), while the vertical position of the plotting point (depth of investigation) is placed at the median depth of investigation (Edward, 1977) of the electrode array used. One quantitative means to put a numerical value on the depth of investigation involves the use of sensitivity function, or the Frechet derivative of the array. The sensitivity function essentially indicates the degree to which a change in the resistivity of a subsurface will influence the potential measured by the array.

The higher the value of the sensitivity function, greater will be the influence of the subsurface region on the measurement. Mathematically, the sensitivity function is given by the Frechet derivative (McGillivray and Oldenburg, 1990). Following Edwards (1977), the median depth of investigation for each electrode configuration is the electrode spacing (a) multiplied by a coefficient K. Table 2.3 shows K-values (as z/a) for each data level. As an example for M2_2D method, consider the simplest possible dipole-dipole configuration shown in Fig. 5.4.

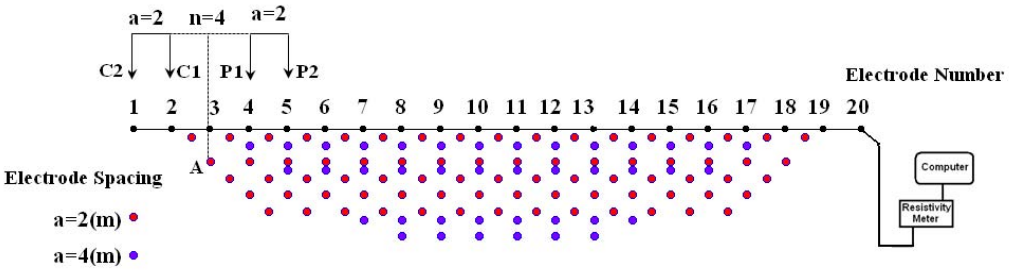

Figure 5. 4. Typical setup for a dipole-dipole configuration with a given number of electrodes along a straight line attached to a multi-core cable.

As shown in above Figure, the current electrode (C2) is located at x=0 (with all electrodes on the ground surface) and the spacing between C2-C1 is denoted by a=2 meters. The measured apparent resistivity corresponding to these electrodes belongs to data level n=4 and is denoted by the letter A. The horizontal location of this point is x=4 (the mid-point of C2 and P2) and its vertical location, which is 2.440 meters (=2×1.220) as listed in Table 2.3. The apparent resistivity and corresponding true resistivity of this point (4, 2.44) can therefore be obtained from the corresponding apparent pseudo-section and resistivity model. The same procedure can be used for all data points. As a result, in our synthetic data

for each data point, there are four characteristics: the x- and z-locations and the apparent and true resistivities.

5.1.1.3. 3D synthetic data creation using the method M1_3D

In this section, it is explained that how the 3D synthetic data are generated, which are required to train and test the ANN. Similar to the 2D model, the 3D model used to produce synthetic data for a homogeneous medium of 100 Ωm resistivity, with an embedded anomalous body of 1000 Ωm. The selection of the number of training and testing datasets is similar to the procedure mentioned for 2D synthetic datasets.

In the method M1_3D, the 3D subsurface model with a homogeneous and isotropic underground condition is divided into a block matrix with a background resistivity of 100 Ωm and an anomalous block of 1000 Ωm moving to all the model mesh element points (Fig. 5.5). As an example, Figure 5.5 shows the schematic model matrix (14×14×8) used to generate synthetic datasets by the method M1_3D. The sizes of the block matrices used to generate the 3D synthetic data for different electrode configurations are shown in Table 5.1. In each position of the anomalous block, forward modeling was performed to calculate the apparent resistivity data using the desire configuration. The apparent resistivity data were considered as the input data, while the resistivities of all mesh elements were used as the output data in the training phase of the ANN.

Using the model shown in Figure 5.5, 1568 training patterns were generated. In order to produce the testing datasets, four anomalous blocks were considered instead of one, which were used to generate the training datasets with a total of 392 testing datasets.

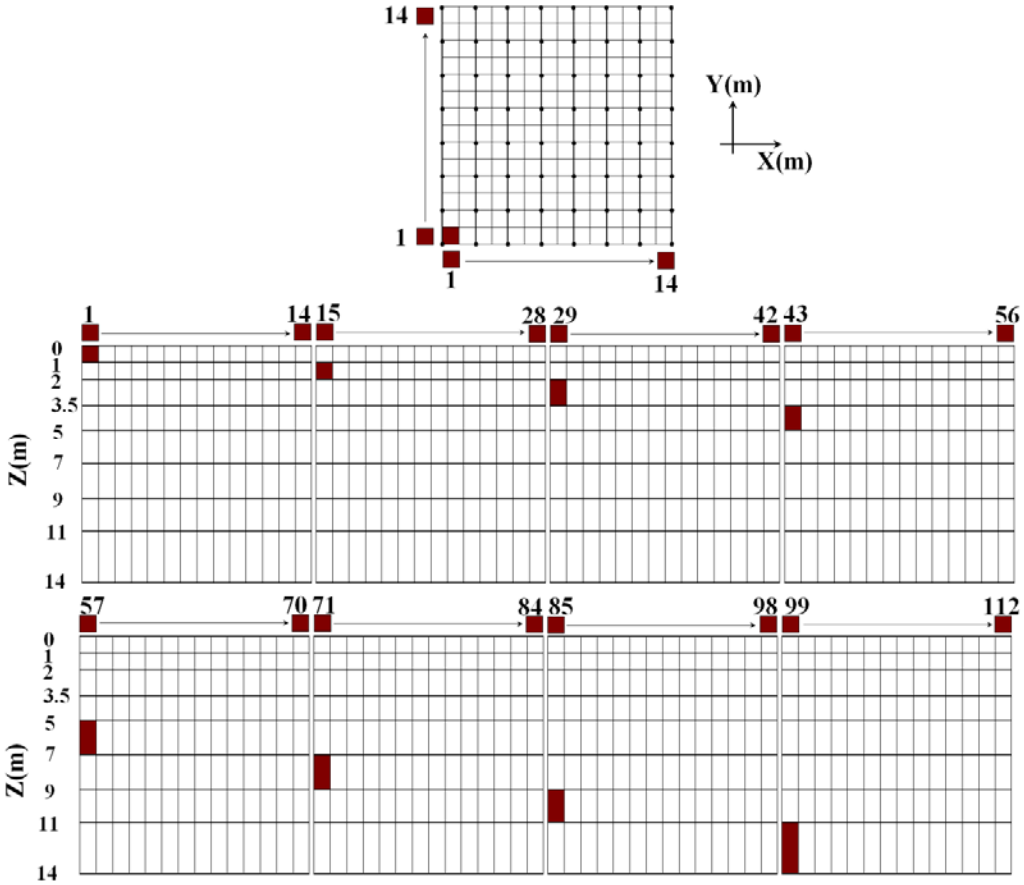

Figure 5. 5. Generation of training datasets using the method M1_3D.

Table 5. 1. Sizes of block matrices used to generate 3D synthetic data for different electrode configurations.

Array	Size of the block matrix
PP	14×14×8
PD	80×14×8
DD	40×12×7
WS	40×12×5
W	40×12×5

5.1.1.4. 3D synthetic data creation using the method M2_3D

In the method M2_3D, the horizontal location of the data point is at mid-point of the set of electrodes used to make that measurement (Loke, 2000). The vertical position of the plotting point is also calculated in a similar way as of the 2D model. As an example, the method M2_3D is explained for PP array. Following Edwards (1977), the median depth of investigation for the PP configuration is found to be 0.867 multiplied by the electrode spacing (a). Consider the simplest possible array configuration shown in Figure 5.6(e) with the current electrode located at (12, 6, 0) and the potential electrode located at (2, 6, 0), i.e., with both the electrodes on the surface and "a=10" meters apart.

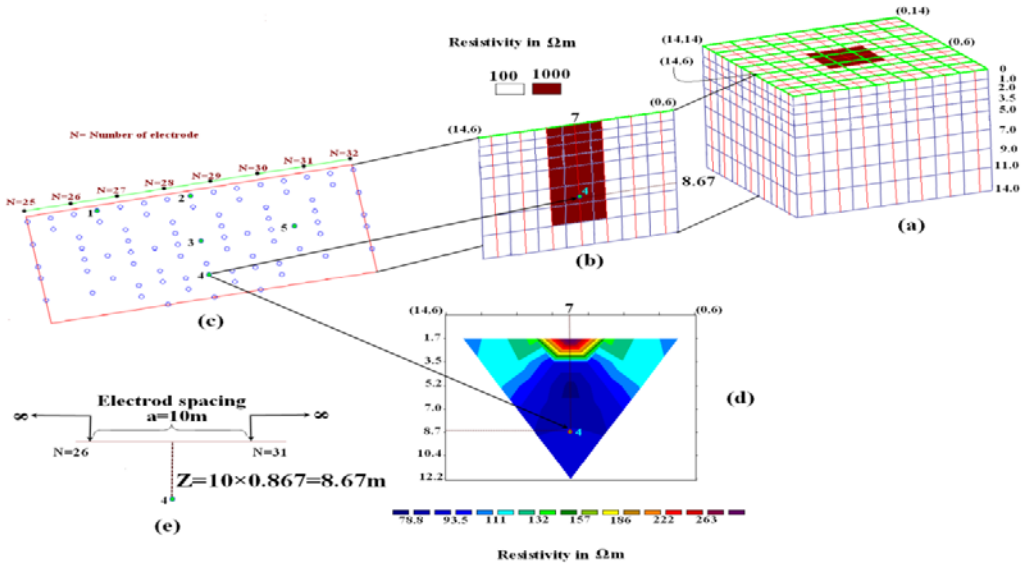

Figure 5. 6. Model used to produce synthetic data using the method M2_3D (a). Vertical section at y=6m (b). Locations of data points in y-direction view (c). Pseudo-section of the measured apparent resistivity along y=6m (d). Pole-pole array with the current electrode located at (12,6,0) and the potential electrode located at (2,6,0), i.e., both electrodes are on the ground surface (e).

The corresponding measured apparent resistivity is denoted by the number four. According to Figures 5.6(b and c), the horizontal location of this point is (7,6) and its vertical location is 8.67 meters (=10×0.867). The apparent resistivity and corresponding

true resistivity of this point (7, 6, 8.67) from Figures 5.5(d and b), can therefore be find respectively. The same could be done for all the data points. For the data point numbers 1, 2, 3, 4 and 5 of Figure 5.6(c), the horizontal and vertical locations together with apparent and true resistivities are shown in Table 5.2. As a result, in our synthetic data at each point, there are five characteristics; the x-, y-, and z-locations, and the apparent and true resistivities.

Table 5. 2. The horizontal location, vertical location, apparent resistivity, and true resistivity for the data points 1, 2, 3, 4 and 5 in Figure 5.6(c).

Data point	1	2	3	4	5
Number of current electrode	26	28	27	26	29
Number of potential electrode	27	29	30	31	32
Location of data point (meters)	(11,6,1.73)	(7,6,1.73)	(7,6,5.20)	(7,6,8.67)	(3,6,5.20)
Measured apparent resistivity (Ωm)	115.83	423.64	50.35	97.70	112.10
True resistivity (Ωm)	100	1000	1000	1000	100

5.2. Training the ANN using 2D and 3D synthetic data

This section presents detailed explanation about training the ANN with 2D synthetic data obtained by the WS, W, DD, PD and PP arrays.

5.2.1. Effect of the input-output data type

The results of the ANN-based parameter recognition depend on the data type used in the training (Spichak, 2000). In order to estimate the effect of input-output data type on inversion results, the following two types of data are investigated:

5.2.1.1. 2D synthetic data generated by the method M1_2D

The synthetic data were produced by the same conditions as in the field data acquisition using the desired array; the number of electrodes used (N_e), the minimum electrode spacing (a) and the ratios of different electrode spacings to the minimum electrode spacing used for each array (K_e) are presented in Table 5.3. The horizontal levels used in Figure 5.1 for each array are shown in Table 5.4. Table 2.3 is used to select the proper horizontal levels, which were approximately in accordance with data levels in the apparent resistivity datasets obtained in the field for each array.

Table 5. 3. Number of electrodes used (Ne), minimum electrode spacing (a) and ratios of different electrode spacings to the minimum electrode spacing used for each array (K_e).

Array	N_e	a (m)	K_e
WS	41	3	1, 2 and 3
W	20	2	1, 2, 3 and 4
DD	20	2	1, 2 and 3
PD	41	1	1, 2 and 3
PP	41	1	1, 2, 3, 4, 5, 6, 7, 8, 9 and 10

Table 5.4 shows the size of the grids used, number of patterns, number of data points in each pattern and total number of data points for each array. 3% noise uniformly in the generated synthetic apparent resistivity data is considered. To train the ANN with such data, the number of nodes in the input layer should be equal to the number of measured apparent resistivities in each pattern. The number of nodes in the output layer should be equal to the number of mesh elements (or of patterns), because the true resistivities of all mesh elements are used as output of the ANN. To gain reliable measurements with DD

array, the "*n*'' values not greater than 6 are used. The "*n*'' values of 1 to 8 have also been used to produce the synthetic data following the WS array. To produce the synthetic data by the PD array, both the forward and reverse methods are considered, which gave a dataset of 1440(=2×720) data points for each set.

5.2.1.2. 3D synthetic data generated by the method M1_3D

The 3D synthetic data were produced by the same conditions as those in the 3D surveys using the five common arrays similar to previous section. One node is considered between each pair of the electrodes in the x- and y- directions.

In the method M1_3D, the 3D subsurface model, for which the underground condition is considered to be homogeneous, was divided into a block matrix with a background resistivity of 100 Ωm and an anomalous block of 1000 Ωm moving to all of the model mesh elements (Fig. 5.5). For each position of the anomalous block, forward modeling using the desired array was performed to calculate the apparent resistivity data. In order to produce the testing datasets, four anomalous blocks were considered instead of the one block that was used to generate the training datasets. The apparent resistivity data were considered as the input data, while the resistivities of all mesh elements were used as the output data in the training phase of the ANN. 3% noise uniformly in the generated synthetic apparent resistivity data is considered. Since for data obtained by the PP array only the cross-diagonal measurements were considered, each synthetic pattern consists of 728 data points.

In the 3D survey of the PP array, the minimum electrode spacing used in a square grid (8×8) was 2 m, and the size of the block matrix was (14×14×8). As shown in Figure 5.5 the horizontal levels (0 to Z8) were 0, 1, 2, 3.5, 5.0, 7.0, 9.0, 11.0 and 14.0 m. Using the PP array, 1568 (=14×14×8) training patterns (1568×728=1141504 data points) were

generated. The number of testing datasets was 392 (392×728=285376 data points). In order to train the ANN with PP data, the number of nodes in the input and output layers must be 728 and 1568, respectively. In the 3D survey of the PD array, the minimum electrode spacings along the x and y directions that is used in an orthogonal grid (41×8) were 1 and 2 m, respectively.

Table 5. 4. Horizontal levels, size of the grids, number of patterns, number of data points in each pattern and total number of data points for each array.

Array	Horizontal levels		Size of grid	Number of data points in each pattern	Number of patterns	Total number of data points
WS	Z1	1.5	40×6	330	240	79200
	Z2	3				
	Z3	5				
	Z4	8.5				
	Z5	12.5				
	Z6	17				
W	Z1	0.52	19×5	50	95	4750
	Z2	1.10				
	Z3	2.20				
	Z4	3.50				
	Z5	5.0				
DD	Z1	0.9	19×6	85	114	9690
	Z2	1.5				
	Z3	2.0				
	Z4	2.5				
	Z5	3.0				
	Z6	4.0				
PD	Z1	0.7	40×6	1440	240	345600
	Z2	2.0				
	Z3	3.5				
	Z4	5.0				
	Z5	7.0				
	Z6	10				
PP	Z1	0.9	40×6	335	240	85200
	Z2	1.7				
	Z3	3.5				
	Z4	5.0				
	Z5	7.0				
	Z6	9.0				

The size of the block matrix was (80×14×8) and the horizontal levels (0 to Z8) were 0, 0.4, 0.9, 2.1, 3.6, 5.6, 7.9, 10.9 and 14.0 m. In each pattern of the PD data, the number of data points in the x- and y- directions were 8032 (=8×1004) and 1189, respectively, making a total of 9221 data points. Accordingly, 8960 (=80×14×8) training patterns are generated and the total number of data points is 82620160 (=8960×9221). The number of testing datasets was 2240 (2240×9221=20655040). To train the ANN with PD data, the number of nodes in the input layer must be 9221 and in the output layer should be 8960.

In the 3D surveys using the four electrode array (i.e., the DD, WS and W arrays) the minimum electrode spacings used along both the x and y directions in an orthogonal grid (21×7) was 2 m. In a block matrix (40×12×7) for the DD array the horizontal levels (0 to Z7) were 0, 0.5, 1.0, 1.5, 2.5, 3.8, 5.3 and 7.0 m. A block matrix (40×12×5) for both the WS and W arrays is considered. The horizontal levels (0 to Z5) for the WS array were 0, 0.5, 1.5, 3.0, 5.0 and 7.0 m and for the W array were 0, 0.8, 1.6, 3.2, 5.0 and 7.0 m. The number of data points in the x- and y- directions, the total number of data points in each pattern and the number of training and testing patterns for the DD, WS and W arrays are shown in Table 5.5. The same table also shows the number of nodes in the input (NI) and output layers (NO).

5.2.1.3. 2D synthetic data generated by the method M2_2D

In the synthetic data produced by the method M2_2D, the position (horizontal location x and vertical location z) and values of the apparent resistivity of each data point were used as input data. The true resistivity was also selected as an output of the ANN output. Thus, the number of nodes in the input and output layers should be 3 and 1, respectively. The model used to produce synthetic data is a homogeneous medium of

Table 5. 5. Number of data points in the x- and y- directions, total number of data points in each pattern and number of training and testing patterns for the DD, WS and W arrays. In this table, NI and No are the number of nodes in the input and output layers, respectively.

Array	DD	WS	W
Number of data points in the x-direction	1302	903	399
Number of data points in the y-direction	220	140	100
Total number of data points in each pattern	1522	1043	499
Number of training patterns	3360	2400	2400
Number of testing patterns	840	600	600
NI	1522	1043	499
NO	3360	2400	2400

resistivity 100 Ωm with an embedded anomalous body of 1000 Ωm (Fig. 5.3). In each synthetic profile, 101 electrodes were used, and the horizontal levels in Figure 5.3 for different arrays were as follows:

- WS array (0 to Z6): 0, 1.5, 3, 5, 8.5,13 and 17 m
- W array (0 to Z5): 0, 0.52, 1.5, 3.0, 5.0 and 7.0m
- DD array (0 to Z6): 0, 0.3, 0.8, 1.3, 1.8, 3.0 and 5.0m
- PD array (0 to Z9): 0, 0.5, 1.0, 1.5, 2.2, 2.8, 3.6, 5.2, 8.0 and 11.0 m
- PP array (0 to Z10): 0, 0.5, 1.0, 1.5, 2.2, 2.8, 3.6, 5.0, 6.5, 8.0 and 11.0 m.

Thus, the sizes of the model grids for the WS, W, DD, PD and PP arrays were 100×6, 100×5, 100×6, 100×9, and 100×10, respectively. Using different electrode spacings, sizes, and positions for the anomalous body, the training and testing patterns for each array was produced. The number of data points in each pattern and the number of training and testing patterns for the five previously mentioned arrays are shown in Table 5.6. This 2D dataset

was generated using a finite element forward modeling code by means of RES2DMOD (Loke, 2007b).

Table 5. 6. Number of data point in each pattern and number of training and testing patterns for the WS, W, DD, PD and PP arrays.

Array	Number of data points in each pattern	Number of training patterns	Number of testing patterns
WS	890	21	16
W	978	16	12
DD	579	21	11
PD	1122	32 (forward+ reverse)	20(forward+ reverse)
PP	1134	16	9

5.2.1.4. 3D synthetic data generated by the method M2_3D

In the synthetic data produced by the method M2_3D, the apparent resistivity position (horizontal locations x, y and vertical location z) and apparent resistivity of each data point were used as input data. The true resistivity was also selected as an output of the ANN. Thus, the number of nodes in the input and output layers should be four and one, respectively. The model used to produce the 3D synthetic data by the PP array is shown in Figure 5.6. However, similar models were used for the PD, DD, WS and W arrays, in which the main difference is the use of orthogonal grids instead of square grids. The sizes of the grids for the PD, DD, WS and W –arrays are (41×8), (21×7), (21×7) and (21×7), respectively. Similar to method M1_3D, one node between each pair of electrodes is to use considered in the x- and y- directions. The horizontal levels and the size of the matrix blocks in the method M2_3D are the same as those used for the method M1_3D. The

anomalous block was placed in different positions within the block matrix. All the possible measurements in the x and y directions were considered using different sizes and positions for the anomalous body. The number of data points in each pattern and the number of training and testing patterns for each array are shown in Table 5.7. The 3D datasets for training and testing the ANN were generated using a finite element forward modeling code adopted from Loke and Barker (1996b).

Table 5. 7. Number of data points in each pattern and number of training and testing patterns for the PP, PD, DD, WS and W arrays.

Array	Number of data points in each	Number of training	Number of testing
PP	2016	18	9
PD	9221	15	8
DD	1522	20	10
WS	1043	28	16
W	499	50	20

5.2.2. Effect of the number of nodes in each layer and the data pool formation

There is no general theory on the dependence of the recognition errors on the number of neurons in hidden layers. However, the approximation properties of an ANN improve when the number of hidden neurons increases (Spichak et al., 2000). Therefore, the effect of the number of neurons in the hidden layers on the performance of the ANN was studied using the 2D and 3D synthetic data generated by the methods M1 and M2.

5.2.2.1. Effect of the number of nodes in each layer and the 2D data pool formation

The ANN architecture was NI- Nh1-Nh2-NO, where NI, Nh1, Nh2 and NO are the number of neurons in the input layer, the first hidden layer, the second hidden layer and the output layer, respectively. The values of NI and NO are discussed in sections 5.2.1.1 and 5.2.1.3. The values of Nh1 and Nh2 were assigned according to the values shown in the appendix Tables A1 to A5 for the WS, W, DD, PD and PP –arrays, respectively. Table 5.8 shows the teaching precision and the number of epochs for each array.

Tables A1 to A5 also show the dependence of the MSE error on the number of neurons in the hidden layers of two types synthetic data produced by methods M1_2D and M2_2D. Although the number of epochs for each array was set to the value mentioned in Table 5.8, in the case of method M2_2D, the MSE performance of the ANN for the WS, W, DD, PD and PP arrays reached the desired performance goal (Table 5.8) after 16, 77, 2282, 1275 and 373 epochs, respectively.

Table 5. 8. Training precision and the number of epochs in training of the ANN with the WS, W, DD, PD and PP –data.

Array	Training precision	Number of epochs
WS	0.000100	4000
W	0.000058	5000
DD	0.000100	8000
PD	0.000200	10000
PP	0.000010	10000

The higher MSE error for method M1_2D could be explained by the size of the elements in the mesh. Because fixed sizes were used for each element of the mesh, which might affect the accuracy of the results. It is therefore concluded that the synthetic data generated by the method M2_2D may be the best data type for training and testing the ANN in this study.

It has been proven theoretically that a three-layer structure network can estimate any kind of logic function, provided that enough neurons are set in the hidden layer (Irie and Miyake, 1988). However, the results of this study shown in the Tables A1 to A5 suggest that an ANN with two hidden layers of the following values for Nh1 and Nh2 has the lowest MSE error for each array:

- WS array: Nh1=28, Nh2= 16
- W array: Nh1=24, Nh2= 80
- DD array: Nh1=28, Nh2= 4
- PD array: Nh1=30, Nh2= 12
- PP array: Nh1=30, Nh2= 90

5.2.2.2. Effect of the number of nodes in each layer and the 3D data pool formation

The effect of the number of neurons in the hidden layers on the performance of the ANN using the 3D synthetic data produced by the methods M1_3D and M2_3D was studied. Similar to the 2D study in the previous section, the ANN architecture was NI-Nh1-Nh2-NO; the values of NI and NO are discussed in sections 5.2.1.2 and 5.2.1.4. The values of Nh1 and Nh2 were selected according to the appendix Tables A6 to A10 for the PP, PD, DD, WS and W –arrays, respectively. The teaching precision and the number of epochs for the above 3D arrays are shown in Table 5.9.

Table 5. 9. The training precision and number of epochs in training of the ANN with the PP, PD, DD, WS and W –data.

Array	Training precision	Number of epochs
PP	0.00030	5000
PD	0.000085	10000
DD	0.0008	8000
WS	0.00025	100000
W	0.00007	10000

Tables A6 to A10 also show the dependence of the MSE error on the number of neurons in the hidden layers for two types of synthetic data produced by methods M1_3D and M2_3D. In the case of method M2_3D, the MSE performance of the ANN for the PP, PD, DD, WS and W arrays reached the desired goal as mentioned in Table 5.9 after 1340, 1560, 700, 34077 and 1677 epochs, respectively. According to Tables A6 to A10, the MSE error for method M1_3D in most cases is higher than that of the method M2_3D. This might be for the same reason as the 2D study. The results of 3D study shown in Tables A6 to A10 suggest that the simplest architectures for the ANN that can reach the desired threshold error (Table 5.9) for the PP, PD, DD, WS and W arrays are (4-84-24-1), (4-35-25-1), (4-35-25-1), (4-45-60-1) and (4-30-50-1), respectively. Since, it is reasonable to select the ANN with simplest architecture, i.e., the smallest number of neurons in each hidden layer, it is concluded that the synthetic data generated by method M2_3D may be the best data type for training and testing the ANN in this study.

5.2.3. Effect of training data pool volume

The optimum training data pool volume required for good generalization has been studied by several authors (e.g., Mehrotra et al., 1991; Spichak, 2000). In fact, large networks and complex input patterns require more training data for optimum generalization (Rajavelu et al., 1989).

5.2.3.1. 2D study of the effect of training data pool volume

In order to study the effect of training data pool volume, three collections of training datasets were made using the method M2_2D for the WS, W, DD, PD and PP –arrays. These collections of datasets are shown in Table 5.10. The ANN architecture for each array was the same as explained in section 5.2.2.1. Tables A11 to A15 show the MSE performance of the ANN for the WS, W, DD, PD and PP –arrays, respectively. In these tables, the MSE performance for each collection after three different numbers of epochs is shown.

Table 5. 10. Three collections of training datasets generated using method M2_2D for the WS, W, DD, PD and PP –arrays.

Array	Dataset	Number of sets	Number of data points
WS	WS2DV1	7	6230
	WS2DV2	21	18690
	WS2DV3	42	37380
W	W2DV1	8	7824
	W2DV2	16	15648
	W2DV3	24	23472
DD	DD2DV1	10	5790
	DD2DV2	21	12159
	DD2DV3	30	17370
PD	PD2DV1	16	17952
	PD2DV2	32	35904
	PD2DV3	64	71808
PP	PP2DV1	8	9072
	PP2DV2	16	18144
	PP2DV3	32	36288

Although the MSE errors for WS2DV3, W2DV3 and DD2DV3 reached the values close to their performance goal, their volumes are more than 1.5 times those of WS2DV2, W2DV2 and DD2DV2, and they need more epochs to attain the threshold error. Since the large data pool volume takes a long time to train the ANN with other learning paradigms, the results of this study, which are shown in Tables A11 to A15, suggest that the data pool volumes of WS2DV2, W2DV2, DD2DV2, PD2DV2 and PP2DV2 should be sufficient for this study.

5.2.3.2. 3D study on the effect of training data pool volume

Similar to the 2D study described in section 5.2.3.1, three collections of datasets are considered for each of the PP, PD, DD, WS and W data in order to study the effect of 3D training data pool volume produced by method M2_3D. The details of these datasets are shown in Table 5.11. The ANN architecture for each array was in accordance with that given in section 5.2.2.2. The results of the MSE performance of the ANN for the PP, PD, DD, WS and W arrays are shown in Tables A16 to A20. In these tables the performance of the ANN is shown after three different numbers of epochs to determine the effect of both the number of epochs and the data pool volumes in training the ANN for each array. The results from this part of the study show that PP3DV2, PD3DV2, DD3DV2, WS3DV2 and W3DV2 might be sufficient. The results in Tables A16 to A20 also show that the datasets PP3DV3, PD3DV3, DD3DV3 and W3DV3 reached the performance goal of training the ANN. However, their volumes and the number of epochs required to reach the performance goal are more than the previous datasets.

There are some limitations to the use of a too-large data pool volume in training the ANN. For example, training the ANN with the LMWB paradigm using too-large data pool

volume may occupies most of the CPU memory of the computers, and sometimes the computer cannot run the training process.

Table 5. 11. Three collections of training datasets generated using method M2_3D for the PP, PD, DD, WS and W arrays

Array	Dataset	Number of sets	Number of data points
PP	PP3DV1	9	18144
	PP3DV2	18	36288
	PP3DV3	27	54432
PD	PD3DV1	8	73768
	PD3DV2	15	138315
	PD3DV3	20	184420
DD	DD3DV1	10	15220
	DD3DV2	20	30440
	DD3DV3	30	45660
WS	WS3DV1	16	16688
	WS3DV2	28	29204
	WS3DV3	56	29204
W	W3DV1	20	9980
	W3DV2	50	24950
	W3DV3	80	39920

5.2.4. Setting the learning rate and momentum

An efficient selection of the training parameters and the network learning paradigm is very important to achieve good performance with ANN (Baum and Hausler, 1989*)*. The momentum and learning rate are obviously related, but their mathematical relation is still not clear (Singh et al., 2005). The effect of these two parameters for five common arrays used in 2D and 3D surveys; the WS, W, DD, PD and PP arrays; were studied. Details of the

analysis are shown in Tables A21 to A30 (in Appendix A) for each array, respectively. The numbers of epochs correspond to the number required to reach the threshold error for each case (Tables A21 to A30). The results of this study suggest the most appropriate learning rate and momentum for each array, as shown in Table 5.12.

Table 5. 12. Selected values of the learning rate and momentum for each array from the results shown in Tables A21 to A30 in Appendix A.

Array		Learning rate	Momentum coefficient
WS	2D	0.20	0.90
	3D	0.20	0.95
W	2D	0.01	0.40
	3D	0.10	0.60
DD	2D	0.01	0.20
	3D	0.20	0.90
PD	2D	0.02	0.20
	3D	0.10	0.90
PP	2D	0.02	0.30
	3D	0.15	0.80

5.2.5. Comparison of the ANN paradigms

The following learning paradigms are tested for networks: BTWB, GDMA, CGFR, LMWB, and RPROP. These paradigms are mostly based on back-propagation, and the weights are updated after each epoch.

5.2.5.1. 2D comparison study

Figures 5.7 to 5.11 show the mean square error (MSE) as a function of the number of iterations during the ANN training by different paradigms. These Figures are related to training the ANN using 2D synthetic data produced by the WS, W, DD, PD and PP arrays, respectively.

According to the variation of the errors, it is concluded that the RPROP paradigm is the most efficient for training the 2D dataset related to all arrays. In the case of WS, W and DD arrays, the initial errors for the RPROP algorithm are about 0.52, 0.001 and 0.4, respectively, and they decrease as the iteration proceeds, until an attainment in value equal to the desired performance goal for each array is achieved, such that the network converges. The other algorithms could not achieve the performance goal even with maximum number of iterations defined for each array. In the case of PD and PP arrays, however, the LMDB paradigm achieved the desired threshold error after 3000 and 2853 iterations, respectively, while the RPROP paradigm attained a value of about 0.0002 after 1275 iterations for the PD array and of about 0.00001 after 373 iterations for the PP array. The initial error for the RPROP algorithm was about 2.61 for the PD array and about 0.035 for the PP array, and decreased as the iteration proceeded. The other algorithms could not achieve the performance goal even after 10000 iterations. The results for each paradigm in terms of training speed and epochs (iterations) are summarized in Table 5.13.

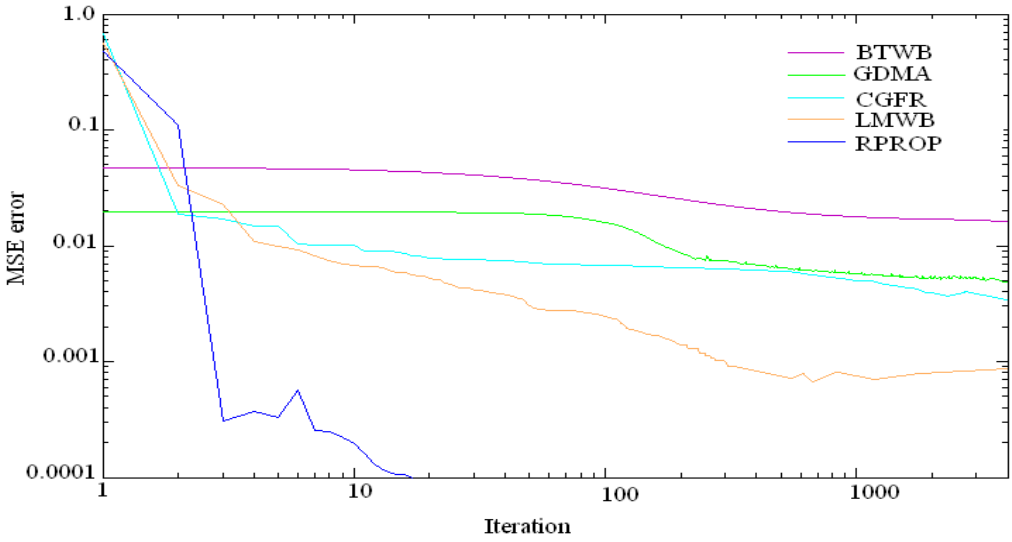

Figure 5. 7. Mean square (MSE) error as a function of the number of iterations during the training of different ANN paradigms for 2D WS data.

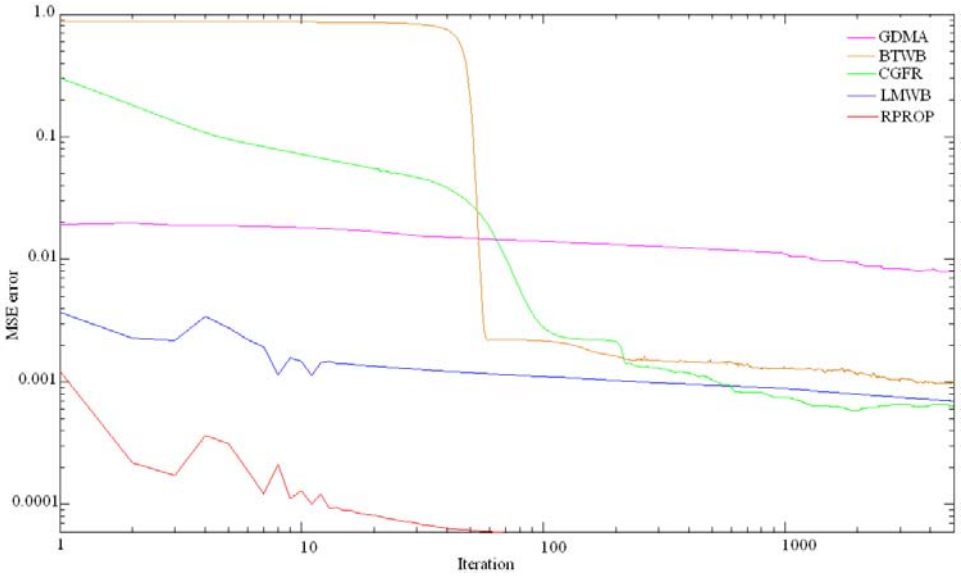

Figure 5. 8. Mean square (MSE) error as a function of the number of iterations during the training of different ANN paradigms for 2D W data.

Table 5. 13. Comparison of the 2D study for each paradigm in terms of training speed and epochs.

Array	Paradigm	Time (s)	Epochs	Training speed	MSE Error
WS	BTWB	2473	4000	1.62	0.0184
	CGFR	1871	4000	2.14	0.0032
	GDMA	20	16	0.80	0.0001
	RPROP	979	4000	4.09	0.0049
	LMWB	1653	4000	2.42	0.0009
W	BTWB	2907	5000	1.72	0.000992
	CGFR	2551	5000	1.96	0.000628
	GDMA	90.6	77	0.85	0.000058
	RPROP	1292	5000	3.87	0.007998
	LMWB	2146	5000	2.33	0.000715
DD	BTWB	11880.7	8000	0.67	0.0004
	CGFR	10980.1	8000	0.73	0.0064
	GDMA	2402.1	2282	0.95	0.0001
	RPROP	10080.2	8000	0.79	0.0009
	LMWB	10341.6	8000	0.77	0.0032
PD	BTWB	4098	10000	2.44	0.00028
	CGFR	4739	10000	2.11	0.00031
	GDMA	2639	10000	3.79	0.00314
	RPROP	1301	1275	0.98	0.00020
	LMWB	2206	3000	1.36	0.00020
PP	BTWB	3703.7	10000	2.70	0.000413
	CGFR	4166.7	10000	2.40	0.000045
	GDMA	8849.6	10000	1.13	0.000012
	RPROP	282.6	373	1.32	0.000010
	LMWB	1135.6	2853	2.50	0.000010

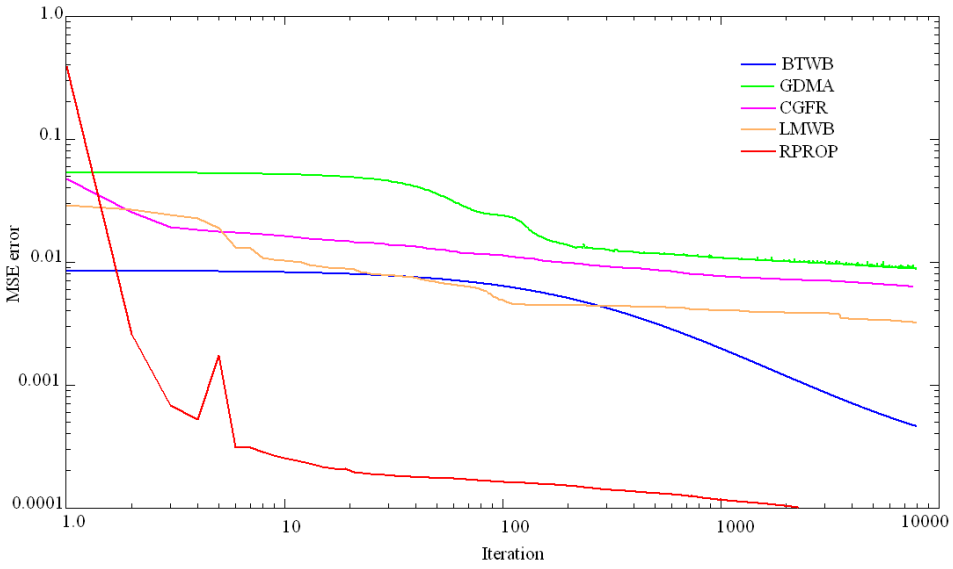

Figure 5. 9. Mean square (MSE) error as a function of the number of iterations during the training of different ANN paradigms for 2D DD data.

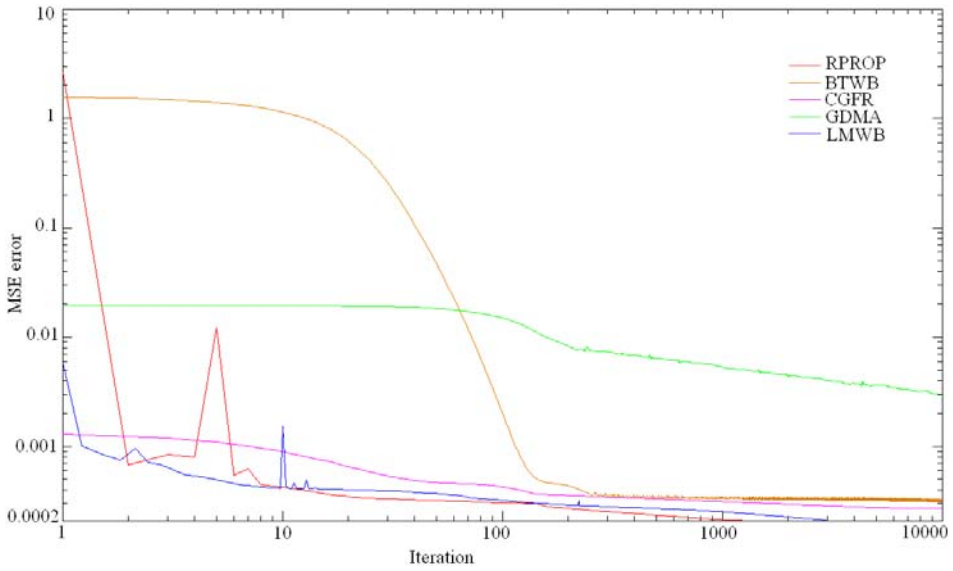

Figure 5. 10. Mean square (MSE) error as a function of the number of iterations during the training of different ANN paradigms for 2D PD data.

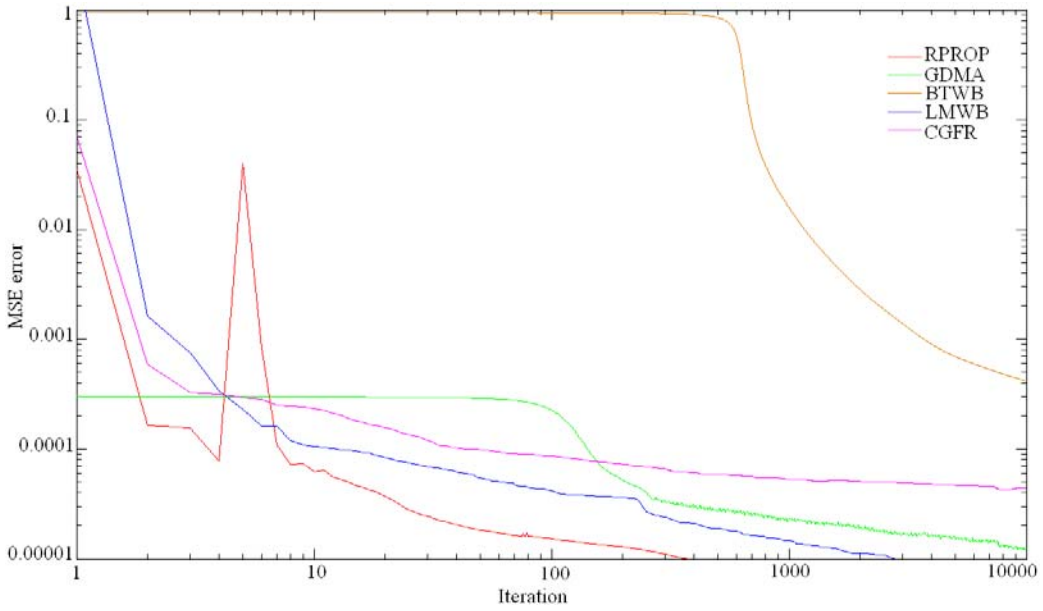

Figure 5. 11. Mean square (MSE) error as a function of the number of iterations during the training of different ANN paradigms for 2D PP data.

5.2.5.2. 3D comparison study

The mean square error (MSE) as function of the number of iterations during the training of the ANN by different paradigms is shown in Figures 5.12 to 5.16 for the PP, PD, DD, WS and W arrays, respectively. In this part of the study, the datasets generated by the method M2_3D have been used.

According to the variation of the errors in Figures 5.12, 5.14, 5.15, 5.16, it is concluded that the RPROP paradigm was the most efficient algorithm for training the ANN using the 3D dataset related to the PP, DD, WS and W arrays. The initial error for the RPROP algorithm in these Figures is about 0.352, 0.002, 0.201 and 0.022, respectively, which decreases as the iteration proceeds such that the network converges to a value equal to the desired performance goal for each array. The other algorithms could not achieve the performance goal even after the maximum number of iterations for each array, i.e., 10000 epochs for the PP, DD and W arrays and 100000 epochs for the WS array. In the case of the PD array, however, the RPROP paradigm achieved a value of about 0.000113 for

performance error of the ANN after 10000 iterations, while the GDMA paradigm attained a value of about 0.000058 after 1560 iterations (Fig. 5.13). The initial error for the GDMA algorithm was about 0.34 and then decreases as the iteration proceeded. The other algorithms could not achieve the performance goal after 10000 iterations. It is therefore concluded that the GDMA paradigm is the most efficient algorithm for training the ANN by the 3D datasets related to the PD array. Similar to 2D comparative study discussed in section 5.2.5.1, the comparative results for each paradigm in terms of training speed and epochs are summarized in Table 5.14. The training procedure was carried out on a 1.73-GHz Dual-Core PC. Once the ANN converged, the weights were adapted and stored. The ANN then performed the inversion of the field data in a few seconds, using the updated weights, without any further training.

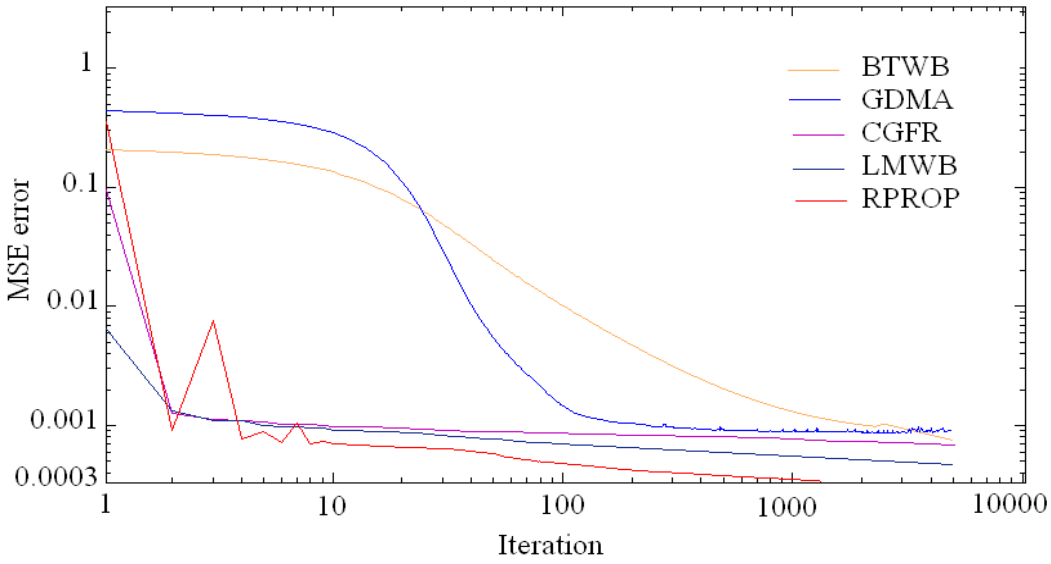

Figure 5. 12. Mean square (MSE) error as a function of the number of iterations during the training of different ANN paradigms for 3D PP data.

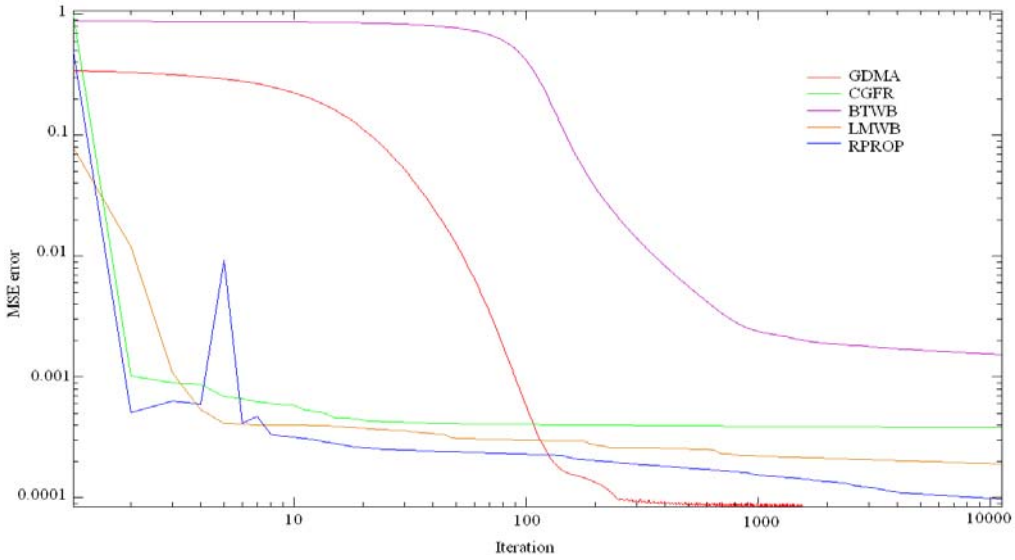

Figure 5. 13. Mean square (MSE) error as a function of the number of iterations during the training of different ANN paradigms for 3D PD data.

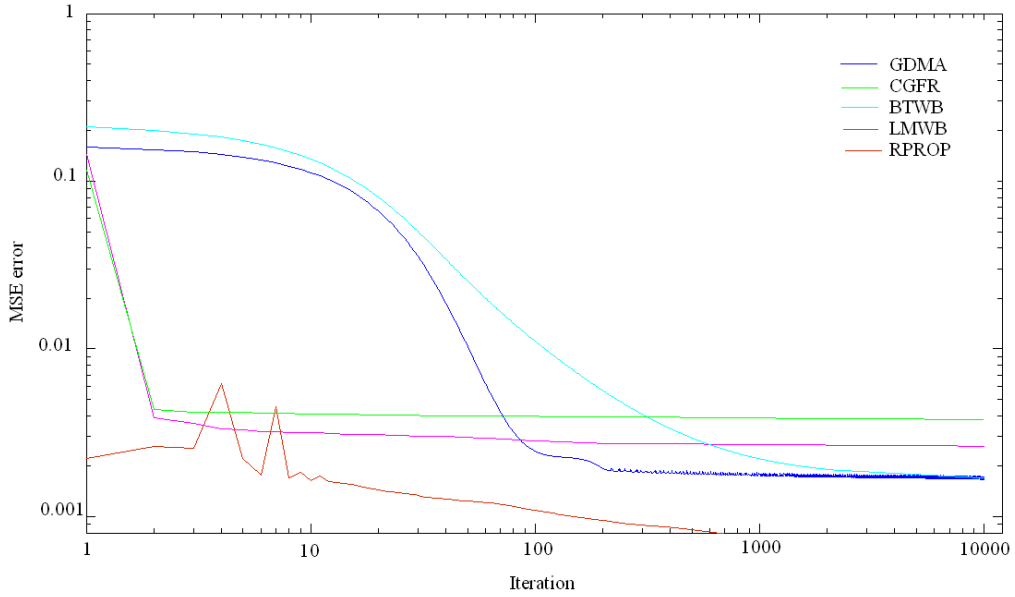

Figure 5. 14. Mean square (MSE) error as a function of the number of iterations during the training of different ANN paradigms for 3D DD data.

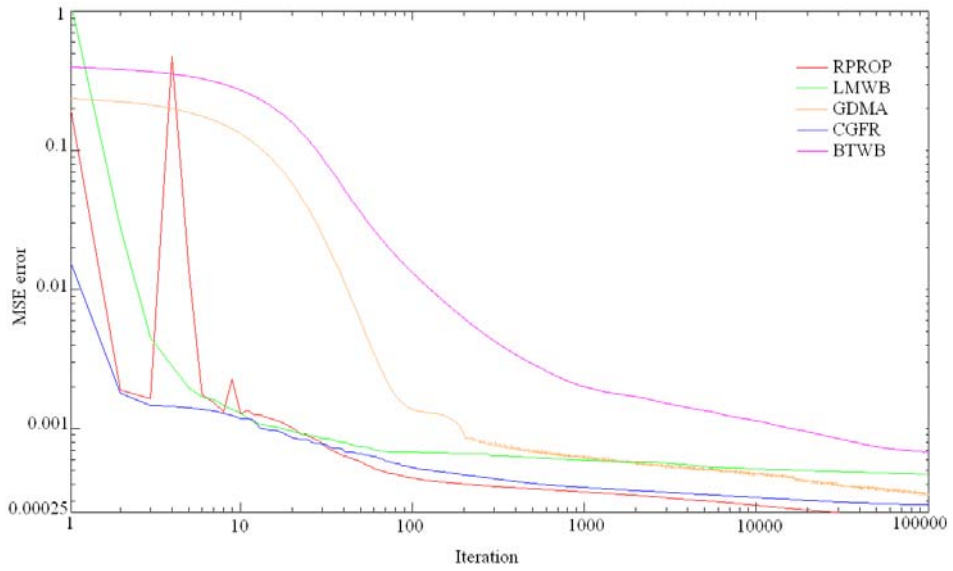

Figure 5. 15. Mean square (MSE) error as a function of the number of iterations during the training of different ANN paradigms for 3D WS data.

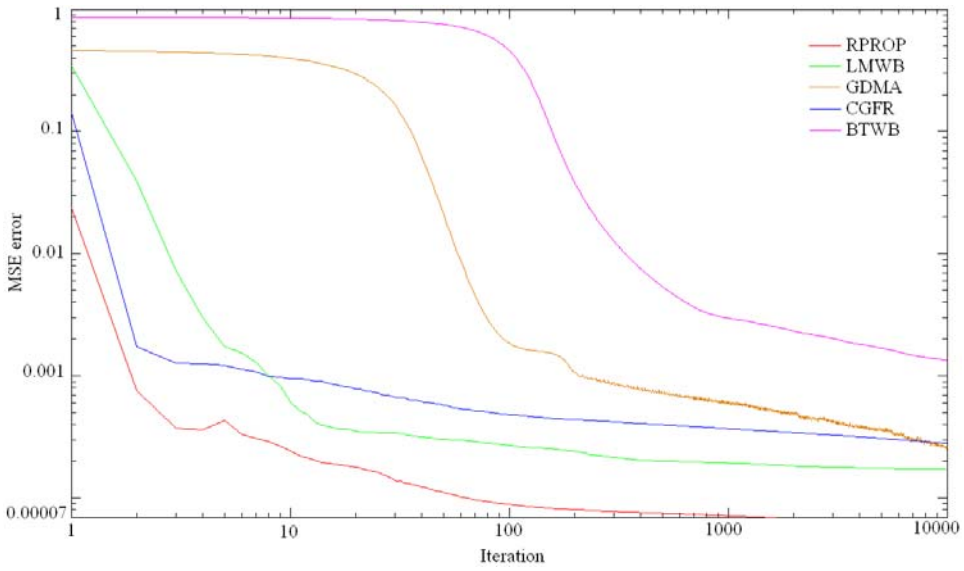

Figure 5. 16. Mean square (MSE) error as a function of the number of iterations during the training of different ANN paradigms for 3D W data.

Table 5. 14. Comparison of the 3D study for each paradigm in terms of training speed and epochs.

Array	Paradigm	Time (s)	Epochs	Training speed	MSE Error
PP	BTWB	4504.5	5000	1.11	0.00075
	CGFR	4424.8	5000	1.13	0.00070
	GDMA	4098.4	5000	1.22	0.00090
	RPROP	917.8	1340	1.46	0.00030
	LMWB	4950.5	5000	1.01	0.00045
PD	BTWB	8000	10000	1.25	0.00171
	CGFR	6993	10000	1.43	0.00039
	GDMA	939.8	1560	1.66	0.00005
	RPROP	5848	10000	1.71	0.00011
	LMWB	9009	10000	1.11	0.00019
DD	BTWB	5714.3	8000	1.40	0.0018
	CGFR	5161.3	8000	1.55	0.0039
	GDMA	4551.2	8000	1.72	0.0018
	RPROP	426.8	700	1.64	0.0008
	LMWB	4968.9	8000	1.61	0.0028
WS	BTWB	72992.7	100000	1.37	0.00070
	CGFR	63694.3	100000	1.57	0.00029
	GDMA	58479.5	100000	1.71	0.00032
	RPROP	18520.1	34077	1.84	0.00025
	LMWB	59171.6	100000	1.69	0.00049
W	BTWB	7692.3	10000	1.30	0.00214
	CGFR	7299.3	10000	1.37	0.00029
	GDMA	6097.6	10000	1.64	0.00026
	RPROP	1096.1	1677	1.53	0.00007
	LMWB	8130.1	10000	1.23	0.00018

5.2.6. ANN interpolation and extrapolation properties

The ANN performance was tested using the generated test datasets for each array. These datasets were not used during the training stage of the ANN. The number of test datasets and their respective error range for the WS, W, DD, PD and PP arrays are summarized in Table 5.15. As evidence from the listed values the errors are higher for the test datasets than the training datasets of each array.

Table 5. 15. Number of test datasets and error range for the test data for the WS, W, DD, PD and PP arrays.

Array		Number of test datasets	Error range
WS	2D	16	0.001 – 0.020
	3D	16	0.020 – 0.040
W	2D	12	0.060 – 0.090
	3D	20	0.030 – 0.070
DD	2D	11	0.010 – 0.060
	3D	10	0.020 – 0.080
PD	2D	20	0.002 – 0.040
	3D	8	0.010 – 0.050
PP	2D	9	0.001 – 0.010
	3D	9	0.003 – 0.060

In order to study the 2D and 3D interpolation and extrapolation properties of the ANN, another 24 synthetic datasets were generated for each array. The total number of test data points for each array is summarized in Table 5.16. The range from 100 – 1000 Ωm was divided into 100, 200, 300, 400, 500, and 600 Ωm as the background resistivity, and different resistivity values were considered for the anomalous body. For example, when the background resistivity was 100 Ωm, the resistivity values for the anomalous body were 300, 700, 2000, and 4000 Ωm to cover the interpolation and extrapolation properties of the ANN. The details of the resistivity distribution for other test sets can be seen in Tables A.31 to A.40 in Appendix A. In these tables, the root mean square (RMS) error between the

results of the ANN and the corresponding true resistivity distributions are shown for each test set. The RMS errors for all interpolation and extrapolation test sets related to each array are summarized in Table 5.16 are in the range of 0.8 – 5.8%. Since the RMS errors for all datasets are in the range of 0.3 - 9.0%, it is thus concluded that the networks are properly designed and trained.

Table 5. 16. Total number of test data points and range of RMS error for each array.

Array		Total number of data points	Error range (%)
WS	2D	21360	0.8 – 5.8
	3D	25032	2.0 – 8.0
W	2D	23472	0.7 – 6.2
	3D	11976	3.0– 9.0
DD	2D	13896	0.9 – 8.2
	3D	36528	3.0 – 8.0
PD	2D	26928	1.0 – 7.1
	3D	221304	2.0 – 6.0
PP	2D	27216	3.0 – 6.5
	3D	48384	0.3 – 9.0

5.3. Summary

In this chapter, the generation of synthetic data used to train and test the ANN is explained. The process of training the ANN and the selection of training parameters are discussed for five common arrays, i.e., the Ws, W, DD, PD and PP arrays, and then used in 2D and 3D surveys.

In order to study the effect of data pool formation in training the ANN, two methods were used to generate the synthetic data. These methods are called M1 and M2, and they basically differ in the type of input-output data used to train the ANN. In the first methods (M1_2D and M1_3D), the apparent resistivity data were considered as the input data and the true resistivities of all mesh elements were used as the output data in the training phase of the ANN. In second method, M2_2D and M2_3D, the locations (x and y for the 2D case and x, y and z for the 3D case) and the apparent resistivity of data points were considered as the input data and the true resistivities of all mesh elements were used as the output data in the training process. The effect of the input-output data (obtained by the methods M1 and M2) was investigated in terms of 2D and 3D surveys. The higher MSE error for the methods M1_2D and M1_3D as compared to that of the methods M2_2D and M2_3D can be explained as an effect of the size of the mesh elements. Because fixed sizes were used for each element of the mesh, this might affect the accuracy of the results. It is therefore concluded that the synthetic data generated using method M2_2D and M2_3D may be the best data type for training and testing the ANN in this study.

The results of the 2D study suggest that the simplest architectures for the ANN that can reach the desired threshold error for the PP, PD, DD, WS and W arrays are (3-30-90-1), (3-30-12-1), (3-28-4-1), (3-28-16-1) and (3-24-80-1), respectively. The simplest architectures for the ANN in the 3D study are (4-84-24-1), (4-35-25-1), (4-35-25-1), (4-45-60-1) and (4-30-50-1). We also evaluated the effect of the training data pool volume in the 2D and 3D parts of our study and determined the sufficient data pool volume for each array.

Five common training paradigms, i.e., BTWB, CGFR, RPROP, GDMA and LMWB, are compared in the cases of 2D and 3D imaging. The results showed that for all arrays of 2D and 3D study with the exception of 3D PD data, the RPROP is the most

efficient algorithm for training the DC resistivity data. In the case of 3D PD data the GDMA algorithm was the most efficient.

In order to study the 2D and 3D interpolation and extrapolation properties of the ANN, another 24 synthetic datasets were generated for each array. The range from 100 – 1000 Ωm was divided into 100, 200, 300, 400, 500, and 600 Ωm as the background resistivity, and different resistivity values for the anomalous body were considered. In the appendix Tables A31 to A40, the root mean square (RMS) error between the results of the ANN and the corresponding true resistivity distributions are shown for each test set. The RMS errors for all interpolation and extrapolation test sets related to each array are in the range of 0.8 – 5.8%. Since the RMS errors for all datasets are less than 9.0%, it is concluded that the networks are properly designed and trained.

Chapter 6
Inversion of 2D and 3D DC resistivity field data using the ANN

The ability of the trained ANNs to invert the DC resistivity imaging data must be checked by real field data related to a site with high resistivity contrast regions. Therefore, in this chapter, the ANN is applied to invert 2D and 3D DC resistivity data obtained by five common electrode configurations, i.e., the WS, W, DD, PD and PP arrays. The inversions of the field data using the ANN are then compared with the results of the inversion using the conventional RIT for each array. Further study using a synthetic example with a condition close to the field data is done for each array in order to compare the reliability of the results of both the ANN and the RIT. Furthermore, known information about the subsurface features of the site help us to check the network performance.

6.1. Study site description

The site used for this study is located south of the University of Malaya, Kuala Lumpur, Malaysia. It consists of an underground concrete wastewater pipe system and its square manhole columns (Fig. 6.1).

The survey area stretches over a flat playground covered with grass. The direct resistivity measurement of the soil at the surface gives values ranging from 150 to 600 Ωm. The soil is relatively porous and very sandy that is probably originated from weathered bedrock. There are, however, areas of more resistive materials within the soil as well. The high resistivity values are caused by construction materials left behind during the construction of the wastewater system. There is a horizontal concrete pipe and

corresponding vertical manhole columns (A and B) at 7 and 6 meters depth, respectively, at the north side of the site (Fig. 6.1). The pipe is almost horizontal, buried at a depth of about 6 m. Column B is located 4 meters southwest of column A and is connected to column F, which is more than ten meters deep. At the north side of the site, column A has been linked to a watercourse at a depth of 8 meters. In addition, the study site consists of a large cavity and a corresponding vertical manhole column (C) approximately at the center of the site (Fig. 6.1). Furthermore, there is another near-horizontal pipe at a depth of about 7 m. This pipe connects the vertical columns D and A. Another horizontal pipe connects the vertical columns D and E. Column E is located at the southwest corner of the study site (Fig. 6.1). In Figure 6.1, the corners of the study area (1 to 4) are shown with blue flags. Columns A, B, C, D, E and F are about one square meter (inner dimension) and set vertically from the surface to the cavity and the pipes.

Table 6.1 shows the longitude and latitude of these flags as well as the vertical columns located in the site. The resistivity values of the concrete, measured directly, range from 950 to 1550 Ωm. Thus, the average resistivity of the concrete is 1250 Ωm. This value is used to determine the boundaries of the concrete structures in the inversion results. Values greater than 1250 Ωm were assumed to correspond to the empty space within the concrete or the cavity. At the study site, several 2D and 3D surveys using W, WS, DD, PD and PP arrays were carried out over the pipes, the columns and the cavity. The details of these surveys are discussed in the corresponding subsections of this chapter.

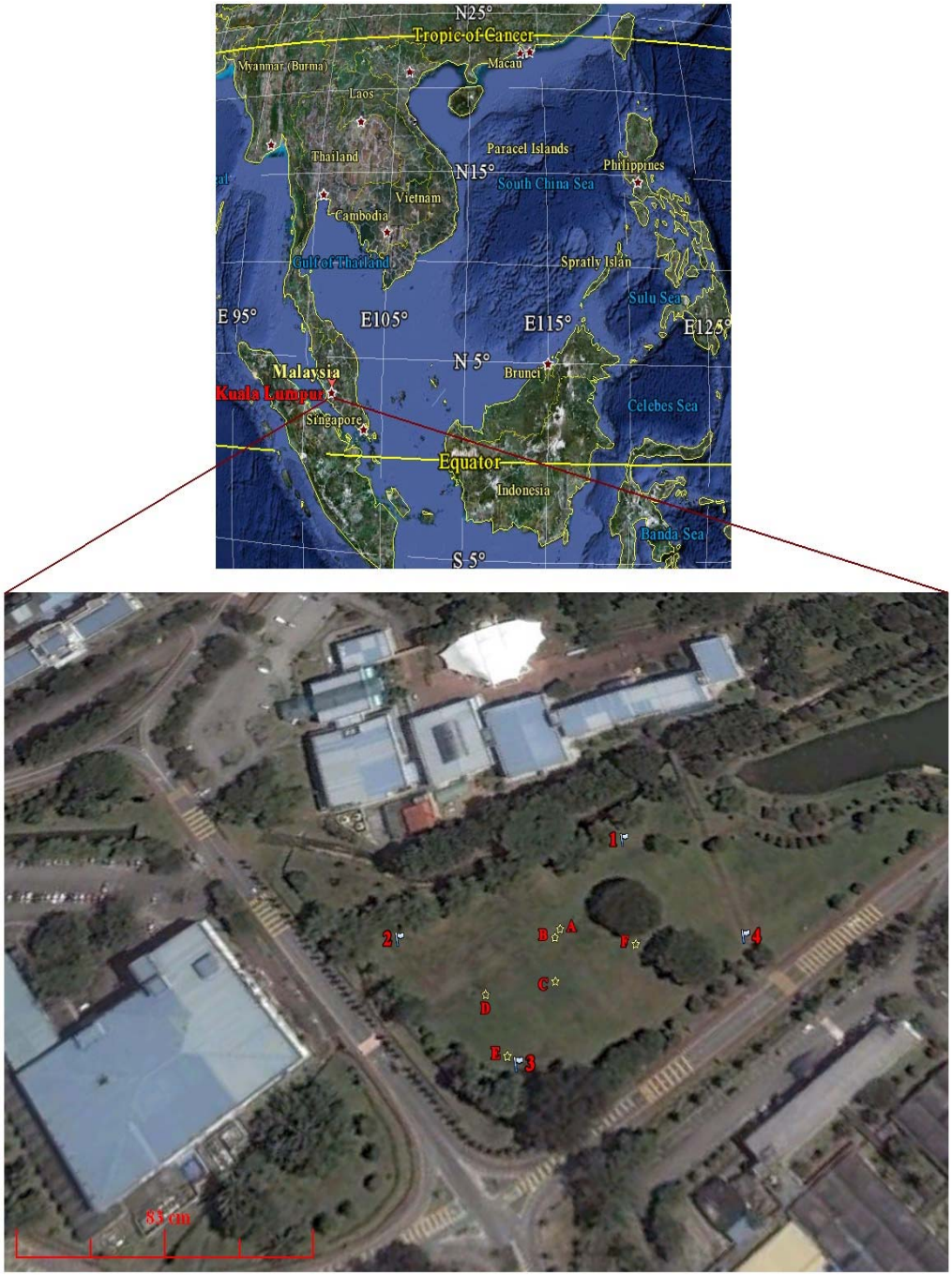

Figure 6. 1. Location of the study site. The longitude and latitude of columns A to F and the corners of the site are shown in Table 6.1.

Table 6. 1. Longitude and the latitude of the corners of the site and the vertical columns located in the site.

	Latitude	Longitude
1	3^0 - 07´- 10.69˝ - N	101^0 - 39´-18.49˝ - E
2	3^0 - 07´- 12.30˝ - N	101^0 - 39´-17.35˝ - E
3	3^0 - 07´- 10.15˝ - N	101^0 - 39´-20.25˝ - E
4	3^0 - 07´- 09.54˝ - N	101^0 - 39´-19.14˝ - E
A	3^0 - 07´- 11.17˝ - N	101^0 - 39´-18.83˝ - E
B	3^0 - 07´- 11.13˝ - N	101^0 - 39´-18.71˝ - E
C	3^0 - 07´- 10.62˝ - N	101^0 - 39´-18.32˝ - E
D	3^0 - 07´- 11.00˝ - N	101^0 - 39´-17.61˝ - E
E	3^0 - 07´- 10.39˝ - N	101^0 - 39´-17.39˝ - E
F	3^0 - 07´- 10.24˝ - N	101^0 - 39´-17.19˝ - E

6.2. Inversion of 2D DC resistivity imaging data using the ANN and RIT

In this section, the ANNs have been trained with 2D synthetic data obtained by the WS, W, DD, PD and PP array to invert a real 2D field data for each array. The ANN architectures found for the WS, W, DD, PD and PP datasets in section 5.2.2.1 are (3-28-16-1), (3-24-80-1), (3-28-4-1), (3-30-12-1) and (3-30-90-1), respectively. The study area and the corresponding profiles used in this part of the study are shown in Figures 6.2 to 6.6 for the WS, W, DD, PD and PP arrays, respectively. The WS, W, DD, PD and PP arrays are used in the 2D field data acquisition along the lines L1-L'1, L2-L'2, L3-L'3, L4-L'4, L5-L'5 (Figs. 6.2 to 6.6), which supposed to be along the x-axes. The latitude and longitude of the first and last electrodes of each profile are summarized in Table 6.2.

Table 6. 2. Latitude and longitude of the first and last electrodes of each profile in the 2D surveys by the WS, W, DD, PD and PP arrays.

Array		latitude	longitude
WS	L1	3^0 - 07´- 9.89˝ - N	101^0 - 39´-20.41˝ - E
	L'1	3^0 - 07´- 12.38˝ - N	101^0 - 39´-17.33˝ - E
W	L2	3^0 - 07´- 11.52˝ - N	101^0 - 39´-19.02˝ - E
	L'2	3^0 - 07´- 10.25˝ - N	101^0 - 39´-19.11˝ - E
DD	L3	3^0 - 07´- 11.45˝ - N;	101^0 - 39´-1852˝ - E
	L'3	3^0 - 07´- 10.23˝ - N	101^0 - 39´-18.47˝ - E
PD	L4	3^0 - 07´- 11.06˝ - N	101^0 - 39´-17.08˝ - E
	L'4	3^0 - 07´- 11.04˝ - N	101^0 - 39´-18.38˝ - E
PP	L5	3^0 - 07´- 10.95˝ - N	101^0 - 39´-17.10˝ - E
	L'5	3^0 - 07´- 10.97˝ - N	101^0 - 39´-18.39˝ - E

Figure 6. 2. Location of line L1-L'1 in the 2D survey using the WS-array.

Figure 6. 3. Location of line L2-L'2 in the 2D survey using the W array.

Figure 6. 4. Location of line L3-L'3 in the 2D survey using the DD array.

Figure 6. 5. Location of line L4-L'4 in the 2D survey using the PD array.

Figure 6. 6. Location of line L5-L'5 in the 2D survey using the PD array.

The cable covers 120 m for the WS array, 38 m for both the W and DD arrays and 40 m for both the PD and PP arrays between the first and last take-out. The minimum electrode spacings for the WS, W, DD, PD and PP arrays are 3, 2, 2, 1, and 1 m, respectively. Three different electrode spacings (at 1 to 3 times the minimum spacing for the WS, DD and PD arrays, at 1 to 4 times the minimum spacing for the W array and at 1 to 10 times the

minimum spacing for the PP array) were measured. We used n=1 to 8 in the field data measuring by the WS array and n=1 to 6 for measurements using the DD array. The numbers of data points in the field dataset for each array are summarized in Table 6.3.

Table 6. 3. Number of data points in the field dataset for each array and the RMS error for the results of the ANN and RIT.

Array	Number of data points	RMS error (%) for the ANN result	RMS error (%) for the RIT result
WS	330	0.60	8.35
W	50	3.70	5.13
DD	85	4.45	5.57
PD	1440 (=2×720)	4.47	5.13
PP	355	3.88	5.03

Figures 6.7 to 6.11 show the measured apparent resistivity and calculated apparent resistivity data using the RIT for the WS, W, DD, PD and PP array, respectively.

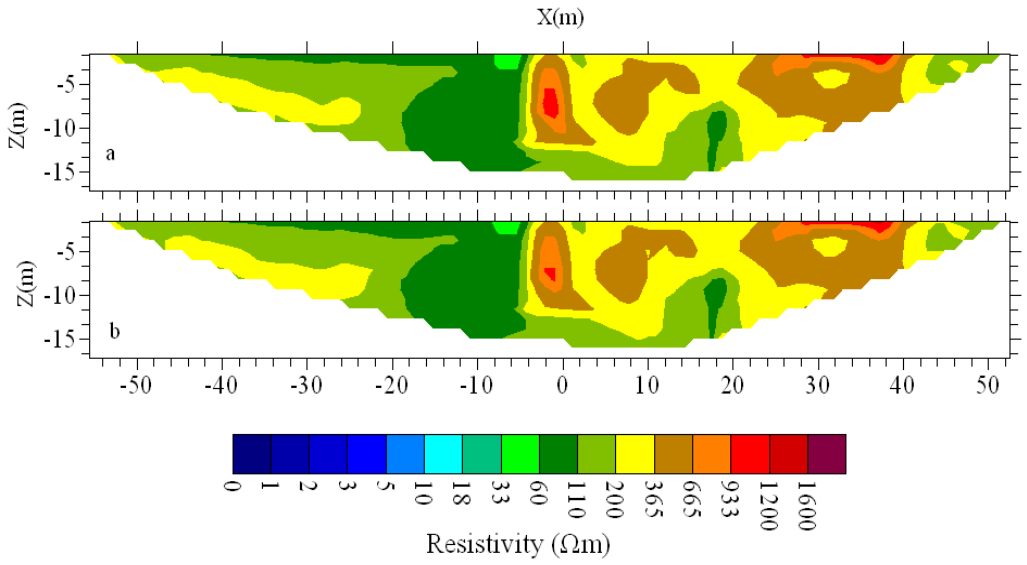

Figure 6. 7. Pseudo-section of measured (a) and calculated (b) apparent resistivity data using the WS array along line L1-L'1.

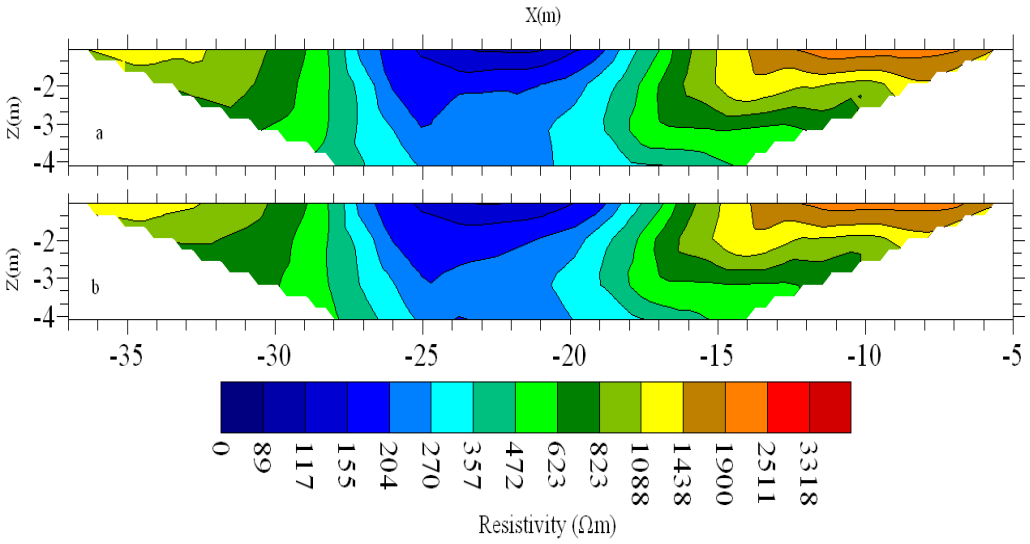

Figure 6. 8. Pseudo-section of measured (a) and calculated (b) apparent resistivity data using the W alpha array along line L2-L'2.

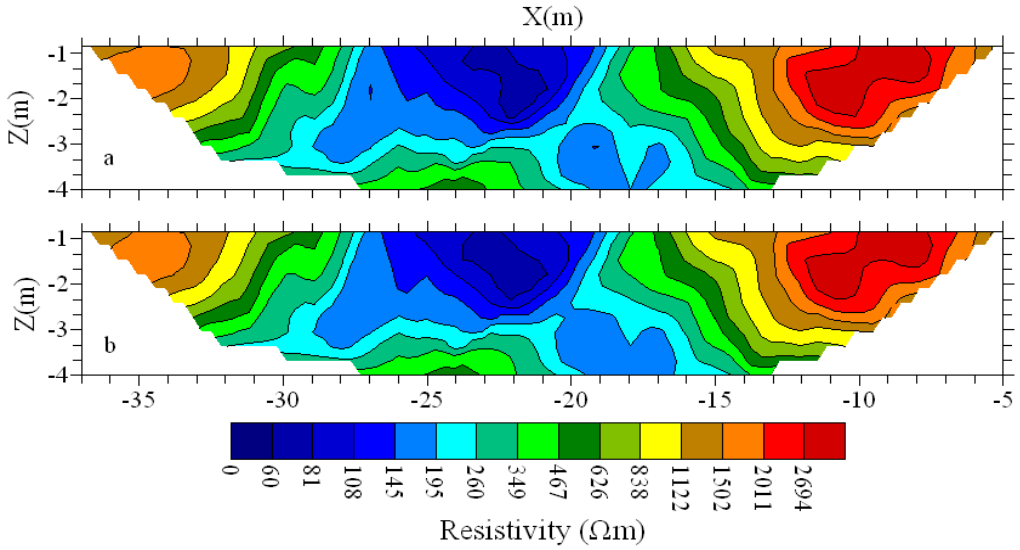

Figure 6. 9. Pseudo-section of measured (a) and calculated (b) apparent resistivity data using the DD array along line L3-L'3.

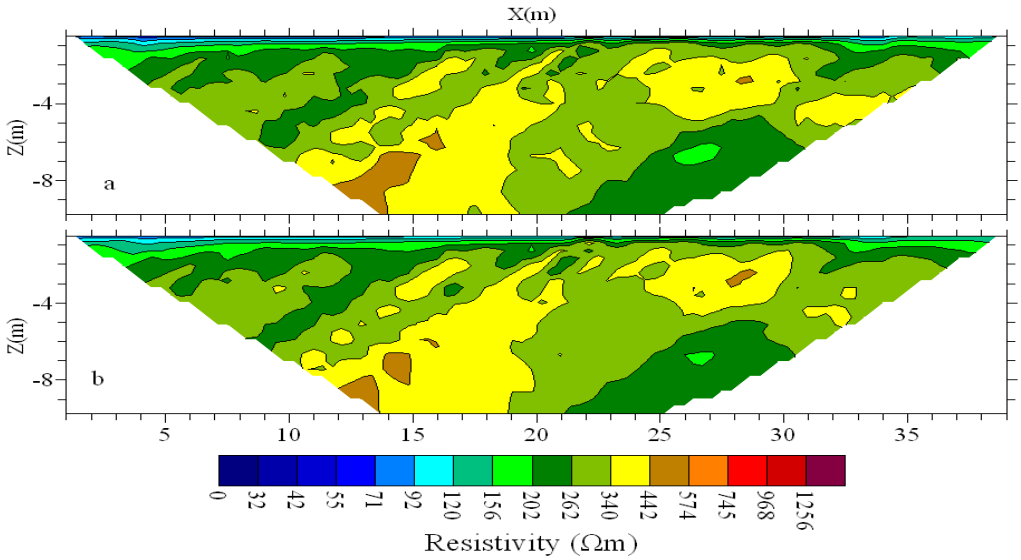

Figure 6. 10. Pseudo-section of measured (a) and calculated (b) apparent resistivity data using the PD array along line L4-L'4.

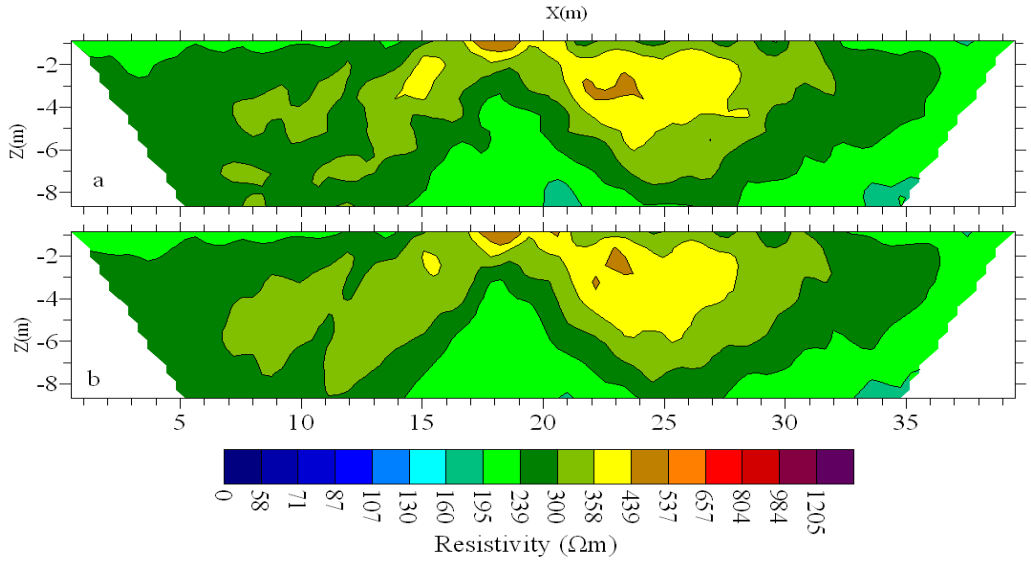

Figure 6. 11. Pseudo-section of measured (a) and calculated (b) apparent resistivity data using the PD array along line L5-L'5.

A 2D cross-section was also constructed using the output data of the ANN for each array together with the result of the inversion using the conventional RIT (Figs. 6.12 to 6.16). The RMS error for the results of the ANN and RIT are summarized in Table 6.3. According to these results, the RMS error for the ANN results is less than that of the RIT.

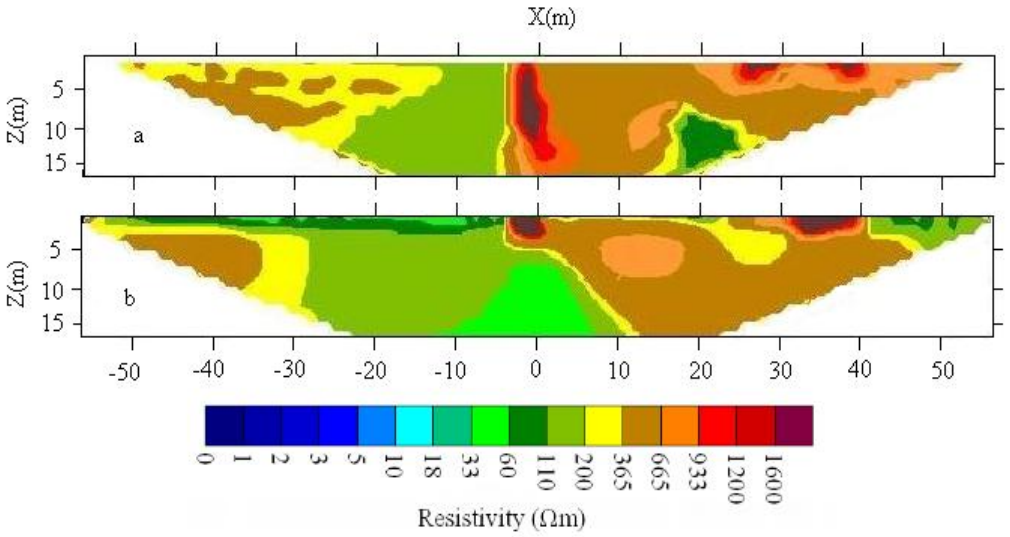

Figure 6. 12. Cross-sections of inverted results for the real field data for the WS array using (a) the ANN and (b) the conventional RIT.

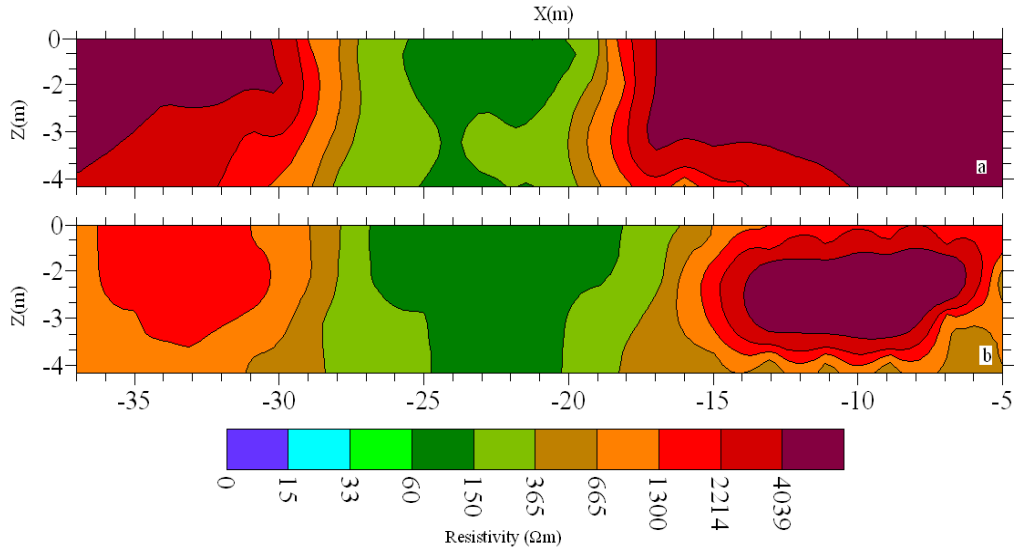

Figure 6. 13. Cross-sections of the inverted results for the real field data for the W array using (a) the ANN and (b) the conventional RIT.

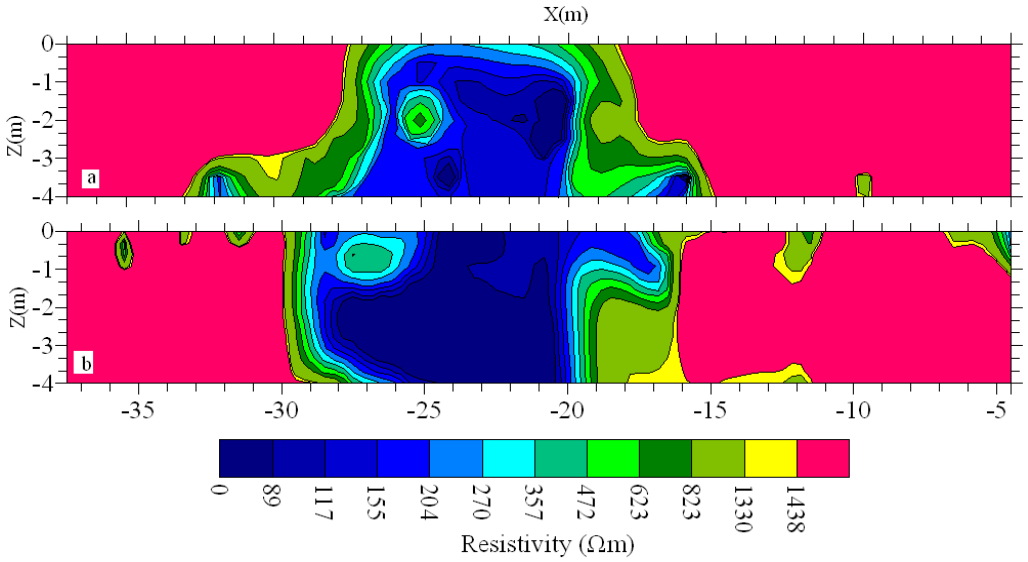

Figure 6. 14. Cross-sections of the inverted results for the real field data for the DD array using (a) the ANN and (b) the conventional RIT.

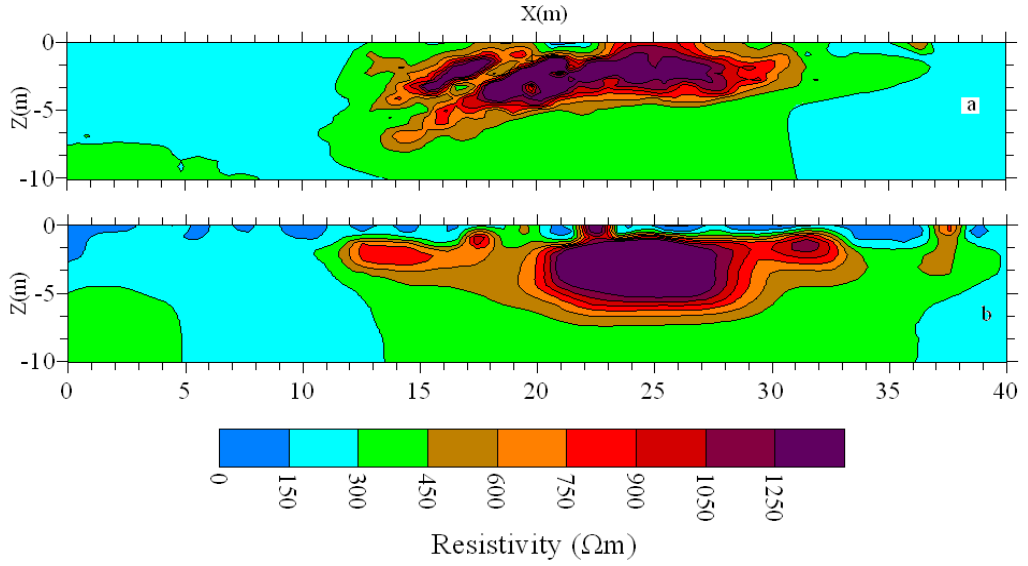

Figure 6. 15. Cross-sections of the inverted results for the real field data for the PD array using (a) the ANN and (b) the conventional RIT.

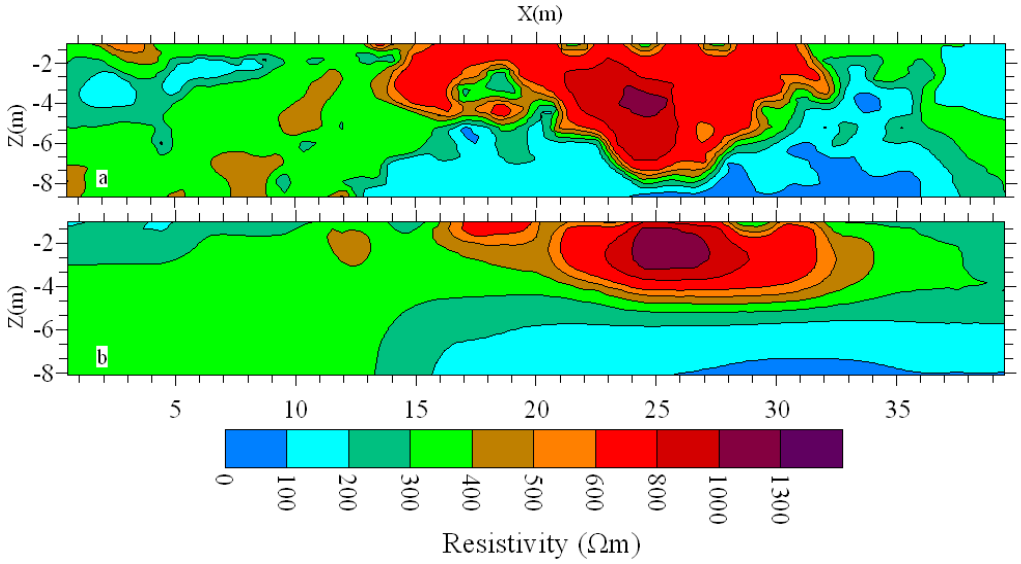

Figure 6. 16. Cross-sections of the inverted results for the real field data for the PP array using (a) the ANN and (b) the conventional RIT.

In Figure 6.12, although all of the subsurface features were resolved both methods, the ANN results, especially for the dimension of the vertical column, are found to be more realistic. In contrast, the RIT produces a smaller vertical dimension than the actual size of the real field data. The resistivity area between 10 and 17 m at the right side of the cross-section (Fig. 6.12) is related to the roots of the tree located between column A and point L1. The near-surface resistive zone (between 15 and 40 m) at the right side of the cross-section is due to construction materials left during the construction of the road near point L1. The high resistivity zone located between -50 and -30 m at the left side of the cross-section in Figure 6.12 is probably due to the roots of the trees near point L'1 in Figure 6.2. This zone is observed in the results of the ANN and RIT.

According to Figure 6.13, the result of the ANN, especially for the depth of the anomalous zones, is more realistic than the results of the RIT. The RIT produces a smaller vertical dimension than the actual size for the real field data. The high resistivity zone between -17 and -5 m at the right side of the cross-section (Fig. 6.13) is related to the horizontal pipe that is connected to columns A and B and the construction materials

(concrete) surrounding the pipe and the columns. The resistive zone (between -38 and -30 m) at the left side of the cross-section (Fig. 6.13) is due to the connection between the columns B and F near point L'2 (Fig. 6.3).

In Figure 6.14, the high resistivity zone between -18 and -5 m at the right side of the cross-section is related to the horizontal pipe that is connected to columns A and B and the construction materials (concrete) surrounding the pipe and the columns. The resistive zone (between -38 and -32 m) at the left side of the cross-section is due to the cavity to which column C connects (Fig. 6.4). High resistivity zones are not observed at a distance between -32 and -20 m (Fig. 6.14).

In the inversion result shown in Figure 6.15, the high resistivity zone between 20 and 27 m in the cross-section is related to the D columns (Fig. 6.5). The resistive zone (between 12 and 18 m) (Fig. 6.15) is probably due to the construction material (concrete) left during the construction of the horizontal pipe located between columns D and B (Fig.6.5). High resistivity zones (> 600 Ωm) were not observed at depths of more than 6.5 m and on both sides of the line L4-L'4.

With respect to the results for the PP array, the high resistivity zone between 21 and 24 m in the cross-section (Fig. 6.16) is related to the connection between columns D and E (Fig. 6.6). The resistive zone colored in red (600 - 800 Ωm), which is located between 15 and 33 m (Fig. 6.16), is probably due to the construction material (concrete) left during the construction of the connection between columns D and E. High resistivity zones (> 400 Ωm) were not observed at depths of more than 5.0 and 7.0 m for the results of the RIT and the ANN, respectively. The depth for the connection between columns D and E produced by the ANN (6.5 m) is more than that produced by the RIT (3.6 m). The depth of column D is measured directly; it was about 7 m. Thus, it is concluded that the produced depth for the

connection between columns D and E by the ANN is more realistic than the result of the RIT.

6.2.1. 2D Synthetic model close to the fieldwork

In order to evaluate the reliability and accuracy of the inversion results using both the ANN and the RIT, a synthetic test model with the corresponding apparent resistivity pseudo-section is constructed for the WS, W, DD, PD and PP arrays as (shown in Figures 6.17 to 6.21, respectively). These models were generated using a finite elements code (Loke and Barker, 1996b). The number of electrodes and the minimum electrode spacing were the same as in the fieldwork. The resistivity of anomalies was 1000 Ωm and the background resistivity 100 Ωm. The resistivity models in Figures 6.17, 6.20 and 6.21 consist of a rectangular shaped anomaly near the middle of the profile. The resistivity model in Figures 6.18 and 6.19 indicate two rectangular shaped as anomalous bodies. The details of the positions and sizes of the anomalies are mentioned in Figures 6.17 to 6.21.

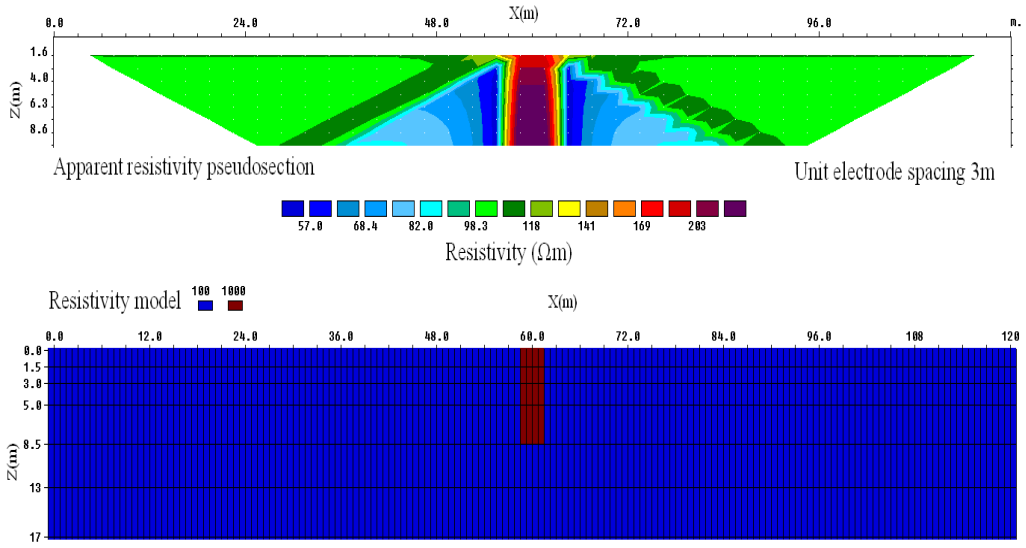

Figure 6. 17. An example of the synthetic test model and its pseudo-section for the WS array.

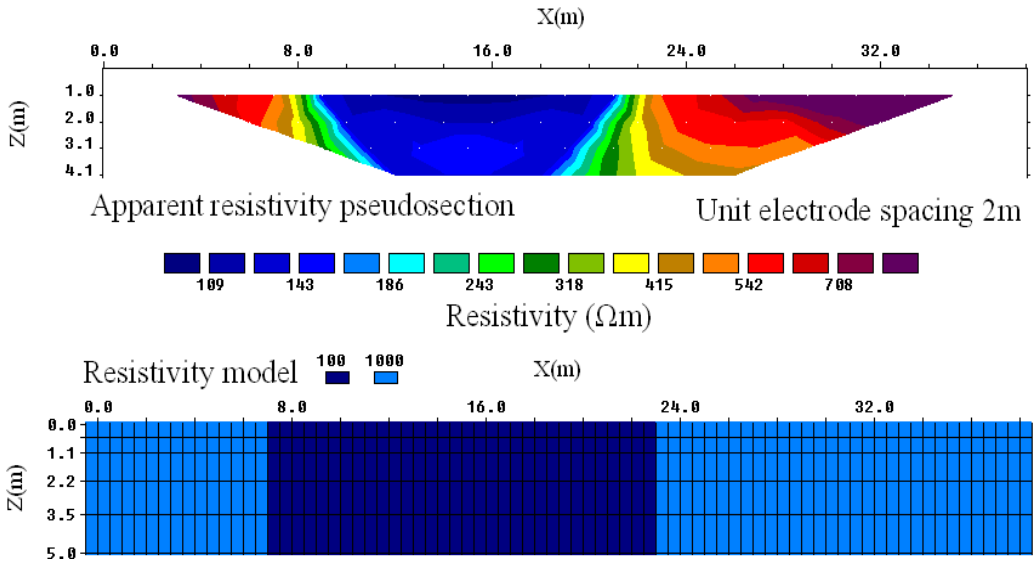

Figure 6. 18. An example synthetic test model and its pseudo-section for the W array.

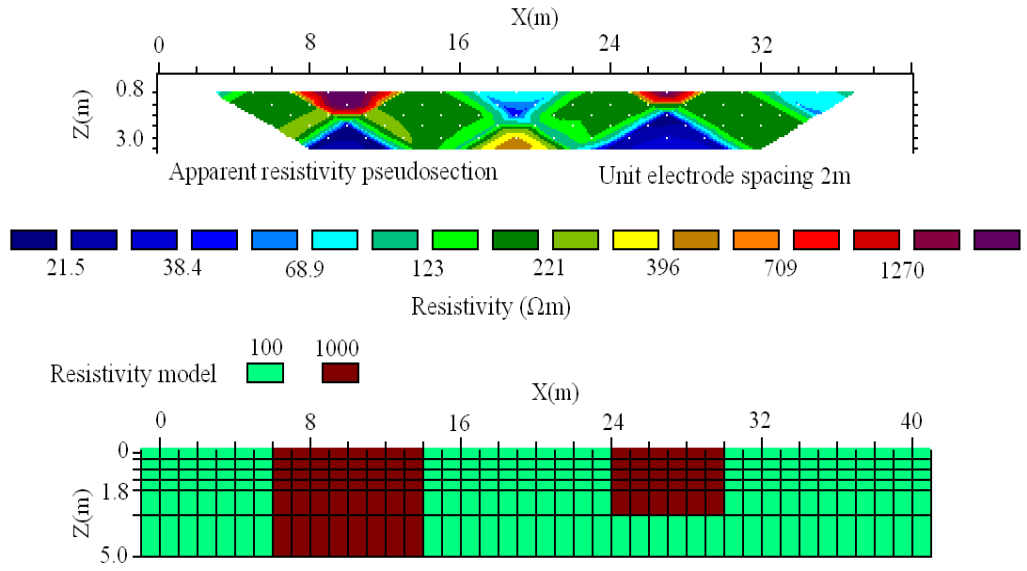

Figure 6. 19. An example synthetic test model and its pseudo-section for the DD array.

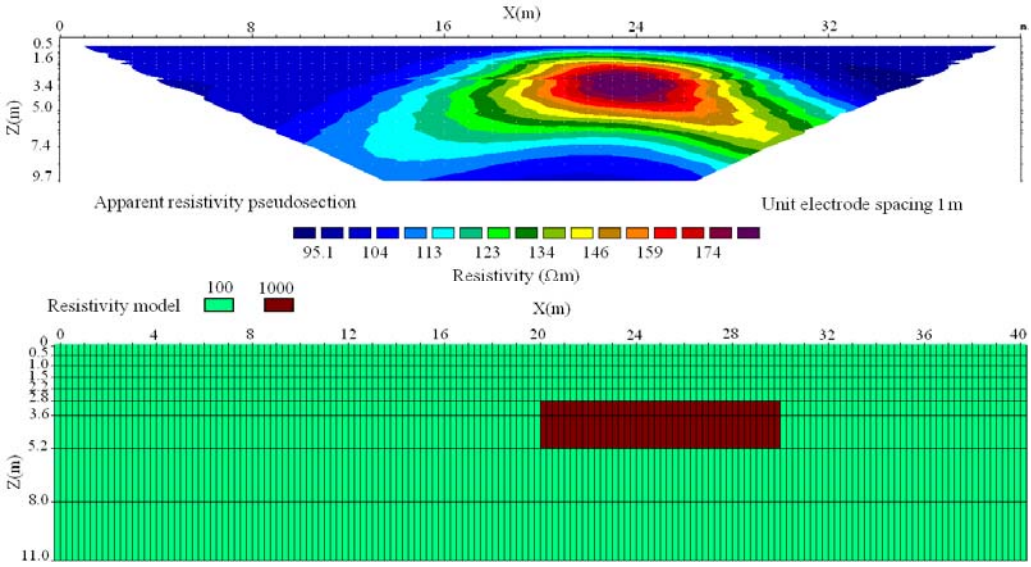

Figure 6. 20. An example synthetic test model and its pseudo-section for the PD array.

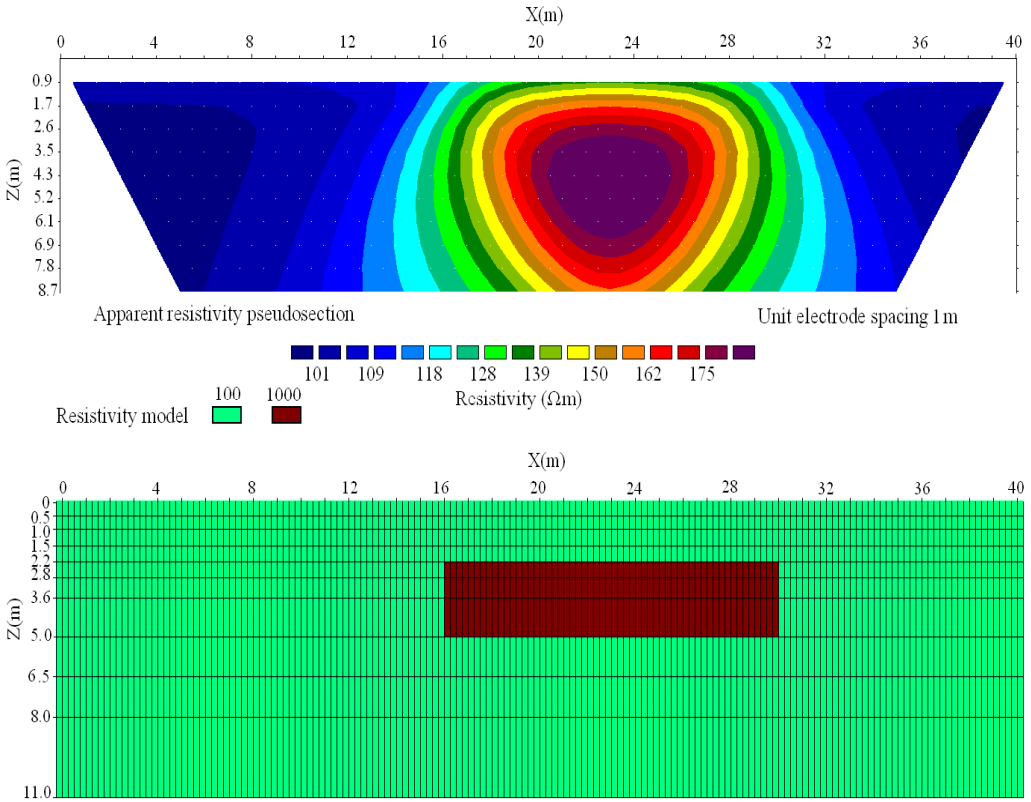

Figure 6. 21. An example synthetic test model and its pseudo-section for the PP array.

Figures 6.22 to 6.26 show the results of the inversion by the RIT and the ANN method for the WS, W, DD, PD and PP arrays, respectively. The RMS errors for the result of the RIT and the ANN are summarized in Table 6.4. A 3% uniform Gaussian noise in the apparent resistivity data is used to obtain these results.

Although both methods could resolve the anomalous bodies, the results from ANN are found as more realistic than those of the RIT. For example, when the inversion results in Figures 6.44 to 6.46 are compared with the resistivity model (Figs. 6.22 to 6.24), the depth of the anomaly in the RIT result is found to be less than the actual size. According to Figures 6.25 and 6.26, the RIT produces smaller resistivity values than the actual values, and the result of the ANN represents the physical model shown in Figures 6.20 and 6.21 better than the result of the RIT. It is therefore concluded that the ANN results produced more accuracy than the RIT results.

Table 6. 4. RMS error in the results of the ANN and RIT for 2D synthetic models close to the investigation field.

Array	RMS error (%) for the result of the ANN	RMS error (%) for the result of the RIT
WS	1.53	4.46
W	1.86	2.99
DD	2.25	2.33
PD	1.55	1.86
PP	3.00	3.30

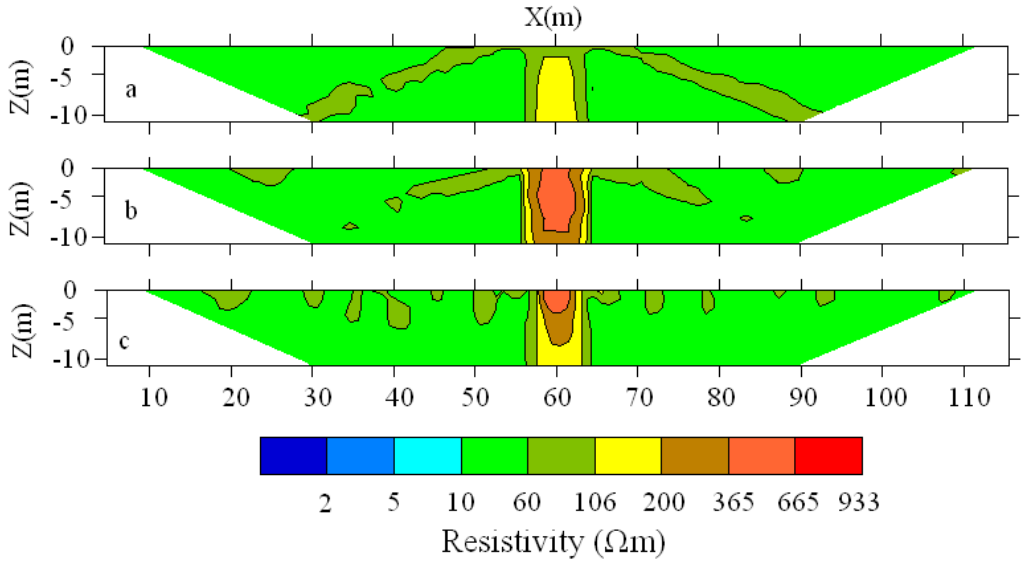

Figure 6. 22. Cross-sections of the inverted results related to the synthetic example model for the WS array: (a) apparent resistivity pseudo-section, (b) the result of the ANN and (c) the result of the RIT.

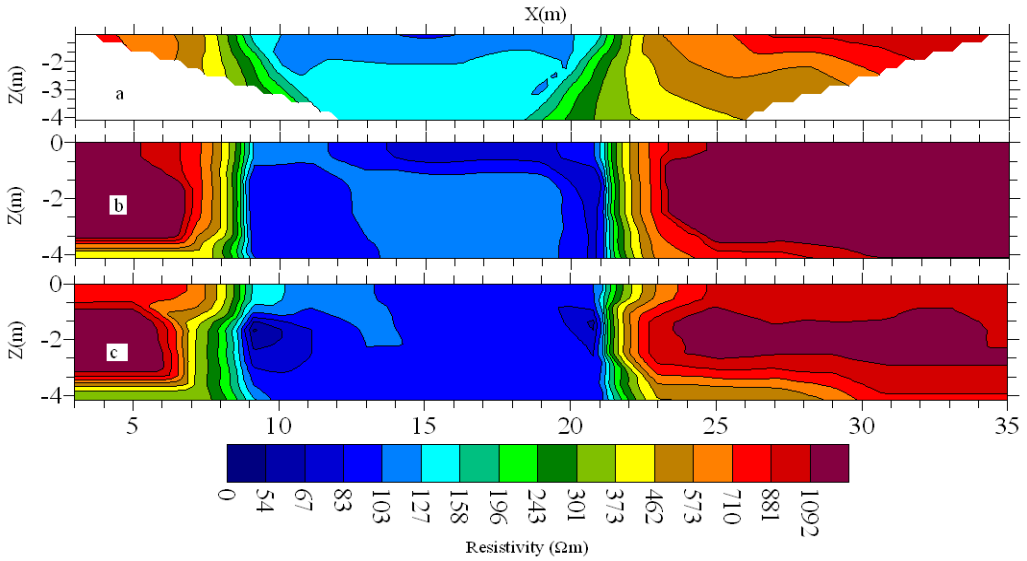

Figure 6. 23. Cross-sections of the inverted results related to the synthetic example model for the W array: (a) apparent resistivity pseudo-section, (b) the result of the ANN and (c) the result of the RIT.

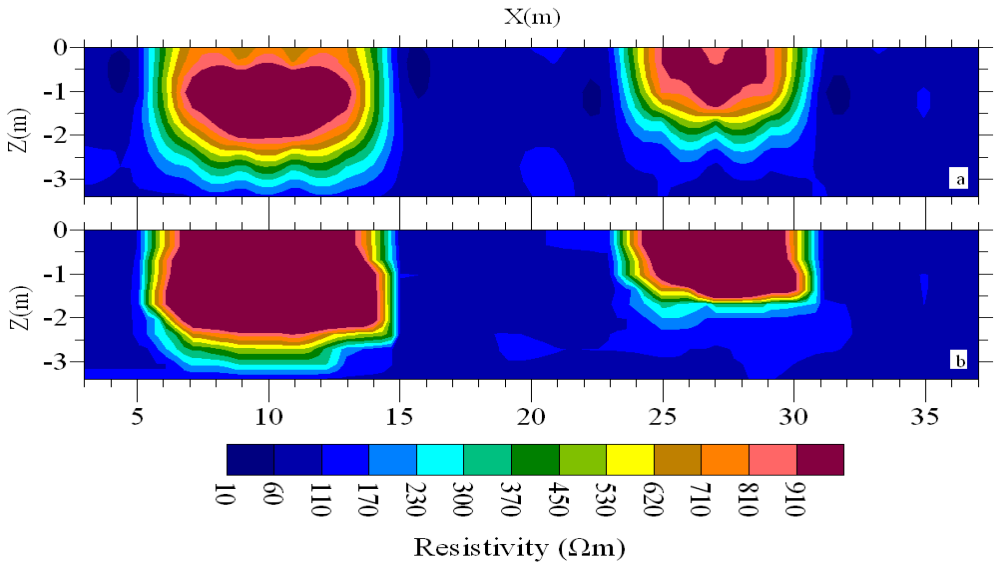

Figure 6. 24. Cross-sections of the inverted results related to the synthetic example model for the DD array: (a) result of the RIT and (b) result of the ANN.

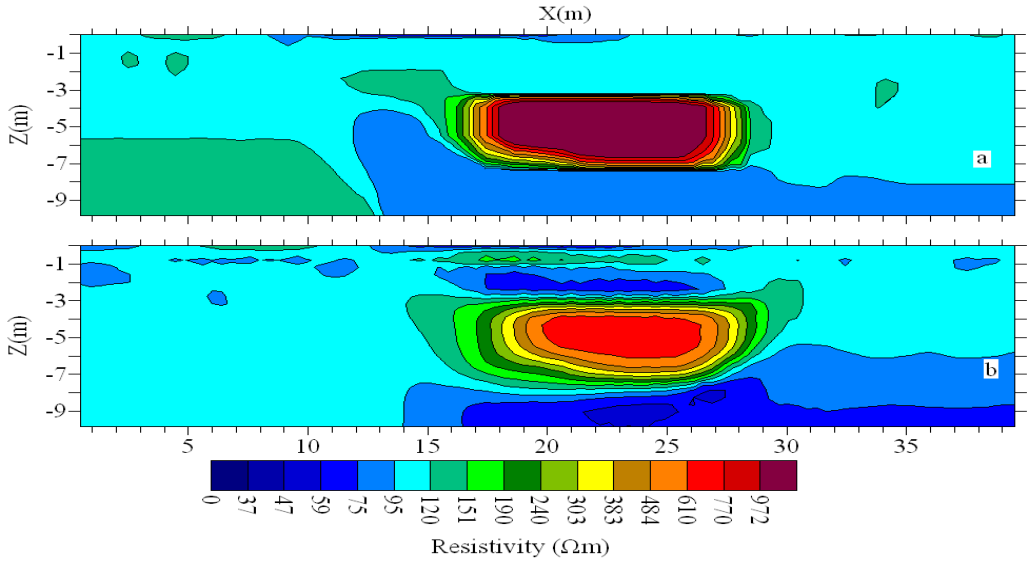

Figure 6. 25. Cross-sections of the inverted results related to the synthetic example model for the PD array: (a) result of the ANN and (b) result of the RIT.

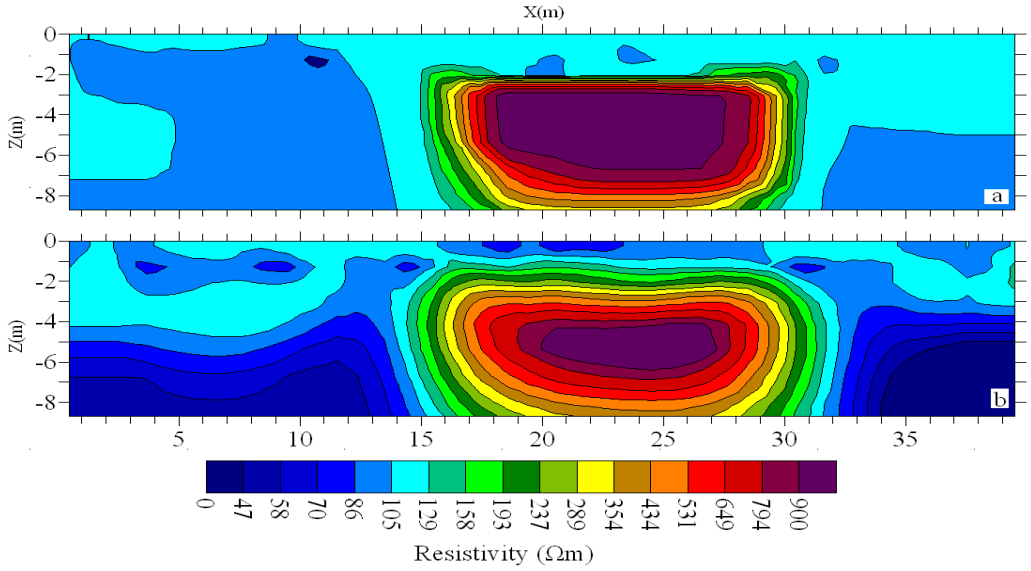

Figure 6. 26. Cross-sections of the inverted results related to the synthetic example model for the PP array: (a) result of the ANN and (b) result of the RIT.

6.3. Inversion of 3D DC resistivity imaging data using the ANN and RIT

The results of the 3D study shown in chapter 5 (section 5.2.2.2) suggest that the simplest architecture for the ANN that can reach the desired threshold error for the PP, PD, DD, WS and W arrays are (4-84-24-1), (4-35-25-1), (4-35-25-1), (4-45-60-1) and (4-30-50-1), respectively. In this section, a trained ANN is applied to a real 3D field dataset for each array. The investigation site and the corresponding grids used in the 3D surveys of this study are shown in Figures 6.27 and 6.28 for the PP and PD arrays, respectively, and in Figure 6.29 for the DD, WS and W arrays.

Figure 6. 27. Location of the square grid in the 3D survey using the PP array. G1, G2, G3 and G4 are the corners of the grid.

Figure 6. 28. Location of the square grid in the 3D survey using the PD array. K1, K2, K3 and K4 are the corners of the grid.

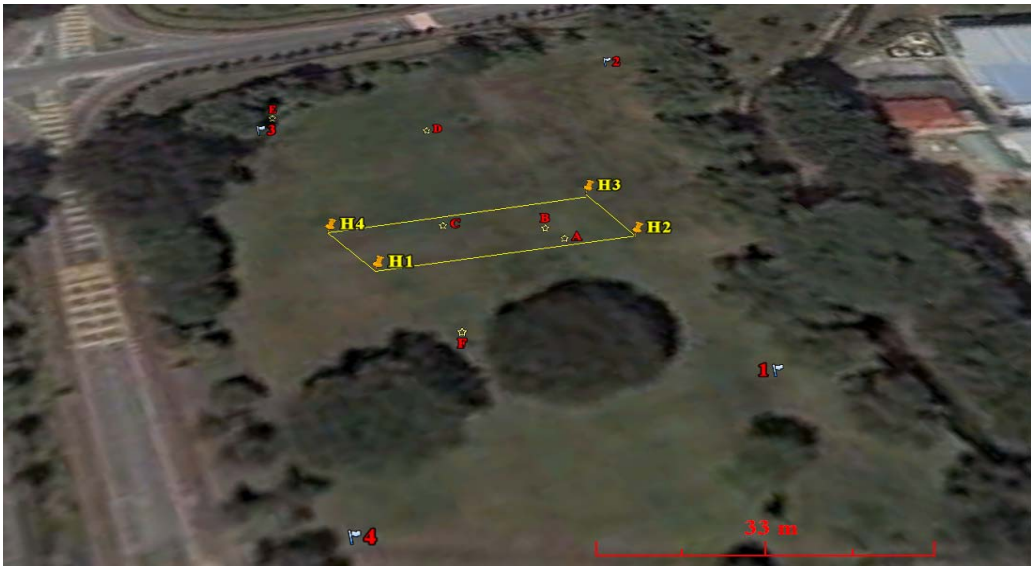

Figure 6. 29. Location of the square grid in the 3D survey using the DD, WS and W arrays. H1, H2, H3 and H4 are the corners of the grid.

The 3D field data were acquired in a square grid (8×8) for the PP array and in a rectangular grid (41×8) for the PD array. A rectangular grid (21×7) is also used for the DD, WS and W arrays. The schematic cable layout for each array is shown in Figures 6.30 to 6.32.

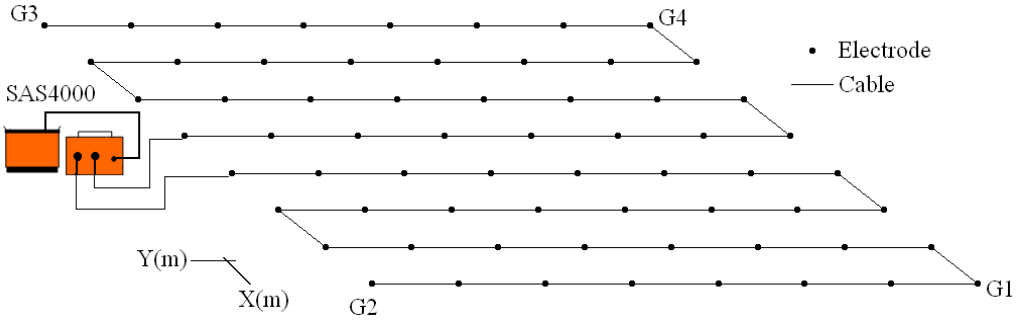

Figure 6. 30. Alignment of the 3D resistivity imaging grid used in the survey with the PP array.

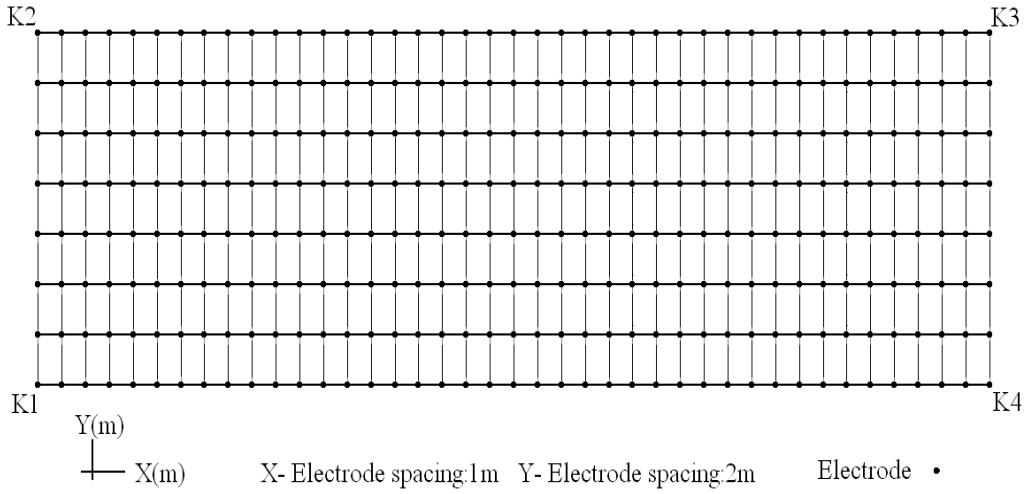

Figure 6. 31. Alignment of the 3D resistivity imaging grid used in the survey with the PD array.

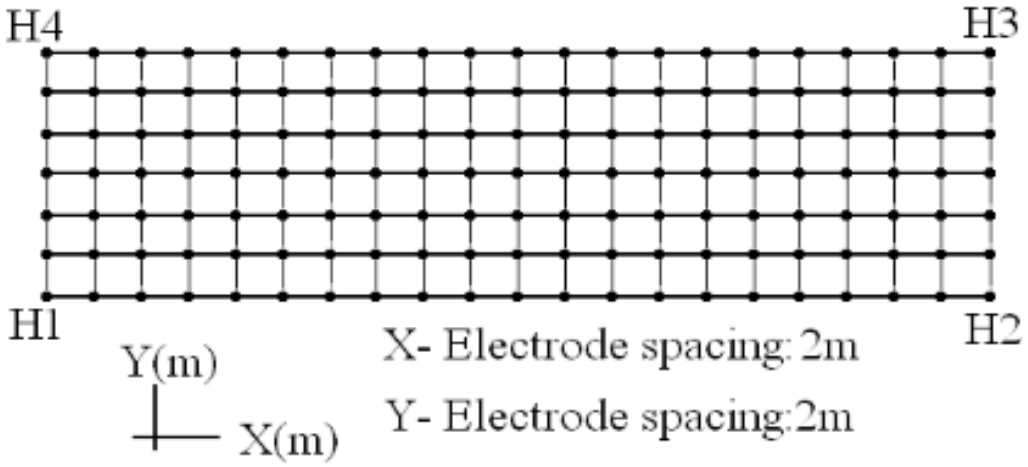

Figure 6. 32. Alignment of the 3D resistivity imaging grid used in the survey with the DD, WS and W arrays.

The latitude and longitude of the grid corners are summarized in Table 6.5. The remote electrodes (C2 and P2) in the 3D survey with the PP array and the remote electrode (C2) in the 3D survey with the PD array were located more than 800 m from the instruments.

The field datasets were inherently noisier than the synthetic data. Figures 6.33 to 6.37 show the horizontal depth slices of the apparent resistivity collected from the 3D surveys of each array.

The numbers of measured data points in the 3D surveys with the PP, PD, DD, Ws and W arrays were 728, 1522, 1043 and 499, respectively. The input data for the ANN consist of the x-, y-, and z-location and the apparent resistivity for all data points of the field data. The set of these data was used as input for the ANN inversion. The output data as a result of the inversion are a set of true resistivity values of all points for which their locations have already been used in the input data for each array.

Table 6. 5. Latitude and longitude of the grid corners used in the 3D surveys.

Array		latitude	longitude
PP	G1	3^{0} - 07´- 11.32˝ - N	101^{0} - 39´-18.96˝ - E
	G2	3^{0} - 07´- 10.87˝ - N	101^{0} - 39´-19.01˝ - E
	G3	3^{0} - 07´- 10.79˝ - N	101^{0} - 39´-18.56˝ - E
	G4	3^{0} - 07´- 11.27˝ - N	101^{0} - 39´-18.50˝ - E
PD	K1	3^{0} - 07´- 11.31˝ - N	101^{0} - 39´-18.20˝ - E
	K2	3^{0} - 07´- 10.84˝ - N	101^{0} - 39´-18.26˝ - E
	K3	3^{0} - 07´- 10.69˝ - N	101^{0} - 39´-16.98˝ - E
	K4	3^{0} - 07´- 11.13˝ - N	101^{0} - 39´-16.92˝ - E
DD, WS and W	H1	3^{0} - 07´- 10.24˝ - N	101^{0} - 39´-18.73˝ - E
	H2	^{0} - 07´- 11.49˝ - N	101^{0} - 39´-18.95˝ - E
	H3	3^{0} - 07´- 11.47˝ - N	101^{0} - 39´-18.50˝ - E
	H4	3^{0} - 07´- 10.16˝ - N	101^{0} - 39´-18.35˝ - E

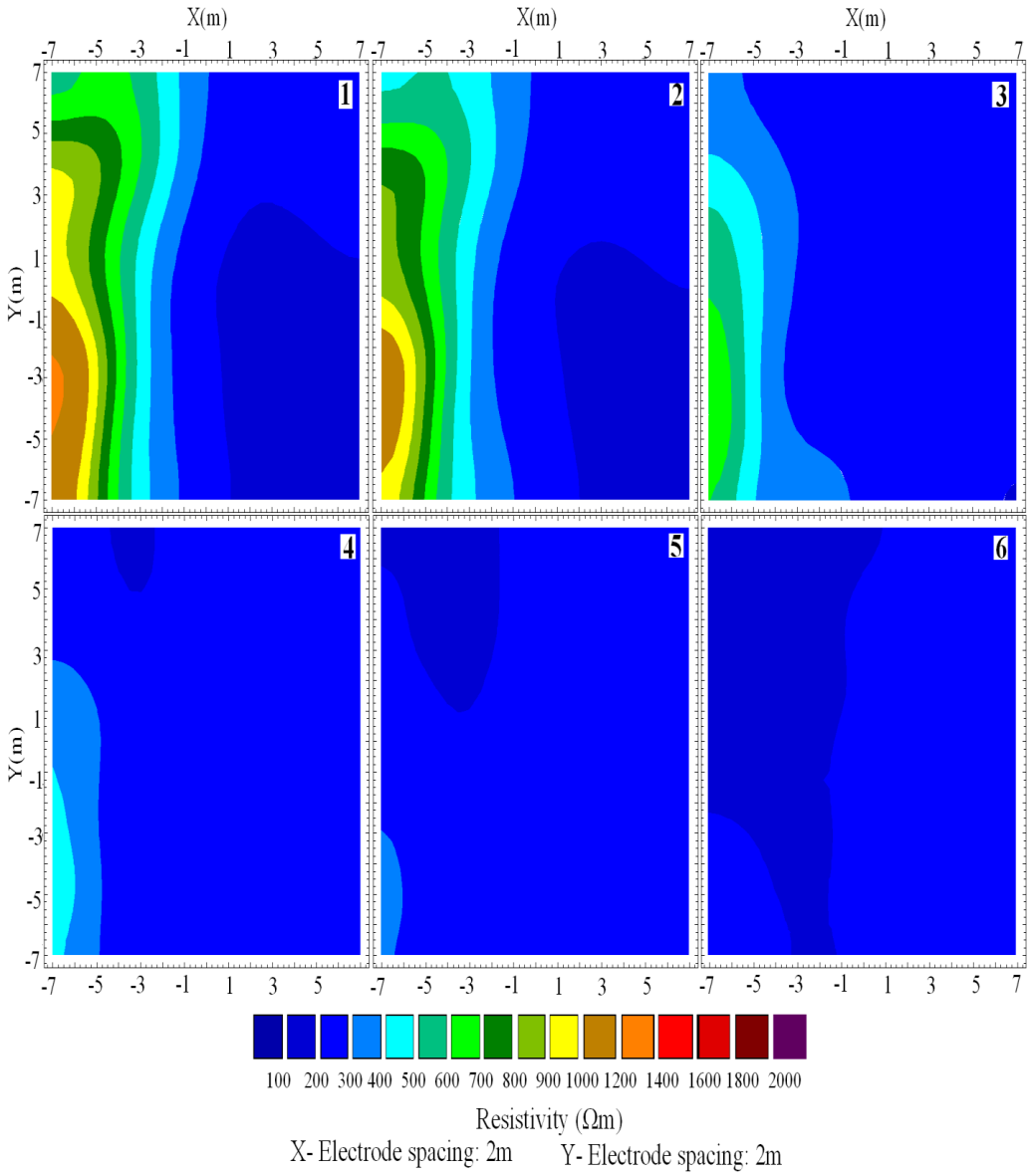

Figure 6. 33. Horizontal depth slices of apparent resistivities collected from the 3D survey with the PP array. The depths (m) for the different layers are: layer (1): 0.0 - 1.5, (2): 1.5 - 3.0, (3): 3.0 – 5.0, (4): 5.0 – 7.0, (5): 7.0 – 9.0, and (6): 9.0 – 12.0.

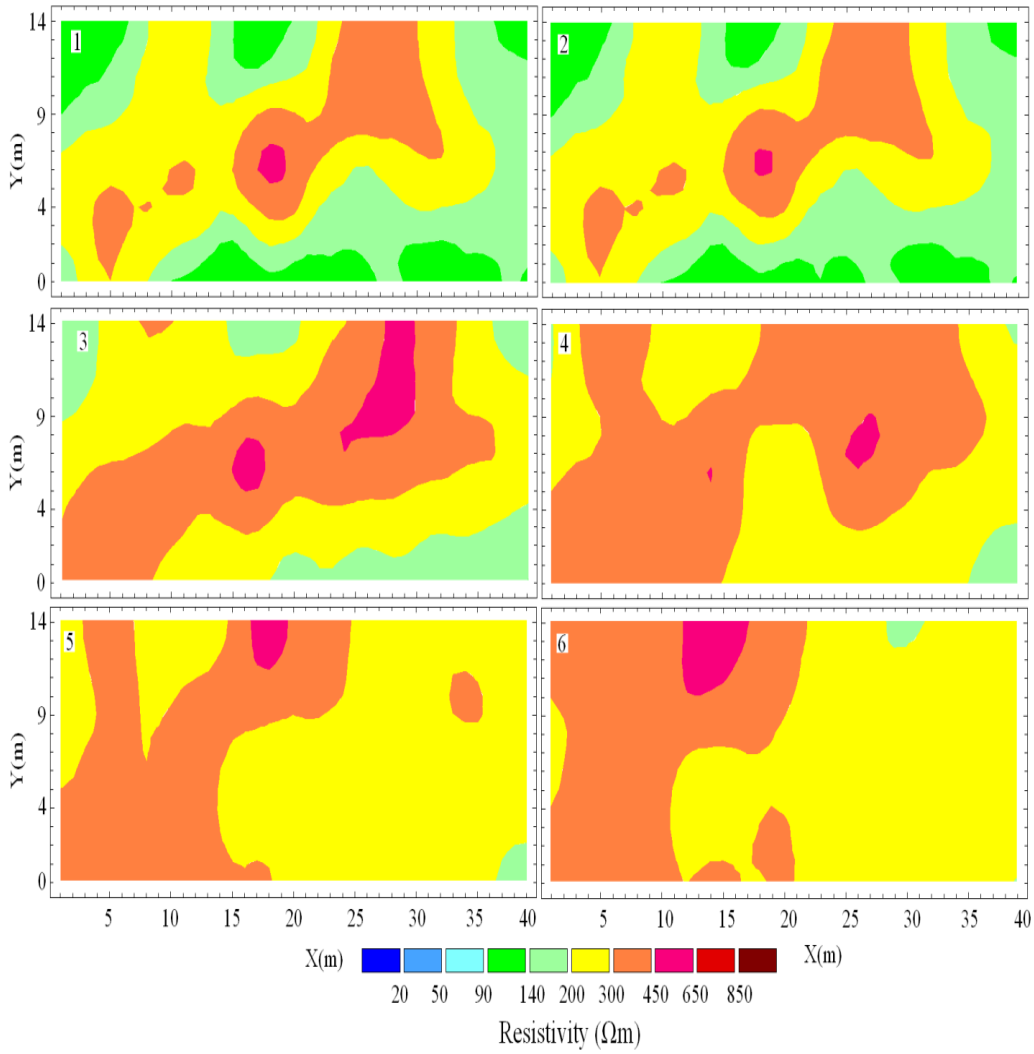

Figure 6. 34. Horizontal depth slices of apparent resistivities collected from the 3D survey with the PD array. The depths (m) for the different layers are: layer (1): 0.0 – 0.5, (2): 0.5 – 1.5, (3): 1.5 – 3.0, (4): 3.0 – 5.0, (5): 5.0 – 7.0, and (6): 7.0 – 10.0.

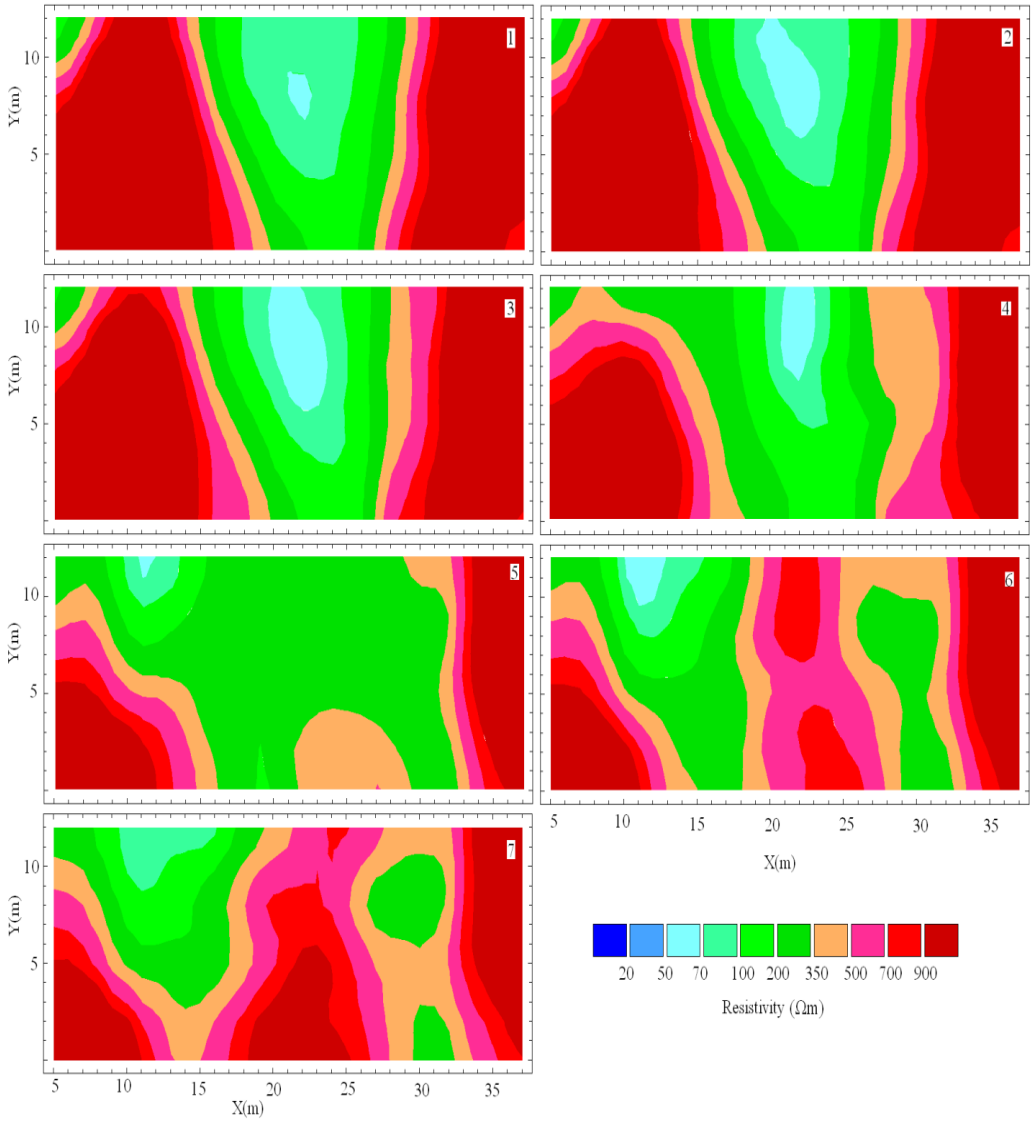

Figure 6. 35. Horizontal depth slices of apparent resistivities collected from the 3D survey with the DD array. The depths (m) for the different layers are: layer (1): 0.0 – 0.5, (2): 0.5 – 1.0, (3): 1.0 – 1.5, (4): 1.5 – 2.5, (5): 2.5 – 3.8, (6): 3.8 – 5.3, and (7): 5.3 – 7.0.

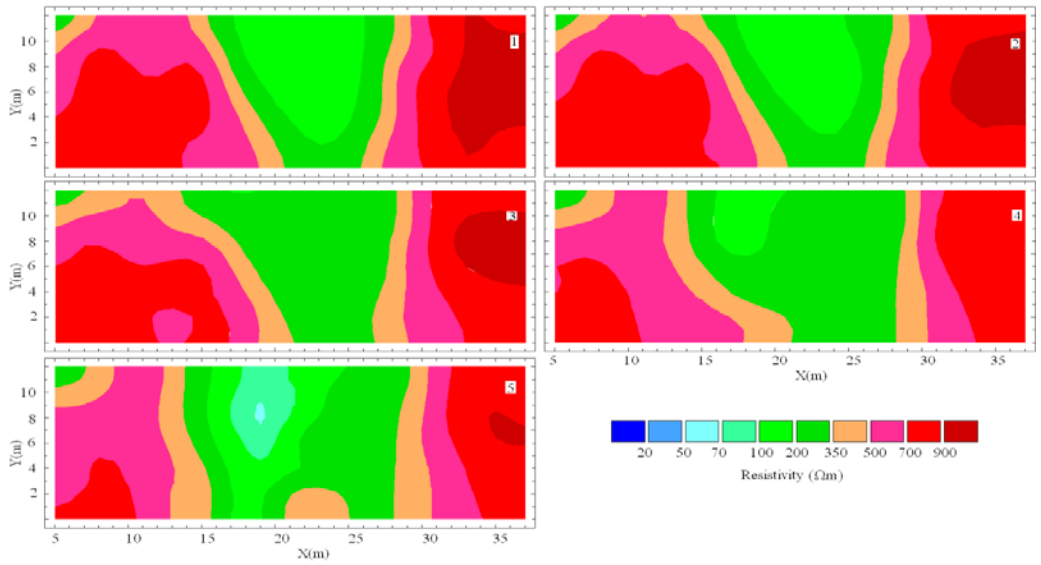

Figure 6. 36. Horizontal depth slices of the apparent resistivities collected from the 3D survey using the WS array. The depths (m) for the different layers are: layer (1): 0.0 – 0.5, (2): 0.5 – 1.5, (3): 1.5 – 3.0, (4): 3.0 – 5.0, and (5): 5.0 – 7.0.

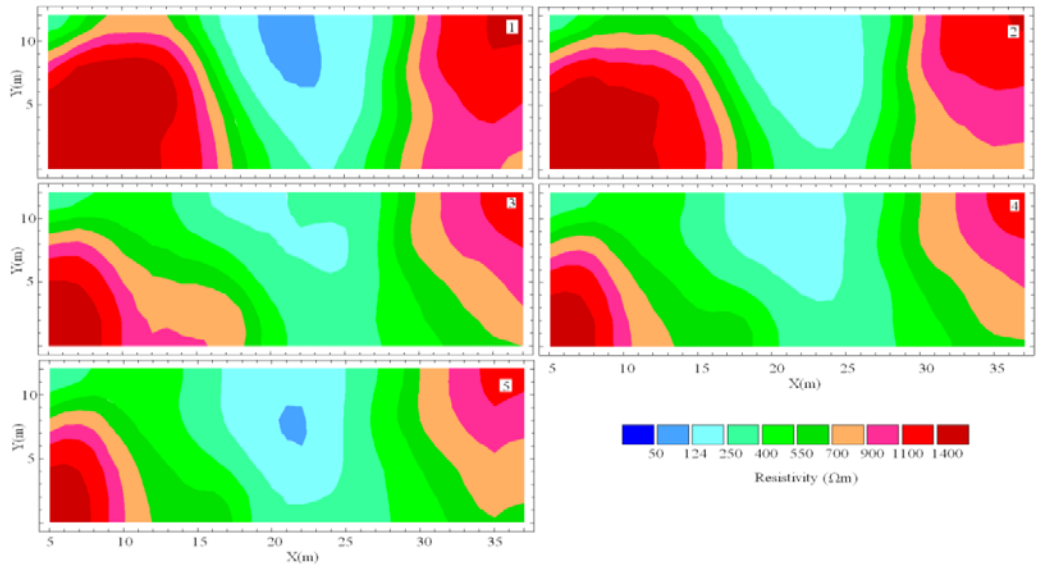

Figure 6. 37. Horizontal depth slices of the apparent resistivities collected from the 3D survey using the W array. The depths (m) for the different layers are: layer (1): 0.0 – 0.8, (2): 0.8 – 1.6, (3): 1.6 – 3.2, (4): 3.2 – 5.0, and (5): 5.0 – 7.0.

3D depth slices were constructed using the results of the ANN (Figs. 6.38 to 6.42). The RMS misfit was calculated between the forward modeling results of the constructed model and the field data (Table 6.5). According to Table 6.6, the RMS error for the ANN results is less than that of the RIT.

According to Figure 6.38, the horizontal part of the wastewater system that connects columns B and D (Fig. 6.27) is detected at a depth of up to 7 meters. The connection between the vertical columns B and F is denoted with the capital letter *L* (Fig. 6.38, layers 4 and 5). This connection continues from a depth of 5 to 10 m. High resistivities (greater than 300 Ωm) are not observed below 10 m. The inversion results of the ANN are in accordance with the findings obtained from the investigation area and sufficient agreement was found.

Table 6. 6. RMS error in the results of the ANN and RIT for 3D field data.

Array	RMS error (%) for the result of the ANN	RMS error (%) for the result of the RIT
PP	0.60	3.42
PD	2.40	4.95
DD	6.22	10.35
WS	2.58	3.07
W	3.80	4.21

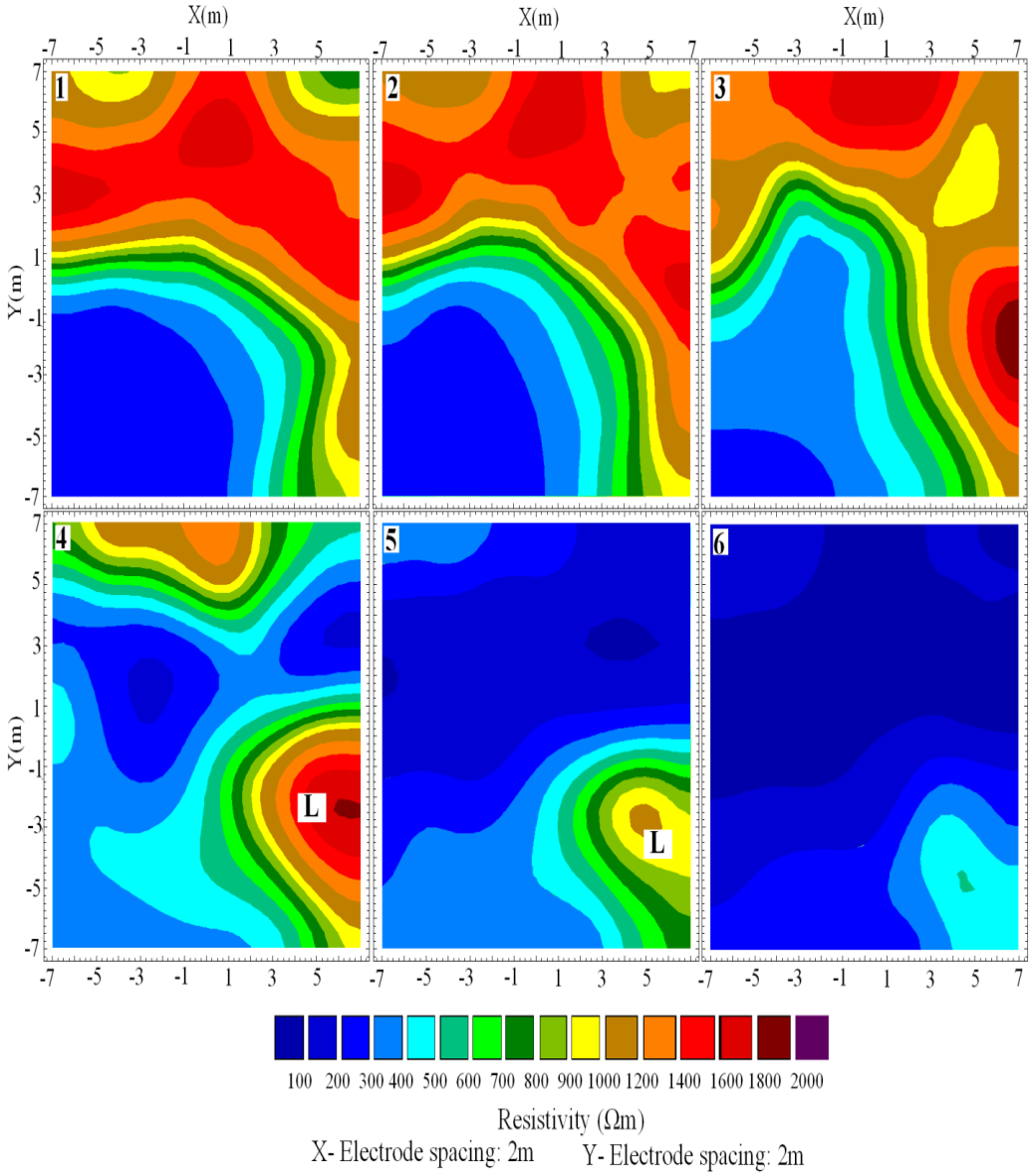

Figure 6. 38. 3D depth slices constructed using the results of the ANN for inverting the PP data. The connection between columns B and F is denoted by (L) and shown in layers 4-5. The depths (m) for the different layers are: layer (1): 0.0 - 1.5, (2): 1.5 - 3.0, (3): 3.0 – 5.0, (4): 5.0 – 7.0, (5): 7.0 – 9.0, and (6): 9.0 – 12.0.

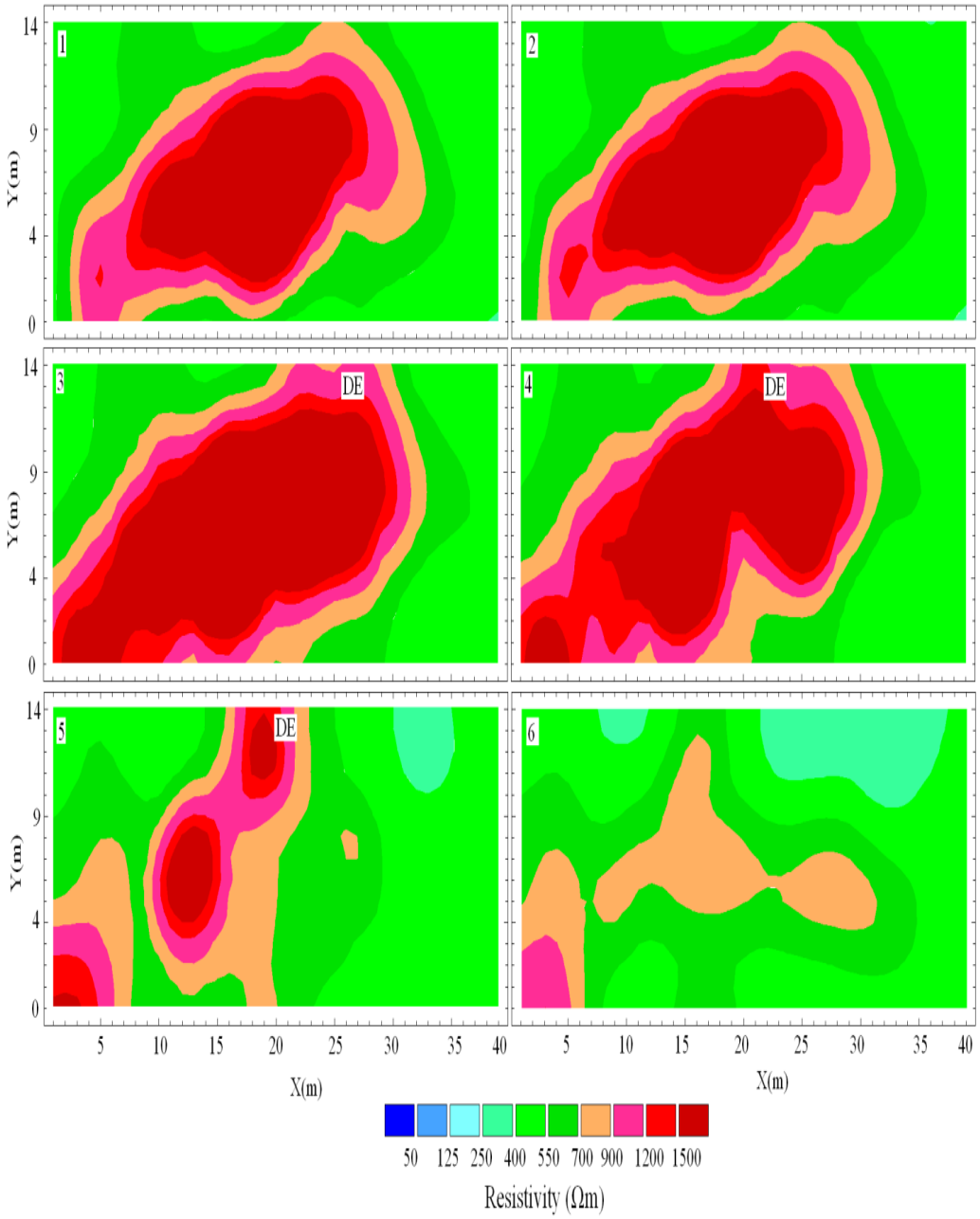

Figure 6. 39. 3D depth slices constructed using the results of the ANN for inverting the PD data. The connection between columns D and E is denoted by (DE) and is shown in layers 3-5. The depths (m) for the different layers are: layer (1): 0.0 – 0.5, (2): 0.5 – 1.5, (3): 1.5 – 3.0, (4): 3.0 – 5.0, (5): 5.0 – 7.0, and (6): 7.0 – 10.0.

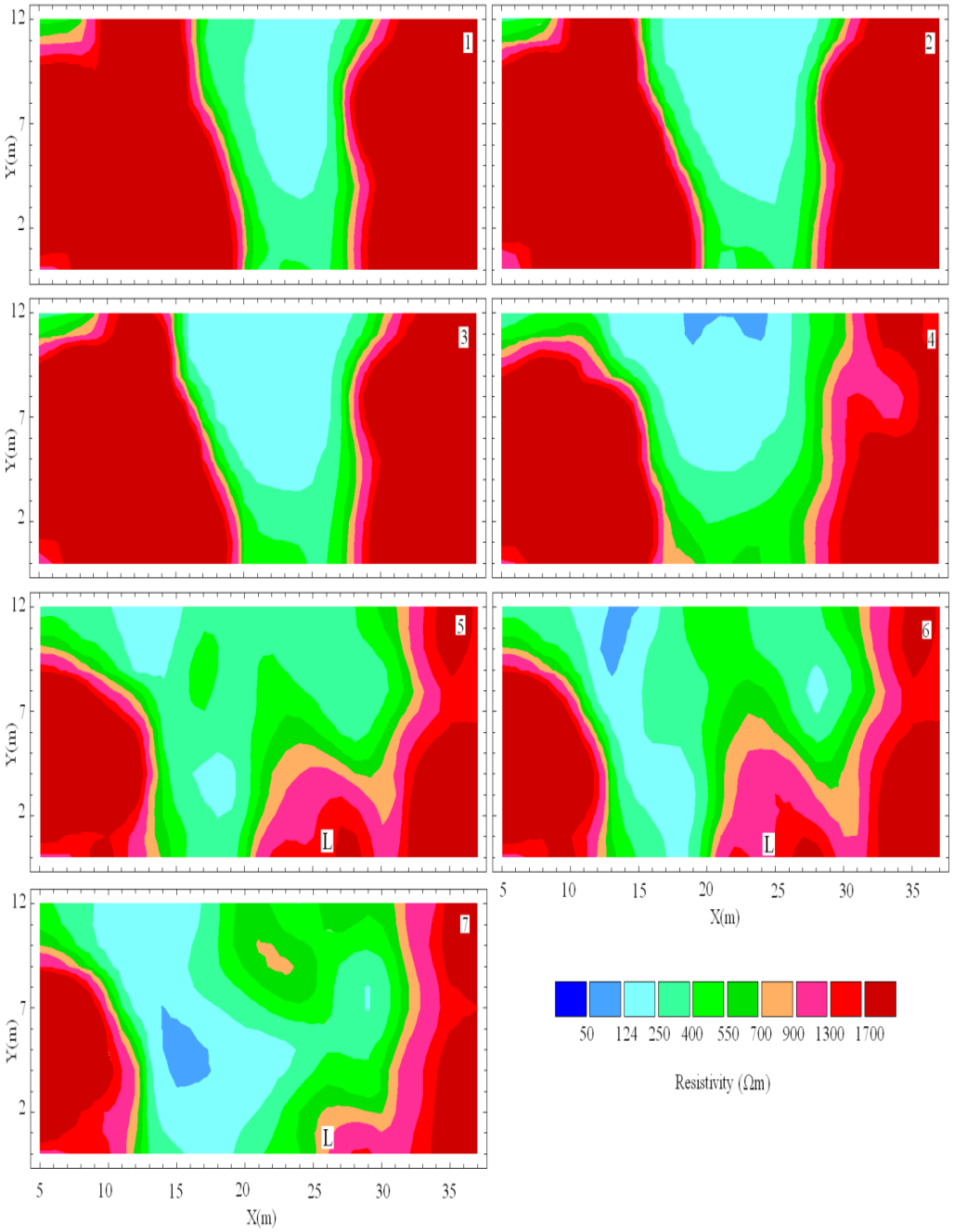

Figure 6. 40. 3D depth slices constructed using the results of the ANN for inverting the DD data. The connection between columns B and F is denoted by (L) and is shown in layers 5-7. The depths (m) for the different layers are: layer (1): 0.0 – 0.5, (2): 0.5 – 1.0, (3): 1.0 – 1.5, (4): 1.5 – 2.5, (5): 2.5 – 3.8, (6): 3.8 – 5.3, and (7): 5.3 – 7.0.

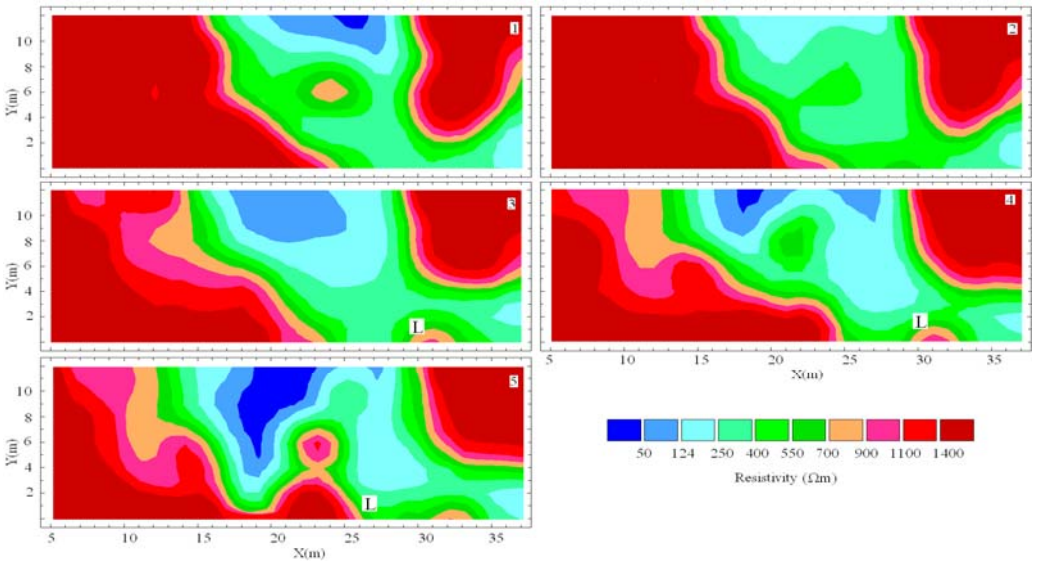

Figure 6. 41. 3D depth slices constructed using the results of the ANN for inverting the WS data. The connection between columns B and F is denoted by (L) and is shown in layers 3-5. The depths (m) for the different layers are: layer (1): 0.0 – 0.5, (2): 0.5 – 1.5, (3): 1.5 – 3.0, (4): 3.0 – 5.0, and (5): 5.0 – 7.0.

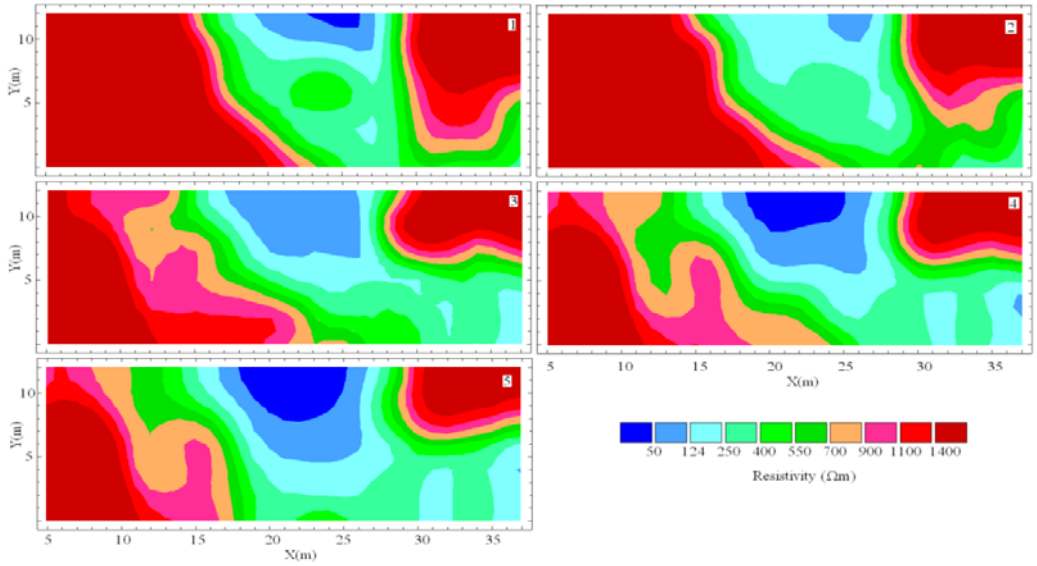

Figure 6. 42. 3D depth slices constructed using the results of the ANN for inverting the W data. The depths (m) for the different layers are: layer (1): 0.0 – 0.8, (2): 0.8 – 1.6, (3): 1.6 – 3.2, (4): 3.2 – 5.0, and (5): 5.0 – 7.0.

According to Figure 6.39, the horizontal pipe that connects columns D and B (Fig. 6.28) is detected at a depth of up to 7 meters. The connection between vertical columns D and E is denoted with the capital letters *DE* (Fig. 6.39 layers 3, 4 and 5). High resistivities (greater than 900 Ωm) are not observed at depths greater than 7 m, except for the small zone located at the left side of layer 6.

In Figures 6.40 and 6.41, the horizontal pipe that connects columns D and B (Fig. 6.29) is detected at depths of up to 7 meters. The connection between vertical columns B and F is denoted with the capital letters L (Fig. 6.40 layers 5, 6 and 7 and Fig. 6.41 layers 3, 4 and 5). High resistivities (greater than 700 Ωm) are not observed in the middle of the investigation area.

With respect to the results of the inversion of the W data (Fig. 6.42), similar to those of the DD and WS data, the horizontal pipe that connects columns D and B (Fig. 6.29) is also observed at depths of up to 7 meters. The connection between vertical columns B and F was not detected clearly in the ANN results. This might be due to insufficient horizontal data coverage and the horizontal resolution of the W array compared to the DD and WS arrays. However, we will show that the connection L is resolved in the synthetic test using the ANN (next section). Note that the field data contain more noise than the synthetic data.

In order to display the three-dimensional extent of high resistivity zones, an isoresistivity surface was also produced from the results of the ANN for each array, which corresponds to resistivities higher than 1500 Ωm for the PP data and 1300 Ωm for the PD, DD, WS and W data. The isoresistivity surface is derived from the data volume by specifying an isovalue that forms an isosurface. The isosurface connects data points of equal resistivity values, yielding the three- dimensional anomaly representation (Figs.6.43 to 6.47).

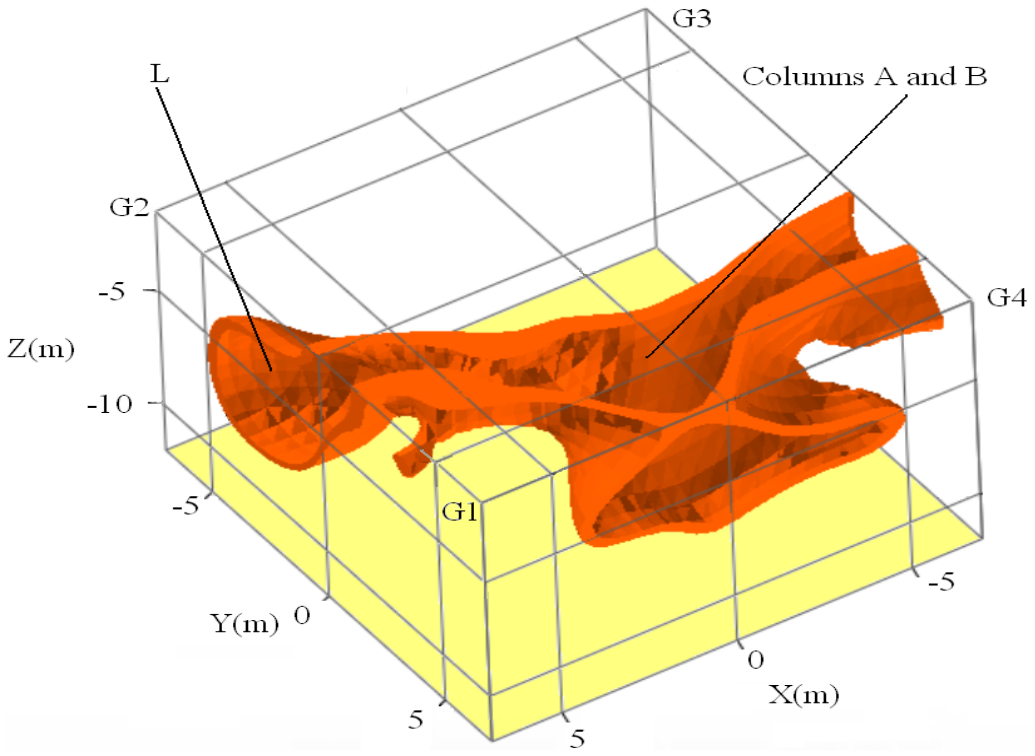

Figure 6. 43. Isoresistivity surface of the resistivity values higher than 1500Ωm (the resistivity of concrete) using the ANN results for the PP-data. The connection between columns B and F was denoted by (L).

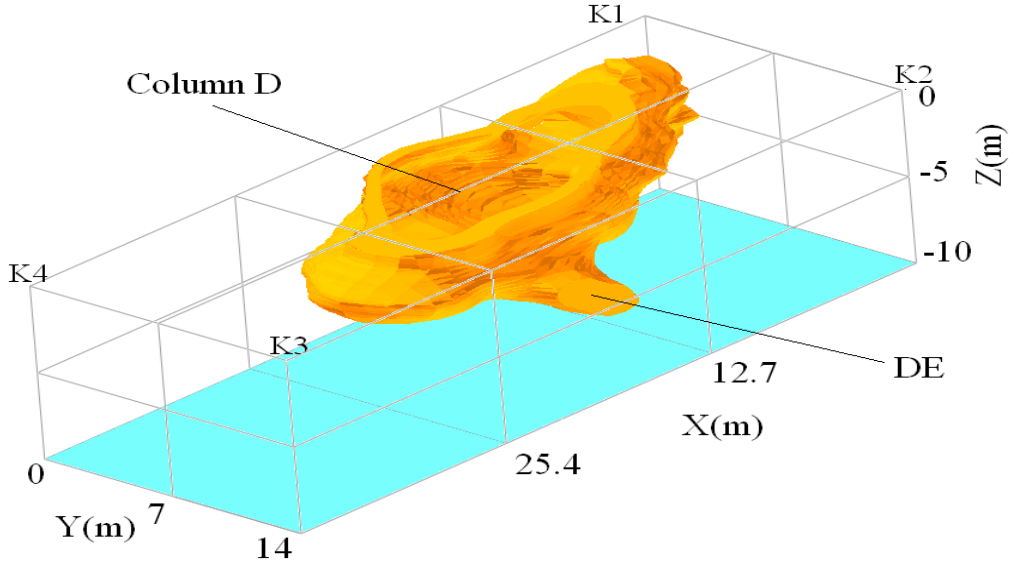

Figure 6. 44. Isoresistivity surface of the resistivity values higher than 1300Ωm using the ANN results for the PD-data. The connection between columns D and E was denoted by (DE).

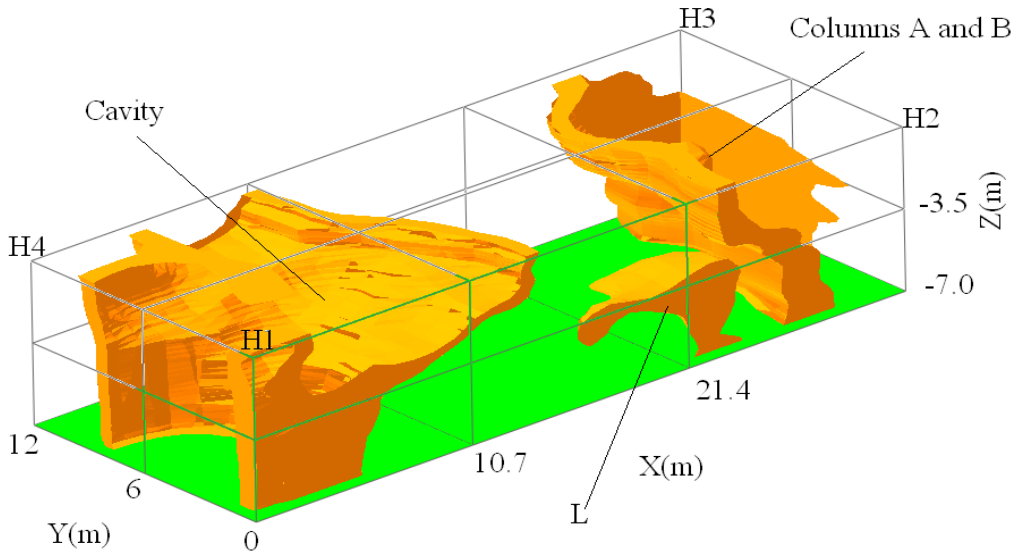

Figure 6. 45. Isoresistivity surface of the resistivity values higher than 1300Ωm using the ANN results for the DD-data. The connection between columns B and Fwas denoted by (L).

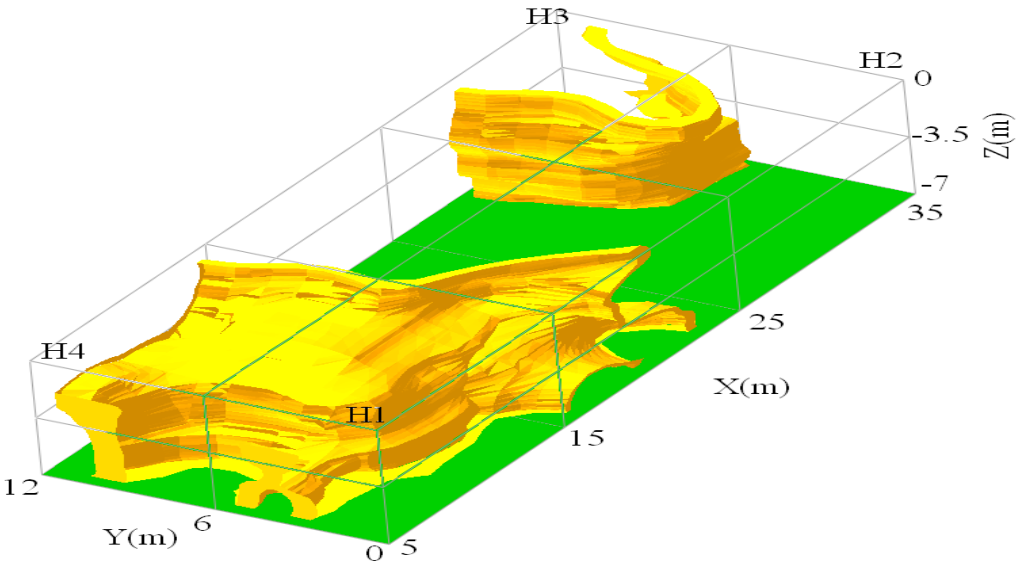

Figure 6. 46. Isoresistivity surface of the resistivity values higher than 1400Ωm using the ANN results for the WS-data.

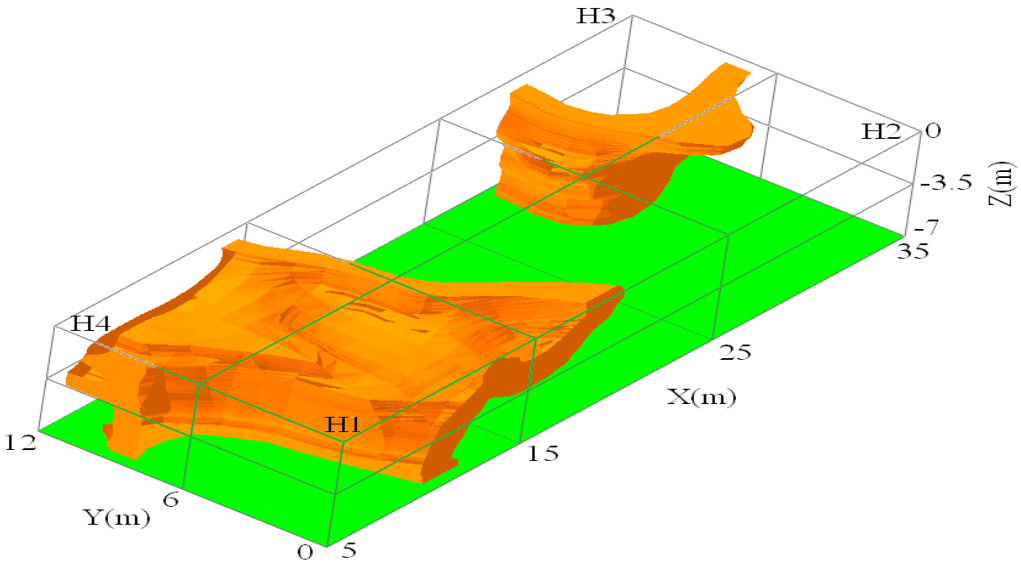

Figure 6. 47. Isoresistivity surface of the resistivity values higher than 1300Ωm using the ANN results for the W-data.

According to the Figure 6.43, the location of the vertical columns (A and B) and the horizontal part of wastewater system in the north are detected clearly. Although the connection (L) between columns B and F is observed in the Figures 6.43 and 6.45 but the same has not been detected it in Figure 6.46 and 6.47, which are related to the results of the WS and W-data. In addition, the resistive zone related to the horizontal pipe (between columns D and B) is also detected approximately at the right place but some parts of this pipe which is near the H2 corner is not accurately detected. This lake of resolution might be due to poor data coverage of the WS and W array near the corners of the grids in the 3D surveys. However, in Figures 6.46 and 6.47, the resistive zone at the left side of the grid (near corners H1 and H4) can be seen clearly. Using the isoresistivity surface produced using the results of the PD data (Fig. 6.44), it can be seen that the locations of the vertical columns (D), the horizontal part of pipe system and the connection (DE) between columns D and E are clearly detected.

To compare the inverted results of the ANN with the conventional RIT, the Res3Dinv software (Loke, 2007) was used to invert the same real field data for each array. In this

connection the RMS errors for each dataset are summarized in Table 6.5. The calculated apparent resistivity data for the PP, PD, DD, WS and W arrays are presented in Figures 6.48 to 6.52 as horizontal depth slices.

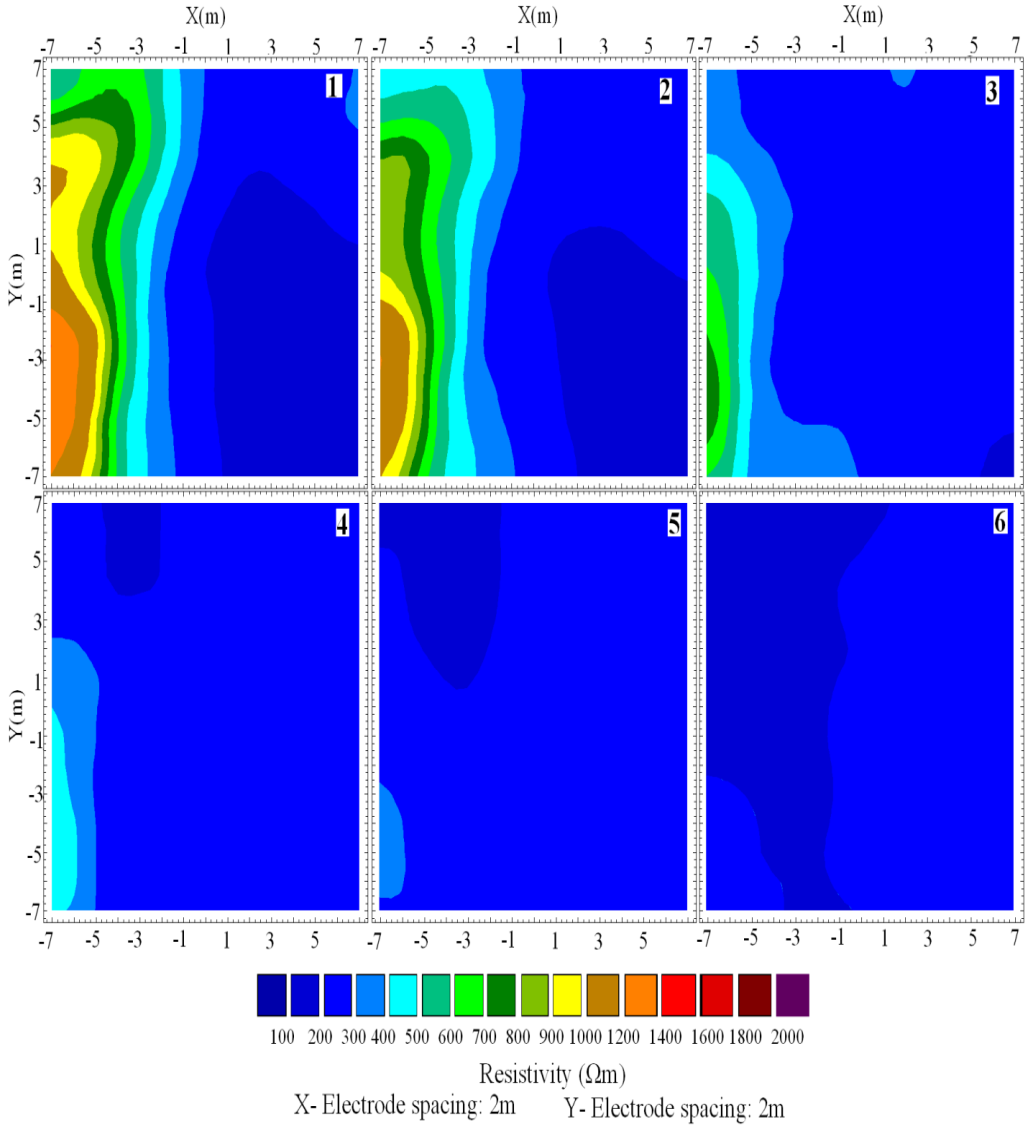

Figure 6. 48. Horizontal depth slices extracted using the calculated apparent resistivities for the PP data. The depths (m) for different layers are: layer (1): 0.0 - 1.5, (2): 1.5 - 3.0, (3): 3.0 – 5.0, (4): 5.0 – 7.0, (5): 7.0 – 9.0, and (6): 9.0 – 12.0.

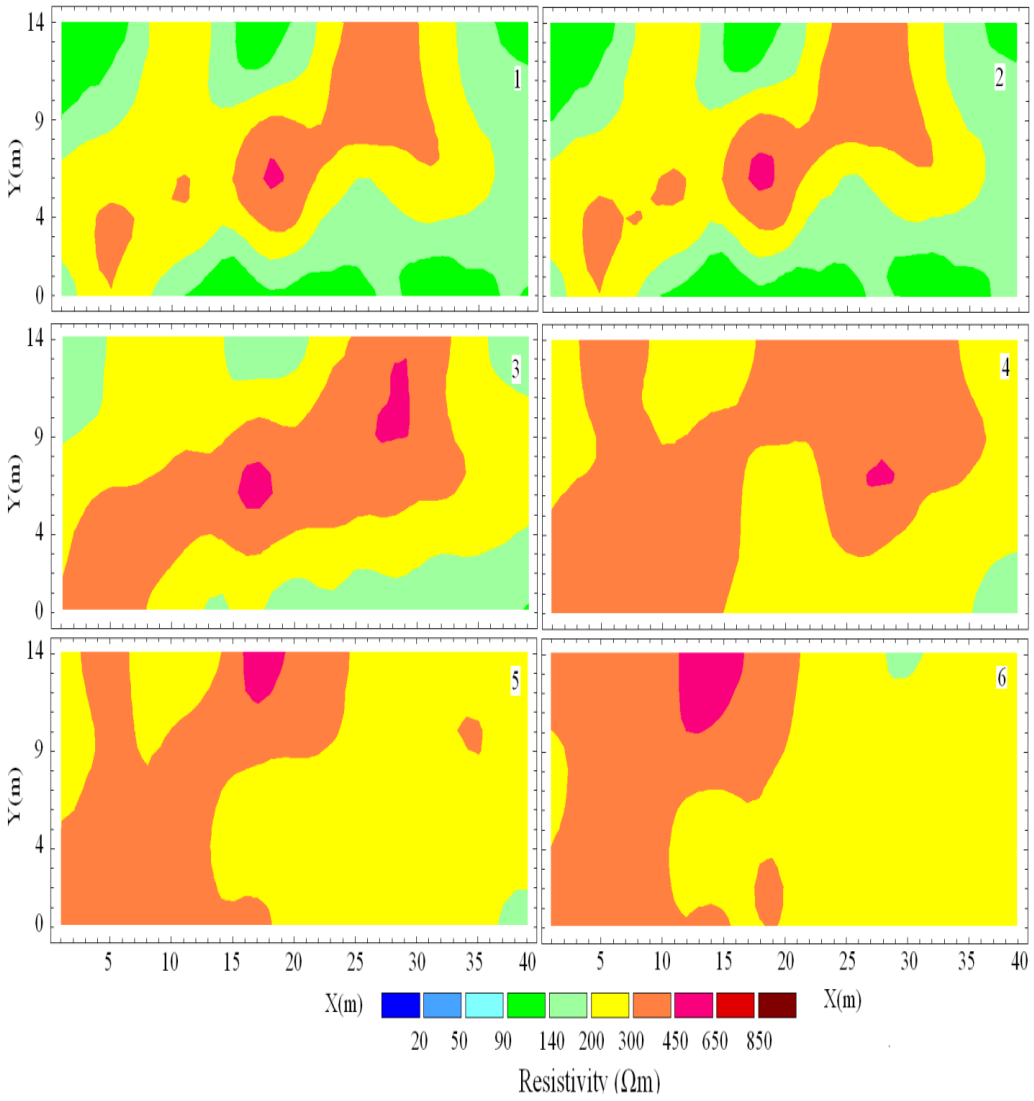

Figure 6. 49. Horizontal depth slices extracted using the calculated apparent resistivities for the PD data. The depths (m) for the different layers are: layer (1): 0.0 – 0.5, (2): 0.5 – 1.5, (3): 1.5 – 3.0, (4): 3.0 – 5.0, (5): 5.0 – 7.0, and (6): 7.0 – 10.0.

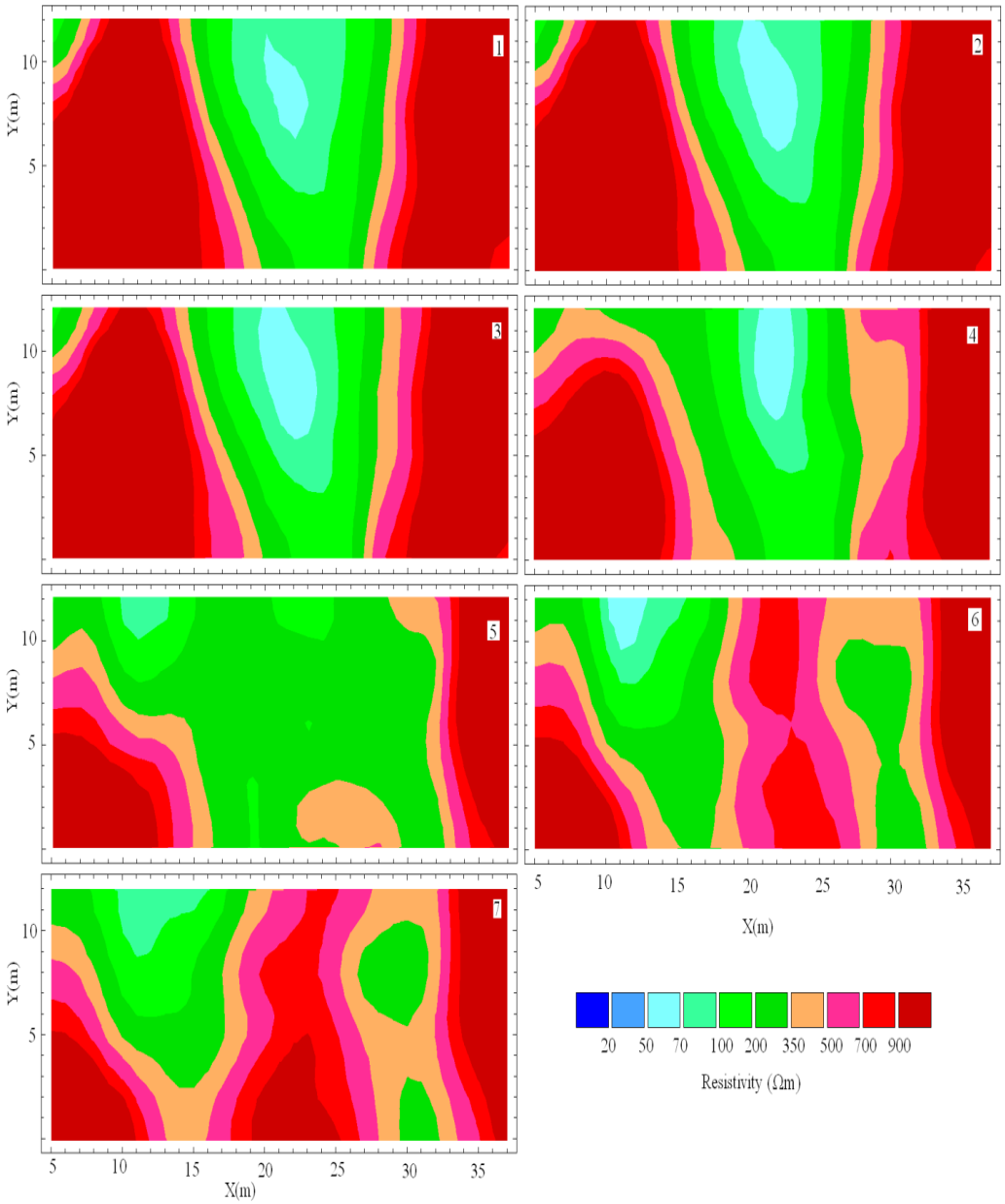

Figure 6. 50. Horizontal depth slices extracted using the calculated apparent resistivities for the DD data. The depths (m) for the different layers are: layer (1): 0.0 – 0.5, (2): 0.5 – 1.0, (3): 1.0 – 1.5, (4): 1.5 – 2.5, (5): 2.5 – 3.8, (6): 3.8 – 5.3, and (7): 5.3 – 7.0.

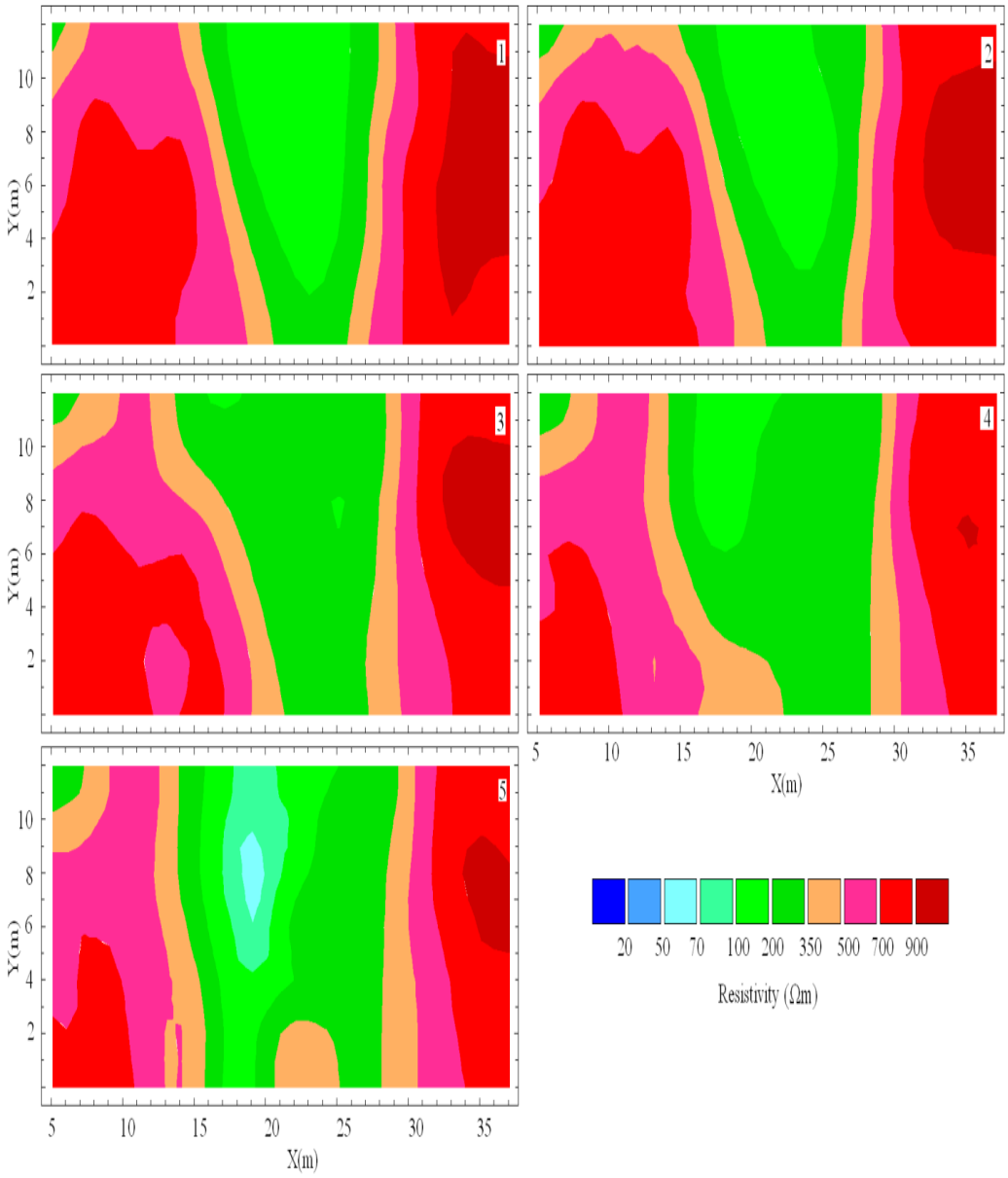

Figure 6. 51. Horizontal depth slices extracted using the calculated apparent resistivities for the WS data. The depths (m) for the different layers are: layer (1): 0.0 – 0.5, (2): 0.5 – 1.5, (3): 1.5 – 3.0, (4): 3.0 – 5.0, and (5): 5.0 – 7.0.

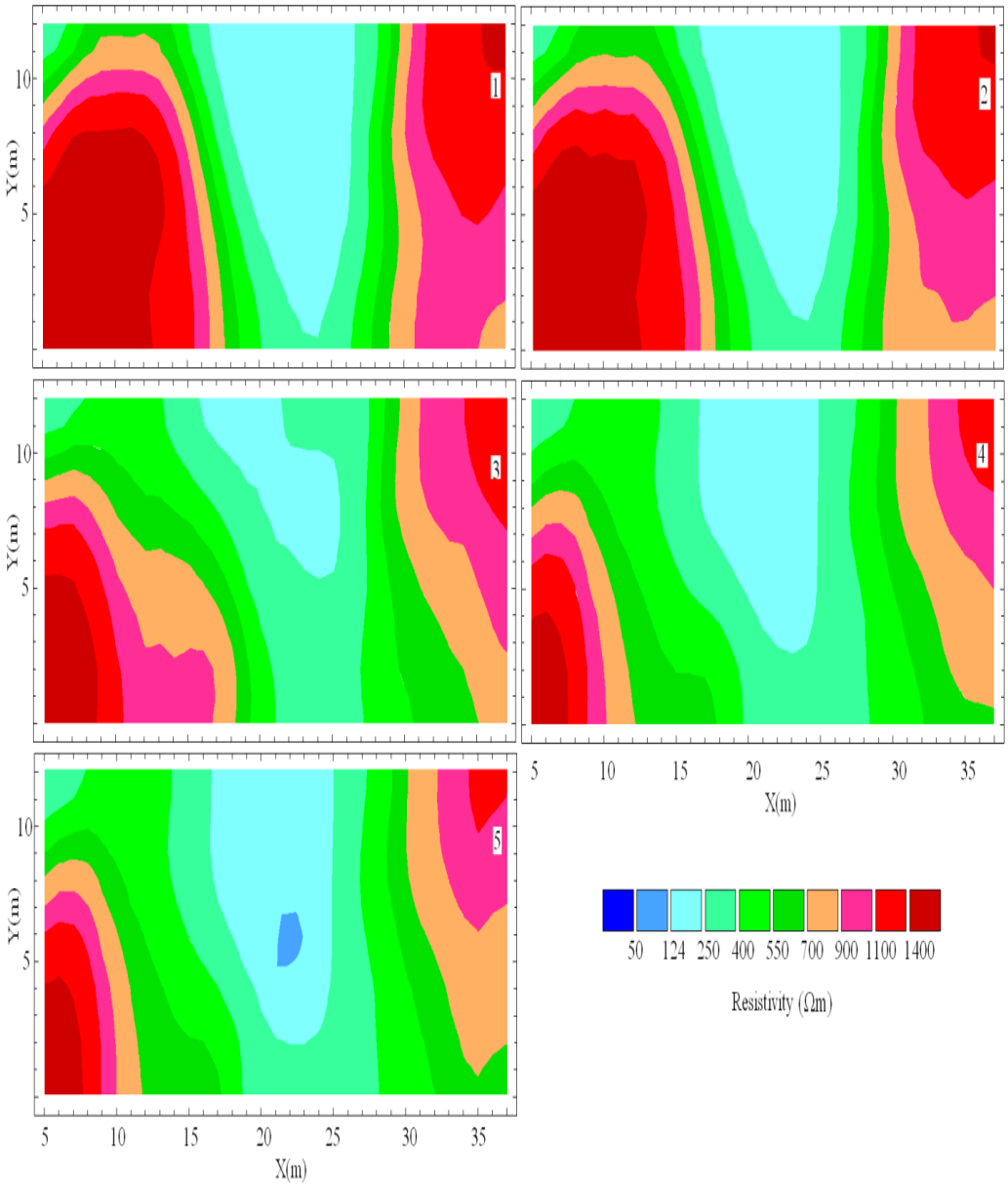

Figure 6. 52. Horizontal depth slices extracted using the calculated apparent resistivities for the W data. The depths (m) for the different layers are: layer (1): 0.0 – 0.8, (2): 0.8 – 1.6, (3): 1.6 – 3.2, (4): 3.2 – 5.0, and (5): 5.0 – 7.0.

Using the RIT result, the horizontal depth slices were also extracted, in order to display the lateral extent of the high resistivity zones for each array (Figs. 6.53 to 6.57). According to the RIT result for the PP data (as shown in Figure 6.48), the horizontal part of the wastewater system is detected at a depth of less than 7 meters, which agrees with the

ANN results. The connection between columns B and F is also shown in the RIT result (Fig. 6.53.6; layers 2, 3, and 4).

With respect to the RIT result for the PD data (Fig. 6.54), the horizontal pipe is detected at depths of up to 5 m, which is less than the depth calculated from the ANN results. The connection between columns D and E is also shown in the RIT result (Fig. 6.54; layers 2- 5). There is an unconfirmed anomalous zone in layers 2 and 3 that is not observed in the ANN results. In the RIT results, high resistivity zones (> 900 Ωm) are not observed at depths greater than 7 m.

According to the RIT result for the DD data, the horizontal pipe (between columns B and D) and its surrounding high resistivity materials located on the right side of the gird are detected at depths of up to 7 m, which agrees with the ANN results (Fig. 6.54). The results of the RIT and the ANN for the anomalous body located on the left side of the slices are the same. Since the RIT result for the real field data does not show the presence of the L connection, it can be concluded that the ANN results are more accurate than the RIT results. Similar to the ANN result, high resistivity zones (> 700 Ωm) are not observed in middle of the study area by the RIT results of the DD data.

Using the RIT result, horizontal depth slices were extracted, in order to display the lateral extent of the high resistivity zones (Fig. 6.55). According to these slices, the horizontal pipe (between columns D and B) is detected at depths of up to 5 m by the RIT result for the WS data (Fig. 6.51) and up to 7 m for the W data (Fig. 6.52). The resistive zone related to connection L is not detected by the RIT results for either the WS or W data (Figs. 6.55 and 6.57), because the RIT result for the real field data does not detect the presence of connection L (Figs. 6.55 and 6.57). The resistive zone near corners H1 and H4 are clearly detected in the RIT results, but the width of this anomaly is found to be greater than its size detected by the ANN results. In the RIT results, high resistivity zones (> 700

Ωm for the WS data and > 900 Ωm for the W data) are not observed in the middle of the study area.

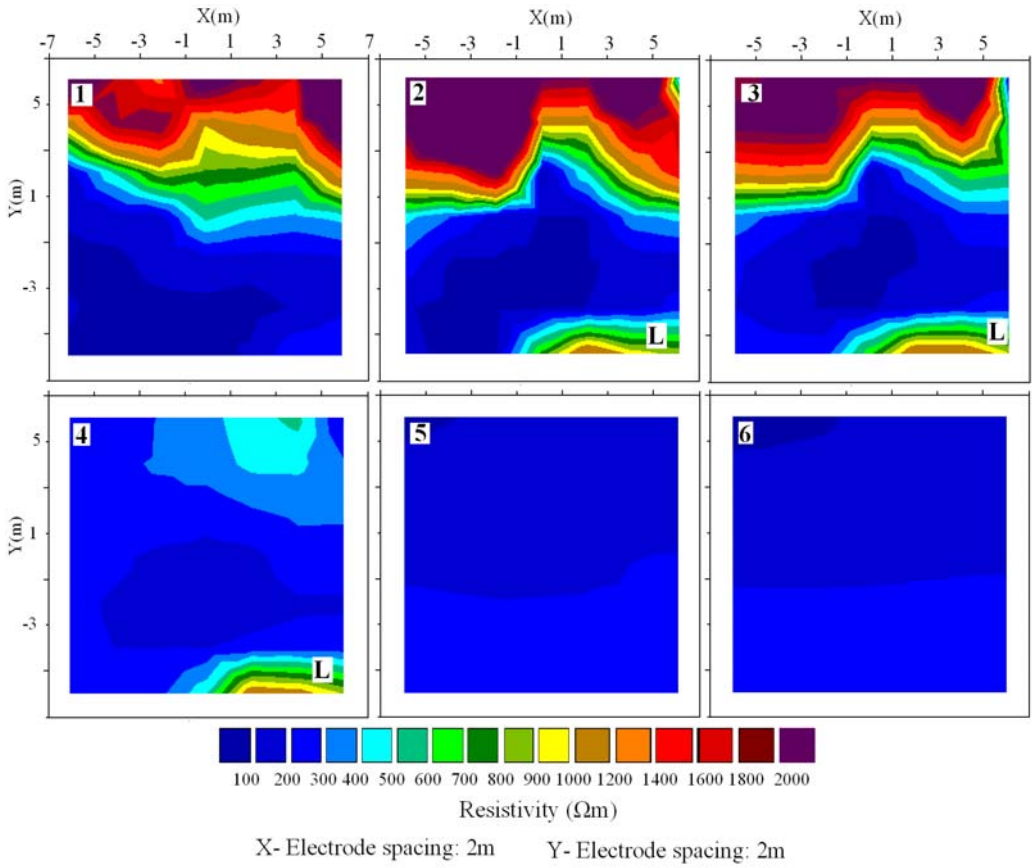

Figure 6. 53. 3D depth slices constructed using the results of the RIT for the PP data. The connection between columns B and C is denoted by (L) and is shown in layers 2-4. The depths (m) for the different layers are: layer (1): 0.0 - 1.5, (2): 1.5 - 3.0, (3): 3.0 – 5.0, (4): 5.0 – 7.0, (5): 7.0 – 9.0, and (6): 9.0 – 12.0.

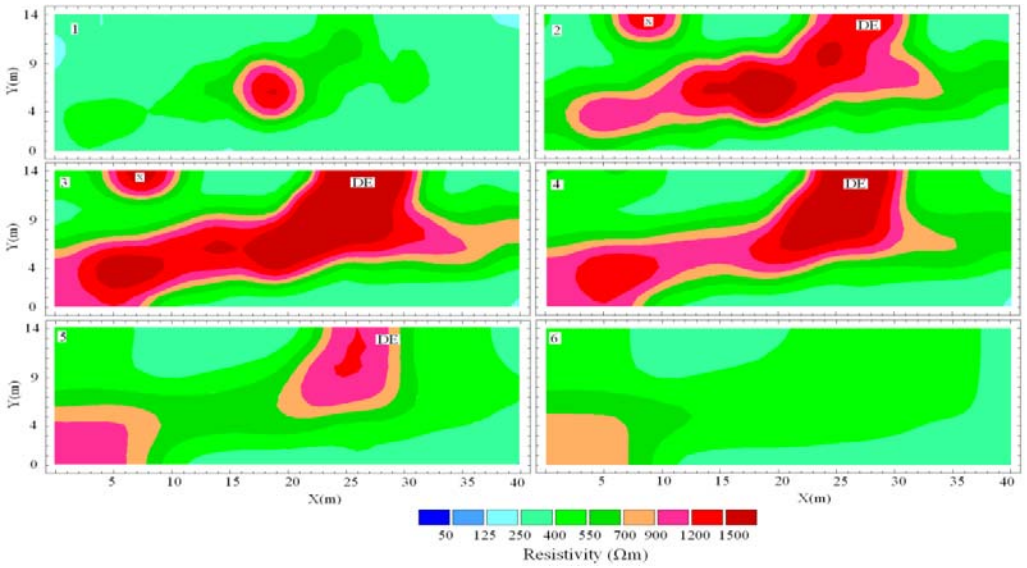

Figure 6. 54. 3D depth slices constructed using the results of the RIT for the PD data. The connection between columns D and E is denoted by (DE) and shown in layers 2-5. An unconfirmed anomaly is also denoted by the letter (x) in layers 2-3. The depths (m) for the different layers are: layer (1): 0.0 – 0.5, (2): 0.5 – 1.5, (3): 1.5 – 3.0, (4): 3.0 – 5.0, (5): 5.0 – 7.0, and (6): 7.0 – 10.0.

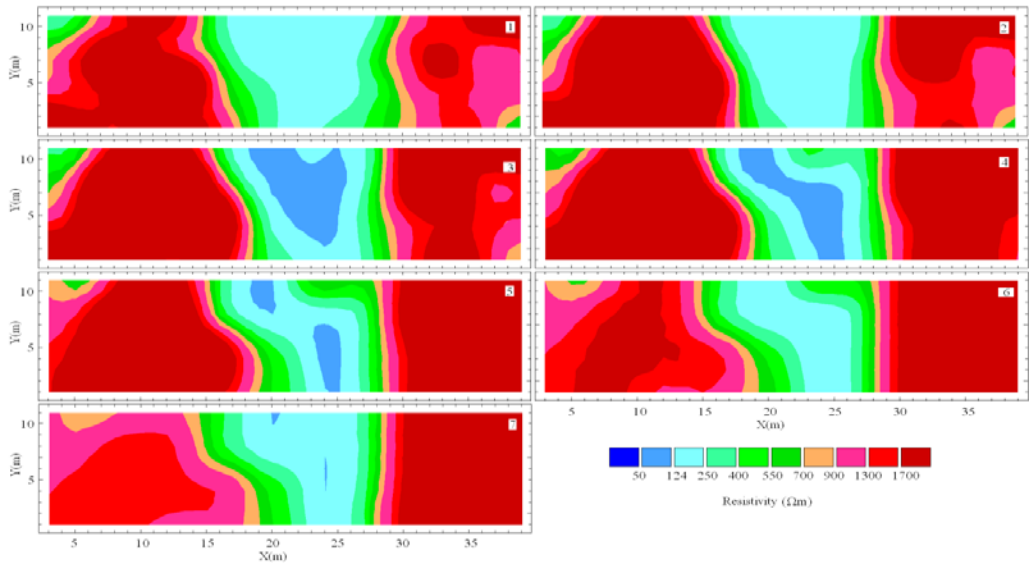

Figure 6. 55. 3D depth slices constructed using the results of the RIT for the DD data. The depths (m) for the different layers are: layer (1): 0.0 – 0.5, (2): 0.5 – 1.0, (3): 1.0 – 1.5, (4): 1.5 – 2.5, (5): 2.5 – 3.8, (6): 3.8 – 5.3, and (7): 5.3 – 7.0.

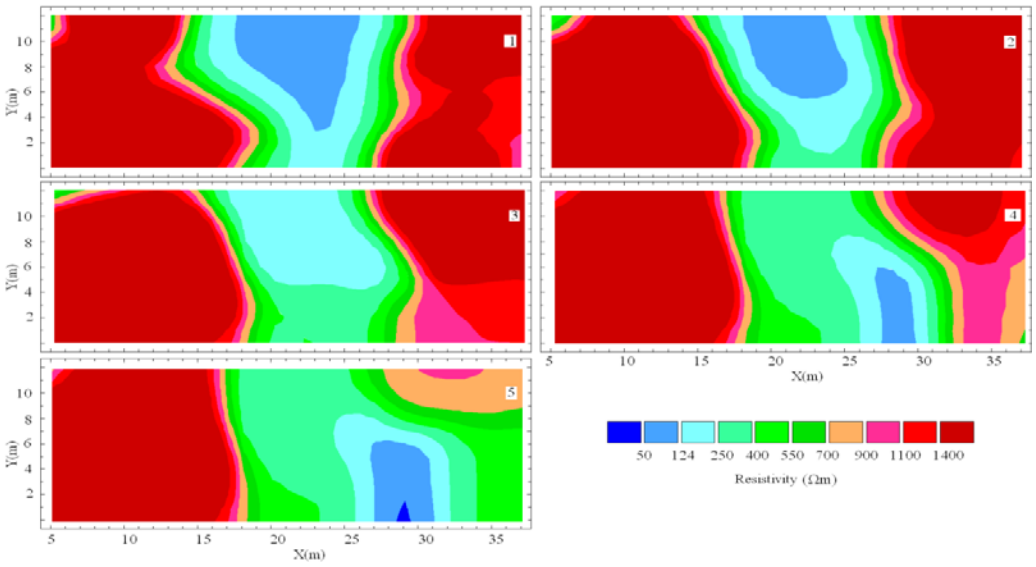

Figure 6. 56. 3D depth slices constructed using the results of the RIT for the WS data. The depths (m) for the different layers are: layer (1): 0.0 – 0.5, (2): 0.5 – 1.5, (3): 1.5 – 3.0, (4): 3.0 – 5.0, and (5): 5.0 – 7.0.

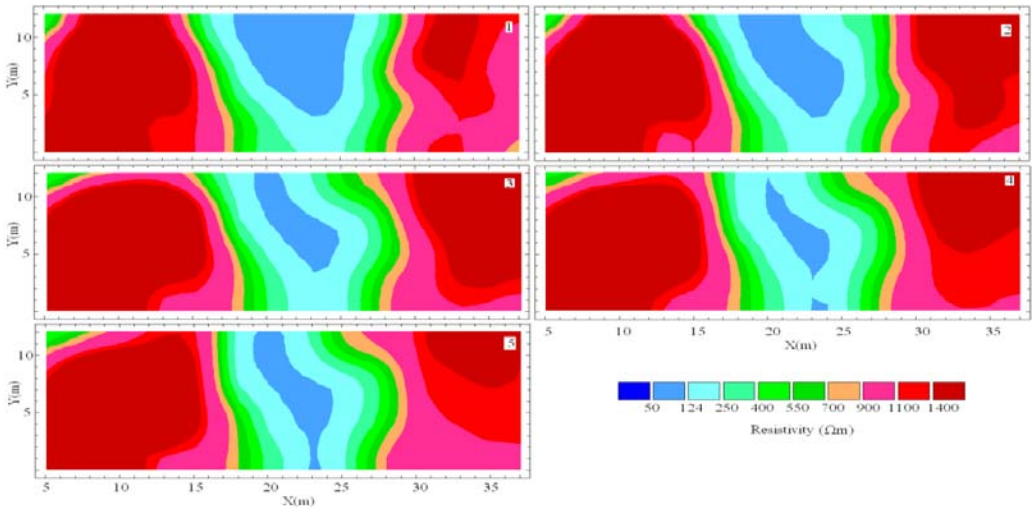

Figure 6. 57. 3D depth slices constructed using the results of the RIT for the W data. The depths (m) for the different layers are: layer (1): 0.0 – 0.8, (2): 0.8 – 1.6, (3): 1.6 – 3.2, (4): 3.2 – 5.0, and (5): 5.0 – 7.0.

6.3.1. 3D Synthetic model close to the fieldwork

Similar to the 2D study, a synthetic test model is also considered that is close to the real field; this model is investigated for each array in order to evaluate the reliability and

accuracy of the inversion results using both the ANN and the RIT methods,. The details of the horizontal location of the anomalous body and the resistivity distribution are shown in Figures 6.58 to 6.62 as a horizontal slice. The depth of the anomalous structure in Figures 6.58 and 6.59 is considered to be 7 meters. The details of the horizontal location of the anomalous body and resistivity distribution for the DD, WS and W data are shown in Figures 6.60 to 6.62. This model was generated using a finite elements code (Loke and Barker, 1996b). In which 3% uniform noise is considered for the generated synthetic apparent resistivity data.

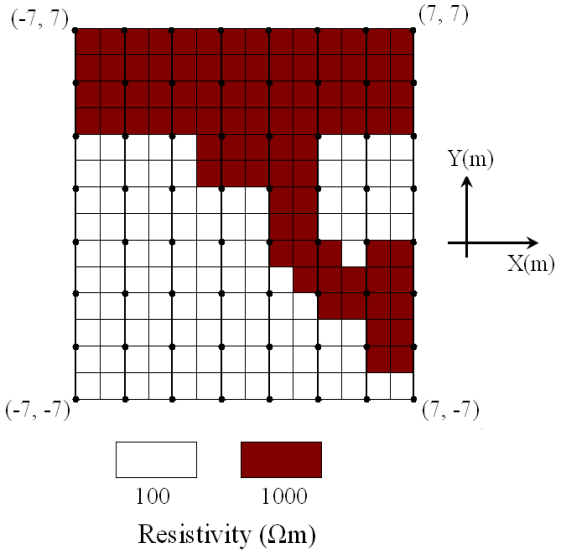

Figure 6. 58. Horizontal location of the anomalous body and resistivity distribution for the synthetic model close to the study site for the PP array. A depth of 7 m is considered for this model.

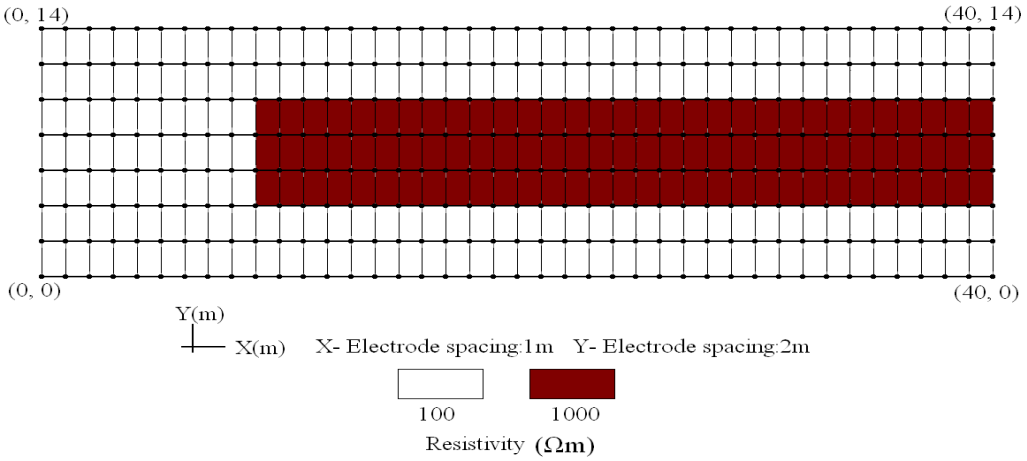

Figure 6. 59. Horizontal location of the anomalous body and resistivity distribution for the synthetic model close to the study site for the PD array. A depth of 7 m is considered for this model.

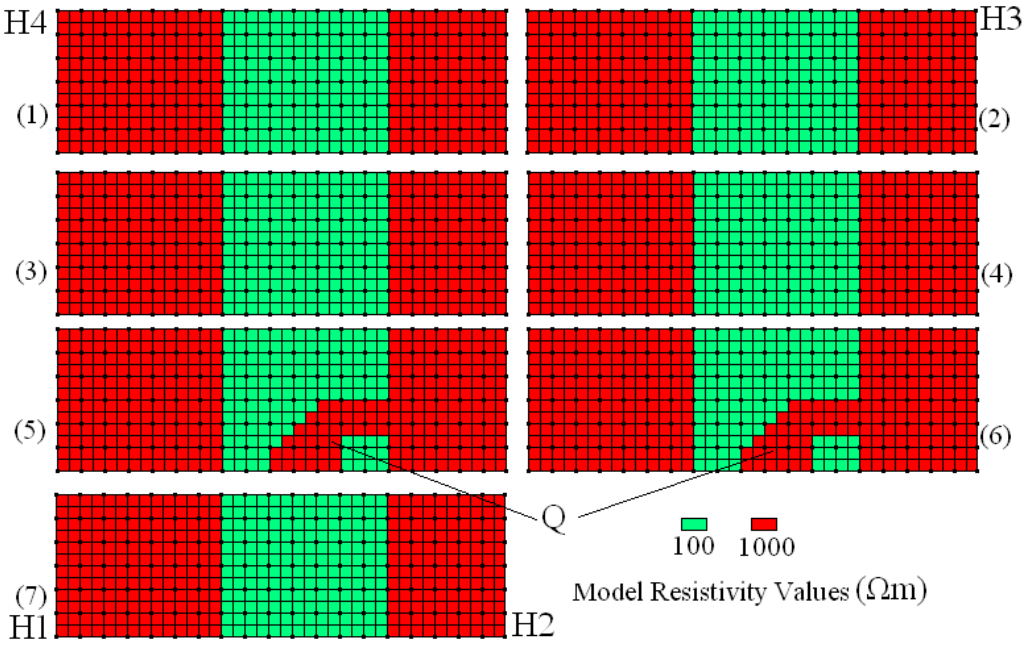

Figure 6. 60. Horizontal location of the anomalous body and resistivity distribution for the synthetic model close to the study site for the DD array. The depths (m) of the different layers are: layer (1): 0.0 – 0.5, (2): 0.5 – 1.0, (3): 1.0 – 1.5, (4): 1.5 – 2.5, (5): 2.5 – 3.8, (6): 3.8 – 5.3, and (7): 5.3 – 7.0.

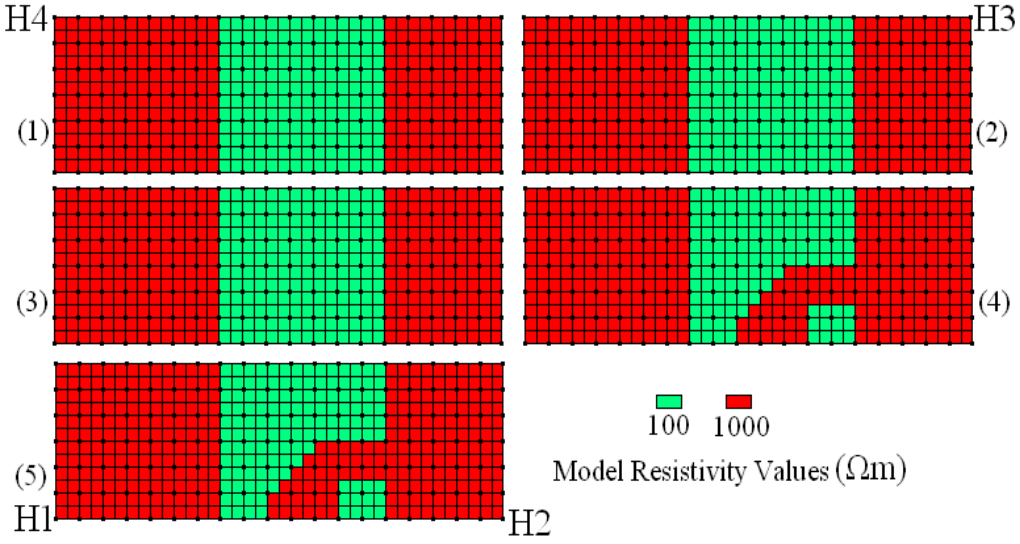

Figure 6. 61. Horizontal location of the anomalous body and resistivity distribution for the synthetic model close to the study site for the WS array. The depths (m) of the different layers are: layer (1): 0.0 – 0.8, (2): 0.8 – 1.6, (3): 1.6 – 3.2, (4): 3.2 – 5.0, and (5): 5.0 – 7.0.

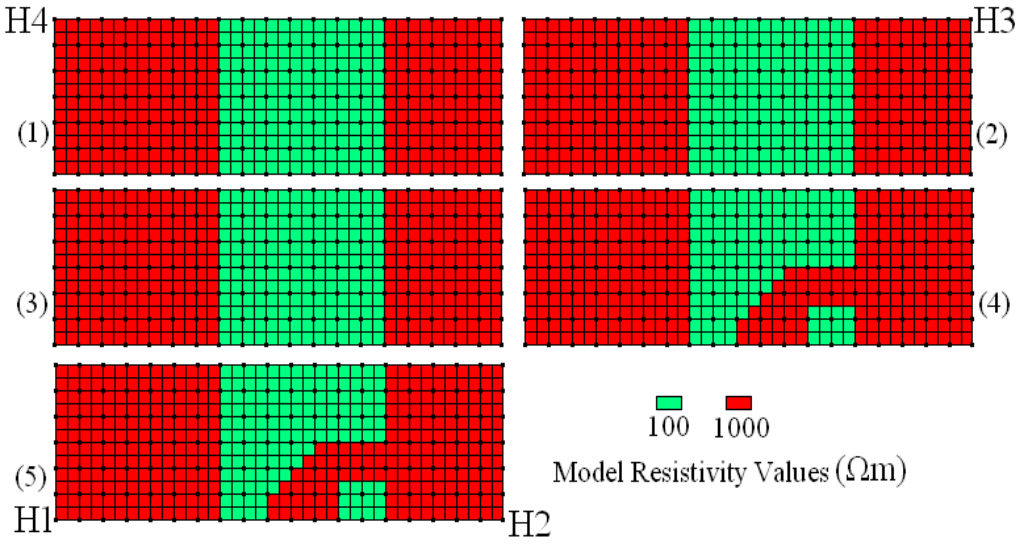

Figure 6. 62. Horizontal location of the anomalous body and resistivity distribution for the synthetic model close to the study site for the W array. The depths (m) for the different layers are: layer (1): 0.0 – 0.8, (2): 0.8 – 1.6, (3): 1.6 – 3.2, (4): 3.2 – 5.0, and (5): 5.0 – 7.0.

The horizontal depth slices were constructed using the ANN results for these examples (Figs. 63.6 to 6.67). According to these slices, most of the anomalous bodies described in Figs. 6.58 to 6.62 are detected at depths of up to 7 meters and are in the right positions.

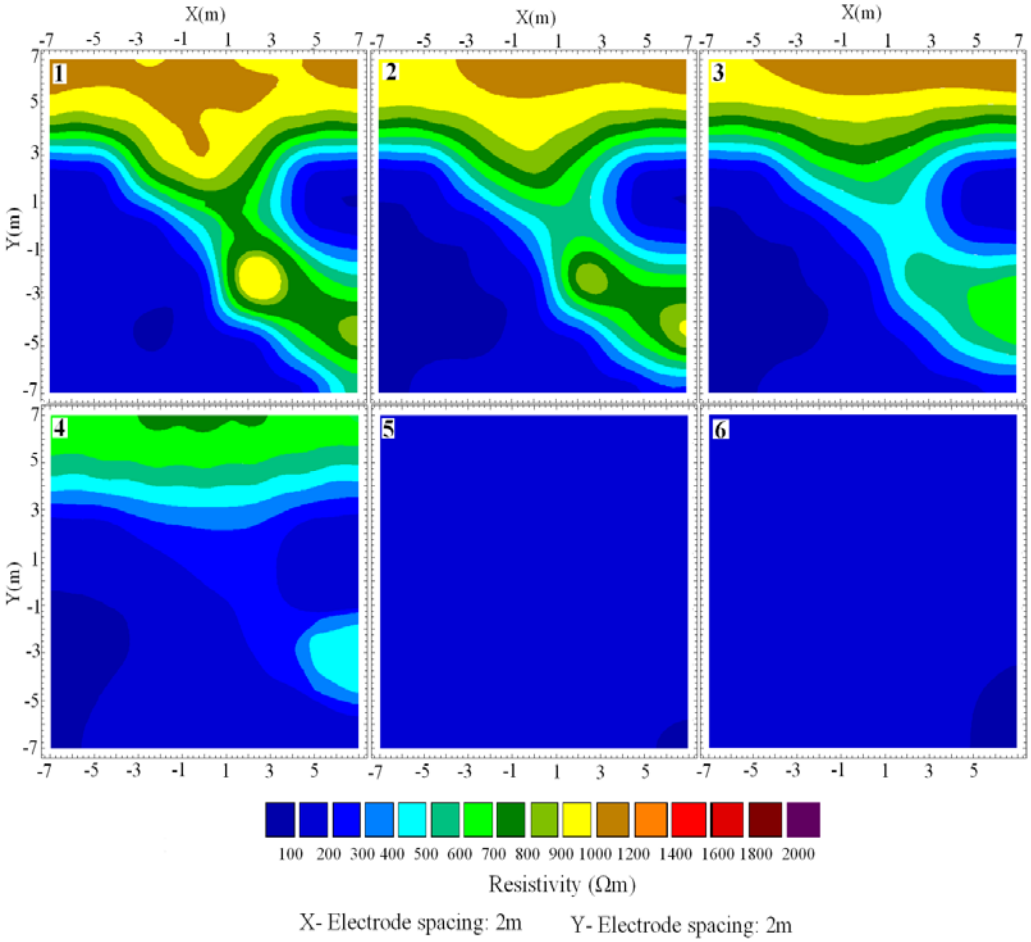

Figure 6. 63. Horizontal depth slices constructed using the ANN results for the example described in Fig. 6.58. The depths (m) for the different layers are: layer (1): 0.0 - 1.5, (2): 1.5 - 3.0, (3): 3.0 – 5.0, (4): 5.0 – 7.0, (5): 7.0 – 9.0, and (6): 9.0 – 12.0.

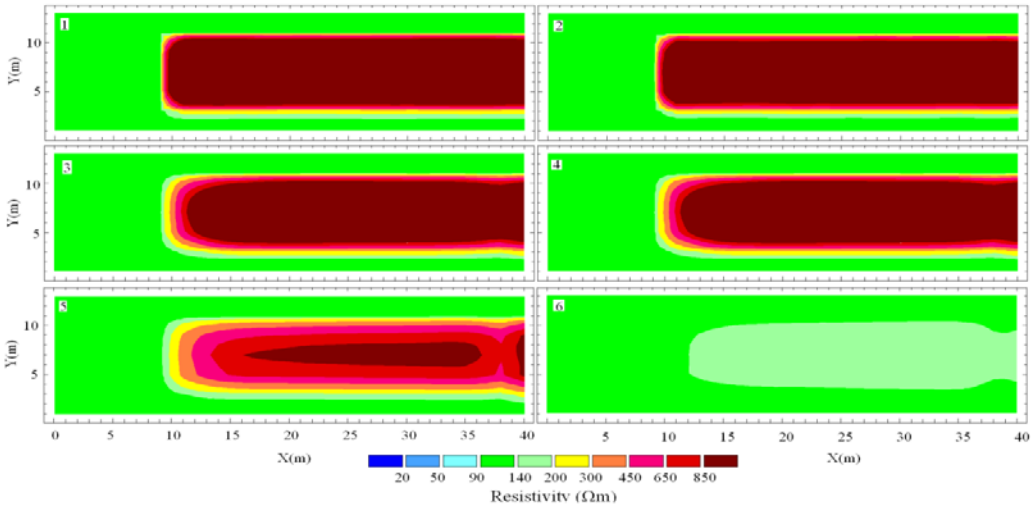

Figure 6. 64. Horizontal depth slices constructed using the ANN results for the example described in Fig. 6.59. The depths (m) for the different layers are: layer (1): 0.0 – 0.5, (2): 0.5 – 1.5, (3): 1.5 – 3.0, (4): 3.0 – 5.0, (5): 5.0 – 7.0, and (6): 7.0 – 10.0.

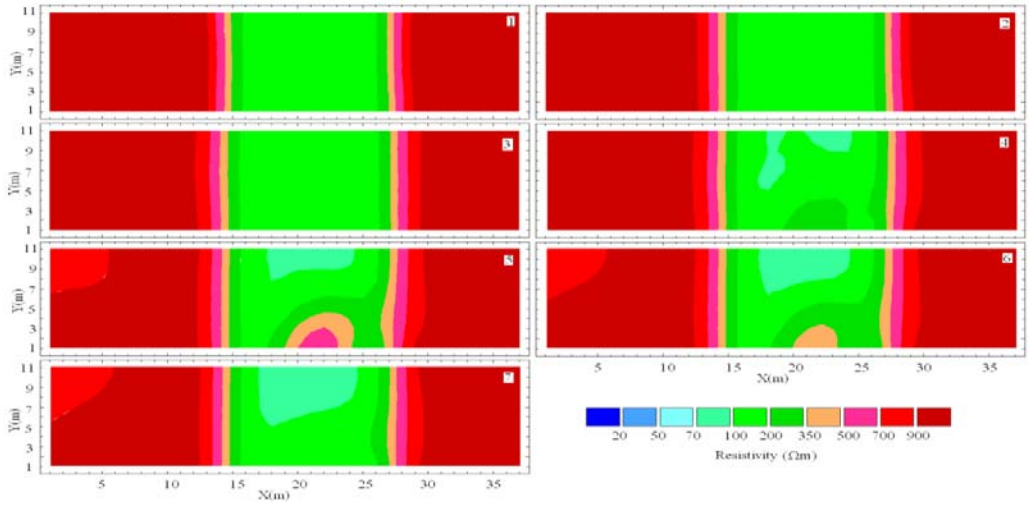

Figure 6. 65. Horizontal depth slices constructed using the ANN results for the example described in Fig. 6.60. The depths (m) for the different layers are: layer (1): 0.0 – 0.5, (2): 0.5 – 1.0, (3): 1.0 – 1.5, (4): 1.5 – 2.5, (5): 2.5 – 3.8, (6): 3.8 – 5.3, and (7): 5.3 – 7.0

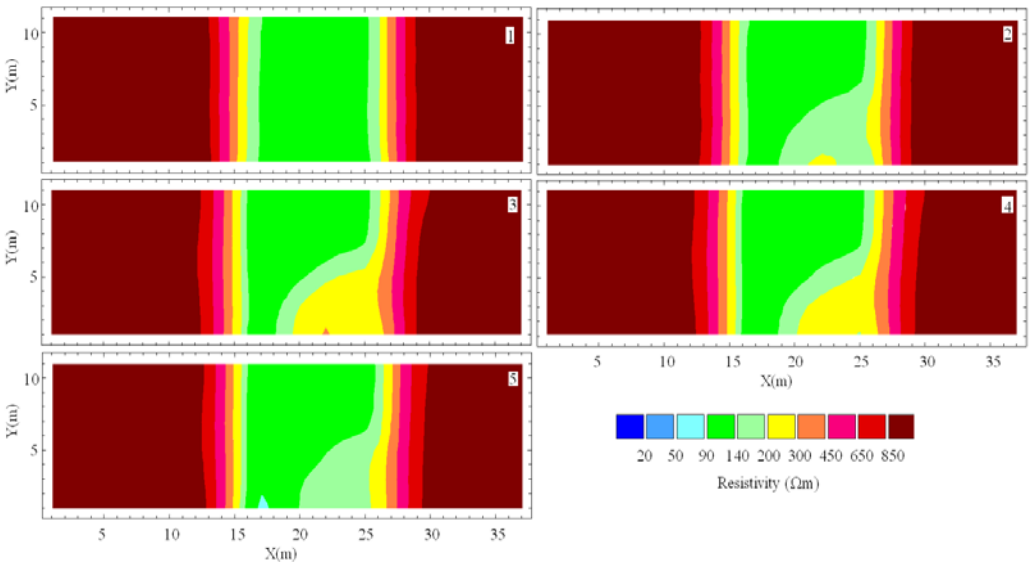

Figure 6. 66. Horizontal depth slices constructed using the ANN results for the example described in Fig. 61.6. The depths (m) for the different layers are: layer (1): 0.0 – 0.5, (2): 0.5 – 1.5, (3): 1.5 – 3.0, (4): 3.0 – 5.0, and (5): 5.0 – 7.0.

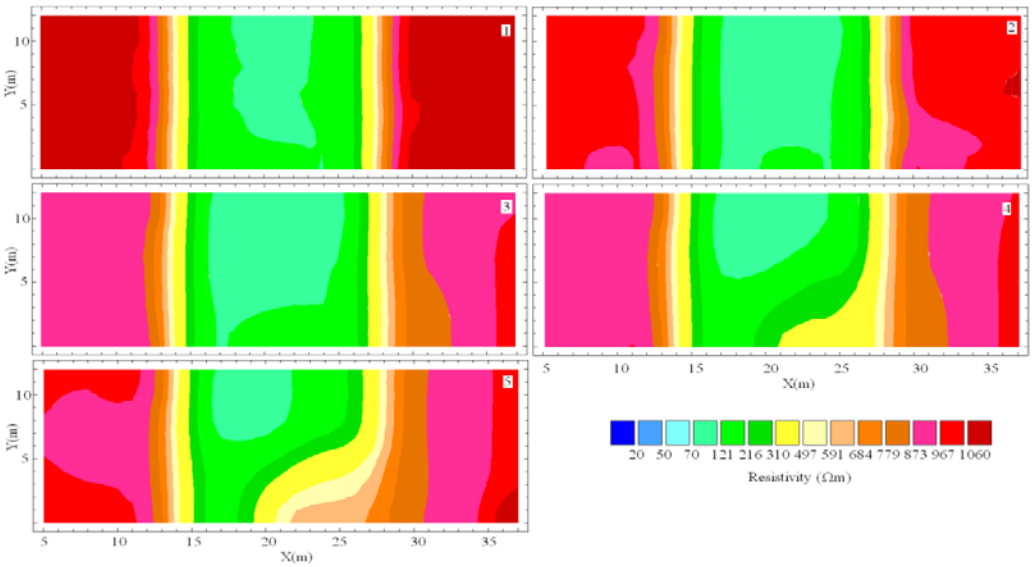

Figure 6. 67. Horizontal depth slices constructed using the ANN results for the example described in Fig. 62.6. The depths (m) for the different layers are: layer (1): 0.0 – 0.8, (2): 0.8 – 1.6, (3): 1.6 – 3.2, (4): 3.2 – 5.0, and (5): 5.0 – 7.0.

In order to compare the results of the ANN with the RIT, the Res3Dinv software was used to invert the same synthetic data. The RMS error for the result of the RIT and the ANN are summarized in Table 6.7. The horizontal depth slices were constructed using the inversion results of each array (Figs. 6.68 to 6.72).

In Figure 6.68, the anomalous body observed by the RIT is seen at depths of up to 7 meters as in the results of the ANN. However, the ANN results show more details of the subsurface structure as compared to RIT. According to Figure 6.69, which is produced using the PD data, the anomalous body is seen at the same horizontal position but its depth is observed at about 5 m, which is 2 m less than the actual depth.

Table 6. 7. RMS error in the results of the ANN and RIT for 3D synthetic models close to the study area.

Array	RMS error (%) for the result of the ANN	RMS error (%) for the result of the RIT
PP	2.54	3.01
PD	1.6	4.12
DD	2.61	3.23
WS	2.17	2.99
W	2.05	2.66

In the results of the DD-data (Fig. 6.70), the anomalous bodies on both sides of the grid are also observed at the same horizontal position, but the anomalous body Q (Fig 6.60, layers 5 and 6) is not clearly resolved. The ANN results are more accurate for the anomaly Q as compared to the RIT results.

With respect to Figures 6.71 and 6.72, the anomalous bodies on both sides of the grid can be seen at the same horizontal positions, but the anomalous body Q (layers 3 and 4 in Fig. 6.61 and Fig.6.62) is not clearly resolved. The ANN results show relatively better results for the anomaly Q as compared to the RIT results for both the WS and W-data.

Although, the connection L (or Q in the synthetic test models) has been detected in the synthetic test by the ANN, its presence was not clear in the inverted result of the field data by both the ANN and RIT and in the synthetic test by the RIT. Therefore, it can be concluded that for such cases, the WS and W arrays might not be the proper arrays to use in the fieldwork.

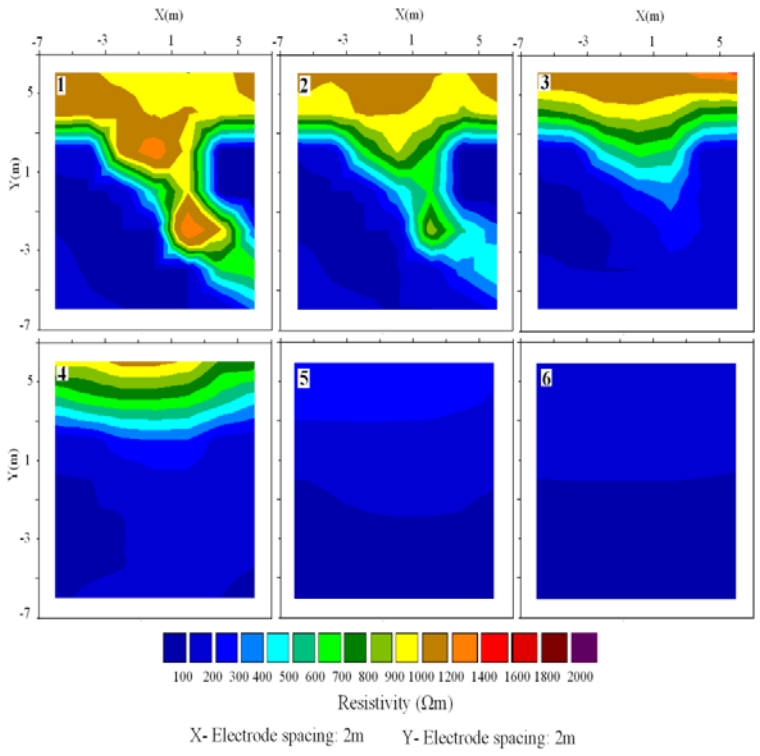

Figure 6. 68. Horizontal depth slices constructed using the results of the RIT for the example described in Fig. 6.58. The depths (m) for the different layers are: layer (1): 0.0 - 1.5, (2): 1.5 - 3.0, (3): 3.0 – 5.0, (4): 5.0 – 7.0, (5): 7.0 – 9.0, and (6): 9.0 – 12.0.

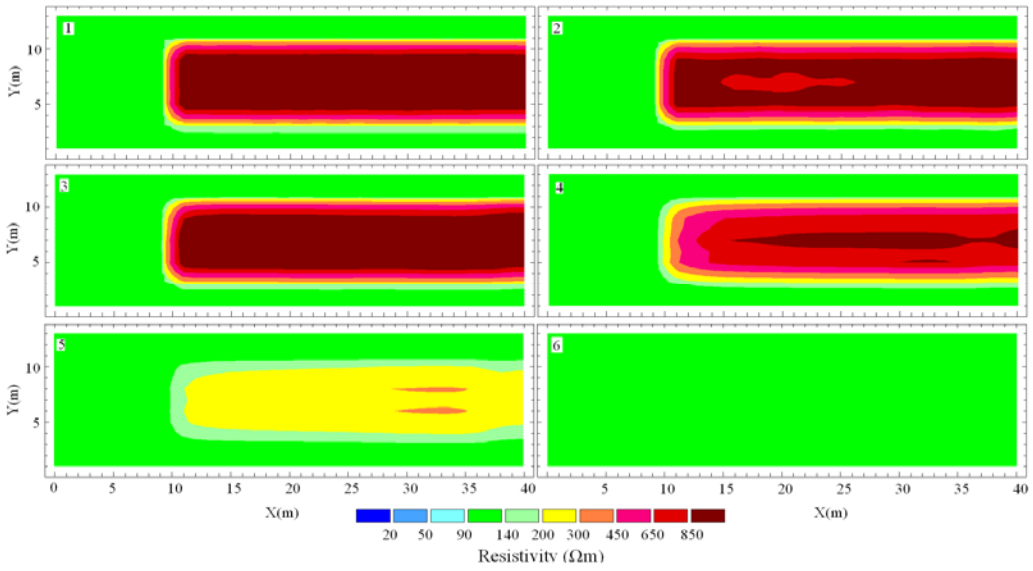

Figure 6. 69. Horizontal depth slices constructed using the results of the RIT for the example described in Fig. 6.59. The depths (m) for the different layers are: layer (1): 0.0 – 0.5, (2): 0.5 – 1.5, (3): 1.5 – 3.0, (4): 3.0 – 5.0, (5): 5.0 – 7.0, and (6): 7.0 – 10.0.

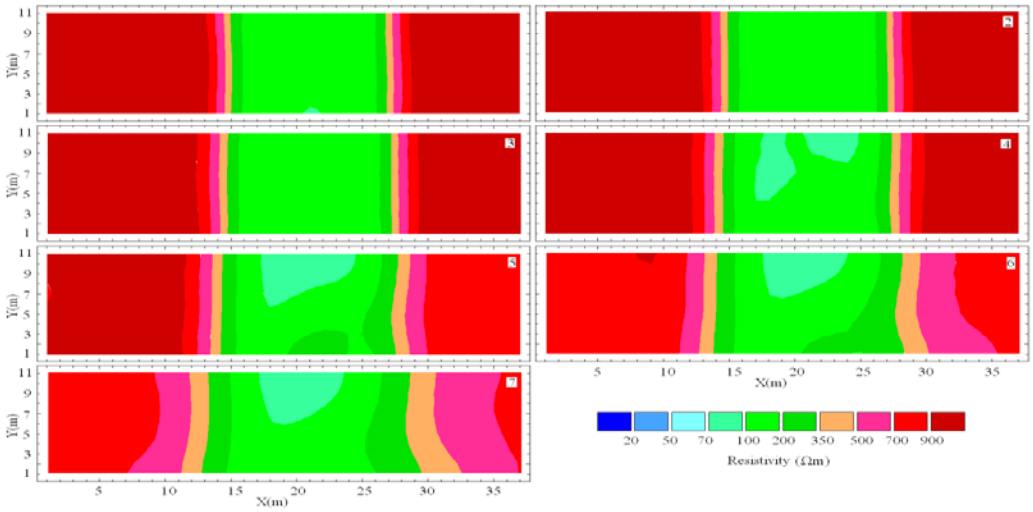

Figure 6. 70. Horizontal depth slices constructed using the results of the RIT for the example described in Fig. 6.60. The depths (m) for the different layers are: layer (1): 0.0 – 0.5, (2): 0.5 – 1.0, (3): 1.0 – 1.5, (4): 1.5 – 2.5, (5): 2.5 – 3.8, (6): 3.8 – 5.3, and (7): 5.3 – 7.0.

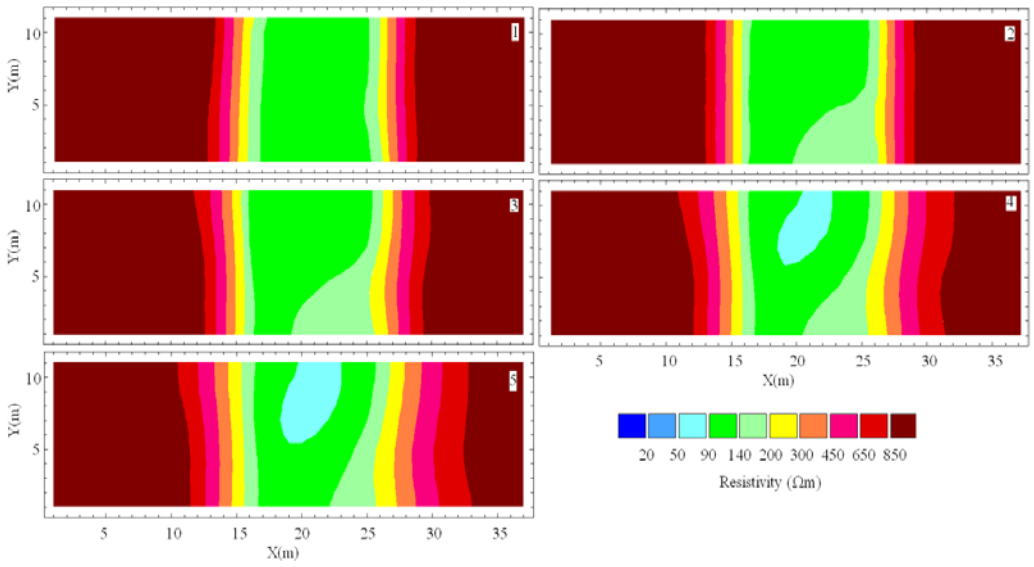

Figure 6. 71. Horizontal depth slices constructed using the results of the RIT for the example described in Fig. 6.61. The depths (m) for the different layers are: layer (1): 0.0 – 0.5, (2): 0.5 – 1.5, (3): 1.5 – 3.0, (4): 3.0 – 5.0, and (5): 5.0 – 7.0.

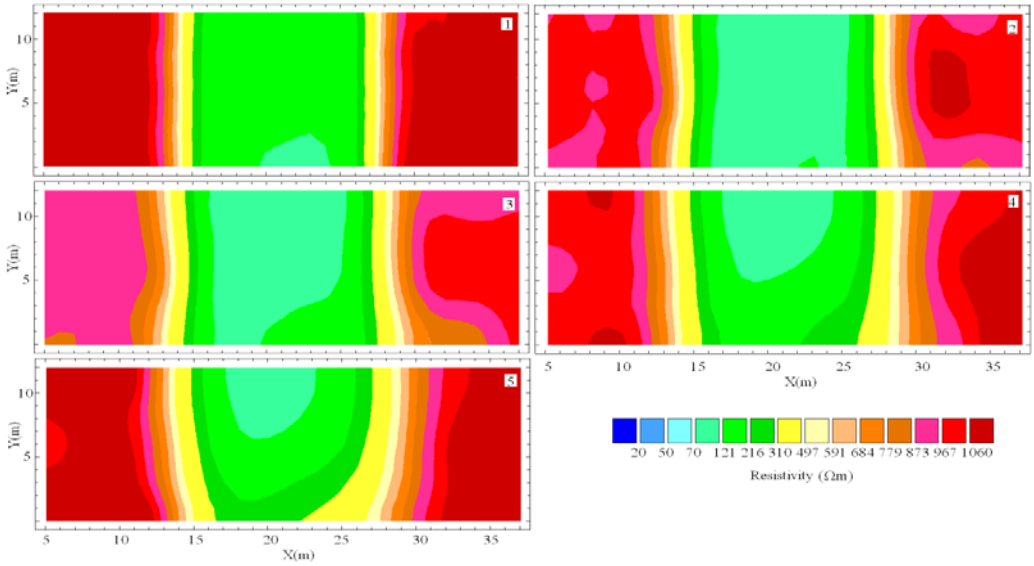

Figure 6. 72. Horizontal depth slices constructed using the results of the RIT for the example described in Fig. 62.6. The depths (m) for the different layers are: layer (1): 0.0 – 0.8, (2): 0.8 – 1.6, (3): 1.6 – 3.2, (4): 3.2 – 5.0, and (5): 5.0 – 7.0.

6.4. Summary

In this chapter, an investigation about the ability of the trained ANNs has been made to invert the 2D and 3D DC resistivity imaging data using real field datasets from a site with high resistivity contrast regions. The study site is located south of the University of Malaya, Kuala Lumpur, Malaysia. It consists of an underground concrete waste water pipe system and its square manhole columns. The survey area stretches over a flat playground covered with grass.

Five common electrode configurations i.e., the WS, W, DD, PD and PP arrays were used in 2D profiles and 3D grids by the DC resistivity surveys. The inversion of the field data using the ANN was then compared with the inversion results from the conventional RIT for each array. In order to evaluate the reliability and accuracy of the inversion results using both the ANN and the RIT, further study using a synthetic example similar to the field data was conducted for each array. Almost all the subsurface features have been resolved by the results of the ANN and RIT. However, the result from the ANN is found to be more realistic (especially for the dimension of the vertical columns and the horizontal pipes), while the RIT produced a smaller vertical dimension than the actual size of the real field data. When the inversion results of both the ANN and the RIT methods for synthetic test models were compared with their corresponding physical resistivity models, it has been observed that the depth of anomalies from the RIT results is smaller than the actual size. In addition, the resistivity values obtained from the RIT were smaller than the actual values, but the ANN produced relatively better physical models. It is therefore concluded that the ANN results are more accurate than the RIT results.

In the inversion results of the 3D W data and 3D WS data, the horizontal pipe that connects columns D and B is observed at a depth of up to 7 meters. However, a connection

between the vertical columns B and F has not been was not detected clearly in the ANN results. This might be due to insufficient horizontal data coverage and poor horizontal resolution of the 3D W and 3D WS arrays as compared to 3D PP, PD and DD arrays. However, the connection L (or Q in the synthetic test models) has been resolved by the synthetic test using the ANN. This anomaly (Q) was not detected by the inversion results of the RIT for either the real field data or the synthetic data. It can be noted that the field data contain more noise than the synthetic data. It is therefore concluded that for such cases, the WS and W arrays might not be the suitable configuration to use separately in 3D DC resistivity surveys. However, in some situations where the field conditions do not allow the use of 3D PP and 3D PD arrays, a combination of the 3D W and 3D DD arrays or the 3D WS and 3D DD arrays can be useful.

Chapter 7
Conclusion

In this thesis, the basis of 1D, 2D and 3D DC resistivity surveys have been discussed. The common arrays used in 2D and 3D surveys were compared, i.e., the WS, W, DD, PD and PP-arrays, with respect to the following characteristics: (i) signal strength, (ii) horizontal data coverage, (iii) sensitivity of the array to horizontal structures, (iv) sensitivity of the array to vertical structures and (v) depth of investigation for each array. The W array is good at showing vertical changes but relatively poor at detecting horizontal changes. This array has the strongest signal strength compared to other arrays. This can be an important factor if the survey is carried in areas with high background noise. However, the horizontal coverage of the W array is relatively poor, as the electrode spacing is increased. The signal strength for the WS array is weaker than that for the W array, but it is stronger than the DD array and twice that of the PP array. The DD array has better horizontal data coverage than the W array. This is an important advantage when the number of electrodes available with the multi-electrode system is small. The PP array has the widest horizontal coverage and the deepest depth. However, it has the poorest resolution compared to other arrays. Nevertheless, it has also been used for 3D surveys. The PD array is more sensitive to vertical structures. Because of its good horizontal coverage, the PD array is useful for surveys with a small number of electrodes. The signal strength is higher than the DD array but lower compared to the W and WS arrays. As a common way to study the suitability of different arrays, in resistivity survey, the sensitivity function for each array in 2D and 3D studies has been calculated. This was important to compare the depth of

investigation and the vertical and horizontal resolutions of arrays used in 2D and 3D surveys.

In order to study the numerical simulation of the measured data for given subsurface parameters, the basis of the finite difference method and different boundary conditions is discussed. The methodologies of non-linear inversion and the common inversion methods (i.e., steepest descent method, nonlinear conjugate gradients method, Newton-type methods and smoothness-constrained least squares methods) have also been explained. Since the convergence rate of the steepest descent technique for ill-posed problems is very slow, much time has to be needed to carry on with forward calculations using this. An implementation of this technique is very simple, but practically it can be rarely used. In the nonlinear conjugate gradients technique, each search direction is used only once. Thus, convergence is fast as compared to the steepest descent method. The Gauss-Newton method has two advantages: 1) the computation is easier than the other methods, and 2) Hessian approximation in this method is positive semi-definite, which guarantees that the Gauss-Newton step is a descent direction. However, the quadratic convergence of the Newton's method loose its applicability as a result of strong non-linearity. The Marquardt-Levenberg modification to the Gauss-Newton equation is one common way to avoid the singularity problem. Another alternative for Newton's method is the quasi- Newton technique, which updates the Hessian approximation by previous gradients. The L2_norm smoothness-constrained optimization method tends to produce a model with a smooth variation of resistivity values. This approach is acceptable if the actual subsurface resistivity varies in a smooth and gradational manner. By L1_ norm smoothness-constrained optimization method the absolute changes in the model resistivity values can be minimized. Technically, this is referred as a blocky inversion method (robust inversion

technique), which can sometimes give significantly better results in areas with high resistivity zones of sharp boundaries. It is therefore concluded that for this study the robust inversion technique (RIT) is the most efficient method among the other least squares methods because the field site used for data acquisition consists of high subsurface resistivity regions. The inversion of field data using the RIT method was contacted to compare the results of the ANN and the conventional least squares inversion methods.

In order to study the effect of data pool formation in training the ANN, two methods were used to generate the synthetic data. These methods are called M1 and M2, which basically differ in the type of input-output data used to train the ANN. In the first method, M1_2D and M1_3D, a cross-section of the subsurface was divided into a mesh of elements with a background resistivity of 100 Ωm and an anomalous element of 1000 Ωm moving to all the model mesh element positions. In this method, the apparent resistivity data were considered as the input data and the true resistivities of all mesh elements were used as the output data in the training phase of the ANN. In the second method, M2_2D and M2_3D, different sizes were selected for the anomalous body, and it was moved to different positions within the homogeneous model mesh elements. In this method, the locations (x and y for the 2D case and x, y and z for the 3D case) and the apparent resistivities of data points were considered as the input data and the true resistivities of all mesh elements were used as the output data in the training process of the ANN. The effect of the input-output data type (obtained by the methods M1 and M2) was investigated in 2D and 3D. The higher MSE error for the method M1_2D and M1_3D compared to the MSE error for the method M2_2D and M2_3D can be explained as due to the sizes of the mesh elements, because the fixed sizes were used for each element of the mesh; this might affect the accuracy of the

results. It is therefore concluded that the synthetic data generated using the method M2_2D and M2_3D may be the best data type for training and testing the ANN in this study.

With respect to the effect of the number of nodes in each layer of the ANN, the results of our 2D study suggest that the simplest architectures for the ANN that can reach the desired threshold error for the PP, PD, DD, WS and W arrays are (3-30-90-1), (3-30-12-1), (3-28-4-1), (3-28-16-1) and (3-24-80-1). The simplest architectures for the ANN in 3D study are (4-84-24-1), (4-35-25-1), (4-35-25-1), (4-45-60-1) and (4-30-50-1), respectively.

The effect of the training data pool volume in the 2D and 3D parts of this study and the sufficient volume for each data type have been also evaluated .

Five common training paradigms, i.e., BTWB, CGFR, RPROP, GDMA and LMWB, in the cases of 2D and 3D have been compared. The results show that for all arrays (2D and 3D) except for 3D PD data, the RPROP is the most efficient algorithm at training the DC resistivity data. In the case of 3D PD data, the GDMA algorithm is the most efficient paradigm.

The interpolation and extrapolation properties of the ANN using another 24 synthetic datasets generated for each array have been studied. The range from 100 – 1000 Ωm was divided into 100, 200, 300, 400, 500, and 600 Ωm as the background resistivity, and different resistivity values for the anomalous body were considered. The RMS errors for all interpolation and extrapolation test sets related to each array are in the range of 0.3 - 9.0% Since the RMS errors for all datasets are less than 9.0%, it can be concluded that the networks are properly designed and trained.

The ability of the trained ANNs to invert the 2D and 3D DC resistivity imaging data was checked by real field datasets related to a site with high resistivity contrast regions. The study site consists of an underground concrete wastewater pipe system and its square manhole columns. Five common electrode configurations, i.e., the WS, W, DD, PD and PP

arrays, were used in 2D profiles and 3D grids in the DC resistivity surveys. The inversion of the field data using the ANN was then compared with the results of the inversion using the conventional RIT for each array. Further study using a synthetic example similar to the field data was done for each array in order to evaluate the reliability and accuracy of the inversion results using both the ANN and RIT methods.

Although all subsurface features were almost resolved in the results of both methods, the ANN results, especially for the dimension of the vertical columns and the horizontal pipes, were more realistic. In contrast, the RIT produced smaller vertical dimensions than the actual size of the real field data.

With respect to the inversion results of both the ANN and RIT methods for synthetic test models, when these results were compared with their corresponding physical resistivity models, it is concluded that the depths of the anomalies in the RIT results were less than the actual size. In addition, the RIT produced resistivity values that were almost smaller than the actual values, and the ANN represented the physical models better than the RIT. Thus, it can be conclude the ANN results are more accurate than the RIT results.

In the inversion of the 3D W data (Fig. 6.42), similar to the inversion of 3D WS data, the horizontal pipe that connects columns D and B (Fig. 6.29) was observed at depths of up to 7 meters. The connection between vertical columns B and F was not detected clearly in the ANN results. This might be due to insufficient horizontal data coverage and poor horizontal resolution of the 3D W and 3D WS arrays compared to the 3D PP, PD and DD arrays. However, connection L (or Q in the synthetic test models) was resolved in the synthetic test using the ANN. This anomaly was not detected by the inversion results of the RIT for either the real field data or the synthetic data. Note that the field data contain more noise than the synthetic data. Therefore, it can be conclude for such cases that the WS and W arrays might not be the proper arrays to use separately in 3D DC resistivity surveys.

However, in some situations in which the field conditions do not allow the use of 3D PP and 3D PD arrays, a combination of the 3D W array and 3D DD array or the 3D WS array and 3D DD array can be useful.

As a suggestion for further work, it would be useful if the ANN were applied to the joint inversion of DC resistivity imaging data obtained by different arrays. For example, the joint inversion of W and DD arrays in 2D surveys using conventional inversion methods would enhance the quality of the results because the W array is good at detecting vertical changes and the DD array can detect horizontal changes in subsurface resistivities. Therefore, the use of the ANN in the joint inversion of W and DD data are promising.

Appendix A

Table A 1. Dependence of the MSE error on the number of neurons in hidden layers for the WS-synthetic data produced by methods M1_2D and M2_2D.

Nh1	Nh2	MSE Error for Method M1_2D	MSE Error for Method M2_2D
7	0	0.3756	0.6604
	8	0.2233	0.1520
	16	0.1225	0.0453
	24	0.2942	0.0606
	32	0.1059	0.0350
	40	0.0450	0.0141
14	0	0.2436	0.0912
	8	0.1929	0.0377
	16	0.0135	0.0066
	24	0.2821	0.0068
	32	0.0989	0.0053
	40	0.0422	0.0031
21	0	0.0846	0.0024
	8	0.0042	0.0041
	16	0.0898	0.0005
	24	0.0022	0.0002
	32	0.0097	0.0007
	40	0.0031	0.0004
28	0	0.0061	0.0006
	8	0.0010	0.0003
	16	0.0004	0.0001
	24	0.0210	0.0004
	32	0.0044	0.0004
	40	0.0072	0.0002
35	0	0.0061	0.0005
	4	0.0091	0.0002
	12	0.0005	0.0005
	20	0.0011	0.0004
	28	0.0004	0.0003
	32	0.0003	0.0002

Table A 2. Dependence of the MSE error on the number of neurons in hidden layers for the W-synthetic data produced by methods M1_2D and M2_2D.

Nh1	Nh2	MSE Error for Method M1_2D	MSE Error for Method M2_2D
6	0	0.004253	0.031252
	20	0.000851	0.007578
	40	0.000912	0.002264
	60	0.000531	0.003028
	80	0.000975	0.001749
	90	0.001347	0.000704
12	0	0.000613	0.004555
	20	0.000714	0.001884
	40	0.001867	0.000329
	60	0.000546	0.000339
	80	0.001005	0.000264
	90	0.001374	0.000154
18	0	0.001072	0.001193
	20	0.002376	0.000204
	40	0.001046	0.000088
	60	0.002657	0.000092
	80	0.002013	0.000076
	90	0.002508	0.000072
24	0	0.002214	0.000999
	20	0.003000	0.000082
	40	0.003397	0.000088
	60	0.001677	0.000069
	80	0.000135	0.000058
	90	0.002142	0.000066
30	0	0.002214	0.000249
	20	0.002040	0.000099
	40	0.003301	0.000072
	60	0.002958	0.000067
	80	0.003397	0.000099
	90	0.003522	0.000629

Table A 3. Dependence of the MSE error on the number of neurons in hidden layers for the DD-synthetic data produced by methods M1_2D and M2_2D.

Nh1	Nh2	MSE Error for Method M1_2D	MSE Error for Method M2_2D
4	0	0.3471	0.1649
	4	0.1195	0.1608
	12	0.1012	0.0251
	20	0.0988	0.0204
	28	1.1382	0.0499
	32	0.0743	0.0225
12	0	0.0326	0.0989
	4	0.0215	0.0793
	12	0.0064	0.0052
	20	0.0010	0.0097
	28	0.0071	0.0088
	32	0.0047	0.0016
20	0	0.068	0.0027
	4	0.0020	0.0050
	12	0.0009	0.0007
	20	0.0055	0.0003
	28	0.0062	0.0008
	32	0.0008	0.0006
28	0	0.082	0.0006
	4	0.0012	0.0001
	12	0.0063	0.0004
	20	0.0621	0.0002
	28	0.0032	0.0006
	32	0.0062	0.0004
32	0	0.0019	0.006
	4	0.0037	0.0009
	12	0.0068	0.0003
	20	0.0014	0.0007
	28	0.0011	0.0004
	32	0.0008	0.0002

Table A 4. Dependence of the MSE error on the number of neurons in hidden layers for the PD-synthetic data produced by methods M1_2D and M2_2D.

Nh1	Nh2	MSE Error for Method M1_2D	MSE Error for Method M2_2D
5	0	0.0393	0.2394
	4	0.0979	0.0341
	12	0.0539	0.0009
	16	0.0293	0.0018
	20	0.0008	0.0003
	24	0.0008	0.0004
15	0	0.0009	0.0009
	4	0.0072	0.0006
	12	0.0012	0.0006
	16	0.0030	0.0004
	20	0.0006	0.0003
	24	0.0006	0.0004
30	0	0.0061	0.0007
	4	0.0017	0.0003
	12	0.0005	0.0002
	16	0.0004	0.0008
	20	0.0069	0.0007
	24	0.0004	0.0008
45	0	0.0015	0.0078
	4	0.0024	0.0010
	12	0.0008	0.0011
	16	0.0003	0.0005
	20	0.0006	0.0004
	24	0.0005	0.0007
60	0	0.0027	0.0073
	4	0.0008	0.0006
	12	0.0004	0.0011
	16	0.0003	0.0005
	20	0.0004	0.0011
	24	0.0003	0.0010

Table A 5. Dependence of the MSE error on the number of neurons in hidden layers for the PP-synthetic data produced by methods M1_2D and M2_2D.

Nh1	Nh2	MSE Error for Method M1_2D	MSE Error for Method M2_2D
10	0	0.00928	0.00237
	15	0.00049	0.00031
	30	0.00053	0.00008
	60	0.00029	0.00019
	90	0.00022	0.00016
	120	0.00019	0.00039
20	0	0.00089	0.00089
	15	0.00071	0.00059
	30	0.00011	0.00059
	60	0.00029	0.00039
	90	0.00059	0.00029
	120	0.00050	0.00039
30	0	0.00385	0.00096
	15	0.00026	0.00009
	30	0.00185	0.00009
	60	0.00008	0.00007
	90	0.00007	0.00001
	120	0.00005	0.00005
40	0	0.00149	0.00779
	15	0.00031	0.00099
	30	0.00079	0.00003
	60	0.00029	0.00004
	90	0.00059	0.00003
	120	0.00049	0.00006
50	0	0.00269	0.00729
	15	0.00017	0.00009
	30	0.00003	0.00006
	60	0.00009	0.00004
	90	0.00003	0.00006
	120	0.00009	0.00003

Table A 6. Dependence of the MSE error on the number of neurons in hidden layers for the PP-synthetic data produced by methods M1_3D and M2_3D.

Nh1	Nh2	MSE Error for Method M1_3D	MSE Error for Method M2_3D
21	0	0.0139	0.0070
	8	0.0072	0.0007
	24	0.0084	0.0008
	48	0.0043	0.0007
	72	0.0066	0.0006
	96	0.0058	0.0006
42	0	0.013	0.0013
	8	0.0010	0.0009
	24	0.0054	0.0006
	48	0.0034	0.0005
	72	0.0008	0.0005
	96	0.0007	0.0004
63	0	0.0571	0.0028
	8	0.0017	0.0051
	24	0.0011	0.0010
	48	0.0008	0.0006
	72	0.0008	0.0006
	96	0.0007	0.0004
84	0	0.0022	0.0025
	8	0.0009	0.0007
	24	0.0007	0.0003
	48	0.0006	0.0004
	72	0.0008	0.0009
	96	0.0005	0.0004
105	0	0.0040	0.0016
	8	0.0009	0.0007
	24	0.0006	0.0006
	48	0.0005	0.0004
	72	0.0005	0.0003
	96	0.0005	0.0003

Table A 7. Dependence of the MSE error on the number of neurons in hidden layers for the PD-synthetic data produced by methods M1_3D and M2_3D.

Nh1	Nh 2	MSE Error for Method M1_3D	MSE Error for Method M2_3D
21	0	0.009267	0.005252
	5	0.004812	0.000525
	15	0.001106	0.000600
	25	0.000865	0.000525
	35	0.000441	0.000401
	45	0.000386	0.000150
28	0	0.008652	0.000275
	5	0.000667	0.000175
	15	0.000536	0.000450
	25	0.002260	0.000375
	35	0.000533	0.000115
	45	0.000466	0.000102
35	0	0.003806	0.002111
	5	0.001132	0.003825
	15	0.000733	0.000751
	25	0.000105	0.000085
	35	0.000096	0.000088
	45	0.000085	0.000085
42	0	0.001466	0.001875
	5	0.000614	0.000165
	15	0.000466	0.000025
	25	0.000098	0.000016
	35	0.000088	0.000012
	45	0.000085	0.000010

Table A 8. Dependence of the MSE error on the number of neurons in hidden layers for the DD-synthetic data produced by methods M1_3D and M2_3D.

Nh1	Nh2	MSE Error for Method M1_3D	MSE Error for Method M2_3D
25	0	0.00729	0.00311
	5	0.00332	0.00431
	15	0.00310	0.00151
	25	0.00274	0.00132
	35	0.00249	0.00112
	45	0.00364	0.00108
30	0	0.00887	0.00714
	5	0.00122	0.00767
	15	0.00127	0.00099
	25	0.00113	0.00096
	35	0.00097	0.00086
	45	0.00091	0.00063
35	0	0.00391	0.00231
	5	0.00120	0.00087
	15	0.00089	0.00086
	25	0.00010	0.00080
	35	0.00086	0.00088
	45	0.00085	0.00089
40	0	0.00156	0.00135
	5	0.00914	0.00286
	15	0.00476	0.00085
	25	0.00088	0.00086
	35	0.00087	0.00084
	45	0.00086	0.00090

Table A 9. Dependence of the MSE error on the number of neurons in hidden layers for the WS-synthetic data produced by methods M1_3D and M2_3D.

Nh1	Nh 2	MSE Error for Method M1_3D	MSE Error for Method M2_3D
15	0	0.06281	0.08937
	15	0.00571	0.00679
	30	0.00563	0.00314
	45	0.00552	0.00255
	60	0.00531	0.00231
	75	0.00441	0.00125
30	0	0.00762	0.00197
	15	0.00201	0.00099
	30	0.00134	0.00058
	45	0.00111	0.00051
	60	0.00055	0.00039
	75	0.00042	0.00036
45	0	0.00219	0.00102
	15	0.00104	0.00099
	30	0.00077	0.00072
	45	0.00058	0.00064
	60	0.00034	0.00025
	75	0.00029	0.00030
60	0	0.0010	0.0011
	15	0.00082	0.00079
	30	0.00060	0.00089
	45	0.00048	0.00046
	60	0.00039	0.00042
	75	0.00025	0.00025

Table A 10. Dependence of the MSE error on the number of neurons in hidden layers for the W-synthetic data produced by methods M1_3D and M2_3D.

Nh1	Nh 2	MSE Error for Method M1_3D	MSE Error for Method M2_3D
20	0	0.009003	0.007638
	5	0.006429	0.002649
	20	0.001127	0.001008
	35	0.000731	0.000988
	50	0.000335	0.000657
	65	0.000241	0.000103
30	0	0.007108	0.000989
	5	0.003999	0.000769
	20	0.003861	0.000099
	35	0.001000	0.000081
	50	0.000412	0.000070
	65	0.000136	0.000074
40	0	0.004256	0.006879
	5	0.001002	0.000869
	20	0.000628	0.000097
	35	0.000211	0.000075
	50	0.000099	0.000079
	65	0.000082	0.000076
50	0	0.004963	0.001650
	5	0.001241	0.000866
	20	0.000967	0.000431
	35	0.000084	0.000079
	50	0.000083	0.000070
	65	0.000075	0.000072

Table A 11. MSE performance of the ANN for different data pool volumes WS2DV1, WS2DV2 and WS2DV3

Data pool volume	MSE error after 16 epochs	MSE error after 1000 epochs	MSE error after 4000 epochs
WS2DV1	0.0049	0.0040	0.0031
WS2DV2	0.0001 Performance goal was Reached	Performance goal was Reached	Performance goal was Reached
WS2DV3	0.0004	0.0002	0.0001 Performance goal was Reached

Table A 12. MSE performance of the ANN for different data pool volumes W2DV1, W2DV2 and W2DV3

Data pool volume	MSE error after 77 epochs	MSE error after 1348 epochs	MSE error after 2500 epochs	MSE error after 5000 epochs
W2DV1	0.006899	0.000664	0.000547	0.0001062
W2DV2	0.000058 Performance goal was Reached	Performance goal was Reached	Performance goal was Reached	Performance goal was Reached
W2DV3	0.000072	0.000060 Performance goal was Reached	Performance goal was Reached	Performance goal was Reached

Table A 13. MSE performance of the ANN for different data pool volumes DD2DV1, DD2DV2 and DD2DV3

Data pool volume	MSE error after 2282 epochs	MSE error after 4258 epochs	MSE error after 8000 epochs
DD2DV1	0.0679	0.0499	0.0097
DD2DV2	0.0001 Performance goal was Reached	Performance goal was Reached	Performance goal was Reached
DD2DV3	0.0004	0.0001 Performance goal was Reached	Performance goal was Reached

Table A 14. MSE performance of the ANN for different data pool volumes PD2DV1, PD2DV2 and PD2DV3

Data pool volume	MSE error after 1275 epochs	MSE error after 5000 epochs	MSE error after 10000 epochs
PD2DV1	0.00074	0.00061	0.00044
PD2DV2	0.00020 Performance goal was Reached	Performance goal was Reached	Performance goal was Reached
PD2DV3	0.00041	0.000037	0.00032

Table A 15. MSE performance of the ANN for different data pool volumes PP2DV1, PP2DV2 and PP2DV3

Data pool volume	MSE error after 1275 epochs	MSE error after 5000 epochs	MSE error after 10000 epochs
PP2DV1	0.000141	0.000071	0.000054
PP2DV2	0.00001 Performance goal was Reached	Performance goal was Reached	Performance goal was Reached
PP2DV3	0.000032	0.000026	0.000022

Table A 16. MSE performance of the ANN for different data pool volumes PP3DV1, PP3DV2 and PP3DV3

Data pool volume	MSE error after 1340 epochs	MSE error after 3000 epochs	MSE error after 5000 epochs
PP3DV1	0.07039	0.04886	0.03539
PP3DV2	0.00032 Performance goal was Reached	Performance goal was Reached	Performance goal was reached
PP3DV3	0.00024 Performance goal was Reached	Performance goal was reached	Performance goal was reached

Table A 17. MSE performance of the ANN for different data pool volumes PD3DV1, PD3DV2 and PD3DV3

Data pool volume	MSE error after 1560 epochs	MSE error after 5000 epochs	MSE error after 10000 epochs
PD3DV1	0.000526	0.000281	0.000212
PD3DV2	0.000085 Performance goal was Reached	Performance goal was Reached	Performance goal was Reached
PD3DV3	0.000016	0.000070 Performance goal was Reached	Performance goal was reached

Table A 18. MSE performance of the ANN for different data pool volumes DD3DV1, DD3DV2 and DD3DV3

Data pool volume	MSE error after 700 epochs	MSE error after 4000 epochs	MSE error after 8000 epochs
DD3DV1	0.00346	0.00125	0.00105
DD3DV2	0.00080 Performance goal was Reached	Performance goal was Reached	Performance goal was Reached
DD3DV3	0.00087	0.000082 Performance goal was Reached	Performance goal was reached

Table A 19. MSE performance of the ANN for different data pool volumes WS3DV1, WS3DV2 and WS3DV3

Data pool volume	MSE error after 34077 epochs	MSE error after 50000 epochs	MSE error after 100000 epochs
WS3DV1	0.00259	0.00106	0.0009
WS3DV2	0.00025 Performance goal was Reached	Performance goal was Reached	Performance goal was Reached
WS3DV3	0.00041	0.00030	0.00027

Table A 20. MSE performance of the ANN for diferent data pool volumes W3DV1, W3DV2 and W3DV3

Data pool volume	MSE error after 1677 epochs	MSE error after 6000 epochs	MSE error after 10000 epochs
W3DV1	0.000267	0.000103	0.000098
W3DV2	0.000070 Performance goal was Reached	Performance goal was Reached	Performance goal was Reached
W3DV3	0.000096	0.000070 Performance goal was Reached	Performance goal was reached

Table A 21. Effect of learning rate and momentum coefficient in training the ANN using the 2D WS-data. The numbers of epochs are corresponding to reach the ANN to the threshold error for each case.

Learning Rate	Momentum	Epoch	Time(s)	Learning speed
0.002	0	3693	3393.3	2.83
	0.1	4315	2713.8	1.59
	0.3	2638	2544.1	1.43
	0.6	2531	1861.0	1.36
	0.9	1384	1224.8	1.13
0.02	0	3647	1814.4	2.01
	0.1	2000	1379.3	1.45
	0.3	2411	1812.8	1.33
	0.6	1308	730.7	1.79
	0.9	637	478.9	1.33
0.2	0	4000	1459.9	2.74
	0.1	483	405.9	1.19
	0.3	209	178.6	1.17
	0.6	176	167.6	1.05
	0.9	16	20	0.8
1	0	635	341.4	1.86
	0.1	739	671.8	1.10
	0.3	518	319.8	1.62
	0.6	219	123.7	1.77
	0.9	183	146.4	1.25

Table A 22. Effect of learning rate and momentum coefficient in training the ANN using the 2D W-data. The numbers of epochs are corresponding to reach the ANN to the threshold error (0.00006) for each case.

Learning Rate	Momentum	Epoch	Time(s)	Learning speed
0.001	0	4900	1611.8	3.04
	0.2	4015	1723.2	2.33
	0.4	2861	1663.4	1.72
	0.6	1673	1013.9	1.65
	0.8	968	864.3	1.12
0.01	0	4216	1825.1	2.31
	0.2	2845	1962.1	1.45
	0.4	77	90.6	0.85
	0.6	1406	1495.7	0.94
	0.8	866	651.1	1.33
0.1	0	4735	2453.4	1.93
	0.2	649	480.7	1.35
	0.4	559	440.2	1.27
	0.6	388	340.4	1.14
	0.8	217	166.9	1.30
1	0	2312	1313.6	1.76
	0.2	934	924.8	1.01
	0.4	416	261.6	1.59
	0.6	157	121.7	1.29
	0.8	218	171.7	1.27

Table A 23. Effect of learning rate and momentum coefficient in training the ANN using the 2D DD-data. The numbers of epochs are corresponding to reach the ANN to the threshold error (0.0001) for each case.

Learning Rate	Momentum	Epoch	Time(s)	Learning speed
0.001	0	18521	9123.65	2.03
	0.2	8659	6097.89	1.42
	0.4	14887	9482.17	1.57
	0.6	10094	5072.36	1.99
	0.8	9553	8027.73	1.19
0.01	0	3269	2867.54	1.14
	0.2	2282	2402.10	0.95
	0.4	5834	3241.11	1.80
	0.6	8159	4458.47	1.83
	0.8	7598	6279.34	1.21
0.1	0	3908	2605.33	1.50
	0.2	5635	2981.48	1.89
	0.4	9601	5106.91	1.88
	0.6	10214	4621.72	2.21
	0.8	12497	8501.36	1.47
1	0	16097	10385.16	1.55
	0.2	9024	8129.73	1.11
	0.4	24511	12832.98	1.91
	0.6	29005	14648.99	1.98
	0.8	42849	26450.00	1.62

Table A 24. Effect of learning rate and momentum coefficient in training the ANN using the 2D PD-data. The numbers of epochs are corresponding to reach the ANN to the threshold error (0.0002) for each case.

Learning Rate	Momentum	Epoch	Time(s)	Learning speed
0.002	0	10000	2207.5	4.53
	0.2	7629	2311.8	3.30
	0.4	5491	2056.6	2.67
	0.6	3720	1653.3	2.25
	0.8	2396	2047.9	1.17
0.02	0	8959	2434.5	3.68
	0.2	1275	1301	0.98
	0.4	6829	3191.1	2.14
	0.6	6137	2324.6	2.64
	0.8	4217	2451.7	1.72
0.2	0	6876	2292	3.0
	0.2	5455	4040.7	1.35
	0.4	3989	1890.5	2.11
	0.6	2391	2321.4	1.03
	0.8	1990	1644.6	1.21
1	0	7869	2649.5	2.97
	0.2	4780	2914.6	1.64
	0.4	3264	2133.3	1.53
	0.6	2483	2458.4	1.01
	0.8	3201	2623.8	1.22

Table A 25. Effect of learning rate and momentum coefficient in training the ANN using the 2D PP-data. The numbers of epochs are corresponding to reach the ANN to the threshold error (0.0002) for each case.

Learning Rate	Momentum	Epoch	Time(s)	Learning speed
0.002	0	10000	7518.8	1.33
	0.1	10000	5319.1	1.88
	0.3	7651	3255.7	2.35
	0.6	3962	1868.9	2.12
	0.9	2968	2104.9	1.41
0.02	0	10000	6211.2	1.61
	0.1	6359	5728.8	1.11
	0.3	373	282.6	1.32
	0.6	5682	2974.9	1.91
	0.9	3901	3120.8	1.25
0.2	0	10000	6097.6	1.64
	0.1	7639	6419.3	1.19
	0.3	4202	2101.0	2.0
	0.6	3266	3170.9	1.03
	0.9	2136	1405.3	1.52
1	0	10000	5076.1	1.97
	0.1	6875	5635.2	1.22
	0.3	4238	3235.1	1.31
	0.6	3244	2680.9	1.21
	0.9	1989	1969.3	1.01

Table A 26. Effect of learning rate and momentum coefficient in training the ANN using the 3D WS-data. The numbers of epochs are corresponding to reach the ANN to the threshold error (0.00025) for each case.

Learning Rate	Momentum	Epoch	Time(s)	Learning speed
0.02	0	100000	103092.8	0.97
	0.15	100000	89285.7	1.12
	0.30	100000	75757.6	1.32
	0.60	87229	57767.5	1.51
	0.95	80766	60726.3	1.33
	1	79580	48524.4	1.64
0.2	0	100000	87719.3	1.14
	0.15	100000	65789.5	1.52
	0.30	100000	83333.3	1.20
	0.60	78694	56586.4	1.32
	0.95	34077	18520.1	1.84
	1	46139	31387.1	1.47
0.6	0	100000	88495.6	1.13
	0.15	100000	87719.3	1.14
	0.30	86972	53357.1	1.63
	0.60	85680	61200.0	1.40
	0.95	54281	43424.8	1.25
	1	54382	41832.3	1.30
1	0	100000	114942.5	0.87
	0.15	100000	90090.1	1.11
	0.30	100000	60241.0	1.66
	0.60	73897	47068.2	1.57
	0.95	46928	34761.5	1.35
	1	53192	3116.8	1.73

Table A 27. Effect of learning rate and momentum coefficient in training the ANN using the 3D W-data. The numbers of epochs are corresponding to reach the ANN to the threshold error (0.00007) for each case.

Learning Rate	Momentum	Epoch	Time(s)	Learning speed
0.01	0	10000	12048.2	0.83
	0.1	10000	9090.9	1.10
	0.3	10000	8000.0	1.25
	0.6	8694	6392.6	1.36
	0.9	8427	6796.0	1.24
	1	4969	3247.7	1.53
0.1	0	10000	8196.7	1.22
	0.1	10000	7042.3	1.42
	0.3	7638	6472.9	1.18
	0.6	1677	1096.1	1.53
	0.9	5618	3304.7	1.70
	1	5226	4248.8	1.23
0.50	0	10000	8264.5	1.21
	0.1	10000	7936.5	1.26
	0.3	10000	6896.6	1.45
	0.6	7692	5614.6	1.37
	0.9	7124	5887.6	1.21
	1	6385	5700.9	1.12
1	0	10000	10869.6	0.92
	0.1	9682	8275.2	1.17
	0.3	7968	5107.7	1.56
	0.6	8326	6077.4	1.37
	0.9	6768	4423.5	1.53
	1	5967	5375.7	1.11

Table A 28. Effect of learning rate and momentum coefficient in training the ANN using the 3D DD-data. The numbers of epochs are corresponding to reach the ANN to the threshold error (0.0008) for each case.

Learning Rate	Momentum	Epoch	Time(s)	Learning speed
0.02	0	8000	9638.6	0.83
	0.1	8000	7017.5	1.14
	0.3	7921	5955.6	1.33
	0.6	7834	4835.8	1.62
	0.9	6682	4877.4	1.37
	1	5140	3337.7	1.54
0.2	0	8000	7272.7	1.10
	0.1	8000	6015.0	1.13
	0.3	7398	6063.9	1.22
	0.6	4979	3800.8	1.31
	0.9	700	426.8	164
	1	3677	2607.8	1.41
0.4	0	8000	8247.4	0.97
	0.1	7698	5744.8	1.34
	0.3	7501	6000.8	1.25
	0.6	6524	4762.0	1.37
	0.9	5124	4132.3	1.24
	1	4018	3043.9	1.32
0.6	0	8000	7920.8	1.01
	0.1	8000	7207.2	1.11
	0.3	5367	3946.3	1.36
	0.6	4972	3382.3	1.47
	0.9	4666	3049.7	1.53
	1	4000	2836.9	1.41
1	0	8000	9876.5	0.81
	0.1	6791	5432.8	1.25
	0.3	4210	2275.7	1.85
	0.6	4613	3442.5	1.34
	0.9	5470	3798.6	1.44
	1	4019	3464.7	1.16

Table A 29. Effect of learning rate and momentum coefficient in training the ANN using the 3D PD-data. The numbers of epochs are corresponding to reach the ANN to the threshold error (0.000085) for each case.

Learning Rate	Momentum	Epoch	Time(s)	Learning speed
0.01	0	10000	10989	0.91
	0.1	9650	9460.8	1.02
	0.3	9816	8112.4	1.21
	0.6	7398	5173.5	1.44
	0.9	6361	4479.6	1.42
	1	3506	2191.3	1.60
0.1	0	10000	9009	1.11
	0.1	8694	6488.1	1.34
	0.3	5361	4786.6	1.12
	0.6	3357	2707.3	1.24
	0.9	1560	939.8	1.66
	1	3201	2406.8	1.33
0.30	0	10000	9708.7	1.03
	0.1	8679	8508.8	1.02
	0.3	8523	5498.7	1.55
	0.6	5386	4240.9	1.27
	0.9	4212	3694.7	1.14
	1	4115	3578.3	1.15
1	0	10000	10204.1	0.98
	0.1	8339	8256.4	1.01
	0.3	5769	3554.1	1.72
	0.6	4662	3700	1.26
	0.9	3914	2680.8	1.46
	1	3700	3245.6	1.14

Table A 30. Effect of learning rate and momentum coefficient in training the ANN using the 3D PP-data. The numbers of epochs are corresponding to reach the ANN to the threshold error (0.0003) for each case.

Learning Rate	Momentum	Epoch	Time(s)	Learning speed
0.05	0	5000	4550.5	1.01
	0.2	5000	4629.6	1.08
	0.4	3721	2976.8	1.25
	0.6	3558	2068.6	1.72
	0.8	2689	1670.2	1.61
	1	2054	1697.5	1.21
0.15	0	5000	3759.4	1.33
	0.2	4262	2899.3	1.47
	0.4	3600	2322.6	1.55
	0.6	2947	2090.1	1.41
	0.8	1340	917.8	1.46
	1	2366	1908.1	1.24
0.30	0	5000	3472.2	1.44
	0.2	3628	3239.3	1.12
	0.4	4577	3415.7	1.34
	0.6	2395	2119.5	1.13
	0.8	2253	2208.8	1.02
	1	3128	2818.0	1.11
1	0	5000	4672.9	1.07
	0.2	3729	3655.9	1.02
	0.4	4015	2658.9	1.51
	0.6	2733	1687.0	1.62
	0.8	1900	1165.6	1.63
	1	2258	1297.7	1.74

Table A 31. RMS error between the results of the ANN and the corresponding true resistivity distributions for each test set of 2D WS-data

Resistivity of back ground (Ωm)	100	Resistivity of anomaly (Ωm)	300	700	2000	4000
		RMS error (%)	5.8	2.6	2.9	4.1
	200	Resistivity of anomaly (Ωm)	400	800	4000	6000
		RMS error (%)	5.2	1.6	4.9	5.0
	300	Resistivity of anomaly (Ωm)	500	700	5000	7000
		RMS error (%)	3.9	1.0	1.4	1.4
	400	Resistivity of anomaly (Ωm)	600	800	6000	8000
		RMS error (%)	2.8	1.3	2.1	2.5
	500	Resistivity of anomaly (Ωm)	700	900	9000	11000
		RMS error (%)	5.3	0.9	1.1	1.1
	600	Resistivity of anomaly (Ωm)	800	900	15000	20000
		RMS error (%)	4.0	1.4	0.8	1.0

Table A 32. RMS error between the results of the ANN and the corresponding true resistivity distributions for each test set of 2D W-data

Resistivity of back ground (Ωm)	100	Resistivity of anomaly (Ωm)	300	700	2000	4000
		RMS error (%)	6.2	2.9	0.7	2.4
	200	Resistivity of anomaly (Ωm)	400	800	4000	6000
		RMS error (%)	5.7	2.5	1.2	3.6
	300	Resistivity of anomaly (Ωm)	500	700	5000	7000
		RMS error (%)	3.9	1.0	0.8	1.4
	400	Resistivity of anomaly (Ωm)	600	800	6000	8000
		RMS error (%)	5.3	3.3	2.9	4.6
	500	Resistivity of anomaly (Ωm)	700	900	9000	11000
		RMS error (%)	6.0	2.2	3.1	2.5
	600	Resistivity of anomaly (Ωm)	800	900	15000	20000
		RMS error (%)	4.7	3.9	1.1	2.4

Table A 33. RMS error between the results of the ANN and the corresponding true resistivity distributions for each test set of 2D DD-data

Resistivity of back ground (Ωm)	100	Resistivity of anomaly (Ωm)	300	700	2000	4000
		RMS error (%)	5.9	2.7	0.93	1.0
	200	Resistivity of anomaly (Ωm)	400	800	4000	6000
		RMS error (%)	5.1	3.3	1.5	2.0
	300	Resistivity of anomaly (Ωm)	500	700	5000	7000
		RMS error (%)	4.6	3.5	1.6	1.6
	400	Resistivity of anomaly (Ωm)	600	800	6000	8000
		RMS error (%)	5.8	3.0	1.8	2.2
	500	Resistivity of anomaly (Ωm)	700	900	9000	11000
		RMS error (%)	8.2	2.6	1.1	1.4
	600	Resistivity of anomaly (Ωm)	800	900	15000	20000
		RMS error (%)	7.3	6.1	2.7	2.4

Table A 34. RMS error between the results of the ANN and the corresponding true resistivity distributions for each test set of 2D PD-data

Resistivity of back ground (Ωm)	100	Resistivity of anomaly (Ωm)	300	700	2000	4000
		RMS error (%)	7.1	6.5	1.0	2.4
	200	Resistivity of anomaly (Ωm)	400	800	4000	6000
		RMS error (%)	5.9	3.7	1.4	3.5
	300	Resistivity of anomaly (Ωm)	500	700	5000	7000
		RMS error (%)	4.4	2.9	3.2	1.8
	400	Resistivity of anomaly (Ωm)	600	800	6000	8000
		RMS error (%)	5.4	3.9	2.1	2.6
	500	Resistivity of anomaly (Ωm)	700	900	9000	11000
		RMS error (%)	6.7	2.0	3.5	1.8
	600	Resistivity of anomaly (Ωm)	800	900	15000	20000
		RMS error (%)	5.6	4.7	1.5	3.4

Table A 35. RMS error between the results of the ANN and the corresponding true resistivity distributions for each test set of 2D PP-data

Resistivity of back ground (Ωm)	100	Resistivity of anomaly (Ωm)	300	700	2000	4000
		RMS error (%)	6.5	5.1	3.7	3.0
	200	Resistivity of anomaly (Ωm)	400	800	4000	6000
		RMS error (%)	6.2	5.7	3.4	3.1
	300	Resistivity of anomaly (Ωm)	500	700	5000	7000
		RMS error (%)	6.0	5.8	4.5	4.1
	400	Resistivity of anomaly (Ωm)	600	800	6000	8000
		RMS error (%)	5.9	6.0	3.7	4.0
	500	Resistivity of anomaly (Ωm)	700	900	9000	11000
		RMS error (%)	6.4	4.2	3.3	3.1
	600	Resistivity of anomaly (Ωm)	800	900	15000	20000
		RMS error (%)	6.5	5.0	3.9	3.8

Table A 36. RMS error between the results of the ANN and the corresponding true resistivity distributions for each test set of 3D WS-data

Resistivity of back ground (Ωm)	100	Resistivity of anomaly (Ωm)	300	700	2000	4000
		RMS error (%)	8.0	8.0	5.1	3.3
	200	Resistivity of anomaly (Ωm)	400	800	4000	6000
		RMS error (%)	7.7	6.5	4.5	4.2
	300	Resistivity of anomaly (Ωm)	500	700	5000	7000
		RMS error (%)	6.4	5.7	4.7	2.1
	400	Resistivity of anomaly (Ωm)	600	800	6000	8000
		RMS error (%)	7.6	7.4	3.7	2.0
	500	Resistivity of anomaly (Ωm)	700	900	9000	11000
		RMS error (%)	6.4	5.3	3.2	2.0
	600	Resistivity of anomaly (Ωm)	800	900	15000	20000
		RMS error (%)	4.7	4.5	2.7	2.1

Table A 37. RMS error between the results of the ANN and the corresponding true resistivity distributions for each test set of 3D W-data

Resistivity of back ground (Ωm)	100	Resistivity of anomaly (Ωm)	300	700	2000	4000
		RMS error (%)	8.4	7.9	5.1	4.3
	200	Resistivity of anomaly (Ωm)	400	800	4000	6000
		RMS error (%)	7.5	6.4	3.8	3.1
	300	Resistivity of anomaly (Ωm)	500	700	5000	7000
		RMS error (%)	9.0	7.3	5.7	5.1
	400	Resistivity of anomaly (Ωm)	600	800	6000	8000
		RMS error (%)	7.3	6.4	4.7	3.0
	500	Resistivity of anomaly (Ωm)	700	900	9000	11000
		RMS error (%)	7.6	6.7	5.4	3.0
	600	Resistivity of anomaly (Ωm)	800	900	15000	20000
		RMS error (%)	6.6	5.5	4.3	3.4

Table A 38. RMS error between the results of the ANN and the corresponding true resistivity distributions for each test set of 3D DD-data

Resistivity of back ground (Ωm)	100	Resistivity of anomaly (Ωm)	300	700	2000	4000
		RMS error (%)	8.0	6.9	6.2	5.5
	200	Resistivity of anomaly (Ωm)	400	800	4000	6000
		RMS error (%)	7.1	5.9	3.2	5.3
	300	Resistivity of anomaly (Ωm)	500	700	5000	7000
		RMS error (%)	5.7	5.7	3.5	3.0
	400	Resistivity of anomaly (Ωm)	600	800	6000	8000
		RMS error (%)	8.0	6.14	5.0	2.7
	500	Resistivity of anomaly (Ωm)	700	900	9000	11000
		RMS error (%)	6.9	7.6	3.4	3.0
	600	Resistivity of anomaly (Ωm)	800	900	15000	20000
		RMS error (%)	7.7	4.1	4.7	3.8

Table A 39. RMS error between the results of the ANN and the corresponding true resistivity distributions for each test set of 3D PD-data

Resistivity of back ground (Ωm)	100	Resistivity of anomaly (Ωm)	300	700	2000	4000
		RMS error (%)	6.0	5.4	3.5	3.2
	200	Resistivity of anomaly (Ωm)	400	800	4000	6000
		RMS error (%)	5.9	5.1	4.6	2.0
	300	Resistivity of anomaly (Ωm)	500	700	5000	7000
		RMS error (%)	5.9	5.5	4.7	3.1
	400	Resistivity of anomaly (Ωm)	600	800	6000	8000
		RMS error (%)	6.0	5.4	3.8	4.0
	500	Resistivity of anomaly (Ωm)	700	900	9000	11000
		RMS error (%)	6.0	4.7	2.4	3.0
	600	Resistivity of anomaly (Ωm)	800	900	15000	20000
		RMS error (%)	5.8	4.5	3.8	2.2

Table A 40. RMS error between the results of the ANN and the corresponding true resistivity distributions for each test set of 3D PP-data

Resistivity of back ground (Ωm)	100	Resistivity of anomaly (Ωm)	300	700	2000	4000
		RMS error (%)	5.8	4.7	3.0	4.1
	200	Resistivity of anomaly (Ωm)	400	800	4000	6000
		RMS error (%)	6.3	5.5	7.0	9.3
	300	Resistivity of anomaly (Ωm)	500	700	5000	7000
		RMS error (%)	5.4	3.6	6.7	7.8
	400	Resistivity of anomaly (Ωm)	600	800	6000	8000
		RMS error (%)		5.3	0.8	0.9
	500	Resistivity of anomaly (Ωm)	700	900	9000	11000
		RMS error (%)	7.2	4.0	0.7	0.3
	600	Resistivity of anomaly (Ωm)	800	900	15000	20000
		RMS error (%)	9.4	8.5	4.0	2

Bibliography

Al-Amri, A.M., (1998). “The Application of geoelectrical vertical soundings in delineating the hydrostratigraphy of the southern Red Sea coastal area, Saudi Arabia Journal of King Abdulaziz University “. Earth Sciences, 10: 73-90.

al Hagrey, S. A., Schubert-Klempnauer, T., Wachsmuth, D., Michaelsen, J., and Meissner, R. (1999). "Preferential flow: first result of a full-scale flow model." Geophysical Journal International 138: 643–654.

Al-Nuaimy, W., Huang, Y., Nakhkash, M., Fang, M. T. C., Nguyen, V. T., and Eriksen, A. (2000). "Automatic detection of buried utilities and solid objects with GPR using neural networks and pattern recognition." Journal of Applied Geophysics 43(2-4): 157-165.

Aristodemou, E., Pain, C., Oliveira, C.D., Goddard, T. and Harris, C. (2005). "Inversion of nuclear well-logging data using neural networks." Geophysical Prospecting 53: 103 - 120.

Ash, T. (1989). "Dynamic node creation in backpropagation neural networks." Connection Science 1: 365-375.

Ashida, Y. (1996). "Data processing of reflection seismic data by use of neural network." Journal of Applied Geophysics 35(2-3): 89-98.

Barker, R. D. (1992). " A simple algorithm for electrical imaging of the subsurface." First Break 10: 53-62.

Barker, R. D. (1991). "Depth of investigation of collinear symmetrical four-electrode arrays." Geophysics 54: 1031-1037.

Battiti, R. (1992). "First and second order methods for learning: Between steepest descent and Newton's method." Neural Computation 4(2): 141-166.

Baum, E., and Haussler, D. (1989). what size net gives valid generalization? Advances in Neural Information Processing Systems I San Mateo, CA, Morgan Kaufman.

Bentley, L. R., and Gharibi, M. (2004). "Two- and three-dimensional electrical resistivity imaging at a heterogeneous remediation site." Geophysics 69: 674–680.

Bishop, C. M. (1995). Neural Networks for Pattern Recognition. Oxford, Clarendon Press.

Bottraud, J. C., Bornand, M., and Servat, E. (1984). ".Mesures de résistivité appliquées à la cartographie en pédologie." Science du Sol 4: 279–294.

Bowden, G. J., Maier, H. R., and Dandy, G. C. (2002). "Optimal division of data for neural network models in water resources applications." Water Resource Research 38(2): 1-11.

Broyden, C. G. (1970). "The Convergence of a Class of Double-rank Minimization Algorithms " Journal of the Institute of Mathematics and Its Applications 6 *:*76-90.

Broyden, C. G. (1972). Quasi-Newton methods. Numerical methods for unconstrained optimization, New York, Academic Press.

Bui, T. D. (2004). Neural Network Analysis of Sparse Datasets – An Application to the Fracture System In Folds of the Lisburne Formation, Northeastern Alaska, Texas A&M University, pp. 196. Ph.D desertation.

Calderon-Macias, C., Sen, M. and Stoffa, P. (2000). "Artificial neural networks for parameter estimation in geophysics." Geophysical prospecting 48: 21-47.

Carpenter, E. W., and Habberjam, G.M. (1956). " A tri-potential method of resistivity prospecting." Geophysical Prospecting 29: 128-143.

Chambers, J. E., Kuras, O., Meldrum, P.I., Ogilvy, R.D. , and Hollands, J. (2006). "Electrical resistivity tomography applied to geologic, hydrogeologic, and engineering investigations at a former waste-disposal site." Geophysics 71(6): 231-239.

Chambers, J. E., Oglivy, R.D., Kuras, O., Cripps, J.C., Meldrum, P.I. (2001). "3D electrical imaging of known targets at a controlled environmental test site." Environmental Geology 41: 690–704.

Chambers, J., Oglivy, R., Meldrum, P., and Nissen, J. (1999). "3D resistivity imaging of buried oil- and tar-contaminated waste deposits." European Journal of Environmental and Engineering Geophysics 4: 3–15.

Chambers, J. E., Wilkinson,P.B., Weller, A.L., Meldrum, P.I., Ogilvy, R.D., and Caunt, S. (2007). "Mineshaft imaging using surface and crosshole 3D electrical resistivity tomography: A case history from the East Pennine Coalfield, UK." Journal of Applied Geophysics 62: 324-337.

Claerbout, J. F., and Muir, F. (1973). "Robust modeling with erratic data." Geophysics 38(1): 826-844.

Cole, K. S., and Cole, R. H. (1941). " Dispersion and absorption in dielectrics, I: Alternating current fields." Journal of Chemistry and Physics 1: 341–351.

Constable, S. C., Parker, R.L. and Constable, C.G. (1987). "Occam's inversion : A practical algorithm for generating smooth models from electromagnetic sounding data." Geophysics 52: 289-300.

Cranganu, C. (2007). "Using Artificial Neural Networks to predict the presence of overpressured Zones in the Anadarko Basin, Oklahoma." Pure and Applied Geophysics 164: 2067-2081.

Dahlin, T., Bernstone, C., and Loke, M.H. (2002). "A 3-D resistivity investigation of a contaminated site at Lernacken, Sweden." Geophysics 67(6): 1692–1700.

Dahlin, T., and Bernstone, C. (1997). A roll-along technique for 3D resistivity data acquisition with multi-electrode arrays. Symposium on the Applications of Geophysics to Engineering and Environmental Problems (SAGEEP ’97), Reno, Nevada Environmental and Engineering Geophysical Society (EEGS)

Dahlin, T., and Loke, M. H. (1998). " Resolution of 2d Wenner resistivity imaging as assessed by numerical modelling." Journal of Applied Geophysics 38: 237-249.

Dahlin, T., and Loke, M.H. (1997). Quasi-3D resistivity imaging-mapping of three dimensional structures using two dimensional DC resistivity techniques. 3rd Meeting of the Environmental and Engineering Geophysical Society, Aarhus, Geophysical Society.

De Villiers, J., and Barnard, E. (1993). "Backpropagation neural nets with one and two hidden layers." Neural Networks 4(2): 136-141.

Dey, A., and Morrison, H. F. (1979a). " Resistivity modeling for arbitrarily shaped three-dimensional structures." Geophysics 44(4): 753-780.

Dey, A., and Morrison, H. F. (1979b). "Resistivity modelling for arbitrarily shaped two-dimensional structures." Geophysical Prospecting 27(1): 106-136.

Dietrich, P. (1999). Konzeption und Auswertung gleichstromgeoelektrischer Tracerversuche unter Verwendung von Sensitivit¨atskoeffizienten. Institut f¨ur Geologie und Pal¨aontologie, T¨ubingen. Ph.D thesis.

Dobrin, M. B., and Savit, C. H. (1988). Introduction to Geophysical Prospecting. New York, McGraw-Hill.

Drahor, M. G., Kurtulmus T.O, Berge M.A., Hartmann M. , and Speidel M.A. (2008). " Magnetic imaging and electrical resistivity tomography studies in a Roman military installation found in Satala archaeological site, northeastern Anatolia, Turkey." Journal of Archaeological Science 35: 259-271.

Edwards, L. S. (1977). "A modified pseudosection for resistivity and induced-polarization." Geophysics 42: 1020-1036.

Elaine, M. F., and Christopher J. B., (2001). "Sub-basalt imaging problems and the application of Artificial Neural Networks." Journal of Applied Geophysics 48(4): 183-197.

Ellis, R.G., and Oldenburg, D.W. (1994). ".The pole-pole 3-D DC-resistivity inverse problem : a conjugate gradient approach." Geophysical Journal International 119: 187-194.

El-Qady, G., Ushijima, K., and El-Sayed A. (2001). "Inversion of DC resistivity data using neural networks." Geophysical Prospecting 49: 417-430.

El-Qady, G., Ushijima, K., and El-Sayed A. (2000). Delineation of a Geothermal Reservoir by 2D inversion of Resistivity data at Hamam Faraun Area, Sina ,Egypt the World Geothermal Congress, Oita, Japan,.

Farquharson, C. G., and Oldenburg, D. W. (1998). "Non-linear inversion using general measures of data misfit and model structure." Geophysical Journal International 134: 213-227.

Fausett, L. (1994). Fundamentals of Neural Networks Architectures, Algorithms, and Applications. Englewood Cliffs, NJ, Prentice Hall

Fei, D. (1995). Neural network inversion-theory -, principle and application, Columbia University,pp.132. Ph.D thesies.

Friedel, S. (2003). "Resolution, stability and effiency of resistivity tomography estimated from a generalized inverse approach." Geophysical Journal International 153: 305-316.

Friedel, S. (2000). Uber die Abbildungseigenschaften der geoelektrischen Impedanztomographie unter Ber¨ucksichtigung von endlicher Anzahl und endlicher Genauigkeit der Messdaten, Shaker, Aachen, Universit¨at Leipzig. Ph.D thesis.

Friedel, S. (1997). Hochaufl¨osende Geoelektrik - Geoelektrische Impedanztomographie M. Beblo, Berlin, Ernst und Sohn.

Friedel, S., Thielen,A., and Springman,S.M. (2006). "Investigation of a slope endangered by rainfall-induced landslides using 3D resistivity tomography and geotechnical testing." Journal of Applied Geophysics 60: 100–114.

Garson, G. D. (1998). Neural networks: An Introductory Guide for Social Scientists. Thousand Oaks, CA, Sage Publications.

Gemail, K., Samir, A., Oelsner, C. , Mousa, S.E., and Ibrahim, S. (2004). "Study of saltwater intrusion using 1D, 2D and 3D resistivity surveys in the coastal depressions at the eastern part of Matruh area, Egypt." Near Surface Geophysics 2(2): 103-109.

Gharibi, M., and Bentley, L.R. (2005). "Resolution of 3-D Electrical Resistivity Images from Inversions of 2-D Orthogonal Lines." Journal of Environmental and Engineering Geophysics 10(4): 339–349.

Griffiths, D. H., and Barker, R.D. (1993). " Two-dimensional resistivity imaging and modelling in areas of complex geology." Journal of Applied Geophysics 29: 211-226.

Griffiths, D.H., and Turnbull, J. (1985). "A multi-electrode array for resistivity surveying " First Break 3(7): 16 - 20.

Griffiths, D. H., Turnbull, J. and Olayinka, A.I (1990). "Two-dimensional resistivity mapping with a computer- controlled array." First Break 8: 121-129.

Habberjam, G. M., and Watkins, G.E. (1967). "The use of a square configuration in resistivity prospecting.". Geophysical Prospecting 15(445 - 467).

Hagan, M. T., and Menhaj, M. (1994). "Training feed forward networks with the Marquardt algorithms." IEEE Transactions on Neural Networks 5(6): 989–993.

Hagan, M. T., Demuth, H. B., and Beale, M. H. (1996). Neural Network Design. Boston, MA, PWS Publishing.

Haykin, S. (1999). Neural Networks: A Comprehensive Foundation. New Jersey, Prentice Hall, pp.842.

Hesse, A., Jolivet, A., and Tabbagh, A. (1986). "New prospects in shallow depth electrical surveying for archeological and pedological applications." Geophysics 51: 585–594.

Hestenes, C. M. R., and Stiefel, E. (1952). "Methods of conjugate gradients for solving linear systems " Journal of Research of the National Bureau of Standards 49: 409-436.

Hirose, Y., Yamashita,K., and Hijiya,S. (1991). "Back-propagation algorithm which varies the number of hidden units." Neural Networks 4(1): 61-66.

Ho, T. L. (2009). "3-D inversion of borehole-to-surface electrical data using a back-propagation neural network " Journal of Applied Geophysics 68(4): 489-499.

Hornik, K., Stinchcombe,M., and White, H. (1990). "Multilayer feed forward neural networks are universal approximations." Neural Networks 3(4): 359-366.

Inman, J. R. (1975). "Resistivity inversion with ridge regression." Geophysics 40: 798-917.

Jackson, P. D., Earl, S.J., and Reece, G.J. (2001). "3D resistivity inversion using 2D measurements of the electric field." Geophysical Prospecting 49(1): 26-39.

Jakosky, J. J. (1950). Exploration geophysics Los Angeles, Trija Pub. Co, 1195 pp.

Kahoo, R.A., Javaherian, A., and Araabi, N.B. (2006). Seismic deconvolution using Hopfield Neural Network. The 8th SEGJ International Symposium: Imaging and Interpretation, Kyoto, Japan, SEGJ.

Koch, K., Wenninger, J. , Uhlenbrook, S., and Bonell, M. (2009). "Joint interpretation of hydrological and geophysical data: electrical resistivity tomography results from a process hydrological research site in the Black Forest Mountains, Germany." Hydrological Processes 23(10): 1501 – 1513.

Koefoed, O. (1979). Geosounding Principles 1 : Resistivity sounding measurements. Amsterdam, Elsevier Science Publishing Company.

Kuras, O. (2002). The Capacitive Resistivity Technique for Electrical Imaging of the Shallow Subsurface. , University of Nottingham, pp.286. Ph.D thesis.

Lebourg, T., Binet, S., Tric, E., Jomard, H., and El Bedoui, S. (2005). " Geophysical survey to estimate the 3D sliding surface and the 4D evolution of the water pressure on part of a deep seated landslide." Terra Nova 17(5): 399 - 406.

LeCun, Y., Denker, J. S. , and Solla,S. A. (1990). Optimal brain damage. Advances in Neural Information Processing System 2, San Mateo, CA, Morgan Kaufmann Publishers.

Li, Y., and Oldenburg, D. W. (1999). 3D inversion of dc resistivity data using an l-curve criterion. pages 251–254. 69th Annual International Meeting Society of Exploration Geophysics, Houston, USA, SEG.

Li, Y., and Oldenburg, D.W. (1994). "Inversion of 3D DC resistivity data using an approximate inverse mapping." Geophysical Journal International 116: 527-537.

Li, Y., and Oldenburg, D. W. (1992). "Approximate inverse mappings in DC resistivity problems " Geophysical Journal International 109: 343-362.

Lines, L. R., and Treitel, S. (1984). "Tutorial : A review of least-squares inversion and its application to geophysical problems." Geophysical Prospecting 32: 159-186.

Lippman, R. (1987). "An introduction to computing with neural nets." IEEE Transactions on Acoustics, Speech and Signal Processing 4: 4-22.

Loke, M. H. (2009). Tutorial: 2-D and 3-D electrical imaging surveys. www.geoelectrical.com

Loke, M. H., and Barker, R. D. (1996a). "Practical techniques for 3D resistivity surveys and data inversion." Geophysical Prospecting 44: 499–523.

Loke, M. H., and Barker, R. D. (1996b). "Rapid least-squares inversion of apparent resistiity pseudosections by a quasi-Newton method." Geophysical Prospecting 44: 131-152.

Loke, M. H., and Barker, R.D. (1995). "Least-squares deconvolution of apparent resistivity pseudosections." Geophysics 60: 1682-1690.

Loke, M. H., and Dahlin, T. (2002). "A comparison of the Gauss-Newton and quasi-Newton methods in resistivity imaging inversion." Journal of Applied Geophysics 49: 149–162.

Lowry, T., Allen, M. B., and Shive, P. N. (1989). "Singularity removal: A refinement of resistivity modeling techniques." Geophysics 54(6): 766–774.

Mackie, R. L., and Madden, T. R. (1993). "Three-dimensional magnetotelluric inversion using conjugate gradients." Geophysical Journal International 115: 215-229.

Mansoor, M., and Slater, L. (2007). "Aquatic electrical resistivity imaging of shallow-water wetlands" Geophysics 72(5): 211–221.

Matias, S. M. J. (2002). "Square array anisotropy measurments and resistivity souding interpretation." Journal of Applied Geophysics 49: 185 - 194.

Maurer, H., Boerner, D. E., and Curtis, A. (2000). "Design strategies for electromagnetic geophysical surveys." Inverse Problems 16: 1097-1117.

McCormack, M. D., Zaucha, I.D. E., and Dusheck, D. W. (1993). "First-break reflection event picking and seismic data trace editing using neural networks." Geophysics 58(1): 67-68.

McGillivray, P.R., and Oldenburg, D.W. (1990). "Methods for calculating Frechet derivatives and sensitivities for the non-linear inverse problem : A comparative study." Geophysical Prospecting 38: 499-524.

Meju, M. A. (1994a). "Biased estimation: A simple framework for inversion and uncertainty analysis." Geophysical Journal International 119: 521-528.

Menke, W. (1989). Geophysical Data Analysis: Discrete Inverse Theory International Geophysics Series. 45.

Merrick, N. P. (1997). "A new resolution index for resistivity electrode arrays." Exploration Geophysics 28: 106-109.

Minsky, M. L., and Papert, S.A. (1969). Perceptron. Cambridge, MIT press.

Mufti, I. R. (1976). "Finite-difference resistivity modeling for arbitrarly shaped twodimensional structures." Geophysics 41: 62-78.

Murat, M., Rudman, A. (1992). "Automated first arrival picking: a neural network approach." Geophysical Prospecting 40: 587-604.

Narayan, S. (1992). Vertical resolution of two-dimensional dipole-dipole resistivity inversion. 62nd Annual Internationa Meeting of Society Eploration Geophysics, USA, SEG.

Nyquist, J. E., and Roth, M.J.S. (2005). "Improved 3D pole-dipole resistivity surveys using radial measurement pairs." Geophysical Research Letters 32(21): L21504.

Ogilvy, R., Meldrum,P., Chambers, J., and Williams, G. (2002). "The use of 3D electrical resistivity tomography to characterise waste and leachate distributions within a closed landfill, Thriplow, UK." Journal of Environmental and Engineering Geophysics 7: 11–18.

Oglivy, R., Meldrum, P., and Chambers, J. (1999). "Imaging of industrial waste deposits and buried quarry geometry by 3-D resistivity tomography." European Journal of Environmental and Engineering Geophysics 3: 103-113.

Oldenburg, D.W., and Li, Y., (1994). " Inversion of induced polarization data." Geophysics 59: 1327–1341.

Oldenburg, D. W., McGillivray, P. R., and Ellis, R. G. (1993). "Generalized subspace methods for large-scale inverse problems." Geophysical Journal International 114: 12-20.

Pain, C. C., Herwanger, J. V., Saunders, J. H., Worthington, M. H., and de Olivieira, C. R. E. (2003). "Anisotropic resistivity inversion. ." Inverse Problems 19: 1081-1111.

Parasnis, D. S. (1997). Principles of Applied Geophysics. London, Chapman & Hall.

Park, S., Kim, C., Son, J., Yi, M., and Kim, J. (2009). "Detection of cavities in a karst area by means of a 3D electrical resistivity technique." Exploration Geophysics 40: 27–32.

Park, S. K., and Van, G.P. (1991). "Inversion of pole-pole data for 3-D resistivity structure beneath arrays of electrodes." Geophysics 56(7): 951-960.

Pazdirek, O., and Blaha, V. (1996). Examples of resistivity imaging using ME-100 resistivity field acquisition system. EAGE 58th Conference and Technical Exhibition Amsterdam.

Poulton, M., and El-Fouly, A. (1991). Preprocessing GPR signatures for cascading neural network classification. 61st SEG meeting, Houston, USA.

Poulton, M., Sternberg, K., and Glass, C. (1992). "Neural network pattern recognition of subsurface EM images." Journal of Applied Geophysics 29: 21-36.

Powell, M. J. D. (1977). "Restart procedures for the conjugate gradient method." Mathematical programming 12: 241-254.

Pozdnyakova, L., Pozdnyakov, A., and Zhang, R. (2001). ".Application of geophysical methods to evaluate hydrology and soil properties in urban areas." Urban Water 3: 205 – 216.

Press, F. (1968). "Earth models obtained by Monte Carlo inversion." Journal of Geophysical Research 73: 5223-5234.

Reynolds, J. M. (1997). An introduction to applied and environmental geophysics. New York, John Wiley & Sons.

Rhoades, J. D., and Schilfgaarde, V.J. (1976). " An electrical conductivity probe for determining soil salinity." Soil Science Society of America Journal 40: 647–651.

Riedmiller, M., and Braun, H. (1993). A direct adaptive method for faster backpropagation learning:The RPROP algorithm. Proceedings of the IEEE International Conference on Neural Networks (ICNN), San Francisco.

Ripley, B. D. (1996). Pattern Recognition and Neural Networks. Cambridge, Cambridge University Press

Rodi, W., and Mackie, R. L. (2001). " Nonlinear conjugate gradients algorithm for 2-d magnetotelluric inversion." Geophysics 66(1): 174-187.

Rosenblatt, F. (1962). Principles of neuro-dynamics, Spartan books.

Roy, A., and Apparao, A. (1971). " Depth of investigation in direct current methods." Geophysics 36: 943-959.

Rumelhart, D. E., and McClelland,J. L. (1986). Parallel Distributed Processing: Explorations in the Microstructure of Cognition Cambridge, MA, MIT Press.

Sasaki, Y. (1994). "3D resistivity inversion using the finite-element method." Geophysics 59(12): 1839–1848.

Sasaki, Y. (1992). "Resolution of resistivity tomography inferred from numerical simulation." Geophysical Prospecting 40: 453-464.

Scales, L. E. (1985). Introduction to non-linear optimization. New York, Springer-Verlag.

Seaton, W. J., and Burbey, T.J. (2002). "Evaluation of two-dimensional resistivity methods in a fractured crystalline-rock terrane." Journal of Applied Geophysics 51: 21–41.

Seigel, H. O. (1959). "Mathematical formulation and type curves for induced polarization." Geophysics 24
547–565.

Shewchuk, J. R. (1994). An introduction to the conjugate gradient method without the agonizing pain, Carnegie Mellon University.

Singh, U. K., Tiwari, R. K., and Singh, S. B. (2005). "One-dimensional inversion of geoelectrical resistivity sounding data using artificial neural networks-a case study." Computers & Geosciences 31: 99–108.

Soupios, P. M., Loupasakis, C., and Vallianatos, F. (2008). "Reconstructing former urban environments by combining geophysical electrical methods and geotechnical investigations—an example from Chania, Greece." Journal of Geophysics and Engineering 5: 186–194.

Spitzer, K. (1999). Development of three-dimensional finite difference resistivity, sensitivity, and IP forward modeling techniques and their application to surface and borehole surveys., University of Leipzig. Habilitation thesis.

Spitzer, K. (1998). "The three-dimensional dc sensitivity for surface and subsurface sources." Geophysical Journal international 134: 736–746.

Spitzer, K. (1995). "A 3-*D* finite-difference algorithm for dc resistivity modelling using conjugate gradient methods." Geophysical Journal International 123: 903-914.

Spitzer, K. , and Wurmstich, B. (1995). Speed and Accuracy in 3D Resistivity Modeling. International Symposium on Three-Dimensional Electromagnetics, Ridgefield, Connecticut,USA, Schlumberger-Doll Research.

Stummer, P., Maurer, H., and Green, A. G. (2004). "Experimental design: Electrical resistivity data sets that provide optimum subsurface information." Geophysics 69(1): 120–139.

Sugimoto, Y. (1999). "Shallow high-resolution 2–d and 3–d electrical crosshole imaging " The Leading Edge 18: 1425–1428.

Tarantola, A. (1986). " A strategy for nonlinear elastic inversion of reflection data." Geophysics 51: 1893 - 1903.

Tarantola, A. (1987). Inverse problem theory, methods for data fitting and model parameter estimation. Amsterdam and New York, Elsevier.

Telford, W. M., Geldart, L. P., and Sheriff, R. E. (1990). Applied Geophysics, Cambridge University Press.

Thomas, G. (2004). Inversion Methods and Resolution Analysis for the 2D/3D Reconstruction of Resistivity Structures from DC Measurements, university of Freiberg, pp.160 Ph.D thesis.

Tong, L. a. Y., C. (1990). "Incorporation of topography into two-dimensional resistivity inversion " Geophysics 55(3): 354–361.

Tripp, A. C., Hohmann, G. W., and Swift, C. M. (1984). " Two-dimensional resistivity inversion." Geophysics 49(10): 1708-1717.

Van, N. R., and Cook, K.L. (1966). Interpretation of resistivity data Washington: 310.

Vogel, C. R. (2002). Computational Methods for Inverse Problems. Frontiers in applied mathematics. Philadelphia, PA, Society for Industrial and Applied Mathematics.

Wang, L. X., and Mendel, J.M. (1992). "Adaptive minimum perdiction – error deconvolution and source wavelet estimation." Geophysics 57: 670-679.

Werbos, P. J. (1994). The roots of Back-propagation New York, John Wiley &Sons, Inc.

Wessels, L., and Barnard, E. (1992). "Avoiding false local minima by proper initialization of connections." IEEE Transactions on Neural Networks 3: 899-905.

Wiener, J., Rogers, J., Moll, R. (1991). Predicting carbonate permeabilities from wireline logs using a back-propagation neural network. 61st SEG meeting, Houston, USA.

Winkler, E. (1994). Inversion of electromagnetic data using neural networks. 56th EAEG meeting, Vienna, Austria, p.124.

Yi, M. J., Kim,J.H., Song,Y., Cho, S.J., Chung, S.H., and Suh, J.H. (2001). "Three-dimensional imaging of subsurface structures using resistivity data." Geophysical Prospecting 49: 483-497.

Zhang, J., Mackie, R. L., and Madden, T. R. (1995). "3D resistivity forward modeling and inversion using conjugate gradients." Geophysics 60(5): 1313-1325.

List of publications

The following technical papers have been published based on the basis of this research:

1) Neyamadpour, A; Taib, S; Abdullah, WATW; Neyamadpour, B. (2010). **"Comparison of Wenner and dipole-dipole arrays in the study of an underground three dimensional cavity"** *Journal of Geophysics and Engineering,* 7, 1, 30-40.

2) Neyamadpour, A; Taib, S; Abdullah, WATW. (2010). **"Use of Artificial Neural Networks to Invert Quasi-3D DC Resistivity Imaging Data"**. *Journal of Earth System Science*, 119, 1**,** 1-14

3) Neyamadpour, A; Taib, S; Abdullah, WATW. (2010)**." Use of four–electrode arrays in three-dimensional electrical resistivity imaging survey"**. *Studia Geophysica et Geodaetica,* 54, 2, 299 – 311.

4) Neyamadpour, A; Taib, S; Abdullah, WATW; Neyamadpour, D. (2010). **"Inversion of 3D DC data using artificial neural networks".** Accepted to publish in *Studia Geophysica et Geodaetica*

5) Neyamadpour, A; Taib, S; Abdullah, WATW. **"Field test to compare 3D imaging capabilities of three arrays in a site with high resistivity contrast regions"**. Accepted to publish in *Studia Geophysica et Geodaetica.*

6) Motadelrou, Y., Taib, S., Hashim, R., Neyamadpour, A. (2010). **"** Geoelectrical and hydrochemical study of Taman Beringin landfill, Kuala Lumpur, Malaysia*".* *Submitted to Journal of Geophysics and Engineering.*

7) Neyamadpour, A; Taib, S; Abdullah, WATW. (2009).**" Using artificial neural networks to invert 2D DC resistivity imaging data for high resistivity contrast regions: A MATLAB application"**. *Computers & Geosciences*, 35, 11, 2268-2274.

8) Neyamadpour, A; Taib, S; Abdullah, WATW. (2009). "**An application of three-dimensional electrical resistivity imaging for the detection of an underground waste-water system**"**,** *Studia Geophysica et Geodaetica,* 53, 3, 389-402.

9) Neyamadpour, A; Abdullah, WATW; Taib, S. (2009). **"Use of Artificial Neural Networks to Invert 3D Electrical Resistivity Imaging Data"**. *Frontiers in Physics, 3rd International Meeting on Fronties in Physics*, *JAN 12-16, 2009 Kuala Lumpur MALAYSIA,***,** 1150, 210-213.

10) Neyamadpour, A; Taib, S; Abdullah, WATW. (2008). **"Inversion of 2D DC resistivity data for high resistivity contrast regions using artificial neural network"**. *New Aspects of Engineering Mechanics, Structures, Engineering Geology, WSEAS International Conference on Engineering Mechanics, Structures, and Engineering Geology*, *JUL 22-24, 2008 Heraklion GREECE* ,186-194.

11) Neyamadpour A., Samsudin Taib & Abdullah W.A.T.W. (2008). **"Comparative study on inversion of 2D DC resistivity conventional procedures to a newly developed artificial neural network approach"**. *Geoconservation, geotourism and geohazard" June 1-3 2008, Impiana Casuarina Hotel, Ipoh, Perak Darul Ridzuan, Malaysia, submitted to Journal of Geological Society of Malaysia.*

Ahmad Neyamadpour
Kuala Lumpur, Malaysia
January, 2010